Dissertation zur Erlangung
des akademischen Grades des
Doktors der Naturwissenschaften (Dr. rer. nat.)
an der Universität Konstanz
Fachbereich Physik

vorgelegt von

Luca Chirolli

QUANTUM CONTROL AND QUANTUM MEASUREMENT IN SOLID STATE QUBITS

Tag der mündlichen Prüfung:
12.01.2010

Referenten:

Prof. Dr. Guido Burkard

Prof. Dr. Rosario Fazio

Konstanzer Online-Publikations-System (KOPS)
URN: http://nbn-resolving.de/urn:nbn:de:bsz:352-opus-12510
URL: http://kops.ub.uni-konstanz.de/volltexte/2010/12510/

Abstract

In the past two decades significant theoretical and experimental efforts have been devoted to the study and development of mesoscopic devices, that exploit quantum coherence at the nanoscale. Quantum computing represents an emerging promising field of science and technology and is currently subject of extensive investigation. One of the fundamental issues, that still represents a major obstacle to the realization of a quantum computer, is certainly decoherence. The interaction of a quantum system with the external environment is what ultimately limits the efficiency of a quantum device. On the other hand, in order to perform precise tasks and implement quantum algorithms, it is necessary to address the quantum devices from the lab. It is therefore desirable to achieve full control and to minimize the detrimental residual interaction. Control protocols and read out schemes are still performed on a basic level and many aspects of the communication between the quantum systems and the external environment need still to be investigated from a fundamental point of view.

In this thesis we address two fundamental topics: the control and the measurement of quantum bits. We mostly focus our attention on a particular type of superconducting two-level systems (qubits), the flux qubit, that may represent the fundamental building block of a scalable architecture for quantum computing based on superconducting solid state devices.

We begin with an Introduction (Ch. 1). Then in the chapter 2 we study a voltage-controlled version of the superconducting flux qubit and show that full control of qubit rotations on the entire Bloch sphere can be achieved. Circuit graph theory is used to study a setup where voltage sources are attached to the two superconducting islands formed between the three Josephson junctions in the flux qubit. Applying a voltage allows qubit rotations about the y axis, in addition to pure x and z rotations obtained in the absence of applied voltages. The orientation and magnitude of the rotation axis on the Bloch sphere can be tuned by the gate voltages, the external magnetic flux, and the ratio α between the Josephson energies via a flux-tunable junction. We compare the single-qubit control in the known regime $\alpha < 1$ with the previously unexplored range $\alpha > 1$ and estimate the decoherence due to voltage fluctuations.

In chapter 3 we theoretically describe the weak measurement of a qubit and quantify the degree to which such a qubit measurement has a quantum non-demolition (QND) character. The qubit is coupled to a harmonic oscillator which undergoes a projective measurement. Information on the qubit state is extracted from the oscillator measurement outcomes, and the QND character of the measurement is inferred from the result of subsequent measurements of the oscillator. We use the positive operator valued measure (POVM) formalism to describe the qubit measurement. Two mechanisms lead to deviations from a

perfect QND measurement: (i) the quantum fluctuations of the oscillator, and (ii) quantum tunneling between the qubit states $|0\rangle$ and $|1\rangle$ during measurements. Our theory can be applied to QND measurements performed on superconducting qubits coupled to a circuit oscillator.

In chapter 4 we depart from qubit systems and consider the electronic transport through coherent and partially coherent systems. Based on novel and prototypical electronic interferometric setups, we show that it is possible to realize interaction free measurements in solid state nanodevices. We discuss three different implementations. The first one is very close to the optical proposal and it is based on a series of concatenated Mach-Zehnder interferometers. We also discuss the case in which the interaction free measurement is realized by means of an asymmetric Aharonov-Bohm ring and the case in which coherent single-electron sources are used. For all the three cases we show how to detect the effect through a measurement of the current passing through the device. Beside the interest in realizing a fundamental interferometric effect with electrons known from measurements measured with photons, interaction free measurements in nanoelectronics may play a fundamental role as very accurate measuring devices. We show this by discussing how to reveal the presence of a dephasing source. In addition to the accuracy the new key ingredient here is that a flux of electrons may measure noise without any degradation of its coherence properties.

In chapter 5 we theoretically propose to directly observe the chiral nature of charge carriers in graphene mono- and bilayers within a controlled scattering experiment. The charge located on a capacitively coupled scanning probe microscope (SPM) tip acts as a scattering center with controllable position on the graphene sheet. Unambiguous features from the chirality of the particles in single and bilayer graphene arise in the ballistic transport in the presence of such a scattering center. To theoretically model the scattering from the smooth potential created by the SPM tip, we derive the space-dependent electron Green function in graphene and solve the scattering problem within first-order Born approximation. We calculate the current through a device with an SPM tip between two constrictions (quantum point contacts) as a function of the tip position.

In chapter 6 we consider a system of two superconducting transmission line resonators coupled by an externally driven SQUID. In the low temperature regime, each of the two resonators can be described by its lowest frequency bosonic degree of freedom. The SQUID dynamics can be effectively described by an externally controllable inductance that mediates a quadratic interaction between the two transmission line resonators. Such a system is suitable for the implementation of a qubit in which one photon is shared between the two superconducting transmission line resonators. In the direction of linear optics quantum computation, we consider a beam splitting operation in this system. An equal weight superposition of the states $|1\rangle_1|0\rangle_2$ and $|0\rangle_1|1\rangle_2$ is obtained by applying a driving to the initial state $|1\rangle_1|0\rangle_2$. We study the quality of rotating wave approximation by computing the fidelity of the beam splitting operation with the exact solution of the time dependent problem and compare it to the fidelity in the rotating wave approximation.

Zusammenfassung

In den letzen zwei Jahrzehnten sind erhebliche theoretische und experimentelle Anstrengungen zur Erforschung und Entwicklung von mesoskopischen Bauteile, die Quantenkohärenz auf der Nanometerskala nutzen, unternommen worden. Das Quantenrechnen stellt ein neues und vielversprechendes Gebiet der Wissenschaft und Technik dar und ist derzeit Gegenstand von umfassenden Untersuchungen. Ein fundamentales Hindernis bei der Realisierung eines Quantencomputers ist sicherlich Dekohärenz. Es ist die Interaktion mit der Aussenwelt, die letztendlich die Effizienz eines quantenmechanischen Bauteils begrenzt. Um aber effektive Quantenalgorithmen implementieren zu können, ist es notwendig, dass die Bausteine mit der Umgebung kommunizieren. Es ist daher notwendig, volle Kontrolle über die ablaufenden Prozesse zu erlangen und die unerwünschten Wechselwirkungen auf ein Minimum zu reduzieren. Die Entwicklung von Kontroll- und Auslesealgorithmen befindet sich derzeit noch immer auf einer elementaren Ebene. Viele Aspekte der Kommunikation zwischen Quantensystemen untereinander sowie mit ihrer Umgebung bedürfen auch weiterhin grundlegender Untersuchungen.

In dieser Arbeit befassen wir uns im wesentlichen mit zwei grundlegenden Themen: Dem Kontrollieren und Auslesen von Quantenbits. Wir wenden unser Hauptaugenmerk auf einen speziellen Typus supraleitender Zwei-Zustandssysteme (d.h. Qubits), dem sogenannten Flussqubit (flux qubit). Dieses ist prädestiniert als fundamentaler Baustein für die Realisierung von skalierbaren, auf supraleitender Technologie basierenden Quantencomputern.

Nach einer Einleitung in Kapitel 1, untersuchen wir in Kapitel 2 die spannungskontrollierte Version des supraleitenden Flussqubits und demonstrieren, dass die volle Kontrolle über Rotationen auf der Blochkugel möglich ist. Mit Hilfe der Schaltungsgraphentheorie untersuchen wir eine Anordnung bei der zwei Spannungsquellen an die beiden supraleitenden Inseln, die sich zwischen den drei Josephsonkontakten im Flussqubit bilden, angeschlossen sind. Das Anlegen einer Spannung erlaubt die Rotation des Qubits um die y-Achse, zusätzlich zu den reinen Rotationen um die x- und die z-Achse, die auch in Abwesenheit einer externen Spannung auftreten. Die Größe und Orientierung der Drehung auf der Blochkugel lässt sich steuern durch Elektrodenspannung, dem externen magnetischen Fluss, sowie dem Verhältnis α der Josephsonenergien. Wir vergleichen die Kontrolle eines einzelnen Qubits in dem bekannten Regime $\alpha < 1$ mit dem bisher unerforschtem Regime $\alpha > 1$ und geben Abschätzungen der Dekohärenz aufgrund von Spannungsschwankungen.

In Kapitel 3 widmen wir uns der theoretischen Beschreibung der schwachen Messung eines Qubits und quantifizieren in welchem Grad eine solche Messung einen nichtzerstörenden (quantum nondemolition, QND) Charakter besitzt. Das Qubit ist an einen harmonischen Oszillator gekoppelt, an welchem eine projektive Messung durchgeführt wird. Über

Messungen des Oszilators lassen sich Informationen über den Zustand des Qubits erhalten, sowie Aussagen über den QND Charakter der Messungen ableiten. Wir verwenden den POVM Formalismus um die Messung am Qubit zu beschreiben. Zwei Mechanismen führen zu Abweichungen von einer idealen QND Messung: (i) die Quantenfluktuationen des Oszilators, sowie (ii) das Quantentunneln zwischen den Qubitzuständen $|0\rangle$ und $|1\rangle$ während des Messvorgangs. Unsere Theorie lässt sich auf nichtzerstörende Messungen an Oszilatoren in der Schaltung gekoppelte supraleitenden Qubits anwenden.

In Kapitel 4 verlassen wir das Gebiet der supraleitenden Qubits und wenden uns dem elektronischen Transport in kohärenten und semikohärenten Systeme zu. Wir zeigen, dass es möglich ist, mit Hilfe von neuartigen und prototypischen elektronischen Interferometern, wechselwirkungsfreie Messungen in Nanostrukturen durchzuführen. Wir diskutieren drei verschiedene Implementierungen. Die erste ist an Vorschläge aus der Optik angelehnt und basiert auf einer Reihe von verketteten Mach-Zehnder Interferometern. Ferner betrachten wir den Fall in dem wechselwirkungsfreie Messungen mit Hilfe eines asymmetrischen Aharanov-Bohm Rings möglich sind, sowie den einer kohärenten Elektronenquelle. Für alle drei Fälle zeigen wir wie sich der Effekt durch die Messung von Strömen durch die Strukturen nachweisen lässt. Neben der Möglichkeit der Realisierung von fundamentalen interferometrischen Effekten mit durch Photonen gemessenen Elektronen, bildet die QND Messung die Grundlage für ultrapräzise neuartige Messmethoden. Wir demonstrieren dies, in dem wir zeigen, wie sich die Anwesenheit von Dekohärenz induzierenden Quellen nachweisen lässt. Zusätzlich zu der hohen Genauigkeit ist ein wesentlicher Bestandteil, dass mit Hilfe des Elektronenflusses Rauschen gemessen werden kann, ohne Verlust der Kohärenz.

In Kapitel 5 zeigen wir, wie es theoretisch möglich ist die chirale Natur der Ladungsträger in ein- und zweilagigem Graphen mit Hilfe eines kontrollierten Streuexperiments direkt zu beobachten. Die Ladung auf der Spitze eines Rastersondenmikroskops (SPM) agiert dabei als frei positionierbares Streuzentrum auf der Graphenoberfläche. Die besonderen Merkmale der chiralen Teilchen treten in solchen ballistischen Transportexperimenten in Anwesenheit von Streuzentren in Erscheinung. Um die Streuprozesse an dem, von der SPM-Spitze verursachtem, glatten Potential theoretisch zu modellieren, leiten wir die ortsabhängige elektronische Green-Funktion her und lösen das Streuproblem in der Bornschen Näherung. Wir berechnen den Strom durch die Nanostruktur mit einer SPM-Spitze zwischen den beiden seitlichen Begrenzungen (Quantenpunktkontakte) als Funktion der Position der Spitze.

In Kapitel 6 betrachten wir das Problem zweier supraleitender Transmission Line Resonatoren, welche durch ein extern gesteuertes SQUID gekoppelt sind. Bei niedrigen Temperaturen kann jeder der Resonatoren durch seinen tiefsten bosonischen Freiheitsgrad beschrieben werden. Die Dynamik des SQUIDs lässt sich kann durch eine extern kontrollierte Induktivität, welche eine quadratische Wechselwirkung zwischen den beiden Transmission Line Resonatoren vermittelt. Ein solches System eignet sich für die Implementierung eines Qubits, in welchem ein Photon in beiden Resonatoren lebt. Mit Hinblick auf Quantenrechnen mit linearer Optik untersuchen wir einen Strahlteiler in diesem System. vollständige Superposition der Zustände $|1\rangle_1|0\rangle_2$ und $|0\rangle_1|1\rangle_2$ wird durch anlegen eines Wechselfeldes aus dem Zustand $|1\rangle_1|0\rangle_2$ erzeugt. Wir untersuchen die Anwendbarkeit der

Rotating Wave Approximation, indem wir die Güte der Strahlteilungsoperation mit Hilfe der exakten Lösung des zeitabhängigen Problems berechnen und das Ergebnis mit der, in der Rotating Wave Approximation, berechnete Güte vergleichen.

Acknowledgments

It is a great pleasure for me to thank my thesis supervisor Prof. Guido Burkard for his trust and support during four years of work in a very interesting field of physics. I am thankful for the time he spent with me in explaining physics, for sharing his points of view in invaluable discussions and for the possibility he gave me to make new physics together with him. Under his guidance I learnt to always look for a clear physical explanation. We have traveled a lot together, we moved two times and it was demanding for me, but I'm very very glad that at the end I was able to make it. That was actually a great occasion of human and scientific growth for me. I had the possibility live in different countries, to learn from many different scientific environments, to share a lot of ideas with very good physicists and to meet a lot of friends, starting from the very beginning in Basel, going through Aachen, Pisa and finally arriving in Konstanz.

In particular I thank Prof. Guido Burkard for the possibility he gave me to spend one year in Pisa for an invaluable scientific collaboration with Prof. Rosario Fazio and his group. I am very grateful to Prof. Rosario Fazio for the many discussions we had and for the time he spent with me doing physics. My thanks in particular to Dr. Vittorio Giovannetti and Dr. Fabio Taddei with whom I had many interesting and useful discussions.

During the period in Basel I had to possibility to share a lot with the very interesting and dynamical groups of Prof. Daniel Loss and Prof. Christoph Bruder. I learned a lot by taking part to numerous discussions and I am very grateful to all the people that I met there.

Besides the omnipresent invaluable contribution of Prof. Guido Burkard, I would like to acknowledge the contributions to this thesis due to Prof. Rosario Fazio, Dr. Vittorio Giovannetti, Dr. Fabio Taddei, Dr. Vincenzo Piazza, Dr. Elia Strambini, Dr. Matthias Braun and Dr. David DiVincenzo.

In four years I shared my office with many people and my thanks go to all of them. In particular, Hugo Ribeiro, with whom I shared many discussions in the office, Philipp Struck, that helped me with the German language, Dr. Dimitrije Stepanenko and Dr. Matthias Braun, that where part of the group in Basel and Aachen, and all the new entries of the group in Konstanz. From the people that I met in Aachen certainly I want to mention Christian Kasztelan and Dr. Guillaume Roux, with whom I spent a great time. I would like to thank all the many colleagues that I had in Basel, in particular Dr. Bill Coish, Dr. Massoud Borhani, Dr. Jörg Lehmann, Dr. Charles Doiron, Jan Fischer, Oded Zilberberg and Dr. Andreas Kleine, with whom I spent most of my time and had a lot of fun.

Finally, I would like to thank my brother, my parents and all my dearest friends in Italy that never thought that distance could keep us apart.

Contents

Abstract i

Zusammenfassung iii

Acknowledgments vii

1 Introduction 1
- 1.1 Quantum computation 2
  - 1.1.1 The qubit 2
  - 1.1.2 Quantum logic gates 4
  - 1.1.3 Decoherence and Bloch equations 6
  - 1.1.4 Superconducting qubits 7
- 1.2 The measurement process 10
  - 1.2.1 The theory of quantum measurements 12
  - 1.2.2 Indirect measurements 13
  - 1.2.3 Quantum nondemolition measurements 15
- 1.3 Quantum transport 18
  - 1.3.1 Scattering theory 19
  - 1.3.2 The Landauer formula 21
- 1.4 Graphene 22
  - 1.4.1 Tight-binding approach 23
  - 1.4.2 Massless Dirac fermions 23
- References 25

2 Voltage Controlled Flux Qubit 27
- 2.1 Introduction 27
- 2.2 The circuit 29
- 2.3 Born-Oppenheimer approximation 32
- 2.4 Quantum dynamics 33
- 2.5 Bloch theory 35
  - 2.5.1 The periodic problem 35
  - 2.5.2 Tight-binding approximation 36
  - 2.5.3 Effect of a voltage bias 38
- 2.6 Calculation of t_1 and t_2 39
- 2.7 Full control for $\alpha > 1$ 43
- 2.8 Charge decoherence 45

2.9 Results and conclusions 49
References 50

3 QND measurement of a qubit coupled to a harmonic oscillator 53

3.1 Introduction 53
3.2 Model: quadratic coupling 56
3.3 Single measurement 58
3.4 Effects of the tunneling $\boldsymbol{\sigma}_X$ term 60
3.5 Two subsequent measurements 61
3.6 Ideal single measurement 63
  3.6.1 Short time 64
3.7 Corrections due to tunneling 65
3.8 QND character of the qubit measurement 69
  3.8.1 Ideal QND measurement 69
  3.8.2 First order contribution 70
  3.8.3 Second order contribution 71
3.9 Rabi oscillations between measurements 71
3.10 Conclusion 75
References 76

4 Electronic implementations of Interaction-Free Measurements 79

4.1 Introduction 79
4.2 Coherent detection of noise with IFMs 81
  4.2.1 Detection of a dephasing noise source 83
  4.2.2 Coherence of the outgoing signal 86
4.3 Detection of the coherent signal 87
4.4 Multiple interference in the time domain 89
4.5 IFM with an Aharonov-Bohm ring 93
  4.5.1 Transmission in the presence of a dephasing field 96
  4.5.2 Current as a measure of coherence 97
4.6 Conclusion 99
References 100

5 Scanning probe imaging of chiral charge flow in graphene 103

5.1 Introduction 103
5.2 Green's function in graphene 105
5.3 Stepwise cylindrical potential 106
5.4 Imaging chiral charge flow 108
5.5 Conclusion 110
References 110

6 Photon beam splitting with superconducting resonators 113

6.1 Introduction 113

- 6.2 Effective model 114
  - 6.2.1 Quantum Hamiltonian 116
- 6.3 Rotating wave approximation 116
  - 6.3.1 Beam splitting fidelity in the RWA 118
- 6.4 Equations of motion 118
- 6.5 Beam splitting fidelity 120
- 6.6 Conclusion 123
- References 123

A Matrices $\mathcal{C}$, C_V , M_0, and N 125

B The functions $\mathcal{F}_1$ and $\mathcal{F}_\phi$ 127

C Perturbation theory in Δ 129

D First and Second order contribution to the two-measurement POVM 131

E Eigenvalue problem 133

F Double ring transmission and reflection amplitudes 135

G Electron-hole switch 137

H Inductance Matrices 139

Curriculum Vitae 141

Publications 143

1. Introduction

The world that we experience in our every day life is governed by the classical laws of physics. The description of the physics of macroscopic objects hinges upon few simple and elegant concepts about the motion of objects and their mutual interaction. Our understanding of physics as the rules of the game, our conscious and unconscious awareness of what happens and why, our physical intuition are truly based on these principles.

At the beginning of the 20th century a scientific revolution took place with the discovery of a new world, that was unaccessible before, and was not describable with the knowledge at that time available and referable to the classical laws of motion. The advances in the technology made it possible to experimentally address objects whose microscopic scale had always confined their cognizance solely to a speculative level. A new point of view started to be shared among physicists, according to which concepts of wavefunction and quantized levels were more suitable to describe the physics of a particle, rather than exact position and exact momentum, that in turn became no longer simultaneously accessible. A more complex mathematical approach made it possible to understand an innumerable quantity of phenomena, like the quantization of the atomic spectra, based on the energy level quantization, the photoelectric effect, that associates a particle-like nature to light, until the very atomic structure itself. The scientific observation and speculation, guided by the application of the principle of cause and effect, gave birth in 1900 to the theory of quantum mechanics, that describes the physics of the microscopic world.

After decades of theoretical clarifications and predictions and experimental confirmations and achievements had consolidated the theory of quantum mechanics, physicists began to wonder about the possibilities that the knowledge acquired about the quantum world could provide them in terms of applications. The idea of using the quantum laws as a new playground for solving very hard problems, together with the technological advances in the realization and control of systems at the microscopic scale, gave birth to a new perspective, in which the quantum world is a resource.

The idea of a quantum computer, in which objects that work according to the laws of quantum mechanics may perform very difficult tasks and provide a new tool in the future for our every day life, broke through at the end of the 20th century and is currently subject of extensive study. The very concepts on which a quantum computer is based are fundamental issues of the quantum world, with no classical analogue. The state of a quantum system may be a superposition of fundamental states, that individually may have a classical counterpart, but represent, once superimposed, a completely new manifestation of a system. Such a property goes under the name of superposition principle. More systems can share non-local correlations between their constituting parts, that cannot be understood classically. Such states contain a resource of paramount importance for the new applications of a quantum computer, known as quantum entanglement.

1.1 Quantum computation

Coherence, as a property of quantum mechanical phenomena, disappears in the classical world. Our experience of the quantum world is filtered by the environment that surrounds the quantum objects. It is never completely possible to isolate a quantum system from the surrounding world. The system and its surrounding interact and, as a result, a randomization of the phase of the quantum system takes place, resulting in a loss of information. This process is known as decoherence.

Only in recent years, thanks to the advances in technology, it has become possible to study quantum effects involving single quantum objects, like single photons, ions, electron spins, etc... Particular attention has been devoted to see coherence, from an experimental point of view, and to understand its limitation. In fact, though remarkable improvements have been achieved, even nowadays, a lot of effort must be spent to understand how to preserve coherence. In quantum information theory, which deals with the possibilities that quantum rules offer to information processing, coherence is a fundamental requirement. The physical implementation of quantum information processing represents a challenge because one has to deal with the competition between fast and reliable quantum control, that requires interaction with the outside world, and good isolation of the quantum devices in order to ensure long coherence times.

1.1.1 The qubit

Classical information is based on binary logic, in which information is encoded in a series of bits (binary digits) that can assume only two values, 0 or 1. A typical example is a switch, with its two possible states “on” and “off”, which are separated by a potential barrier sufficiently large to avoid spontaneous switching. In classical information, dissipation typically stabilizes the classical bits. All classical logical operations can be implemented as algorithms based on one- and two-bit operations, the so-called logic gates.

The building block of quantum information is the quantum bit, or qubit. Using the Dirac notation, the two fundamental states that characterize the qubit are $|0\rangle$ and $|1\rangle$ and they represent the quantum counterpart of the classical 0 and 1. A fundamental law of quantum mechanics is the superposition principle, which according to R. P. Feynman “contains the essence of quantum mechanics” [1]. A general pure state of a qubit can be written as a coherent superposition of the two fundamental qubit states

$$|\psi\rangle = \alpha|0\rangle + \beta|1\rangle, \tag{1.1}$$

with α and β complex numbers, characterized by a relative phase and by $|\alpha|^2 + |\beta|^2 = 1$. According to “Born's rule”, $|\alpha|^2$ represents the probability for the qubit to be in the state $|0\rangle$, whereas $|\beta|^2$ represents the probability to be in $|1\rangle$. This means that if we prepare many copies of the same system in the state $|\psi\rangle$, a measurement of the state of the qubit

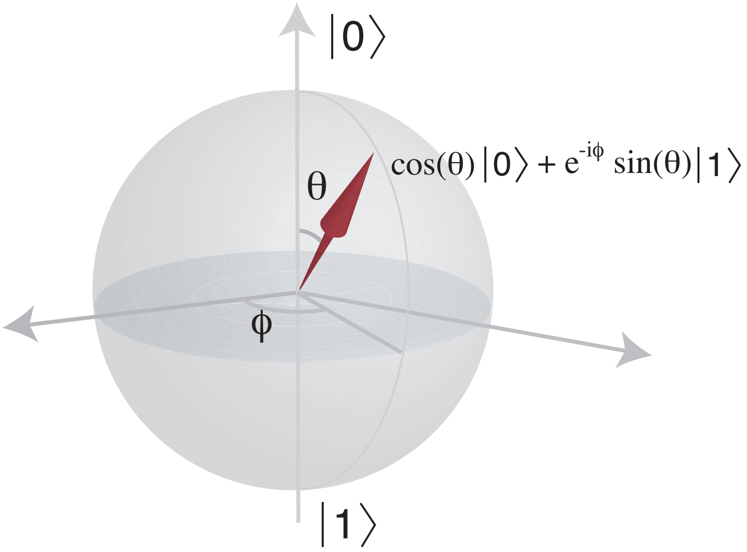

Figure 1.1: Schematic illustration of a Bloch sphere. The north pole corresponds to the qubit state $|0\rangle$ and the south pole to the state $|1\rangle$. A generic pure state of the qubit can be represented by a unit vector pointing along a direction specified by the azimuth ϕ and the zenith θ.

will produce the outcome 0 with probability $|\alpha|^2$, and the outcome 1 with probability $|\beta|^2$. The two states $|0\rangle$ and $|1\rangle$ form a basis of the Hilbert space $\mathcal{H} = \text{span}\{|0\rangle, |1\rangle\}$ of the qubit.

It is important to notice that the state described in Eq. (1.1) is a pure state and it represents a coherent superposition of the two fundamental qubit states, rather than an incoherent mixture of "0" and "1". The essential point is that a pure state points along a precise direction in the space that has a zenith θ and an azimuth φ with respect to the quantization axis,

$$|\psi(\theta,\phi)\rangle = \cos(\theta/2)|0\rangle + e^{-i\phi}\sin(\theta/2)|1\rangle, \tag{1.2}$$

as schematically depicted in the Bloch representation of a qubit in Fig. 1.1. Conversely, a completely mixed state has no information about the azimuthal angle, that represents the coherence of the superposition and it is given by the relative phase between the complex numbers α and β. A good example of a qubit is a spin 1/2, for which the two logical states are the spin up $|\uparrow\rangle$ and the spin down $|\downarrow\rangle$. In order to show the coherent character of a superposition of states, we describe an interference procedure for a spin 1/2 particle. Suppose we prepare the spin in the state $|\psi_0\rangle = |\uparrow\rangle$, that is with probability 1 to find it parallel with respect to a certain direction z in the space, that we choose as quantization axis. We then rotate the spin by an angle $\pi/2$ about an axis perpendicular to z, i.e. the y axis. The result is the state

$$|\psi_1\rangle = e^{-i\frac{\pi}{4}\sigma_y}|\uparrow\rangle = \frac{1}{\sqrt{2}}(|\uparrow\rangle + |\downarrow\rangle). \tag{1.3}$$

We then let the spin cross a region in which there is a magnetic field that points in the positive z direction, $\mathbf{B} = (0, 0, B)$. Due to the presence of the magnetic field, the two states $|\uparrow\rangle$ and $|\downarrow\rangle$ accumulate a relative phase 2φ, that depends on the magnitude of the magnetic field and the time t spent in the region with the $\mathbf{B}$ field, and that for simplicity we leave unspecified. Up to an overall phase, the state of the system that comes out from the region with a magnetic field is given by

$$|\psi_2\rangle = \frac{1}{\sqrt{2}} \left(|\uparrow\rangle + e^{2i\varphi}|\downarrow\rangle\right), \tag{1.4}$$

with the phase $\varphi = g\mu_B Bt/2$. Now, we again rotate the spin of $\pi/2$ about the y direction, and obtain

$$|\psi_3\rangle = e^{-i\frac{\pi}{4}\sigma_y}|\psi_2\rangle = e^{i\varphi}\left[\cos(\varphi)|\uparrow\rangle + i\sin(\varphi)|\downarrow\rangle\right]. \tag{1.5}$$

If we now measure the state of the spin, we obtain $|\uparrow\rangle$ with probability $\cos^2(\varphi)$ and $|\downarrow\rangle$ with probability $\sin^2(\varphi)$. We clearly see, now, that the relative phase can really affect the state of a quantum system. This procedure is known as Ramsey interference [2] and it is used in experiments to detect coherent oscillations in the transverse spin component. In a typical experiment the oscillation displays a damping that is due to interaction of the spin with the surrounding environment. Such a damping, known as decoherence, represents a major obstacle in a quantum computation scheme.

1.1.2 Quantum logic gates

The qubits represent the quantum analog of the classical bits and are the fundamental constituents of a quantum computer. Quantum logical gates provide a quantum analog for the classical logical gates. The way a quantum computer works is via operations on the qubits. Each qubit is represented by a physical system, that can be described by a Hamiltonian, and the qubits may interact and process the information in a controlled manner. A system of qubits can be initialized in a precise state and by means of a global unitary evolution, governed by a controllable global Hamiltonian, a desired quantum algorithm can be performed. Any however complicated many-qubit unitary evolution can be implemented as a sequence of single-qubit and two-qubit gates and, upon final read out of the final state of the system, the processed quantum information can be extracted. Any physical system can be considered as a candidate for quantum computing as long as it fulfills five requirements, known as the DiVincenzo criteria [3, 4]:

- Well defined two-state quantum systems (qubits), well separated from, often present, higher excited states.
- Initial state state preparation with high accuracy.
- Long coherence time, sufficient to allow for a large number of coherent manipulations.
- Sufficient control over a universal set of quantum gates, in particular single-qubit and two-qubit operations to perform the necessary unitary operations.

- The ability to perform quantum measurement to read out the quantum information, either at the end of the process or during the computation.

Any physical system whose dynamics can be effectively modeled by a two-state system can be described in a pseudo-spin 1/2 formalism. By external parameters, like magnetic fields, bias currents or voltages, the qubit Hamiltonian $\mathcal{H} = -\mathbf{B} \cdot \boldsymbol{\sigma}/2$ in an effective magnetic field $\mathbf{B}$, with $\boldsymbol{\sigma} = (\sigma_X, \sigma_Y, \sigma_Z)$ the vector of Pauli matrices, can be engineered. Any arbitrary single-qubit gate can be obtained if two of the field components can be controlled, i. e. a qubit Hamiltonian that can be written as

$$\mathcal{H}_{\text{qubit}}(t) = -\frac{1}{2}B_X(t)\sigma_X - \frac{1}{2}B_Z(t)\sigma_Z. \tag{1.6}$$

Time-dependent control on two component of the effective $\mathbf{B}$ field, with the possibility to switch the field on and off and apply pulses allow to perform any single-qubit gate. If we want to generate the pure state $|\psi(\theta, \phi)\rangle$ Eq. (1.2) starting from the state $|0\rangle$, we can rotate the qubit about the x axis and generate the desired zenith θ and perform a subsequent rotation about the z axis to generate the desired ϕ. In order to perform two-qubit gates, one needs to address the coupling energies between the qubits, with the possibility to switch on and off the interactions and perform the desired operation. A general two-qubit Hamiltonian has the form of a spin exchange term,

$$\mathcal{H}_{\text{int}}(t) = \sum_{ij} J_{ij}(t)\sigma_i^{(1)}\sigma_j^{(2)}, \tag{1.7}$$

that can have some particular form, like an Ising ZZ coupling, an XY coupling or an isotropic Heisenberg coupling.

A general quantum gate arises from controlled unitary evolution of a given many-qubit Hamiltonian $\mathcal{H}(t)$

$$U_{\text{gate}} = \mathcal{T} \exp\left(-\frac{i}{\hbar}\int^t d\tau \mathcal{H}(\tau)\right), \tag{1.8}$$

with $\mathcal{T}$ the time ordering operator. In a way that is completely independent from the particular physical realization, quantum information theory studies quantum algorithms that are able to perform certain tasks by suitable concatenations of qubit gates. In particular, it is often convenient to construct quantum algorithms out of specific, standard single-qubit and two-qubit gates. Two fundamental gates allow to perform any kind of quantum algorithms: single-qubit rotation

$$U_i(\phi) = \exp(i\phi S_i), \tag{1.9}$$

where $\mathbf{S} = \boldsymbol{\sigma}/2$ and the quantum XOR, that allows for a controlled NOT (CNOT) operation,

$$U_{\text{CNOT}} = \begin{pmatrix} 1 & 0 & 0 & 0 \\ 0 & 1 & 0 & 0 \\ 0 & 0 & 0 & 1 \\ 0 & 0 & 1 & 0 \end{pmatrix}. \tag{1.10}$$

In particular, the quantum XOR can be obtained by the combination of single-qubit rotations and the square root of a SWAP gate, that arises from an Heisenberg coupling, and a part from an overall phase factor is given by [5]

$$U_{\sqrt{\mathrm{SWAP}}} = \exp\left(i\frac{\pi}{2}\mathbf{S}^{(1)} \cdot \mathbf{S}^{(2)}\right). \tag{1.11}$$

These basic gates represent a universal set of operations that allow for any quantum computation. However, it is important to notice that almost any two-qubit gate forms a universal set, when combined to single-qubit operations.

1.1.3 Decoherence and Bloch equations

In condensed phases, the coupling to the environment can be relatively strong. However, often a rather complex physical situation can be modelled by a system that consists of few dynamical variables in contact with a huge environment, constituted by a very large or even infinite number of degrees of freedom. In this case the small relevant system alone has to be described as an open system. In many cases it is useful to model the dynamics of an open system by means of an appropriate equation of motion for its density matrix ρ, the so called quantum master equation. The evolution in time of the total density matrix ρ_{SE} that describes the system and the environment is governed by the well known Liouville-von Neuman equation of motion [6]

$$\dot{\rho}_{SE}(t) = -i[H(t), \rho_{SE}(t)] \equiv \mathcal{L}(t)\rho_{SE}(t), \tag{1.12}$$

where $H(t)$ is the Hamiltonian that governs the global dynamics of the system and the environment, and the second equality defines the Liouville operator $\mathcal{L}(t)$.

The density operator of a two state system is a two dimensional positive Hermitian operator with trace one. It can thus be expressed in terms of a basis of Hermitian operators given by the three Pauli operators $\boldsymbol{\sigma} = (\sigma_x, \sigma_y, \sigma_z)$ and the 2×2 identity,

$$\rho = \frac{1}{2}(1 + \mathbf{p} \cdot \boldsymbol{\sigma}), \qquad \mathbf{p} = \mathrm{Tr}[\rho\boldsymbol{\sigma}] = \begin{pmatrix} \rho_{01} + \rho_{10} \\ i(\rho_{01} - \rho_{10}) \\ \rho_{00} - \rho_{11} \end{pmatrix}. \tag{1.13}$$

The vector $\mathbf{p}$ is known as the Bloch vector, and for a spin-1/2 object it represents the expectation values of the spin components $\mathbf{p}/2 \equiv \langle \mathbf{S} \rangle = \mathrm{Tr}[\mathbf{S}\rho]$, where $\mathbf{S} = \boldsymbol{\sigma}/2$, with σ_z diagonal in the $|0\rangle$ $|1\rangle$ basis, $\sigma_z|0\rangle = |0\rangle$ and $\sigma_z|1\rangle = -|1\rangle$.

If the coupling between the system and environment is weak, it can be taken into account at lowest order in the Born approximation. Assuming that the temporal correlations in the environment are short lived and typically lead to exponential decay of the coherence and populations, the master equation within the Born-Markov approximation for the density matrix of a two level system can be expressed as a first order time differential equation for the expectation value of the spin component $\langle \mathbf{S} \rangle = (\langle S_x \rangle, \langle S_y \rangle, \langle S_z \rangle)$ [7–9],

$$\langle \dot{\mathbf{S}} \rangle = \boldsymbol{\omega} \times \langle \mathbf{S} \rangle - R\langle \mathbf{S} \rangle + \langle \mathbf{S}_0 \rangle, \tag{1.14}$$

with $\boldsymbol{\omega} = (0, 0, \omega_{01})$. In case of a spin 1/2 particle in a magnetic field defining the z direction, ω_{01} represents the Zeeman splitting. The relaxation matrix R and the inhomogeneous term $\langle \mathbf{S}_0 \rangle$ depend on the golden rule transition rates between the qubit levels due to coupling to the environment. If $\omega_{01} \gg R_{ij}$, it is possible to make a secular approximation yielding the diagonal form

$$R \approx \begin{pmatrix} T_2^{-1} & 0 & 0 \\ 0 & T_2^{-1} & 0 \\ 0 & 0 & T_1^{-1} \end{pmatrix}, \tag{1.15}$$

with T_1 the relaxation time and T_2 the decoherence time related by the Korringa relation [10]

$$\frac{1}{T_2} = \frac{1}{2T_1} + \frac{1}{T_\phi}, \tag{1.16}$$

with T_ϕ the pure dephasing time. For a system-environment coupling given by a simple bilinear form $H_I = \mathcal{O}_S \otimes \mathcal{X}_E$, with $\mathcal{O}_S$ an operator acting in the system space $\mathcal{H}_S$, and $\mathcal{X}_E$ an operator acting in the environment space $\mathcal{H}_E$, the relaxation and dephasing times T_1 and T_ϕ can be written as

$$\frac{1}{T_1} = 4|\langle 0|\mathcal{O}_S|1\rangle|^2 J(\omega_{01}) \coth\frac{\omega_{01}}{2k_BT}, \tag{1.17}$$

$$\frac{1}{T_\phi} = |\langle 0|\mathcal{O}_S|0\rangle - \langle 1|\mathcal{O}_S|1\rangle|^2 \left.\frac{J(\omega)}{\omega}\right|_{\omega\to 0} 2k_BT, \tag{1.18}$$

where the spectral density $J(\omega)$ is the Fourier transform of the environment time correlator

$$J(\omega) = \int_{-\infty}^{\infty} dt \mathrm{Tr}_E \left[\mathcal{X}_E \mathcal{X}_E(t) \rho_E\right] e^{-i\omega t}. \tag{1.19}$$

The first term in Eq. (1.14) produces a rotation of the Bloch vector along the z direction. If $R = 0$ we have the classical picture of a magnetic moment precessing about the externally applied magnetic field. The second term proportional to R describes an exponential damping of the components of the Bloch vector. T_1 describes the decay of the longitudinal component of the Bloch vector, while T_2 describes the decay of the transverse components.

1.1.4 Superconducting qubits

Superconducting qubits represent a category of promising candidates for the implementation of artificial two-level systems as qubits. The key ingredient in building superconducting qubits is the strong nonlinearity of the current-voltage relation of a Josephson junction. The ability to isolate few charge states on a superconducting island, together with the possibility to let them interact through the coherent tunneling of Cooper pairs through the junction, represent a promising way to control a operate a purely quantum system (charge qubits). The flux quantization together with the strong nonlinear potential, arising from the current-voltage relation, provide a way to isolate few current states and coherently superimpose them (flux qubit).

Superconducting qubits can be included in a more general framework of quantum circuits, that are electrical circuits showing, in the low temperature regime, quantum behavior, including quantum fluctuations [11]. In this context, as LC-circuits provide electrical realizations of quantum harmonic oscillators, Josephson junctions provide an anharmonic counterpart, showing a rich spectrum, with groups of few energy levels well separated from higher bands of the spectrum.

Several types of superconducting qubits based on Josephson junctions have been so far theoretically proposed and experimentally realized [12]. Apart from the particular design of each device, superconducting qubits can be classified according of the working regime of the Josephson elements that constitutes the circuit. Every Josephson junction is characterized by two features: i) a critical current I_c, that is the maximal supercurrent that can flow through the junction; and ii) an effective capacitance that the two superconducting faces have to accumulate charge. Together the Josephson energy associated with the critical current $E_J = I_c\Phi_0/2\pi$ and the charging energy of the associated capacitance $E_C = e^2/2C$ are the two most important parameters that determine the qubit working regime. For $E_C \gg E_J$ the charge degrees of freedom are well defined and the number of Cooper pairs in a superconducting island is a well defined quantum number. Qubits that work in this regime are called charge qubits [13, 14]. To the contrary, for $E_C \ll E_J$ flux degrees of freedom have well defined values, and current states are well defined. Qubits that operate in this regime are called flux qubits [15–17]. Other realizations of superconducting qubits, for different values of the ratio E_J/E_C, and many kinds of possible accessible parameter regimes have been explored. The so called phase qubit [18] operates in the flux regime, but is completely represented by the superconducting phase, and it has no magnetic flux or circulating current associated.

Experimental observation of Rabi oscillations in driven quantum circuits have shown several periods of coherent oscillations, confirming, to some extent, the validity of the two-level approximation and possibility of coherently superimpose the computational two states of the system. Nevertheless, the unavoidable coupling to a dissipative environment surrounding the circuit represents a source of relaxation and decoherence that limit the performances of the qubit for quantum computation tasks. Therefore, for the implementation of superconducting circuits as quantum bits, it is necessary to understand the way the system interacts with the environmental degrees of freedom, and to reduce their effect, if possible.

The superconducting flux qubit

In the working regime $E_J \gg E_C$, three types of circuit designs have been proposed, the Delft flux qubit [15–17], the IBM flux qubit [19], and its gradiometer variety [20].

The flux qubit realized at Delft [17] consists of a superconducting loop interrupted by three Josephson junctions, each characterized by the phase difference φ of the superconducting order parameter. The strong flux regime $E_J \gg E_C$ allows flux quantization of the flux through the loop, $\varphi_1+\varphi_2+\varphi_3+\varphi_L = 2\pi n$, where $\varphi_L = 2\pi\Phi_L\Phi_0$ is the phase associated with the inductive degree of freedom of the loop. For sufficiently low temperatures and for small loop inductance, φ_L can be considered as frozen. Therefore, only two of the three phases of the junctions play the role of dynamical variables and the effective potential $U(\boldsymbol{\varphi})$ is periodic and shows a double well shape, where $\boldsymbol{\varphi} = (\varphi_1, \varphi_2, \varphi_3)^T$. The charging energy of the system here plays the role of the kinetic energy, and the Hamiltonian is written as

$$\mathcal{H} = -2e^2 \nabla_{\boldsymbol{\varphi}}^T \mathcal{C}^{-1} \nabla_{\boldsymbol{\varphi}} + \left(\frac{\Phi_0}{2\pi} \right)^2 U(\boldsymbol{\varphi}), \tag{1.20}$$

where $-2ie\nabla_{\boldsymbol{\varphi}} = \mathbf{Q}$ is the charge operator.

The lowest energy states are two flux states localized in the two well minima $\boldsymbol{\varphi}_L$ and $\boldsymbol{\varphi}_R$, and they correspond to clockwise and counter clockwise circulating currents in the loop, $|L\rangle$ and $|R\rangle$, encoding the logical $|0\rangle$ and $|1\rangle$ states of the qubit. Tunneling through the potential barrier between the wells lifts the degeneracy between the two current states, giving rise to a splitting $\Delta = \langle L|\mathcal{H}|R\rangle$ between the lowest states of the system, that are the symmetric and symmetric superpositions of the current states. An external bias flux can create asymmetry in the double well, $\epsilon = \langle L|\mathcal{H}|L\rangle - \langle R|\mathcal{H}|R\rangle$. The qubit Hamiltonian written in the $\{|L\rangle, |R\rangle\}$ basis takes the form

$$\mathcal{H} = \frac{\Delta}{2}\sigma_x + \frac{\epsilon}{2}\sigma_z. \tag{1.21}$$

Markovian dynamics due to dissipative circuitry

The working regime of the flux qubits, in which the charging energy is much smaller than the Josephson energy, $E_C \ll E_J$, makes the flux qubits insensitive to a large extent to background charge fluctuations. Still, however, other mechanisms can affect their phase coherence and in order to implement them as building blocks for quantum computation schemes, it is necessary to understand which sources of decoherence affect the short time dynamics of flux qubits and to reduce their effect as much as possible.

Several sources of dissipation for flux qubits have been discussed throughout the literature [21], background charge fluctuations ($\tau_\varphi \approx 0.1$ s), as well as quasiparticle tunneling in the superconductor with a non-vanishing subgap conductance ($\tau_\varphi \approx 1$ ms). Nuclear spins in the substrate have also been considered as a possible source of dissipation. A static random magnetic field produced by the nuclear spins may induce shifts in qubit frequencies, but no dephasing is expected until a typical nuclear relaxation time, which can be very long, up to minutes, due to the slow dynamics of nuclear spins [21].

However, the most efficient source of dissipation for flux qubits is represented by fluctuations in the external circuit that produce fluctuating magnetic fluxes through a loop in the circuit. The coupling of flux degrees of freedom of the qubit to the dissipative environmental elements is well described in the graph formalism [19]. In the Born-Markov approximation, the relaxation and pure dephasing rates, T_1^{-1} and T_ϕ^{-1} respectively, are given by Eqs. (1.17,1.18) with the operator $\mathcal{O}_S$ given by $\mathbf{m} \cdot \boldsymbol{\varphi}$ [19]. Here $\mathbf{m} \cdot \boldsymbol{\varphi}$ appears in the Hamiltonian for the system-bath coupling and $\mathbf{m}$ is related to the topology of the dissipative circuitry. Typically, T_ϕ can be made to diverge for an appropriate choice of external fluxes such that $\langle 0|\mathbf{m}\cdot\boldsymbol{\varphi}|0\rangle = \langle 1|\mathbf{m}\cdot\boldsymbol{\varphi}|1\rangle$. However, this divergence is expected to be cut off by other mechanisms.

The two eigenstates of the Hamiltonian Eq. (1.21) are given by

$$
\begin{aligned}
|0\rangle &= \frac{1}{\sqrt{2}}\left(\sqrt{1+\frac{\epsilon}{\omega_{01}}}|L\rangle + \sqrt{1-\frac{\epsilon}{\omega_{01}}}|R\rangle\right), && (1.22)\\
|1\rangle &= \frac{1}{\sqrt{2}}\left(\sqrt{1-\frac{\epsilon}{\omega_{01}}}|L\rangle - \sqrt{1+\frac{\epsilon}{\omega_{01}}}|R\rangle\right), && (1.23)
\end{aligned}
$$

where $\omega_{01} = \sqrt{\epsilon^2+\Delta^2}$. Approximating the localized flux states $|L\rangle$ and $|R\rangle$ as Gaussians centered at the minima of the double well, the relaxation rate T_1^{-1} and the pure dephasing rate T_ϕ^{-1} are given by

$$
\begin{aligned}
\frac{1}{T_1} &\approx \left(\frac{\Delta}{\omega_{01}}\right)^2 |\mathbf{m}\cdot\Delta\boldsymbol{\varphi}|^2 \left(1+\frac{S^2}{2}\right)^2 J(\omega_{01})\coth\frac{\omega_{01}}{2k_BT}, && (1.24)\\
\frac{1}{T_\phi} &\approx \left(\frac{\epsilon}{\omega_{01}}\right)^2 |\mathbf{m}\cdot\Delta\boldsymbol{\varphi}|^2 \left(1+\frac{S^2}{2}\right)^2 \left.\frac{J(\omega)}{\omega}\right|_{\omega\to 0} 2k_BT, && (1.25)
\end{aligned}
$$

where $S = \langle L|R\rangle$ is the overlap between the two Gaussians. The vector $\Delta\boldsymbol{\varphi}$ connects the two minima of the double well. These relations are valid in the Markov limit and in the Born approximation where the system-bath interaction is considered only at first order. By inspection of the previous formula it is clear that a symmetric double well potential, for which $\epsilon = 0$, lets the dephasing time diverge. This is realized for a value of the external applied magnetic flux $\Phi_{\text{ext}} = \Phi_0/2$, because $\epsilon \propto (\Phi_{\text{ext}}/\Phi_0 - 1/2)$. Moreover for $\mathbf{m}\cdot\Delta\boldsymbol{\varphi} = 0$ the environment is decoupled from the system, and both the relaxation and dephasing time diverge.

Conclusion

This introduction to superconducting qubits is a preparation for the material presented in Ch. 2. There, we study a three Josephson junction superconducting flux qubit in which the two superconducting islands between the three Josephson junctions are gated by external voltages. We study how the gate voltages allow to control the qubit Hamiltonian and explore a range of fabrication parameters that give rise to a σ_y term in the qubit Hamiltonian. The ground state and the excited state of the qubit can be made to point along any direction of the Bloch's sphere, allowing for a full control of the system.

1.2 The measurement process

The connection between the microscopic world, in which quantum objects live, and the macroscopic world, in which we live and perform measurements, is a rather complicated and not yet fully understood problem. The so-called correspondence principle, that states that the quantum mechanical description of a quantum system should reproduce the classical physics in the limit of large quantum numbers, represents mostly a guide and *a posteriori* confirmation of the theory, rather than a precise mapping between the quantum and the classical worlds. Nevertheless, an experiment essentially is a measurement that produces outcomes. We interpret these outcomes in the light of quantum theory, that may confirm or refuse a theoretical prediction, so it is important to understand how a microscopic system interfaces the macroscopic world.

A fundamental difference between a classical and a quantum measurement is that the former, at least in an ideal case, has no influence on the system under measurement, whereas the latter needs to drastically change the state of the quantum system. The action of a macroscopic measurement apparatus cannot be seen as a small perturbation on the measured system. One of the fundamental concepts in the description of an ideal quantum measurement is the postulate of reduction of the quantum state of the measured object, due to John von Neumann. The essence of the fundamental postulate of the quantum theory of measurement can be summarized in the following three statements [22]:

- The probability to obtain a certain outcome in a measurement is given by the square of the modulus of the wave function, expressed in the basis of measured observable.

- The measurement action leaves the measured quantity unperturbed. A change occurs in the probability distribution, from an *a priori* wider one, to an *a posteriori* narrower one.

- The quantum measurement induces in the quantity that is canonically conjugate to the measured one a perturbation whose minimum magnitude is given by the Heisenberg uncertainty relation.

Although the validity of the picture according to which the wave function collapses during the measurement can be questioned from a fundamental point of view, it nonetheless contains the main idea behind a quantum measurement, that every measurement represents a rather strong perturbation of the system measured and that the state is inferred after a probabilistic interpretation of the outcomes of the measurements.

In a typical solid state experiments it is necessary to couple the system under study to a detector and to measure a suitable experimentally accessible observable of the detector, that will contain footprints of the state of the system that we want to measure. In order to theoretically describe the measurement procedure it is customary to provide a Hamiltonian for the system under study, a Hamiltonian for the detector, that can as well behave quantum mechanically, and a coupling between the system and the detector. Moreover, the surrounding environment plays a fundamental role in the measurement action, and it is important to understand how the information can be acquired and how the measured system is affected by the measurement back action.

1.2.1 The theory of quantum measurements

The first rigorous description of the action of a quantum measurement is due to John von Neumann, who provided it in the form of a postulate. Consider a general quantum mechanical observable A defined on a Hilbert space $\mathcal{H}$ has a spectral decomposition that allows to write it as

$$A = \sum_i a_i |i\rangle\langle i|, \tag{1.26}$$

with a_i a set of eigenvalues and corresponding orthogonal eigenstates $\{|i\rangle\}$. We assume them for simplicity to be discrete and non degenerate. Von Neumann's potulate of reduction states that:

- The measurement of the observable A on a state described by the density operator ρ produces as outcome one of the eigenvalues a_i, each of them with a probability

  $$P_i = \langle i|\rho|i\rangle. \tag{1.27}$$

- The system after the measurement will be in the state $|i\rangle$, that corresponds to the outcome a_i.

Due to the orthogonality of the basis $\{|i\rangle\}$ it follows that if two subsequent measurements of A are performed, one after the other, the second measurement will produce the same outcome a_i as the first with certainty. Such a measurement goes under the name of orthogonal (or projective) measurement and it refers only to an ideal measurement. In a real measurement the final state of the system can substantially differ from $|i\rangle$ of the idealized one. Orthogonal measurements represent only asymptotic limiting cases and in order to describe real, approximate measurements one has to relax the orthogonality requirement and consider more generalized non-orthogonal measurements.

The generalized theory of quantum measurements has been developed on the basis of few concepts that may bring up a direct generalization of the von Neumann projection postulate of quantum mechanics. They naturally arise from orthogonal measurements defined on larger Hilbert space and provide the theoretical framework to describe any quantum measurement. Let us consider a quantum system described by the density operator ρ and a general measurement scheme that produces a set $\mathcal{M}$ of possible outcomes $m \in \mathcal{M}$. A generalized non-orthogonal measurement states that [6, 22]

- The measurement outcome m represents a classical random number with probability distribution

  $$P_m = \mathrm{Tr}[F_m \rho], \tag{1.28}$$

  with F_m positive operators that form a decomposition of the unity,

  $$\sum_{m \in \mathcal{M}} F_m = \mathbb{I}, \tag{1.29}$$

that guarantees the probability conservation $\sum_{m\in\mathcal{M}} P_m = 1$. The operators F_m are a *positive operator-valued measure* (POVM) and represent the most general quantum measurement. They can provide a description of realistic approximate measurements, from which orthogonal ones represent only a particular asymptotic case, the key difference being the absence of an orthogonality condition.

- After the measurement, the state ρ'_m conditional to an outcome m is described by a density operator
$$\rho'_m = P_m^{-1}\Phi_m(\rho), \tag{1.30}$$
where Φ_m is a positive, hermitian and trace preserving superoperator, that maps a density operators to another density operator and that obeys the condition
$$\operatorname{Tr}\Phi_m(\rho) = \operatorname{Tr}[F_m\rho], \tag{1.31}$$
which ensures the normalization of the density operator ρ'.

- In the case on a non-selective measurement, the state of the system after the measurement is given by
$$\rho' = \sum_m P_m\rho'_m = \sum_m \Phi_m(\rho), \tag{1.32}$$
which thanks to Eqs. (1.29) and (1.31) is normalized, $\operatorname{Tr}\rho' = 1$.

The superoperator Φ_m is required to be a convex, linear, completely positive map that satisfies $0 \leq \operatorname{Tr}\Phi_m \leq 1$ and admits an explicit representation, that follows from an important theorem due to Kraus, which states that there exists a countable set of operators Ω_{mk} that allow to write
$$\Phi_m(\rho) = \sum_k \Omega_{mk}\rho\Omega^\dagger_{mk}, \tag{1.33}$$
with the operatos Ω_{mk} satisfying
$$F_m = \sum_k \Omega_{mk}\Omega^\dagger_{mk} \leq \mathbb{I}. \tag{1.34}$$

1.2.2 Indirect measurements

The quantum description provided by the Schrödinger equation gives rise to a deterministic and reversible evolution of the wave function. This is incompatible with the description of a quantum measurement in terms of reduction of the wave function, since the acquisition of information from the measurement is an irreversible and nondeterministic process. After a measurement is performed it is not possible to return back to the pre-measurement state and, at the same time, the post-measurement state cannot be predicted before the measurement is performed. The ultimate reason why the framework of standard quantum mechanics based on the Schrödinger equation is inadequate to describe a quantum measurement can be traced to the macroscopic size of the receiver of the measurement information.

Quantum measurements can be divided into two categories [22]. In the case the measured quantum object interacts directly with a classical measuring device, one speaks of "direct measurements". In such measurements, typically, there is a substantial amount of randomness in the interaction between the quantum object and the macroscopically large number of degrees of freedom that characterizes the classical measuring device. A direct measurement results in a strong perturbation of the measured object, far beyond the minimum perturbation referable to the uncertainty relation.

A second types of measurement can be thought, that includes am intermediate step: an "indirect measurement". It consists in introducing a quantum probe that is coupled to the quantum object we want to measure. In a first step, the probe and the object undergo a deterministic and reversible evolution, governed by the Schrödinger equation, and no state reduction takes place. In a second step, a particular observable of the probe is addressed by a direct measurement. The state of the probe undergoes a reduction that induces a further reduction in the state of the object, as a result of the correlations arose in the previous unitary evolution. In an indirect measurement, the second step should not start before the first step is completed and the second step should not contribute to the error of the measurement in a significant way.

Formally an indirect measurement can be described in the following way [22, 23]. The quantum probe is initialized in a precise initial state ρ_P, before the measurement starts, and the quantum object in the general initial state ρ_O. In the first step of the measurement, the interaction between the quantum probe and the quantum object results in a global state ρ'_{OP}

$$\rho'_{OP} = U\rho_O\rho_P U^\dagger, \tag{1.35}$$

with U the unitary operator that describes the quantum evolution and induces correlations between the quantum probe and the quantum object. The state of the probe after the interaction is

$$\rho'_P = \mathrm{Tr}_O[U\rho_O\rho_P U^\dagger]. \tag{1.36}$$

In the second step of the measurement a direct measurement of a suitable observable P of the probed is performed. For simplicity one can approximate the direct measurement with an orthogonal measurement, that consists in projecting the probe on a state $|p\rangle$, eigenstate of P corresponding to the eigenvalue p. The probability distribution for the results of the measurement is

$$\mathrm{Prob}(p) = \mathrm{Tr}_P[|p\rangle\langle p|\rho'_P]. \tag{1.37}$$

By defining the POVM operator F_p as

$$F_p = \mathrm{Tr}_P[U^\dagger|p\rangle\langle p|U\rho_P], \tag{1.38}$$

it is possible to express the outcome probability distribution as

$$\mathrm{Prob}(p) = \mathrm{Tr}_O[F_p\rho_O]. \tag{1.39}$$

The density operator of the quantum object, conditional to the outcome p of the measurement, is

$$\tilde{\rho}(p) = \frac{1}{\mathrm{Prob}(p)} \langle p|\rho'_{OP}|p\rangle. \tag{1.40}$$

It is now possible to express the initial state of the probe in a spectral decomposition, with the probability w_j associated to the eigenstates $|\psi_j\rangle$. The action of the measurement on the state of quantum object, conditional to the outcome p, can be expressed as superoperator in a Kraus representation

$$\tilde{\rho}(p) = \frac{1}{\mathrm{Prob}(p)} \sum_j w_j \Omega_{jp} \rho_O \Omega^{\dagger}_{jp}, \tag{1.41}$$

where the operators Ω_{jp} defined by

$$\Omega_{jp} = \langle p|U|\psi_j\rangle. \tag{1.42}$$

It is straightforward to see that they satisfy the relation $\sum_j \Omega_{jp}\Omega^{\dagger}_{jp} = \mathbb{I}$. From this derivation it becomes clear how a nonorthogonal measurement arises as a restriction to the Hilbert space of the quantum object of an orthogonal measurement performed on the larger Hilbert space of the probe and the object.

Indirect measurements play a fundamental role in the study of quantum measurement, as they can accurately describe strong measurement as well as weak measurement. Furthermore, besides taking into account a detailed microscopic model for the interaction between the object and the probe, indirect measurements are suitable for taking into account the interaction with the environment and achieve a deeper understanding of the measurement process.

1.2.3 Quantum nondemolition measurements

The Heisenberg uncertainty relation is one of the cornerstones of the theory of quantum mechanics. It states that for every quantum object any pair of conjugate variables cannot have a simultaneous precise values. It also represents a fundamental property of a measurement process, according to which it is not possible to obtain a simultaneous arbitrarily high precise knowledge of two conjugate variables. Consider the position x and momentum p of a free particle of mass m. The Heisenberg uncertainty relation states that

$$\Delta x \Delta p \geq \frac{\hbar}{2}. \tag{1.43}$$

This means that the higher the precision in the determination of, say, the momentum p, and consequently the smaller Δp, the larger Δx needs to be. Which is now the limit that quantum mechanics allows for a precise measurement? In order to answer this question we consider two measurements of the position of a free particle of mass m [22, 23]. The first measurement is characterized by an error Δx_1 in the value of the position x. After a time τ we perform a second measurement of the position x, that would yield an error Δx_2. Between the two measurements, the spread in the momentum due to the error in the first measurement generates a further error δx in the position given by

$$\delta x = \Delta p_1 \tau / m = \hbar \tau / 2m\Delta x_1. \tag{1.44}$$

From the result x_1 and x_2 of the two position measurements we can infer the value of the momentum p as

$$p = m\frac{x_1 - x_2}{\tau}, \tag{1.45}$$

that will be affected by a total error given my the root mean square (rms)

$$\Delta p = \frac{m}{\tau}\sqrt{\Delta x_1^2 + \Delta x_2^2 + \delta x^2}. \tag{1.46}$$

By minimization of this expression we find that the optimal solution to obtain that most precise measurement of the momentum is to choose $\Delta x_1 = \sqrt{\hbar\tau/2m}$, from which follows

$$\Delta p \geq \Delta p_{SQL} = \sqrt{\frac{\hbar m}{2\tau}}, \tag{1.47}$$

and analogously follows that $\Delta x_{SQL} = \sqrt{2\tau/\hbar m}$. These represent the *standard quantum limit* (SQL) for a quantum measurement [22, 23].

A natural question is whether it is possible or not to overcome the standard quantum limit. Let us consider a measurement of the energy of an electromagnetic resonator. According to quantization of the harmonic oscillator, the energy comes in discrete quanta of energy $E = \hbar\omega$, with ω the frequency of oscillation of the resonator, and it is proportional to the number n of excited quanta that is in turn accessible by sending the resonator signal through an amplifier and by measuring the amplitude of the oscillation. Along with the amplitude, the phase ϕ of the oscillation can be extracted from the amplifier's output [22]. The energy and the phase are canonically conjugate variables and the Heisenberg uncertainty relation holds

$$\Delta E \Delta\phi \geq \frac{\hbar\omega}{2}. \tag{1.48}$$

In order to overcome the standard quantum limit in the measurement of the energy of the resonator, a measuring device should respond only to energy and should not acquire any information about the phase. An example of such a device is a photon counter, but such a device performs a strong direct measurement of the oscillator, ultimately absorbing all its energy. We now couple the resonator, whose energy we want to measure, to another resonator that acts as a quantum probe, and perform a strong direct measurement of the photon number of the probe resonator with a photon counter. If the energy of the first resonator does not change during the measurement of the probe we can perform a measurement that "deceives" the quantum limit. Such a measurement goes under the name of *quantum nondemolition measurement* (QND).

As a general recipe, we consider a quantum system on which we want to measure a suitable observable $\hat{A}$. A measurement procedure is based on coupling the system under consideration to a probe. The global evolution entangles the probe and the system, and a measurement of an observable $\hat{B}$ of the probe provides information on the system. In general, a strong projective measurement on the probe translates into a weak non-projective measurement on the system (see Sec. 1.2.2). This is because the eigenstates of the coupled system differ in general from the product of the eigenstates of the measured observable on the system and those of the probe.

Three criteria that a measurement should satisfy in order to be QND are [24]: i) agreement between the input state and the measurement result; ii) the action of measurement should not alter the observable being measured; iii) repeated measurement should give the same result. These three criteria can be cast in a more precise way: *the measured observable $\hat{A}$ must be an integral of motion for the coupled probe and system* [22]. Formally this means that the observable $\hat{A}$ that we want to measure must commute with the Hamiltonian $\mathcal{H}$, that describes the interacting system and probe,

$$[\mathcal{H}, \hat{A}] = 0. \tag{1.49}$$

Such a requirement represents a sufficient condition such that an eigenstate of the observable $\hat{A}$, determined by the measurement, does not change under the global evolution of the coupled system and probe. As a consequence, a subsequent measurement of the same observable $\hat{A}$ provides the same outcome as the previous one with certainty. As a counterexample for a case in which a quantum nondemolition measurement is not possible, one can consider the measurement of the position of a free particle, for which the system observable is $\hat{A} = \hat{x}$ and the Hamiltonian of the system is $\mathcal{H} = \hat{p}^2/2m$. Clearly one has $[\mathcal{H}, \hat{x}] \neq 0$ and a QND scheme does not work.

Finally, in order to obtain information on the system observable $\hat{A}$ by the measurement of the probe observable $\hat{B}$, it is necessary that the interaction Hamiltonian does *not* commute with $\hat{B}$,

$$[\mathcal{H}_{\text{int}}, \hat{B}] \neq 0, \tag{1.50}$$

where $\mathcal{H}_{\text{int}}$ describes the interaction between the probe and the system,

$$\mathcal{H} = \mathcal{H}_S + \mathcal{H}_{\text{probe}} + \mathcal{H}_{\text{int}}. \tag{1.51}$$

Altogether, these criteria provide an immediate way to determine whether a given measurement protocol can give rise to a QND measurement.

Conclusion

The ideas of quantum measurement and the formalism introduced in this section find an application in Ch. 3 where we study the quantum nondemolition measurement of a qubit coupled to a harmonic oscillator. In particular, the concept of indirect measurement, with a system represented by a qubit and a probe represented by a harmonic oscillator, and the POVM formalism for weak measurements provide us with the mathematical tools that allows us to model a sequence of two qubit measurements and to study the correlations in the conditional probability for the measurement outcomes.

1.3 Quantum transport

The advances in technology made it possible in the last three decades to construct electronic structures whose dimensions are much smaller than the coherence length of electrons. These small electronic conductors are much larger than their microscopic constituents, like atoms, and too small to show an ohmic behavior and be considered macroscopic. They "live" in an intermediate world and they are called mesoscopic systems [26].

The "size" of a conductor, and consequently its behavior, can be inferred by an analysis of three length scales that characterize the electron transport: i) the de Broglie wavelength, determined by the kinetic energy of electrons in the material, ii) the mean free path, that is the average distance an electron travels before two scattering events, and iii) the phase-relaxation length, that is the distance beyond which its initial phase is destroyed. Macroscopic objects have sizes much larger than all of these length scales and typically manifest an ohmic behavior. Microscopic objects have a size on the order of the de Broglie wave length, that in metals is on the order of the inter atomic distances ($\sim$Å), whereas in semiconductor is on order of 40 nm. Mesoscopic systems usually have a size smaller than al least one of these three length scales. The realm of measoscopic systems can vary widely depending on the particular material, the temperature and the magnetic field, and can range between few nanometers to hundreds of microns.

Recent work on mesoscopic structures has been extensively based on semiconductor material systems. These devices are fabricated from heterostructures of GaAs and AlGaAs grown by molecular beam epitaxy. The energy potential along the growth direction of such a structure has a minimum at the interface of the two layers, which is also asymmetric with respect to the growth direction. Free electrons are introduced by doping the AlGaAs layer with Si, which accumulate at the GaAs/AlGaAs interface, deep down in the minimum of the vertical potential, that provides strong confinement of the electrons along the growth direction. At the same time, the electrons are free to move along the interface, where they form a two dimensional electron gas (2DEG), that can have a high mobility and a relatively low electron density (typically $10^5 - 10^7$ cm^2/Vs and $\approx 10^{15}$ m^{-2}). The low density results in a relatively long Fermi wavelength ($\approx$ 40 nm) and a large screening length. Via the application of an electric field, obtained through negatively charged metal gate electrodes, placed on top of the heterostructure, the 2DEG can be locally depleted and by suitable designing the gate structure it is possible to create electron wires and isolate small islands of the 2DEG. When the lateral size of the conductor is compared to the Fermi wavelength, the energy level structure may become discretized, and at temperatures down to tens of mK, the energy separation of the levels becomes much higher than the temperature, such that quantum phenomena start to play a significant role.

The conductance G of a mesoscopic system, defined as the current response function to an applied bias voltage, manifests a behavior that cannot be understood within the framework of a classical theory. The conductance of a two-dimensional large macroscopic sample of width W and length L obeys an ohmic scaling law: $G = \sigma W/L$, with σ a material dependent conductivity. For mesoscopic systems there is an interface resistance that depends on the contacts to the leads and is independent on the length L of the sample, and the conductance does not show a linear dependence on the width W. Quantum phenomena start to be significant and a dependence of the conductance on the discrete number of transverse mode manifests itself in step like behavior. The current through a mesoscopic sample can be expressed as the rate for an electron to be transmitted through it and the linear response conductance can be related to the transmission probability via the Landauer formula [27–29].

1.3.1 Scattering theory

If the size of a mesoscopic conductor is much smaller than the electron phase-relaxation length, the dynamics can be considered to be coherent and it is possible to obtain the transport properties starting from the Schrödinger equation. The scattering matrix formalism [26–29] is a powerful tool that allows to describe the coherent transport through a particular region of the conductor whose size is smaller than the coherence length. The scattering matrix S connects semi-infinite, non-interacting leads, from which electrons may come and towards which electrons may travel, having being transmitted or reflected through the coherent scattering region. It is often convenient to formally divide a mesoscopic conductor into several sections, whose dimensions allow for a coherent treatment, and to describe their effect by means of their individual scattering matrices. The composition of the individual S-matrices allows to combine successive sections of the conductor assuming coherence, partially coherence or complete incoherence among the individually coherent parts of the conductor.

Dealing with a 2DEG one usually considers a two-dimensional problem. In the external leads the electrons are considered as free propagating waves, eigenstates of the momentum, and all the energy levels up to the Fermi energy are occupied, according to the Pauli principle. As the coupling between the leads and the conductor increases, these electron eigenstates become scattering states that are connected via the S-matrix to scattering states of other leads. Inside the conductor the dynamics is described by the Schrödinger equation

$$\frac{1}{2m^*}\left(i\hbar\boldsymbol{\nabla} + e\mathbf{A}(\mathbf{r})\right)^2\psi(\mathbf{r}) + V(\mathbf{r})\psi(\mathbf{r}) = E\psi(\mathbf{r}), \tag{1.52}$$

where m^* is the effective mass, $V(\mathbf{r})$ is a potential, $\mathbf{A}(\mathbf{r})$ is the vector potential, and the boundary conditions are chosen in such a way that the wave function vanishes outside the conductor and the leads. All the magnetic fields and the potential $V(\mathbf{r})$ are assumed to vanish inside the leads. The solution of the Schrödinger equation is a linear combination of plane waves moving to and from the leads. Inside the leads, the solution can be written as a linear combination of incoming and outgoing propagating waves, that have been transmitted or reflected by the conductor, and the transmission and reflection amplitudes constitute the elements of the scattering matrix. Assuming for simplicity that we have only

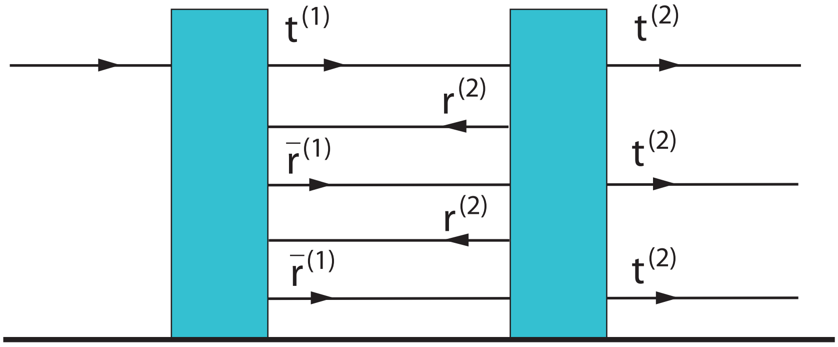

Figure 1.2: Schematic illustration of the transmission through the double barrier structure Eq. (1.58) obtained as a sum of all the paths in which an electron is reflected one time, two times etc. between the two barriers [26].

two leads, we can write the modes in the left (right) lead by ψ^i_{nL} (ψ^i_{nR}) and ψ^o_{nL} (ψ^o_{nR}), where the index i (o) stands for incoming (outgoing) mode, and the quantum number $n = 1, \ldots, N$ labels the N transverse propagating modes, also referred as "channels". We further assume that the left and right leads have the same number of channels N. Solving the Schrödinger equation for initial waves incoming from the left and the right leads, one can write the wave function in the left and right lead as

$$\psi_L = \sum_{n=1}^{N} c^i_{nL}\psi^i_{nL} + c^o_{nL}\psi^o_{nL}, \tag{1.53}$$

$$\psi_R = \sum_{n=1}^{N} c^i_{nR}\psi^i_{nR} + c^o_{nR}\psi^o_{nR}, \tag{1.54}$$

$$\tag{1.55}$$

with the coefficients $c^i_{nL}, c^o_{nL}, c^i_{nR}, c^o_{nR}$ linearly connected by the energy dependent scattering matrix

$$\begin{pmatrix} c^o_{nL} \\ c^o_{nR} \end{pmatrix} = S(E) \begin{pmatrix} c^i_{nL} \\ c^i_{nR} \end{pmatrix}. \tag{1.56}$$

Here the n index has been absorbed in the coefficients $c^{i/o}_{L/R}$, that now have the structure of a N-dimensional vector. The matrix $S(E)$ is the $2N \times 2N$ scattering matrix, that can be grouped in N-dimensional transmission and reflection matrices, r, $\bar{r}$, t, and $\bar{t}$,

$$S = \begin{pmatrix} r & \bar{t} \\ t & \bar{r} \end{pmatrix}. \tag{1.57}$$

From the Schrödinger equation and from current conservation, it follows that the scattering matrix is unitary, $S^\dagger S = \mathbb{I}$.

In the case one has the scattering matrices of two successive sections of a conductor, it is possible to obtain the total scattering matrix the describes the combined effect of the two sections by composing the scattering matrices. One can imaging that the total transmission amplitude can arise by a sum of all paths in which a particle bounces zero, one, two, three, etc. times between the two sections and eventually is totally transmitted, as schematically depicted in Fig. 1.2. The resulting transmission amplitude is given by

$$\begin{aligned} t &= t^{(2)}t^{(1)} + t^{(2)}[\bar{r}^{(1)}r^{(2)}]t^{(1)} + t^{(2)}[\bar{r}^{(1)}r^{(2)}][\bar{r}^{(1)}r^{(2)}]t^{(1)} + \dots \\ &= t^{(2)}[\mathbb{I} - \bar{r}^{(1)}r^{(2)}]^{-1}t^{(1)}, \end{aligned} \tag{1.58}$$

where $t^{(1)}, t^{(2)}, \bar{r}^{(1)}, r^{(2)}$ are the the transmission and reflection amplitude of the first and second scattering matrix. In an analogue way it is possible to reconstruct the entire total scattering matrix.

1.3.2 The Landauer formula

In order to derive the Landauer formula for the linear response conductance, we consider a mesoscopic conductor at zero temperature, that is attached to two leads on the left and on the right side respectively. The two leads are kept at chemical potential μ_L and μ_R by an applied bias voltage V, such that $\mu_L - \mu_R = eV$. The leads are assumed to be ballistic conductors, each having N transverse modes. We further assume that no reflection takes place at the contacts. The current flow takes place only in the energy window $\mu_L - \mu_R = eV$. An incoming flux of electrons from the left lead is partially reflected to the left lead, at chemical potential μ_L, and partially transmitted to the right lead, that has a lower chemical potential. Therefore, the current flow will involve only those electrons that are transmitted and it is given by

$$I = \frac{2e}{h} NT(\mu_L - \mu_R), \tag{1.59}$$

where the factor 2 takes into account the spin degree of freedom. The linear response conductance $G = I/V$ is then given by the Landauer formula

$$G = \frac{2e^2}{h} NT. \tag{1.60}$$

The conductance shows a quantized behavior for $T = 0, 1$, arising from the number of channels N involved in the transport, and the fundamental quantity e^2/h called quantum of conductance.

Conclusion

The scattering theory introduced in this section provides us with the framework for studying a particular transport setup in Ch. 4. There, we consider several electronic implementation of interaction free measurements that were originally proposed in optics. We study complicated electronic interferometric setups in which electrons are split and reunited many times. A region of the interferometer may be affected by external classical noise, that induces random phase shift of the wave function that travels through it and ultimately dephases the electrons, resulting in a reduction of the visibility of the interference fringes. By sending many times a tiny fraction of the electronic wave packet through the region affected by dephasing, we test the region affected by dephasing and learn about the presence or absence of the dephasing source in a way that preserves the electron coherence.

1.4 Graphene

One of the major scientific achievements of the past few years is represented without any doubt by the isolation of graphene, a single layer of carbon atoms arranged in a honey comb lattice structure [30]. The great advance in the discovery of graphene is represented by the fact that it is the first time a material (solid) was made in the lab that was only one atom thick. No one actually expected graphene to exist in a free state. Graphite, a 3D allotrope of carbon, has been known and used for centuries since the invention of the pencil. It is composed by stacks of many layers of graphene that are weakly bound by van der Waals forces. Therefore, producing graphene is relatively easy. Every time we write with a pencil we unfold stacks composed by few layers of graphene. What turns out to be difficult is to find a single layer, that has to be eventually localized with help of an an ordinary optical microscope.

Graphene is the mother of graphite, carbon nanotubes and fullerenes. The carbon atoms in graphene do not form a Bravais lattice. Rather they are arranged in a honey comb structure that can be described as a triangular Bravais lattice with two atoms per unit cell. The electronic structure of carbon atoms leads to the sp^2 hybridization between one s orbital and two p orbitals. A planar trigonal structure arises with the formation of σ bonding between carbon atoms that have a filled shell due to the Pauli principle and are responsible for the structural robustness of the lattice. Perpendicularly to the planar structure, the unaffected p orbital forms a half filled π band by binding covalently with neighboring carbon atoms.

The electronic properties of graphene are determined by the strong tight-binding character of the half filled π bond. In a picture in which free electrons can hop from one carbon atom to the three nearest neighboring carbon atoms, the electronic properties of graphene are described by a dispersion relation that shows a semimetallic behavior. The conduction and the valence bands touch in six points in the Brillouin zone that form a hexagonal lattice. Two of them, K and K', are not equivalent whereas the other points are obtained from these by a Bravais vector displacement. Around the K and the K' points the dispersion relation is linear. It follows that the low energy physics can be described quantum mechanically by the massless Dirac equation.

The possibility to study in a solid state lab a material whose characteristic properties share common features with relativistic particles opens the possibility to experimentally test many theoretical predictions that concern relativistic effects. The massless character of particle in graphene and the consequent chiral behavior allow to a peculiar effect known as

Klein tunneling to take place. In few words, when chiral electrons of positive energy impinge against a step-like barrier of higher energy they find free hole states inside the barrier and therefore tunnel through without being reflected. This strictly speaking happens for propagation orthogonal to an infinite barrier. For a comprehensive review on graphene see [31].

1.4.1 Tight-binding approach

In order to obtain the energy dispersion relation that characterizes the electronic properties of a single layer of graphene, we divide the honey comb structure in two triangular Bravais sublattices, A and B, and associate to every sublattice site-dependent fermionic field operators $a_{i,\sigma}$ and $b_{i,\sigma}$, with spin $\sigma =\uparrow,\downarrow$. The tight-binding Hamiltonian obtained by retaining solely nearest-neighbor hopping terms can be written as

$$H = -t \sum_{\langle i,j\rangle,\sigma} (a^\dagger_{i,\sigma} b_{j,\sigma} + b^\dagger_{j,\sigma} a_{i,\sigma}), \tag{1.61}$$

where $t \approx 2.8$ eV is the nearest-neighbor hopping energy. It is important to notice that every time that an electron hops from one carbon atom to a nearest neighbor it changes sublattice. The electronic dispersion relation in the $\mathbf{k}$-space that follows from Eq. (1.61) can be written as [32]

$$E_\pm(\mathbf{k}) = \pm t\sqrt{3 + 2\cos(\sqrt{3}k_y a) + 4\cos(\sqrt{3}k_y a/2)\cos(3k_x a/2)}, \tag{1.62}$$

with $a \approx 1.2$ Å the carbon-carbon distance. The plus sign refers to the upper (π^*) band and the minus sign refers to the lower (π) band and the spectrum is symmetric around zero energy. The low energy physics is well captured by studying the band structure around the Dirac point K and K'. Close to the $\mathbf{K}$ (or $\mathbf{K}'$) vector, we write $\mathbf{k} = \mathbf{K} + \mathbf{q}$ and for $|\mathbf{q}| \ll |\mathbf{K}|$ can linearize the dispersion relation [32]

$$E_\pm(\mathbf{q}) \approx \pm v_F |\mathbf{q}|, \tag{1.63}$$

where $\mathbf{q}$ is the momentum close to the Dirac point and v_F is the Fermi velocity given by $v_F = 3ta/2 \approx 1 \times 10^6$ m/s. In Fig. 1.3 we depict the linear dispersion relation around the K point.

1.4.2 Massless Dirac fermions

We start from the Hamiltonian Eq. (1.61). Close to the Dirac point $\mathbf{K}$ we can build a pseudo-spin wave function $\psi(\mathbf{r})$ in which the first component refers to the sublattice A and the second component to the sublattice B. The equation of motion can be described by the massless Dirac equation

$$-iv_F \nabla \cdot \boldsymbol{\sigma} \psi(\mathbf{r}) = E\psi(\mathbf{r}), \tag{1.64}$$

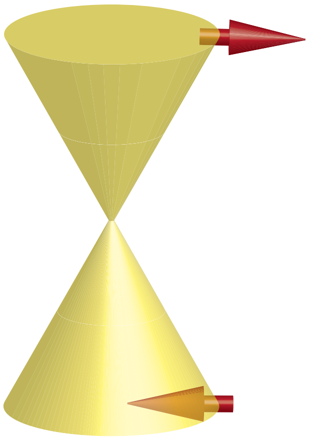

Figure 1.3: Schematic illustration of the Dirac cone. The conduction band and the valence band touch at the Dirac point K. Electrons have positive helicity, with the pseudo-spin along the direction of $\mathbf{p}$, whereas holes have negative helicity, with the pseudo-spin against the direction of $\mathbf{p}$.

where $\boldsymbol{\sigma} = (\sigma_x, \sigma_y)$ is the vector of Pauli matrices in the plane. The operator $\nabla \cdot \boldsymbol{\sigma}$ has only non-zero off-diagonal components, reflecting the fact that each time that an electron hops from one carbon atom to a nearest-neighbor it changes sublattice. In the momentum space the Hamiltonian is $H_K = v_F \mathbf{k} \cdot \boldsymbol{\sigma}$ and the eigenstates are

$$\psi_{\pm,\mathbf{K}}(\mathbf{k}) = \frac{1}{\sqrt{2}} \left(\begin{array}{c} e^{-i\theta_{\mathbf{k}}/2} \\ \pm e^{i\theta_{\mathbf{k}}/2} \end{array} \right), \tag{1.65}$$

where the $\pm$ signs refer to the eigenenergies $\pm v_F k$ for the π^* and π bands, respectively, and $\theta_{\mathbf{k}} = \arctan(k_x/k_y)$ is the angle in momentum space. The Hamiltonian around the $\mathbf{K}'$ Dirac point is given by

$$-iv_F \nabla \cdot \boldsymbol{\sigma}^* \psi(\mathbf{r}) = E\psi(\mathbf{r}), \tag{1.66}$$

and in the momentum space is given by $H_K = v_F \mathbf{k} \cdot \boldsymbol{\sigma}^*$, with $\boldsymbol{\sigma}^* = (\sigma_x, -\sigma_y)$. The eigenstates around the $\mathbf{K}'$ are related to those around the $\mathbf{K}$ point by time-reversal symmetry,

$$\psi_{\pm,\mathbf{K}'}(\mathbf{k}) = \frac{1}{\sqrt{2}} \left(\begin{array}{c} e^{i\theta_{\mathbf{k}}/2} \\ \pm e^{-i\theta_{\mathbf{k}}/2} \end{array} \right). \tag{1.67}$$

If the the phase θ is rotated by 2π the wave function changes sign, revealing the spinorial character of the wave function. Such a π shift is known in the literature as Berry's phase.

The eigenstates of the massless Dirac equation can be characterized by the helicity that is defined as the projection of the momentum operator along the pseudo-spin direction,

$$\hat{h} = \frac{1}{2}\boldsymbol{\sigma} \cdot \frac{\mathbf{p}}{|\mathbf{p}|}. \tag{1.68}$$

From the definition of the helicity operator it is clear that the states $\psi_{\pm,\mathbf{K}}(\mathbf{r})$ and $\psi_{\pm,\mathbf{K}'}(\mathbf{r})$ are also eigenstates of $\hat{h}$,

$$\hat{h}\psi_{\pm,\mathbf{K}}(\mathbf{r}) = \pm\frac{1}{2}\psi_{\pm,\mathbf{K}}(\mathbf{r}), \tag{1.69}$$

$$\hat{h}\psi_{\pm,\mathbf{K}'}(\mathbf{r}) = \mp\frac{1}{2}\psi_{\pm,\mathbf{K}'}(\mathbf{r}). \tag{1.70}$$

This is a consequence of the fact that particle in graphene are massless. It then follows that electron (holes) have a positive (negative) helicity and that the pseudo-spin $\boldsymbol{\sigma}$ points along or against the direction of $\mathbf{p}$. Such a property is known as *chirality* and helicity is a good quantum number only close to the Dirac points K and K'. In Fig. 1.3 we represent the Dirac cone, with the positive and negative energy bands that touch at the Dirac point. In the conduction band the pseudo-spin points along the direction of $\mathbf{p}$ and has positive helicilty, whereas in the valence band the pseudo-spin points against the direction of motion and has negative helicity.

References

[1] R. P. Feynman and A. R. Hibbs, Quantum Mechanics and Path Integrals, McGraw-Hill (1965).

[2] N. F. Ramsey, A molecular beam resonance method with separated oscillating fields, Phys. Rev. **78**, 695 - 699 (1950).

[3] D. P. DiVincenzo, Quantum computation, Science **270**, 255 (1995).

[4] D. P. DiVincenzo, The physical implementation of quantum computation, Fortschr. Phys. **48**, 771 (2000).

[5] D. Loss and D. P. DiVincenzo, Quantum computation with quantum dots, Phys. Rev. A **57**, 120 (1998).

[6] H. -P. Breuer and F. Petruccione, The Theory of Open Quantum Systems, Clarendon Press, Oxford (2006).

[7] A. G. Redfield, Adv. Magn. Reson. 1 (1965), p. 1.

[8] K. Blum, *Density Matrix Theory and Applications*, Plenum Press, New York, 1981.

[9] C. P. Slichter, *Principles of Magnetic Resonance*, Amsterdam, North-Holland, 1987.

[10] A. Abragam, *The principles of nuclear magnetism* (Clarendon Press, Oxford, 1961).

[11] M. H. Devoret, Quantum fluctuations in electrical circuits, (S. Reynaud, E. Giacobino and J. Zinn-Justin, eds., 1997, Elsevier Science)

[12] Y. Makhlin, G. Schön, and A. Shnirman, Quantum-state engineering with Josephson-junction devices, Rev. Mod. Phys. **73**, 357 (2001)

[13] Y. Makhlin, G. Schön, A. Shnirman, Josephson-junction qubits with controlled couplings, Nature **398**, 305-307 (1999)

[14] Y. Nakamura, Yu. A. Pashkin, J. S. Tsai, Coherent control of macroscopic quantum states in a single-Cooper-pair box, Nature **398**, 786-788 (1999)

[15] J. E. Mooij, T. P. Orlando, L. Levitov, Lin Tian, Caspar H. van der Wal, and Seth Lloyd, Josephson Persistent-Current Qubit, Science **285**, 1036 (1999)

[16] C. H. van der Wal, A. C. J. ter Haar, F. K. Wilhelm, R. N. Schouten, C. J. P. M. Harmans, T. P. Orlando, S. Lloyd, and J. E. Mooij, Quantum Superposition of Macroscopic Persistent-Current States, Science **290**, 773 (2000)

[17] I. Chiorescu, Y. Nakamura, C. J. P. M. Harmans, and J. E. Mooij, Coherent Quantum Dynamics of a Superconducting Flux Qubit, Science **299**, 1869 (2003)

[18] J. M. Martinis, S. Nam, J. Aumentado, C. Urbina, Rabi Oscillations in a Large Josephson-Junction Qubit, Phys. Rev. Lett. **89**, 117901 (2002)

[19] G. Burkard, R. H. Koch, D. P. DiVincenzo, Multilevel quantum description of decoherence in superconducting qubits, Phys. Rev. B **69**, 064503 (2004)

[20] R. H. Koch, J. R. Rozen, G. A. Keefe, F. M. Milliken, C. C. Tsuei, J. R. Kirtley, and D. P. DiVincenzo, Low-bandwidth control scheme for an oscillator-stabilized Josephson qubit, Phys. Rev. B **72**, 092512 (2005)

[21] L. Tian, L. S. Levitov, C. H. van der Wal, J. E. Mooij, T. P. Orlando, S. Lloyd, C. J. P. M. Harmans, and J. J. Mazo, Quantum mesoscopic phenomena and mesoscopic devices in microelectronics, edited by I. Kulik and R. Elliatioglu, NATO Science Series C: Mathematical and Physical Science No. 559 (Kluwer Academic, Dordrecht), p. 429 (2000).

[22] V. B. Braginsky and F. Ya. Khalili, Quantum Measurement, Cambridge University Press, Cambridge (1992).

[23] J. Preskill, http://www.theory.caltech.edu/people/preskill/ph229/.

[24] T. C. Ralph, S. D. Bartlett, J. L. O'Brien, G. J. Pryde, and H. M. Wiseman, Phys. Rev. A **73**, 012113 (2006).

[25] B. C. Travaglione, G. J. Milburn, and T. C. Ralph, arXiv: quant-ph/0203130 (2002).

[26] S. Datta, Electronic transport in mesoscopic systems, Cambridge University Press, Cambridge, (1995).

[27] R. Landauer, IBM J. Res. Dev. **1**, 223 (1957).

[28] Y. Imry, Physics of mesoscopic systems in *Direction in Condensed Matter Physics*, G. Grinstein, G. Mazenko, eds., World Scientific, Singapore (1986).

[29] M. Büttiker, Four-Terminal Phase-Coherent Conductance, Phys. Rev. Lett. **57**, 1761 (1986).

[30] K. S. Novoselov, A. K. Geim, S. V. Morozov, D. Jiang, Y. Zhang, S. V. Dubonos, I. V. Gregorieva, A. A. Firsov, Science **306**, 666 (2004).

[31] A. H. Castro Neto, F. Guinea, N. M. R. Peres, K. S. Novoselov, A. K. Geim, Rev. Mod. Phys. **81**, 109 (2009).

[32] P. R. Wallace, Phys. Rev. **71**, 622 (1947).

2. Voltage Controlled Flux Qubit

We study a voltage-controlled version of the superconducting flux qubit [Chiorescu *et al.*, Science **299**, 1869 (2003)] and show that full control of qubit rotations on the entire Bloch sphere can be achieved. Circuit graph theory is used to study a setup where voltage sources are attached to the two superconducting islands formed between the three Josephson junctions in the flux qubit. Applying a voltage allows qubit rotations about the y axis, in addition to pure x and z rotations obtained in the absence of applied voltages. The orientation and magnitude of the rotation axis on the Bloch sphere can be tuned by the gate voltages, the external magnetic flux, and the ratio α between the Josephson energies of the junctions via a flux-tunable junction. We compare the single-qubit control in the known regime $\alpha < 1$ with the unexplored range $\alpha > 1$ and estimate the decoherence due to voltage fluctuations. [1]

2.1 Introduction

Superconducting (SC) circuits can exhibit a great variety of quantum mechanical phenomena and are studied for their potential as devices for quantum information processing. Several different circuit implementations of a SC quantum bit (qubit) have been investigated both theoretically and experimentally [1, 2].

A prototype of a SC flux qubit, characterized by a working regime in which the Josephson energy dominates over the charging energy, $E_J \gg E_C$, has been theoretically designed and experimentally realized [3–7, 14, 29], showing quantum superposition and coherent evolution of two macroscopic states carrying opposite persistent currents that represent the qubit states. The flux qubit state is related to a magnetic moment, and is thus typically controlled via the application of external magnetic fields which create magnetic flux through the loop(s) in the circuit. An advantage of flux qubits is their relative insensitivity to charge fluctuations that can lead to fast decoherence [10–12], while magnetic fluctuations are typically more benign.

A second type of SC qubits, the so called charge qubits [13–17], operates in the limit in which the charge energy dominates, $E_C \gg E_J$, thus being relatively insensitive to magnetic fluctuations, while having a well defined value of the charge on a SC island, in which the presence or absence of an extra Cooper pair determines the state of the qubit. The intermediate regime in which the Josephson and charge energies are comparable, $E_J \approx E_C$, has been investigated and realized in the “quantronium” [18]. Another type of qubit is the Josephson, or phase, qubit, consisting of a single junction [19].

---

[1] This chapter has been published in Physical Review B **74**, 174510 (2006).

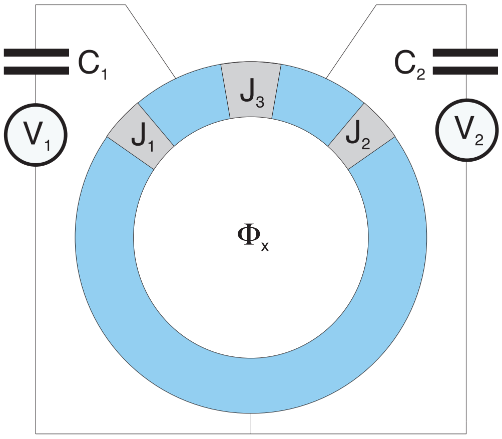

Figure 2.1: The voltage-biased SC flux qubit (schematic). The circuit consists of a SC ring (blue) with three Josephson junctions J_1, J_2, and J_3, threaded by an external magnetic flux Φ_x. The Josephson energy of the middle junction J_3 differs from the other two by a factor of α. A voltage bias V_i is applied to each of the two islands formed by the three junctions via a capacitor C_i.

In this paper, we investigate the possibility of enhancing the control of a SC flux qubit via the application of electrostatic gates [3, 20, 21]. We study the flux qubit proposed by Orlando *et al.* [3]. While in [3], the effect of any applied voltages was kept low in order to avoid charge noise, we explore the possibility of making use of the off-set gate charge as an additional control variable. We define two device parameters. Assuming for simplicity two Josephson junctions to have equal Josephson energies ($E_{J1} = E_{J2} = E_J$), the first parameter is given by the ratio $\alpha = E_{J3}/E_J$ between the Josephson energy of the third junction and the remaining two junctions. The regime of interest here is $0.5 < \alpha \lesssim 1.5$ although in principle larger values are possible. The second parameter is the ratio between the Josephson energy and the charging energy, E_J/E_C which for flux qubits is typically about 10 or larger. We analyze the role of these parameters in detail and, in addition to the well-studied regime $\alpha < 1$, also explore the opposite regime $\alpha > 1$. Particular effort is spent looking for a single-qubit Hamiltonian in which an effective pseudo-magnetic field couples to all three components of the pseudo-spin represented by the circuit. A charge qubit in which a σ_y term in the single-qubit Hamiltonian has been proposed in [22]. The possibility of changing the relative phase of the qubit states, together with the capability to flip them, allows full control over the qubit. Full control on the Bloch sphere is thought to be very useful in the field of adiabatic quantum computation [23–25].

Circuit theory provides us with a systematic and universal method for analyzing any electrical circuit that can be represented by lumped elements [6, 27–29]. Through the language of a graph theoretic formalism, Kirchhoff's laws and the Hamiltonian of the circuit are written in terms of a set of independent canonical coordinates that can easily be quantized. The formalism of [6, 27, 28] is particularly suited for studying circuits containing

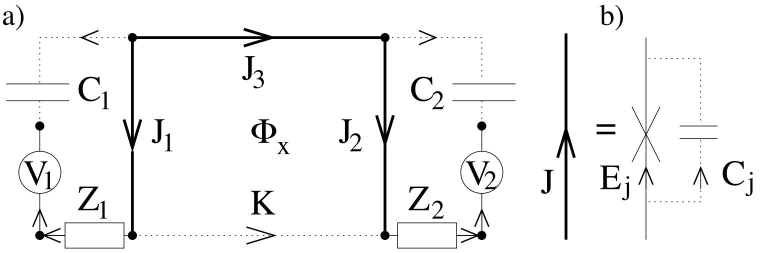

Figure 2.2: a) Circuit of a voltage-biased flux qubit (Fig. 2.1). The main loop contains three Josephson junctions and a (chord) inductance (K). An external magnetic flux Φ_x threads the SC loop. The junctions J_1 and J_2 are biased by two electrostatic gates, representing the main new feature of the circuit. Solid lines represent the tree of the circuit graph, while dotted lines are the chords. b) Each thick solid line represents a Josephson junction shunted by a capacitance C_J.

superconducting elements, like Josephson junctions, that are treated as nonlinear inductors. Here, we make use of the extended circuit theory that accounts for charging effects and can be applied both for charge and flux qubits [27].

Our main result is the identification of the parameter range for α and E_J/E_C in the voltage-controlled flux qubit in which the single qubit Hamiltonian acquires a σ_y term in addition to the σ_x and σ_z terms, thus allowing full control of the qubit rotations on the Bloch sphere. In this regime, we compute the dependence of the single-qubit Hamiltonian on the applied voltages V_1 and V_2. For the quantitative analysis of the qubit dynamics we calculate the tunneling amplitudes appearing in the Hamiltonian as functions of the device parameters.

The paper is structured as follows. In Section 2.2 we briefly review circuit theory [6, 27–29] and apply it to the circuit of Fig. 2.2 to find its Hamiltonian. Section 2.3 contains the derivation of the effective periodic potential in the Born-Oppenheimer approximation. In Section 2.4, we address the quantum dynamics of the circuit and find localized solutions in the periodic potential. In Section 2.5 we apply Bloch's theory in a tight-binding approximation to find general solutions in the presence of a voltage bias. Sec. 2.6 describes the calculation of the tunneling matrix elements appearing in the qubit Hamiltonian and their dependence on the device parameters α and E_J/E_C. In Sec. 2.7, we explore the regime ($\alpha > 1$) and show that a full control on the qubit Hamiltonian is feasible. In Section 2.8, we study the decoherence of the qubit due to the attached voltage sources. Finally, Sec. 2.9 contains a summary of our results and conclusions.

2.2 The circuit

Here we study a version of the Delft flux qubit [3, 7] with an additional voltage control (Fig. 2.1). Typically, such a qubit circuit also comprises a readout SQUID which can be surrounding or attached to the qubit. We concentrate on the qubit itself here and do not include the SQUID in our analysis because the presence of a readout circuit does not alter the analysis and results for single-qubit control presented here. A circuit representation of the studied device is shown in Fig. 2.2. The main loop contains three Josephson junctions and the loop self-inductance (K), and is threaded by an external magnetic flux Φ_x. The junctions form two SC islands to which electrostatic gates with capacitance C_1 and C_2 are attached and voltages V_1 and V_2 are applied. The voltage sources represent the new elements in the circuit. As long as the junctions are built in such a way that the Josephson energy dominates, $E_J \gg E_C$, the qubit is encoded in the orientation of the circulating persistent current, as in Refs. [3, 7].

We represent the circuit as the oriented graph $\mathcal{G}$ shown in Fig. 2.2a, consisting of $N = 8$ nodes (black dots) n_i $(i = 1, \ldots, 8)$ and $B = 13$ branches (thin lines) b_i $(i = 1, \ldots, 13)$, in which each branch b_i represents one of the following lumped circuit elements: a (bare) Josephson junction J, capacitance C, inductance K, voltage source V, and impedance Z. The impedances Z_1 and Z_2 model the imperfect voltage sources attached from outside to the quantum circuit. Every Josephson junction (thick line) consists of 2 branches: a bare Josephson junction (J) and the junction capacitance (C_J) as indicated in Fig. 2.2b. In addition to these two elements, a Josephson junction can also be combined with a shunt resistance [6]. However, these resistances are typically very large and can often be neglected; they are not be of interest here. The circuit graph $\mathcal{G}$ is divided in two parts. The *tree* is a loop-free subgraph which connects all nodes of the circuit and it is represented by solid lines in Fig. 2.2. All the branches f_i $(i = 1, \ldots, F)$ that do not belong to the tree are called *chords* and are represented by dotted lines in Fig. 2.2. In the present case, the number of chords, not counting the junction capacitances C_J, is $F = 3$. There can in principle be inductances contained both in the tree and in the chords which considerably complicate the analysis [6]. However, in our case there are no inductances in the tree (no L inductances), so that our analysis is much simpler than the general one. From now on, we make use of the fact that the circuit graph Fig. 2.2 has no inductances in its tree. When a chord is added to the tree, it gives rise to a unique loop, a *fundamental loop*. In other words, the set of fundamental loops $\mathcal{F}_i$ of the graph consists of all loops which contain exactly one chord f_i. The topological information about the graph is encoded in the fundamental loop matrix $\mathbf{F}^{(L)}$ of the circuit $(i = 1, \ldots, F;\ j = 1, \ldots, B)$,

$$\mathbf{F}^{(L)}_{ij} = \begin{cases} 1, & \text{if } b_j \in \mathcal{F}_i \text{ (same direction)}, \\ -1, & \text{if } b_j \in \mathcal{F}_i \text{ (opposite direction)}, \\ 0, & \text{if } b_j \notin \mathcal{F}_i, \end{cases} \tag{2.1}$$

where the direction of the fundamental loop $\mathcal{F}_i$ is given by the direction of its defining chord f_i. The currents $\mathbf{I} = (I_1, \ldots, I_B)$ and the voltages $\mathbf{V} = (V_1, \ldots, V_B)$ associated with the branches of the graph are divided in into tree and chord currents and voltages,

$$\mathbf{I} = (\mathbf{I}_{\text{tr}}, \mathbf{I}_{\text{ch}}), \qquad \mathbf{V} = (\mathbf{V}_{\text{tr}}, \mathbf{V}_{\text{ch}}). \tag{2.2}$$

With the division into three and chord branches, the fundamental loop matrix assumes the block form

$$\mathbf{F}^{(L)} = (\ -\mathbf{F}^T \ \ | \ \ \mathbb{I}\ ). \tag{2.3}$$

We further split up the current and voltage vectors according to the type of branch [27],

$$\begin{aligned} \mathbf{I}_{\text{tr}} &= (\mathbf{I}_J, \mathbf{I}_V, \mathbf{I}_Z), & \mathbf{I}_{\text{ch}} &= (\mathbf{I}_{C_J}, \mathbf{I}_C, \mathbf{I}_K), \\ \mathbf{V}_{\text{tr}} &= (\mathbf{V}_J, \mathbf{V}_V, \mathbf{V}_Z), & \mathbf{V}_{\text{ch}} &= (\mathbf{V}_{C_J}, \mathbf{V}_C, \mathbf{V}_K), \end{aligned} \tag{2.4}$$

such that the matrix $\mathbf{F}$ acquires the sub-block form,

$$\mathbf{F} = \begin{pmatrix} 1 & \mathbf{F}_{JC} & \mathbf{F}_{JK} \\ \mathbf{0} & \mathbf{F}_{VC} & \mathbf{F}_{VK} \\ \mathbf{0} & \mathbf{F}_{ZC} & \mathbf{F}_{ZK} \end{pmatrix}. \tag{2.5}$$

By inspection of Fig. 2.2, one finds the loop sub-matrices of the circuit according to the rule Eq. (2.1),

$$\begin{aligned} \mathbf{F}_{JC} &= \begin{pmatrix} 1 & 0 \\ 0 & 1 \\ 0 & 0 \end{pmatrix}, & \mathbf{F}_{JK} &= \begin{pmatrix} -1 \\ 1 \\ 1 \end{pmatrix}, \\ \mathbf{F}_{VC} = \mathbf{F}_{ZC} &= \begin{pmatrix} 1 & 0 \\ 0 & 1 \end{pmatrix}, & \mathbf{F}_{VK} = \mathbf{F}_{ZK} &= \begin{pmatrix} 0 \\ 0 \end{pmatrix}. \end{aligned} \tag{2.6}$$

With Eq. (2.3), Kirchhoff's laws have the compact form

$$\mathbf{F}\mathbf{I}_{\text{ch}} = -\mathbf{I}_{\text{tr}}, \tag{2.7}$$

$$\mathbf{F}^T\mathbf{V}_{\text{tr}} = \mathbf{V}_{\text{ch}} - \dot{\mathbf{\Phi}}_x, \tag{2.8}$$

where $\mathbf{\Phi}_x = (\Phi_1, \ldots, \Phi_F)$ is the vector of externally applied fluxes. Only loops with a non-zero inductance are susceptible to an external magnetic flux, thus only one external flux needs to be considered here, $\mathbf{\Phi}_x = (0, 0, \Phi_x)$.

The SC phase differences across the junctions $\boldsymbol{\phi} = (\varphi_1, \varphi_2, \varphi_3)$ are related to the canonical variables, the fluxes $\mathbf{\Phi}$, through the relation

$$\boldsymbol{\phi} = 2\pi \frac{\mathbf{\Phi}}{\Phi_0}, \tag{2.9}$$

while the canonically conjugate momenta are the charges $\mathbf{Q} = (Q_1, Q_2)$ on the junction capacitance. Using circuit theory [27] and ignoring the dissipative circuit elements Z_1 and Z_2 for the moment, we find the following Hamiltonian of the circuit Fig. 2.2,

$$\mathcal{H}_S = \frac{1}{2}(\mathbf{Q} - \mathbf{C}_V\mathbf{V}_V)^T \mathcal{C}^{-1} (\mathbf{Q} - \mathbf{C}_V\mathbf{V}_V) + \mathcal{U}(\mathbf{\Phi}), \tag{2.10}$$

$$\mathcal{U}(\mathbf{\Phi}) = -\mathbf{E}_J\mathbf{cos}2\pi\frac{\mathbf{\Phi}}{\Phi_0} + \frac{1}{2}\mathbf{\Phi}^{\mathbf{T}}\mathbf{M_0}\mathbf{\Phi} + \mathbf{\Phi}^{\mathbf{T}}\mathbf{N}\mathbf{\Phi}_{\mathbf{x}}, \tag{2.11}$$

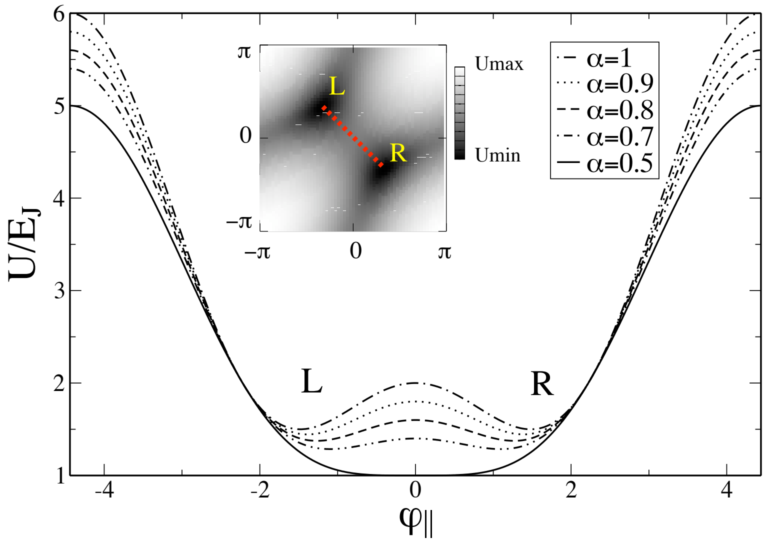

Figure 2.3: Plot of the potential $\mathcal{U}(\boldsymbol{\phi})$ for $\varphi_x = \pi$ along the line $\varphi_1 + \varphi_2 = 0$ as a function of $\varphi_{\|} = \frac{1}{\sqrt{2}}(\varphi_1 - \varphi_2)$ for several values of α. In the curve for $\alpha = 0.5$ the two minima are degenerate, while for $\alpha > 0.5$ they split showing the double well. The inset is a density plot of the potential for $\alpha = 0.8$, showing the two minima and the line $\varphi_1 + \varphi_2 = 0$.

where we have defined $\mathbf{cos}\boldsymbol{\phi} = (\cos\varphi_1, \cos\varphi_2, \cos\varphi_3)$. The Josephson energy matrix is given as

$$\mathbf{E}_J = \left(\frac{\Phi_0}{2\pi}\right)^2 \mathbf{L}_J^{-1} = \mathrm{diag}(E_J, E_J, \alpha E_J), \tag{2.12}$$

where $\Phi_0 = h/2e$ is the SC quantum of magnetic flux. We assume that the Josephson energies and capacitances of the junctions J_1 and J_2 are equal, $E_{J1} = E_{J2} \equiv E_J$ and $C_{J1} = C_{J2} \equiv C_J$, and we define the ratio $\alpha = E_{J3}/E_J$. The capacitance matrices of the circuit are

$$\mathbf{C}_J = \mathrm{diag}(C_J, C_J, C_{J3}), \quad \mathbf{C} = \mathrm{diag}(C_1, C_2). \tag{2.13}$$

The source voltage vector is defined as $\mathbf{V}_V = (V_1, V_2)$. The derived capacitance matrices $\mathcal{C}$ and $\mathbf{C}_V$ and the derived (inverse) inductance matrices $\mathbf{M}_0$ and $\mathbf{N}$ of Eq. (2.10) are given in the Appendix A.

2.3 Born-Oppenheimer approximation

We consider now the limit in which the chord inductance K is small compared to the Josephson inductances, $K \ll L_J$. By means of the Born-Oppenheimer approximation, we derive an effective two-dimensional potential as a function of two “slow” degrees of freedom. Our analysis follows closely that of [29]. For $K \ll L_J$, the potential Eq. (2.11) gives rise to a hard constraint for the variables $\boldsymbol{\phi}$, in the form of the linear equation

$$\mathbf{M}_0\boldsymbol{\phi} + \mathbf{N}\varphi_x = 0, \tag{2.14}$$

where the external magnetic flux is written as $\varphi_x = 2\pi\Phi_x/\Phi_0$. The general solution of the Eq. (2.14),

$$\boldsymbol{\phi} = \begin{pmatrix} \varphi_1 \\ \varphi_2 \\ \varphi_1 - \varphi_2 + \varphi_x \end{pmatrix}, \tag{2.15}$$

depends on the two variables φ_1 and φ_2 only. Thus, in the limit of small K, the dynamics is restricted to a plane in three-dimensional $\boldsymbol{\phi}$ space. The potential, restricted to the plane, is then a function of φ_1 and φ_2 only [3],

$$\mathcal{U}(\boldsymbol{\phi}) = E_J\Big[- \cos(\varphi_1) - \cos(\varphi_2) - \alpha\cos(\varphi_1 - \varphi_2 + \varphi_x)\Big]. \tag{2.16}$$

A density plot of $\mathcal{U}$ for $\alpha = 0.8$ as a function of φ_1 and φ_2 is shown in the inset of Fig. 2.3. The minima of the potential are found by solving the equation grad$\mathcal{U} = 0$, which yields [3]

$$\sin\varphi_1 = -\sin\varphi_2 = -\sin\varphi^*, \tag{2.17}$$

where φ^* is the solution of the self-consistent equation

$$\sin\varphi^* = \alpha\sin(2\varphi^* + \varphi_x). \tag{2.18}$$

The potential forms two wells whose relative depth is determined by the value of the externally applied flux φ_x. In order to have a symmetric double well we choose $\varphi_x = \pi$ which yields two minima at the points $\boldsymbol{\phi}_{\mathrm{R}} = (\varphi^*, -\varphi^*)$ and $\boldsymbol{\phi}_{\mathrm{L}} = (-\varphi^*, \varphi^*)$ with $\varphi^* = \arccos(1/2\alpha) > 0$. If $\alpha > 0.5$, then there are two distinct minima. Taking into account the periodicity of the potential, a complete set of solutions of Eq. (2.18) is $\boldsymbol{\phi} = \pm(\varphi^*, -\varphi^*)^T + 2\pi(n, m)$, with integer n, m. We plot the double well potential between the two minima in Fig. 2.3 for different values of α in the symmetric case $\varphi_x = \pi$.

2.4 Quantum dynamics

In this section, we look for localized solutions of the Schrödinger equation $\mathcal{H}\Psi = E\Psi$, with the Hamiltonian of Eq. (2.10). We expand the potential around the two minimum configurations, keeping contributions up to the second order in $\boldsymbol{\phi}$, and solve the Schrödinger equation in these two different points (denoting them L and R for left and right). We obtain the quadratic Hamiltonian

$$\mathcal{H}_{\mathrm{L,R}} = \frac{1}{2}\left[\mathbf{Q}^T\mathcal{C}^{-1}\mathbf{Q} + \mathbf{\Phi}^T\mathbf{L}^{-1}_{\mathrm{lin;\ L,R}}\mathbf{\Phi}\right], \tag{2.19}$$

where the linearized inductance $\mathbf{L}_{\mathrm{lin;L,R}}$ is defined as

$$\mathbf{L}^{-1}_{\mathrm{lin;\ L,R}} = \mathbf{M}_0 + \mathbf{L}_J^{-1}\mathbf{cos}\boldsymbol{\phi}_{\mathrm{L,R}}. \tag{2.20}$$

To simplify the kinetic part in Eq. (2.19), we perform a canonical transformation on the variable $\mathbf{\Phi}$ and its conjugate momentum $\mathbf{Q}$ [29],

$$\begin{aligned} \mathbf{\Phi} &= \sqrt{c}\left(\sqrt{\mathcal{C}}^{-1}\right)^T \tilde{\mathbf{\Phi}}, \\ \mathbf{Q} &= \sqrt{\mathcal{C}}\tilde{\mathbf{Q}}/\sqrt{c}, \end{aligned} \tag{2.21}$$

where c is an arbitrary unit capacitance (e.g., $c = C_J$). We define the diagonal matrix $\mathbf{\Omega}^2_{L,R}$ such that it satisfies

$$(\sqrt{\mathcal{C}}^{-1})^T \mathbf{L}^{-1}_{\mathrm{lin;L,R}} \sqrt{\mathcal{C}}^{-1} = \mathbf{O}^T \mathbf{\Omega}^2_{L,R} \mathbf{O}, \tag{2.22}$$

where $\mathbf{O}$ is an orthogonal matrix that diagonalizes the left hand side (lhs) of Eq. (2.22). This allows us to further simplify the Hamiltonian by making the following canonical transformation, preserving the Poisson brackets,

$$\mathbf{\Phi}' = \mathbf{O}\tilde{\mathbf{\Phi}}, \quad \mathbf{Q}' = \mathbf{O}\tilde{\mathbf{Q}}, \tag{2.23}$$

that leads us to the Hamiltonian,

$$\mathcal{H}_{\mathrm{L,R}} = \frac{1}{2}\left(c^{-1}\mathbf{Q}'^2 + \mathbf{\Phi}'^T \mathbf{\Omega}^2_{\mathrm{L,R}} \mathbf{\Phi}'\right). \tag{2.24}$$

In the case of a symmetric potential (when $\varphi_x = \pi$), the matrices $\mathbf{L}_{\mathrm{lin;L,R}}$ of the linearized problem are equal,

$$\mathbf{L}_{\mathrm{lin;L}} = \mathbf{L}_{\mathrm{lin;R}}, \quad \text{and} \quad \mathbf{\Omega}_{\mathrm{L}} = \mathbf{\Omega}_{\mathrm{R}}, \tag{2.25}$$

hence we drop the subscript L and R for simplicity.

We quantize the Hamiltonian by imposing the canonical commutation relations,

$$[\Phi_i, Q_j] = i\hbar\delta_{ij}, \tag{2.26}$$

where Φ_i and Q_j are the components of the vectors $\mathbf{\Phi}$ and $\mathbf{Q}$ respectively. The ground-state wave function is the Gaussian,

$$\Psi_\alpha(\boldsymbol{\varphi}) = \left(\frac{\det \mathcal{M}}{\pi^2}\right)^{1/4} \exp\left[-\frac{1}{2}(\boldsymbol{\varphi} - \boldsymbol{\varphi}_\alpha)^T \mathcal{M} (\boldsymbol{\varphi} - \boldsymbol{\varphi}_\alpha)\right], \tag{2.27}$$

where $\alpha = \mathrm{L}, \mathrm{R}$ and

$$\mathcal{M} = \frac{1}{\hbar}\left(\frac{\Phi_0}{2\pi}\right)^2 \sqrt{\mathcal{C}}\mathbf{O}^T \mathbf{\Omega} \mathbf{O} \sqrt{\mathcal{C}}. \tag{2.28}$$

For the wave function overlap integral between the left and right state, $S = \langle \Psi_L | \Psi_R \rangle$, we find

$$S = \exp\left\{-\frac{1}{4}\mathbf{\Delta}\boldsymbol{\varphi}^T \mathcal{M} \mathbf{\Delta}\boldsymbol{\varphi}\right\}, \tag{2.29}$$

where $\Delta\boldsymbol{\phi} = \boldsymbol{\phi}_{\mathrm{R}} - \boldsymbol{\phi}_{\mathrm{L}} = 2\arccos(1/2\alpha)(1, -1)$ is the distance between the right (R) and left (L) potential minima (Fig. 2.4).

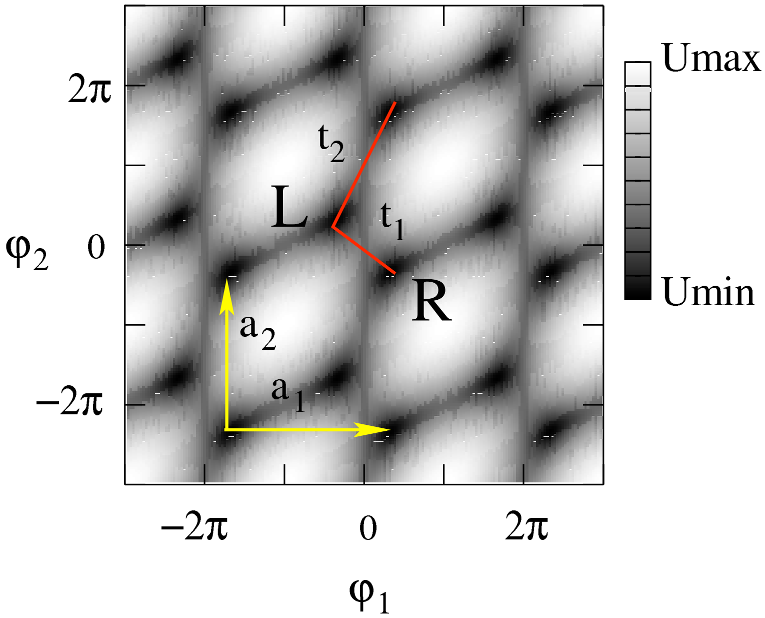

Figure 2.4: Density plot of the double well potential $U(\varphi_1, \varphi_2)$ in units of E_J for $\alpha = 0.8$ on a logarithmic scale. The periodicity of the potential is evident; each unit cell contains two minima (black). The primitive vectors of the Bravais lattice are denoted $\mathbf{a}_1$ and $\mathbf{a}_2$ while t_1 and t_2 are the tunneling matrix elements between the nearest-neighbor minima.

2.5 Bloch theory

Given the periodicity of the problem Eq. (2.10) with the potential Eq. (2.16) in the Born-Oppenheimer approximation, an important question concerns the boundary conditions of the problem, i.e., the choice of the appropriate Hilbert space. The question is whether the domain of $\boldsymbol{\phi}$ should be the infinite plane or the square $T = [-\pi, \pi)^2$ with periodic boundary conditions. This question has been discussed extensively in the literature [30–32]. Since in our case, a shift of φ_1 or φ_2 by 2π creates a state which is physically indistinguishable from the one before the shift, we choose the compact domain T and impose periodic boundary conditions on the wavefunction. However, we are going to extend the domain to the infinite domain in order to facilitate the calculation.

2.5.1 The periodic problem

The approximate solutions constructed in Sec. 2.4 are a good starting point, but they are insensitive to the boundary conditions. However, the boundary conditions are essential if finite bias voltages $\mathbf{V}_V$ are to be taken into account. The problem at hand is defined on the square with side 2π (see inset of Fig. 2.3) with periodic boundary conditions; i.e., the phases $\boldsymbol{\varphi} = (\varphi_1, \varphi_2)^T$ are in the compact domain $T = [-\pi, \pi)^2$ and the wavefunction at opposite edges needs to be identical, $\Psi(-\pi, \varphi_2) = \Psi(\pi, \varphi_2)$ and $\Psi(\varphi_1, -\pi) = \Psi(\varphi_1, \pi)$, such that T acquires the topology of a torus. If the boundary conditions are ignored, e.g., in the case where the wavefunction is known to be vanishingly small at the boundary, then the bias voltages $\mathbf{V}_V$ in the Hamiltonian Eq. (2.10) can be removed completely with a gauge transformation and the solutions will be independent of $\mathbf{V}_V$.

We proceed as follows: We first solve the problem Eq. (2.10) in the infinite two-dimensional plane and then choose those solutions that satisfy the periodic boundary conditions and then restrict them to the compact domain T. We choose this approach because the problem on the infinite domain is well known: the solutions $\psi_{\alpha\mathbf{k}}$ are given by Bloch's theorem for the motion of a particle in a crystal and satisfy

$$\psi_{\alpha\mathbf{k}}(\boldsymbol{\varphi} + 2\pi\mathbf{m}) = \mathrm{e}^{2\pi i\mathbf{m}\cdot\mathbf{k}}\,\psi_{\alpha\mathbf{k}}(\boldsymbol{\varphi}), \tag{2.30}$$

for $\mathbf{m} = (m_1, m_2)$ with integer m_1 and m_2. The minima of our potential, Eq. (2.16), define a two-dimensional square Bravais lattice with a two-point basis, which looks like a sheared hexagonal lattice (although it is a square lattice). The lattice and its primitive vectors $\mathbf{a}_1 = (2\pi, 0)$ and $\mathbf{a}_2 = (0, 2\pi)$ are shown in Fig. 2.4. The lattice basis is given by the vectors $\mathbf{b}_\mathrm{L} = (0, 0)$ and $\mathbf{b}_\mathrm{R} = 2(\varphi^*, -\varphi^*)$. Each lattice point can be identified by the Bravais lattice vector $\mathbf{n}$ and the basis index $\alpha = \mathrm{L}, \mathrm{R}$. As indicated above, not all the Bloch functions satisfying the Schrödinger equation on the infinite domain have a physical meaning, but only those that are also 2π-periodic. In the case of zero applied voltage bias, the only value of $\mathbf{k}$ yielding to a periodic wave function is $\mathbf{k} = \mathbf{0}$.

2.5.2 Tight-binding approximation

In order to construct approximate Bloch states, we first form localized Wannier orbitals ϕ_α by orthonormalizing the localized solutions Ψ_α ($\alpha = \mathrm{L}, \mathrm{R}$) from Eq. (2.27). These Wannier orbitals are centered at arbitrary lattice points, $\phi_{\alpha\mathbf{n}}(\boldsymbol{\phi}) = \phi_\alpha(\boldsymbol{\phi} - 2\pi\mathbf{n})$ and satisfy the orthonormality relations

$$\langle\phi_{\alpha\mathbf{n}}|\phi_{\beta\mathbf{m}}\rangle = \delta_{\alpha\beta}\delta_{\mathbf{nm}}. \tag{2.31}$$

The Bloch states are then related to the Wannier orbitals via a Fourier transform,

$$\psi_{\alpha\mathbf{k}}(\boldsymbol{\varphi}) = \sum_{\mathbf{n}\in\mathbb{Z}^2} \mathrm{e}^{2\pi i\mathbf{k}\cdot\mathbf{n}}\,\phi_{\alpha\mathbf{n}}(\boldsymbol{\varphi}), \tag{2.32}$$

$$\phi_{\alpha\mathbf{n}}(\boldsymbol{\varphi}) = \int_{\mathrm{FBZ}} d\mathbf{k}\,\mathrm{e}^{-2\pi i\mathbf{k}\cdot\mathbf{n}}\,\psi_{\alpha\mathbf{k}}(\boldsymbol{\varphi}), \tag{2.33}$$

where the integration in Eq. (2.33) is over the first Brillouin zone (FBZ), i.e., $k_i \in [-1/2, 1/2)$. The label α plays the role of the energy band label in Bloch theory. The Bloch states $\psi_{\alpha\mathbf{k}}$ form a complete set of orthonormal states in $\mathbf{k}$-space, where $k_i \in [-1/2, 1/2)$,

$$\langle\psi_{\alpha\mathbf{k}}|\psi_{\beta\mathbf{q}}\rangle = \delta_{\alpha\beta}\delta(\mathbf{k} - \mathbf{q}), \tag{2.34}$$

$$\sum_\alpha \int d\mathbf{k}|\psi_{\alpha\mathbf{k}}\rangle\langle\psi_{\alpha\mathbf{k}}| = \mathbb{I}. \tag{2.35}$$

For the completeness relation Eq. (2.35) to hold, we must sum over all bands α, corresponding to a complete set of Wannier functions. Here, in order to describe the low-energy physics of the system, we restrict ourselves to the two lowest bands $\alpha = \mathrm{L}, \mathrm{R}$, related to the left and right potential minimum in the unit cell, and neglect higher excited states of the double wells. This restriction is justified if the energy gap between the lowest two states is much smaller than the gap between the two lowest and all higher states (see Table 3.1). We normalize the Bloch functions on the unit cell T,

$$\int_T d\boldsymbol{\phi} |\psi_{\mathbf{k}\alpha}(\boldsymbol{\varphi})|^2 = 1. \tag{2.36}$$

Now we can expand the Hamiltonian in the Bloch function basis with Eq. (2.35), and then apply Eq. (2.32),

$$\begin{aligned} \mathcal{H} &\simeq \sum_{\alpha\beta} \int d\mathbf{k} d\mathbf{q} |\psi_{\alpha\mathbf{k}}\rangle \langle \psi_{\alpha\mathbf{k}}|\mathcal{H}|\psi_{\beta\mathbf{q}}\rangle\langle\psi_{\beta\mathbf{q}}| \\ &= \sum_{\alpha\beta} \int d\mathbf{k} d\mathbf{q}\, \mathcal{H}^{\alpha\beta}_{\mathbf{kq}} |\psi_{\alpha\mathbf{k}}\rangle\langle\psi_{\beta\mathbf{q}}|, \end{aligned} \tag{2.37}$$

where the approximation in the first line consists in omitting bands that are energetically higher than $\alpha = \mathrm{L}, \mathrm{R}$ (see above). The matrix elements of the Hamiltonian in the Bloch basis are

$$\mathcal{H}^{\alpha\beta}_{\mathbf{kq}} = \sum_{\mathbf{n},\mathbf{m}\in\mathbb{Z}^2} \mathrm{e}^{-2\pi i(\mathbf{k}\cdot\mathbf{n}-\mathbf{q}\cdot\mathbf{m})} \langle\phi_{\alpha\mathbf{n}}|\mathcal{H}|\phi_{\beta\mathbf{m}}\rangle. \tag{2.38}$$

For fixed $\mathbf{k}$ and $\mathbf{q}$, Eq. (2.38) is reduced to a 2×2 hermitian matrix. The main contributions to Eq. (2.38) stem from either tunneling between the two sites in the same unit cell (intra-cell) or between site L in one cell and site R in an adjacent cell (inter-cell), see Fig. 2.4. For the off-diagonal element we can write

$$\mathcal{H}^{\mathrm{LR}}_{\mathbf{kq}} \simeq \sum_{\mathbf{n}\in\mathbb{Z}^2} e^{-2\pi i(\mathbf{k}-\mathbf{q})\cdot\mathbf{n}} \Big[\langle\phi_{\mathrm{L}\mathbf{n}}|\mathcal{H}|\phi_{\mathrm{R}\mathbf{n}}\rangle + \mathrm{e}^{-2\pi i q_1}\langle\phi_{\mathrm{L}\mathbf{n}}|\mathcal{H}|\phi_{\mathrm{R}\mathbf{n}-\mathbf{e_1}}\rangle + \mathrm{e}^{2\pi i q_2}\langle\phi_{\mathrm{L}\mathbf{n}}|\mathcal{H}|\phi_{\mathrm{R}\mathbf{n}+\mathbf{e_2}}\rangle\Big]. \tag{2.39}$$

where $\mathbf{e}_1 = (1,0)$ and $\mathbf{e}_2 = (0,1)$. Due to the lattice periodicity, the quantities (see Fig. 2.4)

$$\epsilon_0 = \langle\phi_{L(R)\mathbf{n}}|\mathcal{H}|\phi_{L(R)\mathbf{n}}\rangle, \tag{2.40}$$

$$t_1 = \langle\phi_{L(R)\mathbf{n}}|\mathcal{H}|\phi_{R(L)\mathbf{n}}\rangle, \tag{2.41}$$

$$t_2 = \langle\phi_{L(R)\mathbf{n}}|\mathcal{H}|\phi_{R(L)\mathbf{n}-\mathbf{e_1}}\rangle \tag{2.42}$$

$$= \langle\phi_{L(R)\mathbf{n}}|\mathcal{H}|\phi_{R(L)\mathbf{n}+\mathbf{e_2}}\rangle, \tag{2.43}$$

are independent of the lattice site $\mathbf{n}$, and thus from Eq. (2.38), we find $\mathcal{H}^{\alpha\beta}_{\mathbf{kq}} \simeq \delta(\mathbf{k}-\mathbf{q})\mathcal{H}^{\alpha\beta}_{\mathbf{k}}$. We can now write the 2×2 Hamiltonian as

$$\mathcal{H}_{\mathbf{k}} = \epsilon_0\mathbb{I} + \frac{1}{2}\begin{pmatrix} 0 & \Delta(\mathbf{k})^* \\ \Delta(\mathbf{k}) & 0 \end{pmatrix}, \tag{2.44}$$

$$\Delta(\mathbf{k}) = 2\left[t_1 + t_2(\mathrm{e}^{2\pi i k_1} + \mathrm{e}^{-2\pi i k_2})\right]. \tag{2.45}$$

The equality in Eq. (2.43) is due to the invariance of the potential under the transformation $(\varphi_1, \varphi_2) \to -(\varphi_2, \varphi_1)$ and it is valid also in the $\varphi_x \neq \pi$ case. The eigenvalues of the problem are

$$\epsilon_\pm(\mathbf{k}) = \epsilon_0 \pm \frac{1}{2}|\Delta(\mathbf{k})|, \tag{2.46}$$

and represent a typical two-band dispersion relation. In the case of zero external applied voltage only the $\mathbf{k} = 0$ Bloch functions satisfy the correct boundary conditions, i.e., are periodic. For $\mathbf{k} = 0$ we recognize the qubit Hamiltonian that, in the symmetric double well case, is given by a σ_x term [3],

$$\mathcal{H} = \epsilon_0 + (t_1 + 2t_2)\sigma_x. \tag{2.47}$$

2.5.3 Effect of a voltage bias

Now, we study the case with an (nonzero) external bias voltage. Given the Bloch function $\psi_{\alpha\mathbf{k}}$ that satisfies the Schrödinger equation for the Hamiltonian Eq. (2.10) for zero applied voltages, $\mathbf{V}_V = 0$, we find for the solution wave function for finite voltages $\mathbf{V}_V \neq 0$,

$$u_{\alpha\mathbf{k}}(\boldsymbol{\varphi}) = \mathrm{e}^{-i\boldsymbol{\varphi}\cdot\mathbf{Q}_g/2e}\,\psi_{\alpha\mathbf{k}}(\boldsymbol{\varphi}), \tag{2.48}$$

where we have defined the gate charge vector as $\mathbf{Q}_g = \mathbf{C}_V\mathbf{V}_V$. The above statement can be directly verified by substituting $u_{\alpha\mathbf{k}}$ from Eq. (2.48) into the Schrödinger equation with Eq. (2.10) while using that $\psi_{\alpha\mathbf{k}}$ solves the problem for $\mathbf{V}_V = 0$. The solutions in the presence of an applied voltage bias satisfy

$$u_{\alpha\mathbf{k}}(\boldsymbol{\varphi} + 2\pi\mathbf{n}) = \mathrm{e}^{2\pi i\mathbf{n}\cdot(\mathbf{k}-\mathbf{Q}_g/2e)}\,u_{\alpha\mathbf{k}}(\boldsymbol{\varphi}). \tag{2.49}$$

For the periodicity of the wave function on the compact domain, we have to choose $\mathbf{k} = \mathbf{Q}_g/2e$. This means that $u_{\alpha\mathbf{k}}$ is the periodic part of the Bloch function for $\mathbf{k} = \mathbf{Q}_g/2e$. By substituting this into Eqs. (2.44) and (2.45), we obtain the qubit Hamiltonian

$$\mathcal{H} = \frac{1}{2}\left[\mathrm{Re}(\Delta)\sigma_x + \mathrm{Im}(\Delta)\sigma_y + \epsilon\sigma_z\right] = \frac{1}{2}\mathbf{B}\cdot\boldsymbol{\sigma}, \tag{2.50}$$

where we have also included the effect of a (small) bias flux that tilts the double well, $\epsilon \simeq 2\alpha\sqrt{1 - 1/4\alpha^2}E_J(\varphi_x - \pi)$, where $\boldsymbol{\sigma} = (\sigma_x, \sigma_y, \sigma_z)$ are the Pauli matrices, and

$$\begin{aligned}\mathrm{Re}(\Delta) &= 2\left[t_1 + 2t_2\cos(\pi k_+)\cos(\pi k_-)\right], & (2.51)\\ \mathrm{Im}(\Delta) &= 4t_2\cos(\pi k_+)\sin(\pi k_-), & (2.52)\end{aligned}$$

with $k_\pm = (C_1V_1 \pm C_2V_2)/2e$. The eigenstates for $\epsilon = 0$ are

$$\begin{aligned}|0\rangle &= \frac{1}{\sqrt{2}}\left(-\mathrm{e}^{-i\theta}|L\rangle + |R\rangle\right), & (2.53)\\ |1\rangle &= \frac{1}{\sqrt{2}}\left(\mathrm{e}^{-i\theta}|L\rangle + |R\rangle\right), & (2.54)\end{aligned}$$

where $\tan\theta = \mathrm{Im}(\Delta)/\mathrm{Re}(\Delta)$. In Eq. (2.50), we have introduced the pseudo-field $\mathbf{B} = (\mathrm{Re}(\Delta), \mathrm{Im}(\Delta), \epsilon)$.

2.6 Calculation of t_1 and t_2

For a quantitative analysis of the single-qubit Hamiltonian Eq. (2.50), we have to calculate the tunneling matrix elements t_1 and t_2. In order to do so, we require a set of orthonormal Wannier functions on the infinite two-dimensional lattice defined by the potential $\mathcal{U}$, Eq. (2.11). We start from the non-orthogonal set of Gaussian orbitals $|\Psi_{\alpha\mathbf{n}}\rangle$ consisting of the solution Eq. (2.27), shifted by a lattice vector $\mathbf{n}$,

$$\Psi_{\alpha\mathbf{n}}(\boldsymbol{\phi}) = \Psi_\alpha(\boldsymbol{\phi} - 2\pi\mathbf{n}). \tag{2.55}$$

The orthonormalized Wannier functions can be written as a linear combination of these Gaussians,

$$|\phi_{\alpha\mathbf{n}}\rangle = \sum_{\mu=L,R,\mathbf{l}\in\mathbb{Z}^2} \mathcal{G}_{\mu\mathbf{l},\alpha\mathbf{n}}|\Psi_{\mu\mathbf{l}}\rangle. \tag{2.56}$$

To form a complete set of orthonormal functions the following relation must be satisfied,

$$\langle\phi_{\alpha\mathbf{n}}|\phi_{\beta\mathbf{m}}\rangle = \left(\mathcal{G}^\dagger S \mathcal{G}\right)_{\alpha\mathbf{n},\beta\mathbf{m}} = \delta_{\alpha\beta}\delta_{\mathbf{nm}}, \tag{2.57}$$

where S is the (real and symmetric) overlap matrix,

$$S_{\alpha\mathbf{n},\beta\mathbf{m}} = \int d\boldsymbol{\varphi} \Psi_{\alpha\mathbf{n}}(\boldsymbol{\varphi})\Psi_{\beta\mathbf{m}}(\boldsymbol{\varphi}). \tag{2.58}$$

We solve Eq. (2.57) with

$$\mathcal{G}^T = \mathcal{G} = \sqrt{S^{-1}}. \tag{2.59}$$

The inverse of S exists due to its positive definiteness. The entries of the overlap matrix S are equal to 1 on the diagonal, whereas the off-diagonal elements are positive and $\ll 1$ because the orbitals $\Psi_{\alpha\mathbf{n}}$ are well localized. We define the matrix $S^{(1)}$ with all matrix elements $\ll 1$ via

$$S = \mathbb{I} + S^{(1)} = \mathbb{I} + \begin{pmatrix} S_{\mathrm{LL}} & S_{\mathrm{LR}} \\ S_{\mathrm{LR}}^T & S_{\mathrm{RR}} \end{pmatrix}, \tag{2.60}$$

and find, keeping only first order terms in $S^{(1)}$,

$$\mathcal{G} \simeq \sqrt{S^{-1}} \simeq \mathbb{I} - \frac{1}{2}S^{(1)}. \tag{2.61}$$

Note that S_{LL} and S_{RR} have zeros on the diagonal.

In our tight-binding approximation, we consider five unit cells, a center cell with its four nearest neighbors, corresponding to the lattice vectors $\{(0,0),(\pm1,0),(0,\pm1)\}$. This means that S and $\mathcal{G}$ are 10×10 matrices, which can also be expressed as 2×2 block matrices, each block of dimension 5×5. The two largest values are given by $s_1 = S_{\mathbf{Ln},\mathbf{Rn}}$ and $s_2 = S_{\mathbf{Ln},\mathbf{Rn}-\mathbf{e}_1} = S_{\mathbf{Ln},\mathbf{Rn}+\mathbf{e}_2}$ with the nearest neighbor cell. Taking only these two

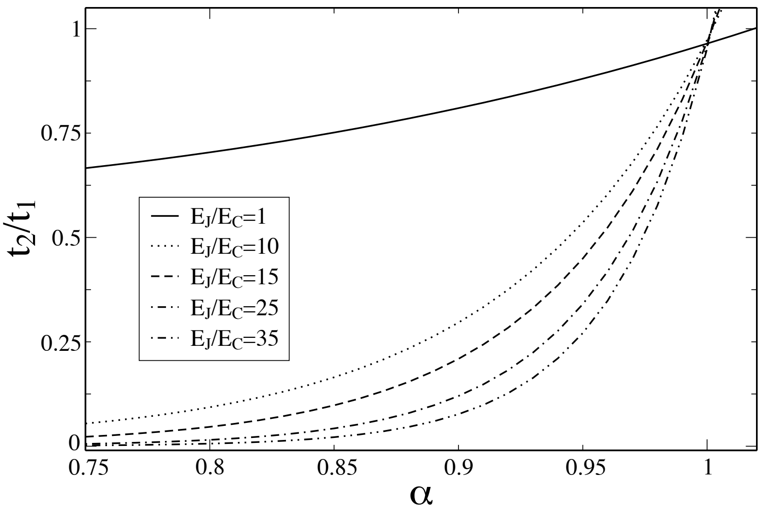

Figure 2.5: The ratio t_2/t_1 between the tunneling matrix elements, plotted as a function of $\alpha \leq 1$ for several values of E_J/E_C.

largest overlaps into account, we obtain $S_{\rm LL} = S_{\rm RR} \simeq 0$ and

$$S_{\rm LR} \simeq \begin{pmatrix} s_1 & s_2 & s_2 & 0 & 0 \\ 0 & s_1 & 0 & 0 & 0 \\ 0 & 0 & s_1 & 0 & 0 \\ s_2 & 0 & 0 & s_1 & 0 \\ s_2 & 0 & 0 & 0 & s_1 \end{pmatrix}. \tag{2.62}$$

Having the matrix $\mathcal{G}$ and S we can calculate the tunneling matrix

$$\mathcal{T}_{\alpha\mathbf{n},\beta\mathbf{m}} = \langle\phi_{\alpha\mathbf{n}}|\mathcal{H}|\phi_{\beta\mathbf{m}}\rangle = (\mathcal{G}^\dagger T\mathcal{G})_{\alpha\mathbf{n},\beta\mathbf{m}}, \tag{2.63}$$

where the entries of the matrix T are given as

$$T_{\alpha\mathbf{n},\beta\mathbf{m}} = \langle\Psi_{\alpha\mathbf{n}}|\mathcal{H}|\Psi_{\beta\mathbf{m}}\rangle. \tag{2.64}$$

Since both the $|\Psi_{\alpha\mathbf{n}}\rangle$ and the $|\phi_{\alpha\mathbf{n}}\rangle$ states are localized at the lattice position $\mathbf{n}$, the matrices T and $\mathcal{T}$ both have the same non-zero entries as S. The tunneling matrix $\mathcal{T}$ has the same block form as S with $\mathcal{T}_{\rm LL} = \mathcal{T}_{\rm RR} = \epsilon_0\mathbb{I}$ and $\mathcal{T}_{\rm LR}$ having the same structure as $S_{\rm LR}$ with s_1 and s_2 replaced by t_1 and t_2, given as $t_1 = \mathcal{T}_{\rm L\mathbf{n},R\mathbf{n}}$ and $t_2 = \mathcal{T}_{\rm L\mathbf{n},R\mathbf{n}-\mathbf{e}_1} = \mathcal{T}_{\rm L\mathbf{n},R\mathbf{n}+\mathbf{e}_2}$. The overlaps s_1 and s_2, together with the transition amplitudes t_1 and t_2, depend exponentially on the two parameters α and E_J/E_C. A detailed analysis is given below; here, we anticipate the approximate relations $t_1/t_2 > 1$ if $\alpha < 1$, $t_1/t_2 < 1$ if $\alpha > 1$, and $t_1/t_2 \approx 1$ if $\alpha = 1$, and $t_1/t_2 = 1$ if $C_1 = C_2 = 0$.

Now, we numerically determine the tunneling matrix elements t_1 and t_2 from Eqs. (2.63) and (2.64) and analyze their dependence on the external parameters. This dependence

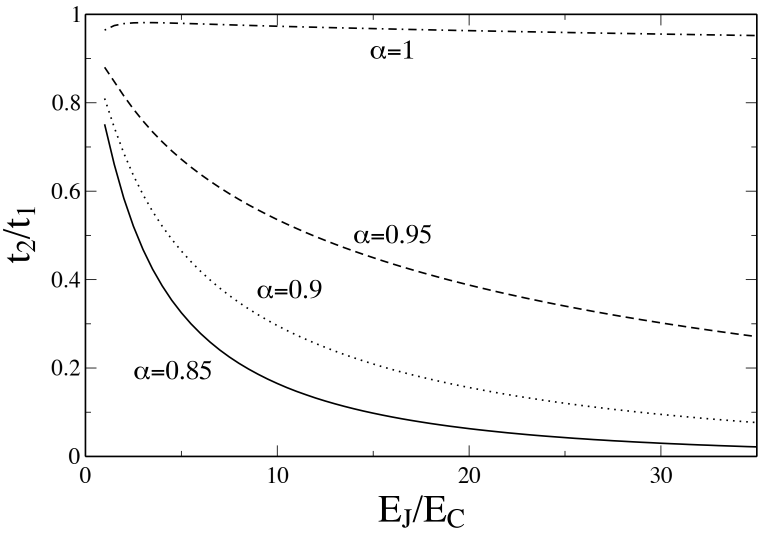

Figure 2.6: The ratio t_2/t_1 between the tunneling matrix elements, plotted as a function of E_J/E_C for several values of $\alpha \leq 1$.

can then be used to control the qubit Hamiltonian. The external parameters fall into two categories, those that can be varied freely, like magnetic fields and bias voltages, and the device parameters, that are fixed for a specific device. Two main types of device parameters characterize the Hamiltonian: (i) the junction capacitance C_J that determines the charging energy $E_C = e^2/2C_J$ and (ii) the Josephson inductance L_J which determines the Josephson energy $E_J = (\Phi_0/2\pi)^2/L_J$. In addition, we have the ratio $\alpha = E_{J3}/E_J$.

The potential $\mathcal{U}(\boldsymbol{\phi})$ can be modified in two ways. The external magnetic flux $\Phi_x = \Phi_0\varphi_x/2\pi$ is responsible for the symmetry of the double well within a unit cell and can give rise to a σ_z term in the single qubit Hamiltonian while α determines the height of the barrier between the wells in a cell and between two nearest neighbor unit cells. Thus α affects the values of the tunneling amplitudes between different sites in the lattice. Although α is a fixed device parameter for the set-up shown in Fig. 2.1, a modified set-up in which the middle junction is made flux-tunable has been proposed [1, 3]; a flux tunable junction is achieved by “shunting” the third junction with a further junction and using an external magnetic field to tune it.

In the tight-binding picture, the off-diagonal element Δ of the qubit Hamiltonian is a complex quantity that depends on the two tunneling amplitudes t_1 and t_2, whose relative strength can be set by α and the ratio E_J/E_C. The latter enters as a common factor into the frequencies of the Gaussian localized orbitals, determining the size of their overlaps and affecting only the energy gap $|\Delta|$. An increase of the value of α implies a decrease of the tunneling amplitudes t_1 and t_2, caused by an increase of the height of the barriers. Thus a careful choice of the two parameters is crucial in determining the behavior of the system. From Eq. (2.45), we find that if $t_2/t_1 \ll 1$ then Δ will be (almost) real. In order to obtain a sizable imaginary part of Δ, t_2/t_1 must be sufficiently large. In Fig. 2.5, we plot

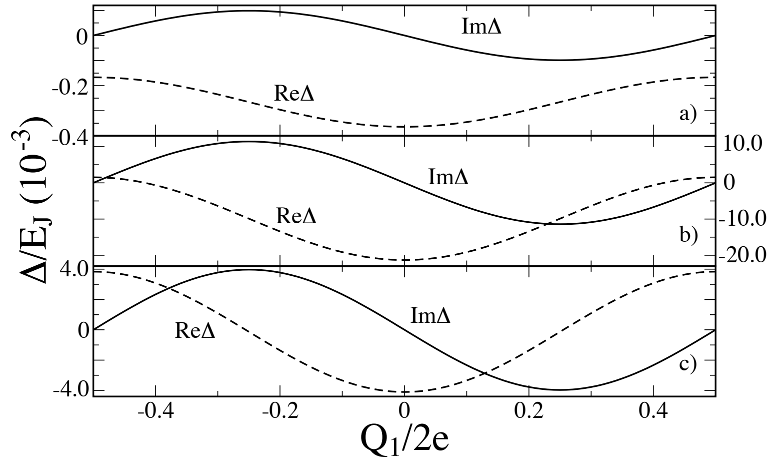

Figure 2.7: Plot of the real and imaginary part of Δ as a function of $Q_1/2e = CV_1/2e$ for $CV_2/2e = 0.5$ for a) $\alpha = 0.95$, $E_J/E_C = 35$; b) $\alpha = 0.95$, $E_J/E_C = 10$; and c) $\alpha = 1$, $E_J/E_C = 15$.

the ratio t_2/t_1 versus α, for several values of the E_J/E_C. Although all the curves approach the value $t_2/t_1 \approx 1$ for $\alpha \to 1$, as soon as $\alpha < 1$, a strong variation in t_2/t_1 is observed for large E_J/E_C. In Fig. 2.6, we plot t_2/t_1 versus E_J/E_C for different values of α. For $\alpha = 1$, the curve is almost a constant. In Table 3.1, we report a set of quantities calculated by varying both α and E_J/E_C, such as to keep the energy gap Δ_0 at zero applied voltage of the order of $\approx 0.1E_C$.

The parameters of an experimentally realized flux qubit (Delft qubit) [7] are $\alpha = 0.8$ and $E_J/E_C = 35$ and are given in the first row of Table 3.1. In this case, the ratio t_2/t_1 is very small and the contribution of t_2 is negligible. This choice of parameters of the Delft

α	E_J/E_C	t_2/t_1	t_1/E_J $\times 10^{-3}$	t_2/E_J $\times 10^{-5}$	$\frac{\lvert\Delta\rvert_0}{E_J}$	$\frac{\lvert\Delta\rvert_{\min}}{\lvert\Delta\rvert_0}$	$\frac{E_{12}}{\lvert\Delta\rvert_0}$
0.80	35	0.0062	-2.9	-1.8	0.0059	0.98	82
0.85	30	0.030	-1.9	-5.8	0.0040	0.88	126
0.90	25	0.12	-1.5	-18	0.0037	0.61	149
0.95	20	0.39	-1.5	-59	0.0054	0.12	116
1.00	15	0.97	-2.05	-198	0.012	0	61
1.05	10	1.77	-4.2	-740	0.038	0	24

Table 2.1: Values of t_1, t_2, their ratio t_2/t_1, the energy gap $|\Delta|_0$ at zero applied voltage, and the minimum of the gap $|\Delta|_{\min}$ for a series of values of α and E_J/E_C. In the last column we report the ratio of the energy difference E_{12} between the second and first excited state and the qubit gap $|\Delta|_0$.

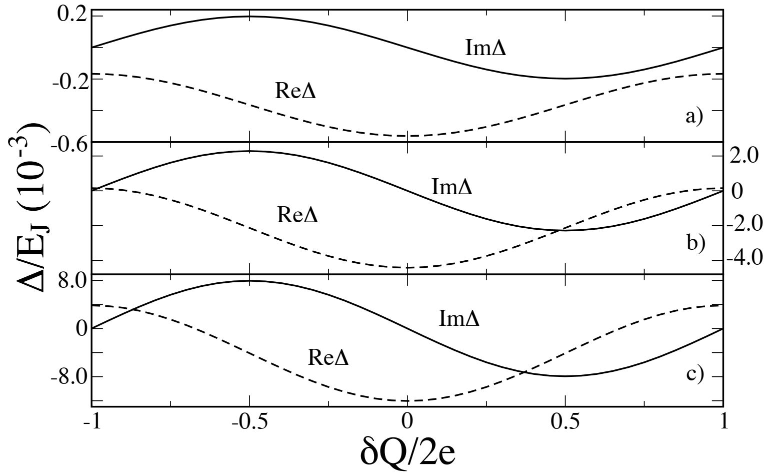

Figure 2.8: Plot of the real and imaginary part of Δ as a function of $\delta Q/2e = C(V_1 - V_2)/2e$ for $V_1 + V_2 = 0$ choosing a) $\alpha = 0.95$, $E_J/E_C = 35$, b) $\alpha = 0.95$, $E_J/E_C = 10$ and c) $\alpha = 1$, $E_J/E_C = 15$.

qubit therefore does not allow the manifestation of a significant σ_y term in the single-qubit Hamiltonian, for any value of the bias voltage.

In Fig. 2.7, we plot the real and imaginary part of Δ as a function of the applied voltage V_1, expressed in the gate charge $Q_1 = C_1V_1$, while keeping the other gate voltage fixed such that $Q_2/2e = C_2V_2/2e = 0.5$. If the real part of Δ can be tuned from a finite value to zero while the imaginary part of Δ remains finite (as in Fig. 2.7c), then the pseudo-field $\mathbf{B}$ can point along arbitrary angles in the equator plane of the Bloch sphere. The magnitude of the pseudo-field can be controlled in principle by changing α, e.g., with a flux-tunable junction. In Fig. 2.8, we plot the real and imaginary part of Δ in the case where both voltages are varied simultaneously such that $V_1 = -V_2$ as a function of $\delta Q/2e = C(V_1 - V_2)/2e$. In Fig. 2.9 we plot the gap $|\Delta|$ as a function of $\delta Q/2e = C(V_1 - V_2)/2e$ (solid line) and of $(Q_1 + Q_2)/2e = C(V_1 + V_2)/2e$ (dashed line) for this set of parameters.

2.7 Full control for $\alpha > 1$

The flux qubit realized at Delft [7] operates with a ratio $\alpha = 0.8 < 1$ between the Josephson energies of its junctions. As shown in Table 3.1, the ratio of tunneling matrix elements for this parameter choice is $t_2/t_1 = 0.0062$, thus the effect of the applied voltages is negligible. Two other regimes for α are interesting, namely $\alpha \approx 1$ and $\alpha > 1$.

In the former, t_1 and t_2 are approximately equal. In this case, $\boldsymbol{\phi}$ can tunnel from a left minimum (L) to a right one (R) via both an intra-cell or an inter-cell tunneling process with almost equal probability. However, while inter-cell tunneling can be controlled via the applied voltages V_1 and V_2, allowing superposition with non-zero relative phase of the qubit states, the intra-cell transition amplitude remains constant, once the parameters α

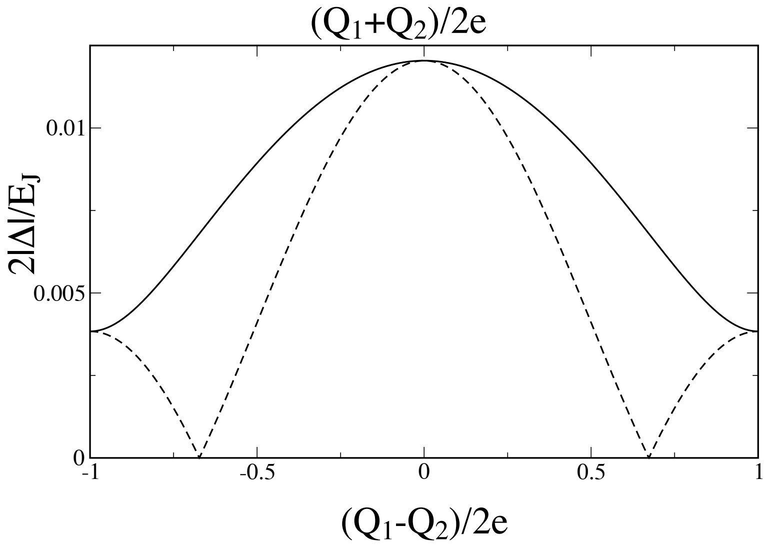

Figure 2.9: Plot of the gap versus $\delta Q/2e = \gamma C_J(V_1 - V_2)/2e$ (solid line) and $\gamma C_J(V_1 + V_2)/2e$ (dashed line), for $\alpha = 1$ and $E_J/E_C = 15$. In this case both the amplitude of oscillation and the cross region of the curves are appreciable.

and E_J/E_C are fixed, thus leading only to qubit flips. In Table 3.1, for each value of $\alpha < 1$, the minimum of the gap is a finite quantity and can be calculated by minimization of equation Eq. (2.46) with respect to **k**. However, for $\alpha \geq 1$ there is a value of the external applied voltage for which the gap goes to zero (Fig. 2.9).

We are particularly interested in the regime $\alpha > 1$. In this case $t_1 < t_2$, i.e., the intra-cell tunneling between two minima is inhibited and, with a suitable choice of α, can be completely suppressed (Figs. 2.10 and 2.11). In this situation, the system can be described by a one-dimensional chain in which every even (odd) site is labeled as a "left" minimum L while the remaining sites are labeled "right" minima R, see Fig. 2.12. The tunneling matrix element between the sites is t_2 ($t_1 = 0$). Note that, due to the periodicity of the system, all L (R) sites have to be identified with each other, since they describe the same configuration.

From Eqs. (2.51) and (2.52), we immediately find that, for $t_1/t_2 \to 0$, we gain full control of the direction of the effective pseudo-field **B** in the equatorial plane of the Bloch sphere, since

$$\Delta(k_+, k_-) = 4t_2 \cos(\pi k_+) e^{i\pi k_-}, \tag{2.65}$$

where $k_\pm = (C_1V_1 \pm C_2V_2)/2e$. The sum and difference of the gate charges therefore independently control the qubit energy gap and the angle θ of the pseudo-field,

$$|\Delta| = 4|t_2 \cos(\pi k_+)|, \qquad \theta = \pi k_-. \tag{2.66}$$

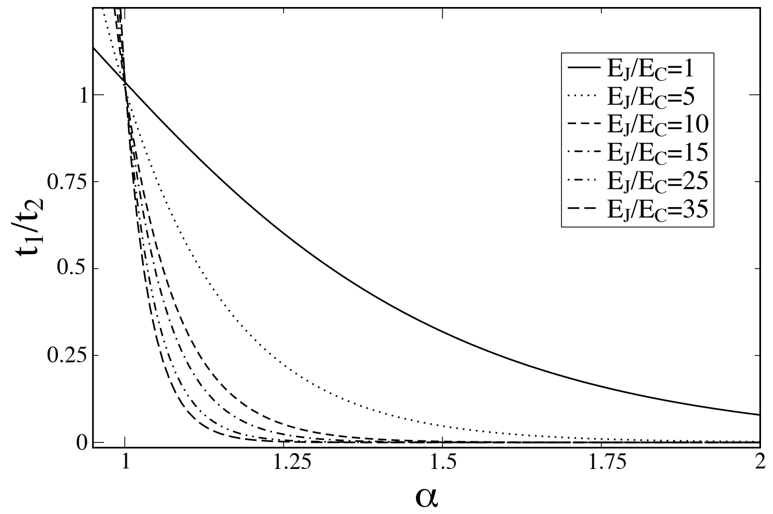

Figure 2.10: The ratio t_1/t_2 between the tunneling matrix elements, plotted as a function of $\alpha \geq 1$ for several values of E_J/E_C.

2.8 Charge decoherence

Voltage fluctuations from imperfect voltage sources or other fluctuating charges in the environment lead to charge fluctuations on the two islands in the circuit and thus to decoherence of the qubit. Moreover, we are considering here a situation where the sensitivity to external voltages has been deliberately enhanced and therefore it can be expected that charge fluctuations cannot be ignored. An estimate of the decoherence time for the same circuit has been developed in [10], where it is found to be 0.1 s.

In order to model bias voltage fluctuations, we include the two impedances Z_1 and Z_2 (Fig. 2.2) in our analysis. From circuit theory [27], we can then obtain a Caldeira-Leggett model for the system coupled to its charge environment,

$$\mathcal{H} = \mathcal{H}_S + \mathcal{H}_B + \mathcal{H}_{SB}, \tag{2.67}$$

where $\mathcal{H}_S$ from Eq. (2.10) describes the dissipationless elements of the circuit, and

$$\mathcal{H}_B = \sum_{j=1,2} \sum_{\nu} \left(\frac{p_{j\nu}^2}{2m_{j\nu}} + \frac{1}{2} m_{j\nu} \omega_{j\nu}^2 x_{j\nu}^2 \right), \tag{2.68}$$

is the Hamiltonian of the degrees of freedom of two independent baths of harmonic oscillators that are used to model the two impedances, and finally

$$\mathcal{H}_{SB} = \sum_{j=1,2} \mathbf{m}_j \cdot \mathbf{Q} \sum_{\nu} c_{j\nu} x_{j\nu}, \tag{2.69}$$

describes the system-bath coupling, where $\mathbf{m}_1 = \mathcal{C}^{-1}(C_1, 0)^T$ and $\mathbf{m}_2 = \mathcal{C}^{-1}(0, C_2)^T$. The

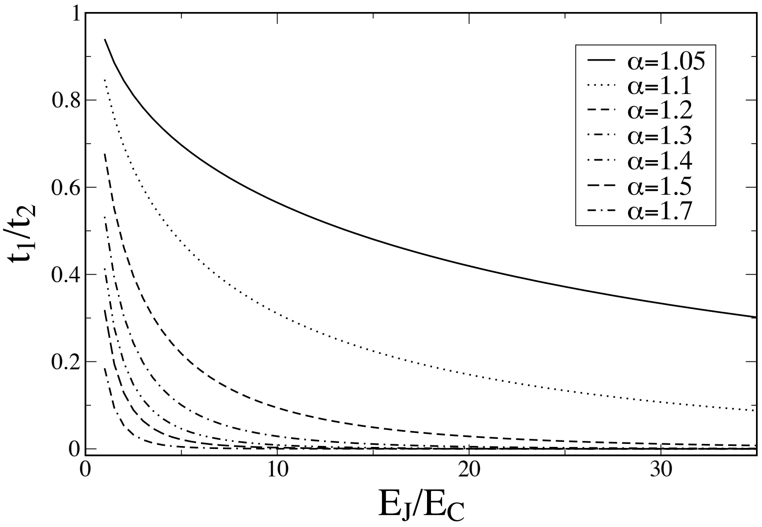

Figure 2.11: The ratio t_1/t_2 between the tunneling matrix elements, plotted as a function of E_J/E_C for several values of $\alpha \geq 1$.

coupling constants $c_{j\nu}$ are related to Z_j via the spectral densities

$$J_j(\omega) = -\omega \mathrm{Re} Z_j(\omega) = \frac{\pi}{2} \sum_{\nu} \frac{c_{j\nu}^2}{m_{j\nu}\omega_{j\nu}} \delta(\omega - \omega_{j\nu}). \tag{2.70}$$

The decoherence rates in the Born-Markov approximation are given by [27]

$$\frac{1}{T_1} = \frac{4}{\hbar^2} \sum_{j=1,2} \left|\mathbf{m}_j \cdot \langle 0|\mathbf{Q}|1\rangle\right|^2 \Delta \mathrm{ReZ}_j(\Delta) \coth \frac{\Delta}{2k_B T}, \tag{2.71}$$

$$\frac{1}{T_\phi} = \frac{1}{\hbar^2} \sum_{j=1,2} \left|\mathbf{m}_j \cdot (\langle 0|\mathbf{Q}|0\rangle - \langle 1|\mathbf{Q}|1\rangle)\right|^2 \mathrm{ReZ}_j(0) 2k_B T. \tag{2.72}$$

Now we compute the matrix elements of the charge operator $\mathbf{Q} = -2ie\boldsymbol{\nabla}$ in the $|0\rangle$, $|1\rangle$ basis. Following the derivation of the Hamiltonian in Sec. 2.5.2, we start from

$$\langle u_{\alpha\mathbf{k}}|\mathbf{Q}|u_{\beta\mathbf{k}}\rangle = -2e\mathbf{k}\delta_{\alpha\beta} - 2ie\langle\psi_{\alpha\mathbf{k}}|\boldsymbol{\nabla}|\psi_{\beta\mathbf{k}}\rangle. \tag{2.73}$$

The matrix elements of $\mathbf{Q}$ between the Bloch states

$$\langle\psi_{\alpha\mathbf{k}}|\mathbf{Q}|\psi_{\beta\mathbf{k}}\rangle = \sum_{\mathbf{n},\mathbf{m}\in\mathbb{Z}^2} \mathrm{e}^{2\pi i\mathbf{k}\cdot(\mathbf{n}-\mathbf{m})}\, \mathbf{Q}_{\alpha\mathbf{m},\beta\mathbf{n}}, \tag{2.74}$$

are given in terms of the matrix elements of $\boldsymbol{\nabla}$ between the Wannier functions

$$\begin{aligned} \mathbf{Q}_{\alpha\mathbf{n},\beta\mathbf{m}} &= -2ei\langle\phi_{\alpha\mathbf{n}}|\boldsymbol{\nabla}|\phi_{\beta\mathbf{m}}\rangle \\ &= -2ei\left(\mathcal{G}^T\mathbf{P}\mathcal{G}\right)_{\alpha,\mathbf{n},\beta\mathbf{m}}, \end{aligned} \tag{2.75}$$

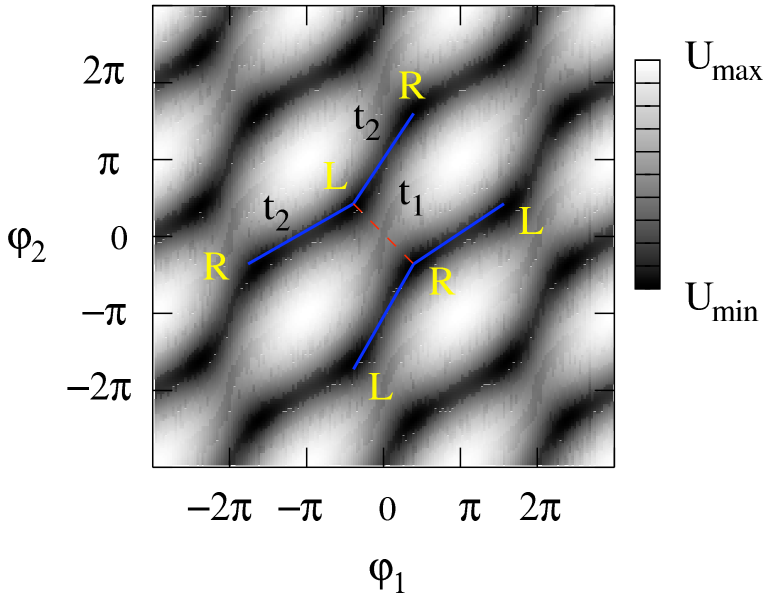

Figure 2.12: Density plot of the double well potential $U(\varphi_1, \varphi_2)$ for $\alpha = 1.4$, on a logarithmic scale. Two equivalent one-dimensional chains with nearest neighbor interaction are highlighted in the figure.

and, in turn, through the $\mathcal{G}$-matrix, they are expressed in terms of the Gaussian states,

$$\mathbf{P}_{\alpha\mathbf{n},\beta\mathbf{m}} = \langle \Psi_{\alpha\mathbf{n}} | \boldsymbol{\nabla} | \Psi_{\beta\mathbf{m}} \rangle = \frac{1}{2} \mathcal{M} \Delta\boldsymbol{\phi}_{\alpha\mathbf{n},\beta\mathbf{m}} S_{\alpha\mathbf{n},\beta\mathbf{m}}, \tag{2.76}$$

where the matrix $\mathcal{M}$ is defined in Eq. (2.28), $\Delta\boldsymbol{\phi}_{\alpha\mathbf{n},\beta\mathbf{m}} = \boldsymbol{\phi}_\beta - \boldsymbol{\phi}_\alpha + 2\pi(\mathbf{m} - \mathbf{n})$, and the S-matrix is defined in Eq. (2.58).

We only keep the leading matrix elements s_1 and s_2 in the overlap matrix S when calculating the $\mathcal{G}$ and $\mathbf{P}$ matrices (see Sec. 2.6). Since the largest contributions of $\mathbf{P}$ are proportional to s_1 and s_2, we can use $\mathcal{G} \approx \mathbb{I}$, and thus $\mathbf{Q}_{\alpha\mathbf{n},\beta\mathbf{m}} \simeq \mathbf{P}_{\alpha\mathbf{n},\beta\mathbf{m}} \propto \mathbf{S}_{\alpha\mathbf{n},\beta\mathbf{m}}$. We consider the diagonal term and the off-diagonal term separately and obtain,

$$\begin{aligned} \langle u_{\alpha\mathbf{k}} | \mathbf{Q} | u_{\alpha\mathbf{k}} \rangle &= -\mathbf{Q}_g, & (2.77) \\ \langle u_{\mathrm{L}\mathbf{k}} | \mathbf{Q} | u_{\mathrm{R}\mathbf{k}} \rangle &= -ei\mathcal{M} \Big[s_1 \Delta\boldsymbol{\phi} + s_2 (\Delta\boldsymbol{\phi} - 2\pi\mathbf{e}_1)\, \mathrm{e}^{2\pi i k_1} \\ &\quad + s_2 (\Delta\boldsymbol{\phi} + 2\pi\mathbf{e}_2)\, \mathrm{e}^{-2\pi i k_2} \Big], & (2.78) \end{aligned}$$

where s_1, s_2, $\Delta\boldsymbol{\phi} = \boldsymbol{\phi}_{\mathrm{R}} - \boldsymbol{\phi}_{\mathrm{L}}$, and the matrix $\mathcal{M}$ depend on $\alpha = E_{J3}/E_J$ and E_J/E_C. In the qubit basis we find,

$$\begin{aligned}\langle 0|\mathbf{Q}|0\rangle &- \langle 1|\mathbf{Q}|1\rangle = -e\mathcal{M}\Big[s_1\sin(\theta)\Delta\boldsymbol{\phi} \\ &+ s_2\sin(\theta+2\pi k_1)(\Delta\boldsymbol{\phi}-2\pi\mathbf{e}_1) \\ &+ s_2\sin(\theta-2\pi k_2)(\Delta\boldsymbol{\phi}+2\pi\mathbf{e}_2)\Big], \qquad (2.79) \\ \langle 0|\mathbf{Q}|1\rangle &= ie\mathcal{M}\Big[s_1\cos(\theta)\Delta\boldsymbol{\phi} \\ &+ s_2\cos(\theta+2\pi k_1)(\Delta\boldsymbol{\phi}-2\pi\mathbf{e}_1) \\ &+ s_2\cos(\theta-2\pi k_2)(\Delta\boldsymbol{\phi}+2\pi\mathbf{e}_2)\Big], \qquad (2.80)\end{aligned}$$

where $\tan\theta = \mathrm{Im}\Delta/\mathrm{Re}\Delta$ is a function of $k_{1,2} = C_{1,2}V_{1,2}/2e$. Using Eqs. (2.71), (2.72), (2.79), and (2.80) we can express the decoherence rates in a more explicit way,

$$\begin{aligned}\frac{1}{T_1} &= 2\pi\frac{E_J}{\hbar}\frac{\mathrm{Re}Z}{R_Q}\left(\frac{C}{C_J}\right)^2 s_2^2\,\mathcal{F}_1(V_1,V_2), \qquad (2.81) \\ \frac{1}{T_\phi} &= 2\pi\frac{2k_BT}{\hbar}\frac{\mathrm{Re}Z}{R_Q}\left(\frac{C}{C_J}\right)^2 s_2^2\,\mathcal{F}_\phi(V_1,V_2), \qquad (2.82)\end{aligned}$$

where s_2, $\mathcal{F}_1$, and $\mathcal{F}_\phi$ are given in the Appendix B. $\mathcal{F}_1$ and $\mathcal{F}_\phi$ are periodic functions of the applied voltages V_1 and V_2 that depend on the parameters α, E_J/E_C, and on s_1/s_2. They can be estimated to be at most of order one, depending on the choice of parameters and the applied voltages. In Eqs. (2.81) and (2.82) we chose $Z \approx Z_1 \approx Z_2$, and $R_Q = h/e^2$ is the quantum of resistance.

In the regime $\alpha > 1$ we have $s_2 \gg s_1$. For $\alpha = 1.4$, $E_J/E_C = 15$ and $C/C_J = 0.02$ we find that $s_2 = 8\cdot 10^{-4}$. An estimate for $T \approx 100\,\mathrm{mK}$, $\mathrm{Re}Z \approx 1\,\mathrm{k}\Omega$ and $E_J = 250\,\mathrm{GHz}$ produces decoherence times in the millisecond range,

$$\begin{aligned}\frac{1}{T_1} &\simeq \frac{\mathcal{F}_1(V_1,V_2)}{\mathcal{F}_{1,\max}}\frac{1}{6\,\mathrm{ms}}, \qquad (2.83) \\ \frac{1}{T_\phi} &\simeq \frac{\mathcal{F}_\phi(V_1,V_2)}{\mathcal{F}_{\phi,\max}}\frac{1}{12\,\mathrm{ms}}. \qquad (2.84)\end{aligned}$$

For some particular values of V_1 and V_2 the functions $\mathcal{F}_1$ or $\mathcal{F}_\phi$ vanish, implying that $1/T_1 \to 0$ or $1/T_\phi \to 0$. In particular, $\mathcal{F}_1 = 0$ for $(C_1V_1, C_2V_2)/2e = \pm(1/2,0)$, $\pm(0,1/2)$, $\pm(1/4,1/4)$, $\pm(1/8,-1/8)$, $\pm(3/8,-3/8)$ in the FBZ, and $\mathcal{F}_\phi = 0$ for $(C_1V_1, C_2V_2)/2e = (n/2, m/2)$, $\pm(1/4,-1/4)+(n,m)$, with $n,m \in \mathbb{Z}$. The two functions have a common set of zeros, namely $\pm(n/2,0), \pm(0,m/2)$, with $n,m \in \mathbb{Z}$. In these cases, both $1/T_1, 1/T_\phi \to 0$.

For the regime $\alpha < 1$ we have that $s_1 \gg s_2$ and we can neglect terms containing s_2. Choosing $\alpha = 0.8$ and $E_J/E_C = 35$ we find $s_1 = 1.3\cdot 10^{-5}$. It follows that the decoherence rates are strongly suppressed and an estimate shows that they are below 1 Hz. This means that in this case the main process that causes decoherence is not due to the charge degrees of freedom. In fact for the Delft qubit [7], that operates in this regime, the dephasing and the relaxation times caused by other mechanisms are much smaller, $T_\phi = 20$ ns and $T_1 = 900\,\mathrm{ns}$.

The physical reason for the small decoherence and relaxation rates found here is that, despite the voltage bias, we are still dealing with a flux qubit whose states are indistinguishable from their charge distribution, as seen from Eq. (2.77).

2.9 Results and conclusions

By means of circuit theory and a tight-binding approximation, we have analyzed a voltage-controlled SC flux qubit circuit that allows full control of the single-qubit Hamiltonian Eq. (2.50), with σ_x, σ_y and σ_z terms, in order to allow arbitrary single qubit operations.

One of the main results of this work is the computation of the tunneling matrix elements appearing in the single qubit Hamiltonian as a function of the device parameters α and E_J/E_C. This allowed us to explore new possible working regimes of the system, looking for a range of parameters for which a full control on qubit rotations is feasible. Substantially, the qubit can work in two different regimes, $\alpha < 1$ and $\alpha > 1$, showing different features. In particular, for $\alpha > 1$, the pseudo magnetic field $\mathbf{B}$ that couples to the qubit in the Hamiltonian has a non-zero y-component. This allows full control of qubit rotations on the Bloch sphere through the applied voltages V_1 and V_2. In fact, in the Hamiltonian, Eq. (2.50), the off-diagonal term Δ, given in Eq. (2.45), contains the voltages $V_{1,2}$ and the sensitivity to $V_{1,2}$ is determined by the tunneling parameters t_1 and t_2 in Eqs. (2.41), (2.43).

For $\alpha \leq 1$, we find $t_1 \gtrsim t_2$. The effect of t_2, and thus of the applied voltages, for the value of parameters of the Delft qubit [7], is negligible as shown in Table 3.1, but can be greatly enhanced for a suitable choice of α and E_J/E_C (see Figs. 2.5 and 2.6), thus allowing good control in the real and imaginary parts of Δ, as shown in Eqs. (2.51) and (2.52) and in Figs. 2.7 and 2.8.

In the case $\alpha > 1$, the roles of t_1 and t_2 are interchanged, as shown in Figs. 2.10, 2.11, and a new regime in which a full control of the single-qubit Hamiltonian becomes possible. For a suitable choice of α and E_J/E_C, the tunneling parameter t_1 become vanishingly small, giving rise to a simple dependence of Δ on the voltages, as found in Eqs. (2.65) and (2.66).

Our analysis is based on the two-level approximation, i.e., we assume that we can neglect all high levels besides the two lowest ones. This approximation is justified if the energy gap E_{12} between the two lowest levels and any higher level is sufficiently large, in particular, larger than the qubit gap $E_{01} = |\Delta|$. The gap E_{12} can be roughly estimated as the plasma frequency, i.e., the smallest of the frequencies of the (anisotropic) harmonic oscillator arising from the linearization of the equation of motion around the minimum configurations of the potential. This frequency is given by (also see Appendix A) $\omega_{LC} = 1/\sqrt{C_J L_J} = \sqrt{8 E_J E_C}/\hbar$. In Table 3.1, we report the ratio of E_{12} and the qubit gap $|\Delta_0|$ at zero applied voltage. For all parameter values studied, E_{12} exceeds $2|\Delta_0|$ by more than a factor of 20, in many relevant cases even by two orders of magnitude, thus justifying the two-level approximation.

Finally, we have studied the decoherence due to charge fluctuations of the voltage sources. Our result for the T_1^{-1} and T_ϕ^{-1} rates is given in Eqs. (2.81) and (2.82), an estimate of which yields a coherence time longer than $\approx 1\,\mathrm{ms}$, leading to the conclusion that charge fluctuations are not the main source of decoherence, even in the regime in which the sensitivity to external voltages is enhanced. The coherence of the system is well preserved, since the qubit is still essentially a SC flux qubit, i.e., the $|0\rangle$ and $|1\rangle$ states have nearly identical charge configurations.

In conclusion, based on our analysis we find that full control of single-qubit operations in a SC flux qubit should be feasible, provided that the right choice of the device parameters is made.

References

[1] Y. Makhlin, G. Schön, and A. Shnirman, Rev. Mod. Phys. **73**, 357 (2001).

[2] M. H. Devoret, A. Wallraff, and J. M. Martinis, *Superconducting Qubits: A Short Review,* cond-mat/0411174.

[3] T. Orlando, J. E. Mooij, L. Tian, C. H. van der Wal, L. S. Levitov, S. Lloyd, and J. J. Mazo, Phys. Rev. B **60**, 15398 (1999).

[4] J, E. Mooij, T. P. Orlando, L. Levitov, L. Tian, C. H. van der Wal, S. Lloyd, Science **285**, 1036 (1999).

[5] J. R. Friedman, V. Patel, W. Chen, S. K. Tolpygo, J. E. Lukens, Nature **406**, 43 (2000).

[6] C. H. van der Wal, A. C. J. ter Haar, F. K. Wilhelm, R. N. Schouten, C. J. P. M. Harmans, T. P. Orlando, S. Lloyd, J. E. Mooij, Science **290**, 773 (2000).

[7] I. Chiroescu, Y. Nakamura, C. J. P. M. Harmans, and J. E. Mooij, Science **299**, 1869 (2003).

[14] P. Bertet, I. Chiorescu, G. Burkard, K. Semba, C. J. P. M. Harmans, D. P. DiVincenzo, and J. E. Mooij, Phys. Rev. Lett. **95**, 257002 (2005).

[29] F. Yoshihara, K. Harrabi, A. O. Niskanen, Y. Nakamura, and J. S. Tsai, cond-mat/0606481.

[10] L. Tian, L. S. Levitov, C. H. van der Wal, J. E. Mooij, T. P. Orlando, S. Lloyd, C. J. P. M. Harmans, and J. J. Mazo, in *Quantum Mesoscopic Phenomena and Mesoscopic Devices in Microelectronics*, edited by I. O. Kulik and R. Ellialtioglu (Kluwer, Dordrecht, 2000), pp. 429–438 [cond-mat/9910062].

[11] L. Tian, S. Lloyd, and T. P. Orlando, Phys. Rev. B **65**, 144516 (2002).

[12] C. H. van der Wal, F. K. Wilhelm, C. J. P. M. Harmans, and J. E. Mooij, Eur. Phys. J. B **31**, 111 (2003).

[13] D. V. Averin, Solid State Commun. **105**, 659 (1998).

[14] Y. Makhlin, G. Schön, and A. Shnirman, Nature **398**, 305 (1999).

[15] Y. Nakamura, Yu, A. Pashkin, and J. S. Tsai, Nature **398**, 786 (1999).

[16] Y. A. Pashkin, T. Yamamoto, O. Astafiev, Y. Nakamura, D. V. Averin, and J. S. Tsai, Nature **421**, 823 (2003).

[17] T. Yamamoto, Y. A. Pashkin, O. Astafiev, Y. Nakamura, and J. S. Tsai, Nature **425**, 941 (2003).

[18] D. Vion, A. Aassime, A. Cottet, P. Joyez, H. Pothier, C. Urbina, D. Esteve, and M. H. Devoret, Science **296**, 886 (2002).

[19] J. M. Martinis, S. Nam, J. Aumentado, and C. Urbina, Phys. Rev. Lett. **89**, 117901 (2002).

[20] M. H. S. Amin, Phys. Rev. B **71**, 024504 (2005).

[21] M. H. S. Amin, Phys. Rev. B **71**, 140505(R) (2005).

[22] G. Falci, R. Fazio, G. M. Palma, J. Siewert, and V. Vedral, Nature **407**, 355 (2000).

[23] D. Aharonov, W. van Dam, J. Kempe, Z. Landau, S. Lloyd, and O. Regev, quant-ph/0405098.

[24] R. Oliveira and B. M. Terhal, quant-ph/0504050.

[25] S. Bravyi, B. M. Terhal, and D. P. DiVincenzo, unpublished.

[6] G. Burkard, R. H. Koch, and D. P. DiVincenzo, Phys. Rev. B **69**, 064503 (2004).

[27] G. Burkard, Phys. Rev. B **71**, 144511 (2005).

[28] G. Burkard, D. P. DiVincenzo, P. Bertet, I. Chiorescu, and J. E. Mooij, Phys. Rev. B **71**, 134504 (2005).

[29] D. P. DiVincenzo, F. Brito, and R. H. Koch, cond-mat/0510843.

[30] D. V. Averin, A. B. Zorin, and K. K. Likharev, Sov. Phys. JETP **61**, 407 (1985).

[31] K. K. Likharev and A. B. Zorin, J. Low Temp. Phys. **59**, 347 (1985).

[32] M. Iansiti, M. Tinkham, A. T. Johnson, W. F. Smith, C. J. Lobb, and Phys. Rev B **39**, 6465 (1989).

3. Quantum non-demolition measurements of a qubit coupled to a harmonic oscillator

We theoretically describe the weak measurement of a two-level system (qubit) and quantify the degree to which such a qubit measurement has a quantum non-demolition (QND) character. The qubit is coupled to a harmonic oscillator which undergoes a projective measurement. Information on the qubit state is extracted from the oscillator measurement outcomes, and the QND character of the measurement is inferred from the result of subsequent measurements of the oscillator. We use the positive operator value measurement (POVM) formalism to describe the qubit measurement. Two mechanisms lead to deviations from a perfect QND measurement: (i) the quantum fluctuations of the oscillator, and (ii) quantum tunneling between the qubit states $|0\rangle$ and $|1\rangle$ during measurements. Our theory can be applied to QND measurements performed on superconducting qubits coupled to a circuit oscillator. [1]

3.1 Introduction

The possibility to perform repeated quantum measurements on a system with the least possible disturbance was first envisioned in the context of measuring gravitational waves[1]. In quantum optics the optical Kerr effect provided an early playground for studying QND measurements[2–4], that were extended to the framework of cavity quantum electrodynamics (cavity-QED) and mesoscopic mechanical oscillators. [5–9]

The application of such a scheme to quantum information has stimulated great interest, in particular in the field of quantum computation, where fast and efficient readout is necessary, and error correction plays an important role[10]. Schemes for qubit QND measurements have been theoretically proposed and experimentally realized with a superconducting qubit coupled to harmonic oscillators, either represented by an external tank LC-circuit [11–17], or by a superconducting resonator that behaves as a one mode quantum harmonic oscillator in circuit-QED. [18–24] A measurement scheme based on the Josephson bifurcation amplifier (JBA) [25, 26] has been adopted with the aim to perform QND measurements of superconducting qubit [27, 28]. In these experiments a deviation of $\sim 10\%$ from perfect QND behavior has been found.

---

[1] This chapter has been accepted for publication in Physical Review B.

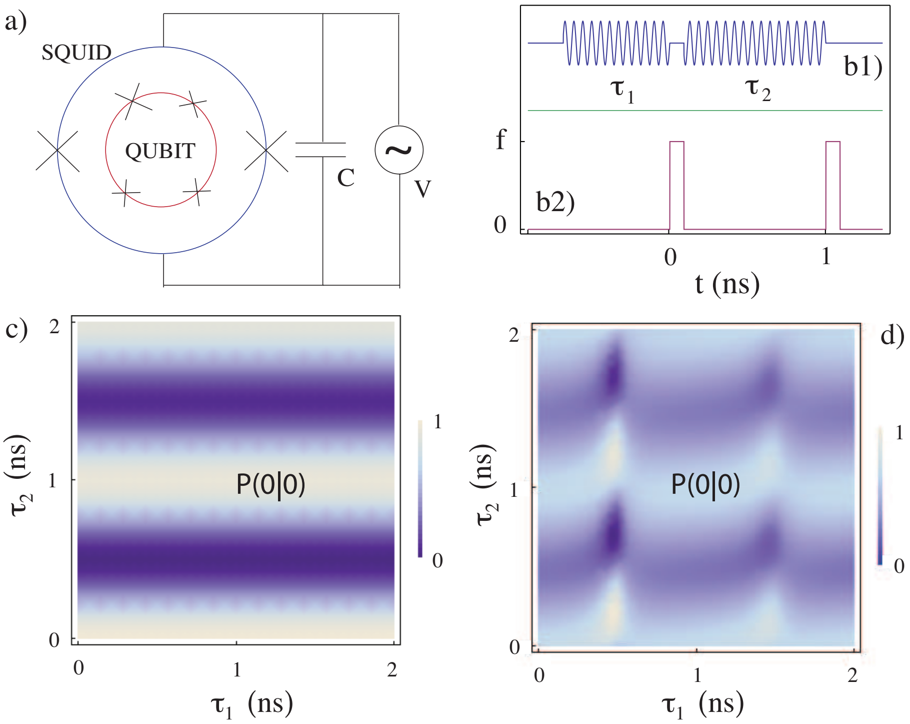

Figure 3.1: (Color online) a) Schematics of the 4-Josephson junction superconducting flux qubit surrounded by a SQUID. b) Measurement scheme: b1) two short pulses at frequency $\sqrt{\epsilon^2+\Delta^2}$, before and between two measurements prepare the qubit in a generic state. Here, ϵ and Δ represent the energy difference and the tunneling amplitude between the two qubit states. b2) Two pulses of amplitude f and duration $\tau_1 = \tau_2 = 0.1$ ns drive the harmonic oscillator to a qubit-dependent state. c) Perfect QND: conditional probability $P(0|0)$ for $\Delta = 0$ to detect the qubit in the state "0" vs driving time τ_1 and τ_2, at Rabi frequency of 1 GHz. The oscillator driving amplitude is chosen to be $f/2\pi = 50$ GHz and the damping rate $\kappa/2\pi = 1$ GHz. d) Conditional probability $P(0|0)$ for $\Delta/\epsilon = 0.1$, $f/2\pi = 20$ GHz, $\kappa/2\pi = 1.5$ GHz. A phenomenological qubit relaxation time $T_1 = 10$ ns is assumed.

Motivated by those recent experimental achievements, we analyze a measurement technique based on the coupling of the qubit to a driven harmonic oscillator. A quadrature of the harmonic oscillator is addressed via a projective measurement. The qubit that is coupled to the oscillator affects the outcomes of the measurement of the oscillator and information on the qubit state can be extracted from the results of the projective measurement of the oscillator. We aim to shed some light on the possibilities to perform qubit QND measurements with such a setup, and to understand whether deviations from the expected behavior could arise from quantum tunneling between the qubit states. Such a tunneling process, although made small compared to the qubit energy splitting, violates the QND conditions.

One of the possible implementations of the system under consideration is the four-junction persistent current qubit [14, 27, 29] (flux qubit) depicted in Fig 4.1a). It consists of a superconducting loop with four Josephson junctions and its low temperature dynamics is confined to the two lowest-energy states. For an external magnetic flux close to a half-integer multiple of $\Phi_0 = h/2e$, the superconducting flux quantum, the two lowest-energy eigenstates are combinations of clockwise and counter clockwise circulating current states. These two states represent the qubit. The measurement apparatus consists of a superconducting quantum interference device (SQUID), composed by two Josephson junctions, inductively coupled to the qubit loop. The SQUID behaves as a non-linear inductance and, together with a shunt capacitance, forms a non-linear LC-oscillator, which is externally driven. The two qubit states produce opposite magnetic field that translate into a qubit dependent effective Josephson inductance of the SQUID. The response of the driven SQUID is therefore qubit-dependent.

In order to treat the problem in a fully quantum mechanical way, we linearize the SQUID equation of motion, such that the effective coupling between the driven LC-oscillator and the the qubit turns out to be quadratic. The qubit Hamiltonian is $\mathcal{H}_S = \epsilon\boldsymbol{\sigma}_Z/2 + \Delta\boldsymbol{\sigma}_X/2$. In the experiment [27], the tunneling amplitude Δ between the two qubit current states is made small compared to the qubit gap $E = \sqrt{\epsilon^2 + \Delta^2}$, therefore also $\Delta \ll \epsilon$, such that it can be considered as a small perturbation. The absence of the tunneling term would yield a perfect QND Hamiltonian (see below). From the experimental parameters $\Delta = 5$ GHz and $E = 14.2$ GHz [27, 33], it follows that $\Delta/\epsilon \approx 0.38$, yielding a reduction of the visibility in Fig. 4.1 d) on the order of 10%.

The QND character of the qubit measurement is studied by repeating the measurement. A perfect QND setup guarantees identical outcomes for the two repeated measurements with certainty. In order to fully characterize the properties of the measurement, we can initialize the qubit in the state $|0\rangle$, then rotate the qubit by applying a pulse of duration τ_1 before the first measurement and a second pulse of duration τ_2 between the first and the second measurement. The conditional probability to detect the qubit in the states s and s' is expected to be independent of the first pulse, and to show sinusoidal oscillation with amplitude 1 in τ_2. Deviations from this expectation witness a deviation from a perfect QND measurement. The sequence of qubit pulses and oscillator driving is depicted in Fig. 4.1b). The conditional probability $P(0|0)$ to detect the qubit in the state "0" twice in sequence is plotted versus τ_1 and τ_2 in Fig. 4.1c) for $\Delta = 0$, and in Fig. 4.1d) for $\Delta/\epsilon = 0.1$. We anticipate here that a dependence on τ_1 is visible when the qubit undergoes a flip in the first rotation. Such a dependence is due to the imperfections of the mapping between the qubit state and the oscillator state, and is present also in the case $\Delta = 0$. The effect of the non-QND term $\Delta\boldsymbol{\sigma}_X$ results in an overall reduction of $P(0|0)$.

In this paper we study the effect of the tunneling term on the quality of a QND measurement. Many attempts to understand the possible origin of the deviations from perfect QND behavior appearing in the experiments have been concerned with the interaction with the environment[22–24, 30–33]. The form of the Josephson non-linearity dictates the form of the coupling between the qubit and the oscillator, with the qubit coupled to the photon number operator of the driven harmonic oscillator, $\boldsymbol{\sigma}_Z a^\dagger a$, rather than to one quadrature, $\boldsymbol{\sigma}_X(a + a^\dagger)$, and the effect of the tunneling term $\boldsymbol{\sigma}_X$ present in the qubit Hamiltonian is considered as a small perturbation.

The work we present is not strictly confined to the analysis of superconducting flux qubit measurements. Rather, it is applicable to a generic system of coupled qubit and harmonic oscillator that can find an application in many contexts. Moreover, the analysis we present is based on the general formalism of the positive operator valued measure (POVM), that represents the most general tool in the study of quantum measurements.

The paper is structured as follows: in Sec. 3.2 we derive the quadratic coupling between the qubit and the oscillator and the Hamiltonian of the total coupled system. In Sec. 3.3 we construct the qubit single measurement with the POVM formalism and in Sec. 3.4 we consider the effect of the non-QND term in the POVM that describes the single measurement. In Sec. 3.5 we construct the two- measurement formalism, by extending the formalism of POVM to the two subsequent measurement case. In Sec. 3.6 we consider the single measurement in the case $\Delta = 0$ and study the condition for having a good QND measurement. In Sec. 3.7 we calculate the contribution at first order and second order in Δ/ϵ to the POVM and to the outcome probability for the qubit single measurement. In Sec. 3.8 we calculate the contribution at first and second order in Δ/ϵ to the POVM and to the outcome probability for the two subsequent qubit measurement. In Sec. 3.9 we study the QND character of the measurement by looking at the conditional probability for the outcomes of two subsequent measurements when we rotate the qubit before the first measurement and between the first and the second measurement.

3.2 Model: quadratic coupling

As far as the application of our model to the measurement of a persistent current qubit with a SQUID is concerned, we provide here a derivation of the quadratic coupling mentioned in the introduction.

We identify the system with a flux qubit that will be described by the Hamiltonian $\mathcal{H}_S$. The meter is represented by a SQUID and it is inductively coupled to a flux qubit via a mutual inductance, in such a way that the qubit affects the magnetic flux through the loop of the SQUID. The Hamiltonian that describes the SQUID and the interaction with the qubit can be written as

$$\mathcal{H}_{\mathrm{meter}} + \mathcal{H}_{\mathrm{int}} = \frac{\hat{Q}^2}{2C} - \frac{\Phi_0^2}{L_J} \cos\left(2\pi\hat{\Phi}/\Phi_0\right) \cos\hat{\varphi} \tag{3.1}$$

where $\hat{\varphi} = \hat{\varphi}_1 - \hat{\varphi}_2$ is the difference of the phases of the two Josephson junctions $\hat{\varphi}_1$ and $\hat{\varphi}_2$ that interrupt the SQUID loop, L_J the Josephson inductance of the junctions (nominally equal), and $\hat{Q}$ is the difference of the charges accumulated on the capacitances C that shunt the junctions. Up to a constant factor, $\hat{\varphi}$ and $\hat{Q}$ are canonically conjugate variables that satisfy $[\hat{\varphi}, \hat{Q}] = 2ei$. We split the external flux into a constant term and a qubit dependent term, such that $\cos(2\pi\hat{\Phi}/\Phi_0) = \cos(2\pi\Phi_{\rm ext}/\Phi_0 + 2\pi M I_q \boldsymbol{\sigma}_Z/\Phi_0) \equiv \lambda_0 + \lambda_1 \boldsymbol{\sigma}_Z$, with I_q the current in the qubit loop and M the mutual inductance between qubit and SQUID loop. Expanding the potential up to second order in $\hat{\varphi}$, one obtains

$$\mathcal{H}_{\rm meter} + \mathcal{H}_{\rm int} \approx \frac{\hat{Q}^2}{2C} + (\lambda_0 + \lambda_1 \boldsymbol{\sigma}_Z) \left(\frac{\Phi_0}{2\pi}\right)^2 \frac{\hat{\varphi}^2}{2L_J}. \tag{3.2}$$

with $\lambda_0 = \cos(2\pi\Phi_{\rm ext}/\Phi_0)\cos(2\pi M I_q/\Phi_0)$ and $\lambda_1 = -\sin(2\pi\Phi_{\rm ext}/\Phi_0)\sin(2\pi M I_q/\Phi_0)$. We introduce the zero point fluctuation amplitude $\sigma = (L_J/\lambda_0 C)^{1/4}$, the bare harmonic oscillator frequency $\omega_{\rm ho} = \sqrt{\lambda_0/L_J C}$, and the in-phase and in-quadrature components of the field

$$\begin{aligned} \frac{\Phi_0}{2\pi}\hat{\varphi} \equiv \hat{X} &= \sigma\sqrt{\frac{\hbar}{2}}(a + a^\dagger), && (3.3) \\ \hat{Q} \equiv \hat{P} &= -\frac{i}{\sigma}\sqrt{\frac{\hbar}{2}}(a - a^\dagger), && (3.4) \end{aligned}$$

with a and $a^\dagger$ harmonic oscillator annihilation and creation operators satisfying $[a, a^\dagger] = 1$. Apart from a renormalization of the qubit splitting, the Hamiltonian of the coupled qubit and linearized SQUID turns out to be

$$\begin{aligned} \mathcal{H}_{\rm meter} + \mathcal{H}_{\rm int} &= \hbar\omega_{\rm ho}(1 + \tilde{g}\boldsymbol{\sigma}_Z)a^\dagger a \\ &+ \hbar\omega_{\rm ho}\tilde{g}\boldsymbol{\sigma}_Z(a^2 + a^{\dagger 2}), \end{aligned} \tag{3.5}$$

with $\tilde{g} = \lambda_1/2\lambda_0 = \tan(2\pi\Phi_{\rm ext}/\Phi_0)\tan(2\pi M I_q/\Phi_0)/2$. The frequency of the harmonic oscillator describing the linearized SQUID is then effectively split by the qubit.

The Hamiltonian can now be written as (from here on we set $\hbar = 1$)

$$\mathcal{H}(t) = \mathcal{H}_S + \mathcal{H}_{\rm meter} + \mathcal{H}_{\rm int} + \mathcal{H}_{\rm drive}(t). \tag{3.6}$$

The qubit Hamiltonian written by means of the Pauli matrices $\boldsymbol{\sigma}_i$ (we denote 2x2 matrices in qubit space with bold symbols) in the basis of the current states $\{|0\rangle, |1\rangle\}$ is

$$\mathcal{H}_S = \frac{\epsilon}{2}\boldsymbol{\sigma}_Z + \frac{\Delta}{2}\boldsymbol{\sigma}_X, \tag{3.7}$$

where $\epsilon = 2I_q(\Phi_{\rm ext} - \Phi_0/2)$ represents an energy difference between the qubit states and Δ the tunneling term between these states. The Hamiltonian of the oscillator (or SQUID) is

$$\mathcal{H}_{\rm meter} = \omega_{\rm ho} a^\dagger a. \tag{3.8}$$

The Hamiltonian that describes the coupling between the qubit and the harmonic oscillator in the rotating wave approximation (RWA), where we neglected the terms like a^2 and $a^{\dagger 2}$, is given by

$$\mathcal{H}_{\rm int} = g\boldsymbol{\sigma}_Z a^\dagger a, \tag{3.9}$$

with $g = \omega_{\mathrm{ho}}\tilde{g}$ [34], and the external driving of the harmonic oscillator is described by

$$\mathcal{H}_{\mathrm{drive}}(t) = f(t)(a + a^\dagger). \tag{3.10}$$

and throughout this work, we choose a harmonic driving force $f(t) = 2f\cos(\omega_d t)$. Neglecting the fast rotating terms $ae^{-i\omega_d t}$ and $a^\dagger e^{i\omega_d t}$, after moving in the frame rotating with frequency ω_d, the Hamiltonian becomes time independent,

$$\mathcal{H} = \mathcal{H}_S + \Delta\boldsymbol{\omega}_Z a^\dagger a + f(a + a^\dagger), \tag{3.11}$$

with $\Delta\boldsymbol{\omega}_Z = \boldsymbol{\omega}_Z - \omega_d$, and the qubit-dependent frequency given by $\boldsymbol{\omega}_Z = \omega_{\mathrm{ho}}(1 + \tilde{g}\boldsymbol{\sigma}_Z)$.

The qubit observable that we want to measure is $\hat{A} \equiv \boldsymbol{\sigma}_Z$ and, due to the presence of the term $\Delta\boldsymbol{\sigma}_X/2$, it does not represent an integral of the motion for the qubit, $[\mathcal{H}_S, \boldsymbol{\sigma}_Z] \neq 0$. Therefore the measurement is not supposed to be QND, Eq. (1.49) not being satisfied. However, for $\Delta \ll \epsilon$ the variation in time of $\boldsymbol{\sigma}_Z$ becomes slow on the time scale determined by $1/\epsilon$ and one expects small deviations from an ideal QND case. The presence of the non-QND term $\boldsymbol{\sigma}_X$ in $\mathcal{H}_S$ inhibits an exact solution and a perturbative approach will be carried out in the small parameter $\Delta/\epsilon \ll 1$.

3.3 Single measurement

The weak measurement of the qubit is constructed as follows. We choose the initial density matrix ($t = 0$) of the total coupled system to be the product state $\boldsymbol{\rho}(0) = \boldsymbol{\rho}_0 \otimes |\hat{0}\rangle\langle\hat{0}|$, with the qubit in the unknown initial state $\boldsymbol{\rho}_0$ and the oscillator in the vacuum state $|\hat{0}\rangle$, and we let the qubit and the oscillator become entangled during the global time evolution. We then assume that at time t we perform a strong measurement of the flux quadrature $\hat{X} = \sigma(a + a^\dagger)/\sqrt{2}$, by projecting the oscillator on to the state $|x\rangle\langle x|$. Such a state of the oscillator is quite unphysical, it has infinite energy and infinite indeterminacy of the $\hat{P} = (a - a^\dagger)/\sqrt{2}i$ quadrature. More realistically, what would happen in an experiment is that the oscillator is projected on to a small set of quadrature states centered around x. This can be described as a convolution of the projector $|x\rangle\langle x|$ with a distribution characteristic of the measurement apparatus, that can be included in the definition of the qubit weak measurement. However, we choose to keep the model simple and to work with an idealized projection.

In the interaction picture, the projection on the state $|x\rangle\langle x|$ corresponds to the choice to measure the quadrature $\hat{X}(t) = \sigma(ae^{-i\omega_{\mathrm{ho}} t} + a^\dagger e^{i\omega_{\mathrm{ho}} t})/\sqrt{2}$,

$$\begin{aligned} x(t) &= \mathrm{Tr}[\hat{X}\boldsymbol{\rho}(t)] = \mathrm{Tr}\left[\hat{X}(t)\boldsymbol{\rho}_R(t)\right], & (3.12)\\ \boldsymbol{\rho}_R(t) &= \mathcal{U}_R(t)\ \boldsymbol{\rho}(0)\ \mathcal{U}_R^\dagger(t). & (3.13) \end{aligned}$$

where an expression of $\mathcal{U}_R(t)$ and its derivation is given by Eq. (C.5) in Appendix C. The operator $\mathcal{U}_R(t)$ describes the time-evolution of $\boldsymbol{\rho}$ in the rotating frame. The probability to detect the outcome x can then be written as

$$\begin{aligned}\mathrm{Prob}(x,t) &= \mathrm{Tr}\left[\langle x|\boldsymbol{\rho}_R(t)|x\rangle\right] \\ &= \mathrm{Tr}\left[\langle x|\mathcal{U}_R(t)|\hat{0}\rangle\ \boldsymbol{\rho}_0\ \langle\hat{0}|\mathcal{U}_R^\dagger(t)|x\rangle\right],\end{aligned} \tag{3.14}$$

where the trace is over the qubit space, and $\{|x\rangle\}$ is a basis of eigenstates of $\hat{X}(t)$. We define the operators

$$\mathbf{N}(x,t) = \langle x|\mathcal{U}_R(t)|\hat{0}\rangle, \tag{3.15}$$

$$\mathbf{F}(x,t) = \mathbf{N}^\dagger(x,t)\mathbf{N}(x,t), \tag{3.16}$$

acting on the qubit and, using the property of invariance of the trace under cyclic permutation, we write

$$\mathrm{Prob}(x,t) = \mathrm{Tr}\ \mathbf{F}(x,t)\boldsymbol{\rho}(0). \tag{3.17}$$

The state of the system after the measurement is $\boldsymbol{\rho}(x,t)\otimes|x\rangle\langle x|$, with the qubit in the state

$$\boldsymbol{\rho}(x,t) = \frac{\mathbf{N}(x,t)\boldsymbol{\rho}(0)\mathbf{N}^\dagger(x,t)}{\mathrm{Prob}(x,t)}. \tag{3.18}$$

The operators $\mathbf{F}(x,t)$ are positive, trace- and hermiticity-preserving superoperators (i.e. they map density operators into density operators) acting on the qubit Hilbert space. Moreover, they satisfy the normalization condition

$$\int_{-\infty}^{\infty} dx\mathbf{F}(x,t) = \mathbb{I}, \tag{3.19}$$

from which the conservation of probability follows. Therefore, they form a positive operator valued measure (POVM), and we will call the operators $\mathbf{F}(x,t)$ a *continuous* POVM. We point out here that modeling a more realistic scenario, by including a convolution of the projector $|x\rangle\langle x|$ with a distribution characteristic of the measurement apparatus, corresponds to the construction of a more general POVM of the harmonic oscillator, that would not alter qualitatively the description of the qubit measurement in terms of POVM.

The probability distribution $\mathrm{Prob}(x,t)$ depends strongly on the initial qubit state $\boldsymbol{\rho}_0$. In general $\mathrm{Prob}(x,t)$ is expected to have a two-peak shape, arising from the two possible states of the qubit, whose relative populations determine the relative heights of the two peaks, one peak corresponding to $|0\rangle$ and the other to $|1\rangle$.

We now define an indirect qubit measurement that has two possible outcomes, corresponding to the states "0" and "1". As a protocol for a single-shot qubit measurement, one can measure the quadrature $\hat{X}$ and assign the state "0" or "1" to the qubit, according to the two possibilities of the outcome x to be greater or smaller than a certain threshold value x_{th}, $x > x_{\mathrm{th}} \rightarrow |0\rangle$ or $x < x_{\mathrm{th}} \rightarrow |1\rangle$, as depicted in Fig. 4.2. Alternatively, we can infer the qubit state by repeating the procedure many times and constructing the statistical distribution of the outcome x. We then assign the relative populations of the qubit states $|0\rangle$ and $|1\rangle$ by respectively integrating the outcome distribution in the regions $\eta(1) = (x_{\rm th}, \infty)$, $\eta(-1) = (-\infty, x_{\rm th})$.

We formally condensate the two procedures and define a two-outcome POVM, that describes the two possible qubit outcomes, by writing

$$\begin{aligned} \mathbf{F}(s,t) &= \int_{\eta(s)} dx \mathbf{F}(x,t), & (3.20) \\ \mathrm{Prob}(s,t) &= \mathrm{Tr}[\mathbf{F}(s,t)\boldsymbol{\rho}(0)], & (3.21) \end{aligned}$$

with $s = \pm 1$. We will call $\mathbf{F}(s,t)$ a *discrete* POVM, in contrast to the continuous POVM $\mathbf{F}(x,t)$ defined above. Here, we introduce a convention that assigns $s = +1$ to the "0" qubit state and $s = -1$ to the "1" qubit state. The probabilities $\mathrm{Prob}(s,t)$ are therefore obtained by integration of $\mathrm{Prob}(x,t)$ on the subsets $\eta(s)$, $\mathrm{Prob}(s,t) = \int_{\eta(s)} dx \mathrm{Prob}(x,t)$. On the other hand, the probability distribution $\mathrm{Prob}(x,t)$ is normalized on the whole space of outcomes which leads to $P(0,t) + P(1,t) = 1$ at all times. Typically, it is not possible to have a perfect mapping of the qubit state.

3.4 Effects of the tunneling $\boldsymbol{\sigma}_X$ term

Deviations from an ideal QND measurement can arise due to the presence of a non-zero $\boldsymbol{\sigma}_X$ term in the qubit Hamiltonian. In SC flux qubits, such a term is usually present; it represents the amplitude for tunneling through the barrier that separates the two wells of minimum potential, where the lowest energy qubit current states are located. This term cannot be switched off easily.

We can expand the full evolution operator $\mathcal{U}_R(t)$ in powers of Δt, as in Eq. (C.11), and obtain a formally exact expansion of $\mathbf{F}(x,t)$,

$$\mathbf{F}(x,t) = \sum_{n=0}^{\infty} \mathbf{F}^{(n)}(x,t). \tag{3.22}$$

Due to the transverse ($X \perp Z$) character of the perturbation it follows that the even terms in this series (corresponding to even powers of Δt) have zero off-diagonal entries, whereas the odd terms have zero diagonal entries. Due to the normalization condition Eq. (3.19), valid at all orders in Δt, it can be shown that

$$\int dx \mathbf{F}^{(n)}(x,t) = \delta_{n,0}\mathbb{I}, \tag{3.23}$$

and consequently,

$$\sum_{s=\pm 1} \mathbf{F}^{(n)}(s,t) = \delta_{n,0}\mathbb{I}. \tag{3.24}$$

As a result, the probability $\mathrm{Prob}(s,t)$ is given as a power expansion in the perturbation

$$\mathrm{Prob}(s,t) = \sum_{n=0}^{\infty} \mathrm{Prob}^{(n)}(s,t), \tag{3.25}$$

where $\sum_{s=\pm 1}\text{Prob}^{(n)}(s,t)=\delta_{n,0}$.

The expansion of the evolution operator and consequently of the continuous and discrete POVMs is in the parameter Δt. The requirement that the deviations introduced by the tunneling $\boldsymbol{\sigma}_X$ term in the time-evolution behave as perturbative corrections sets a time scale for the validity of the approximation, namely $t \ll 1/\Delta$, for which we will truncate the expansion up to second order. The tunneling non-QND term is considered as a perturbation in that experimentally one has $\Delta/\epsilon \ll 1$. It turns out to be convenient to choose as a time scale for the qubit measurement $t \sim 1/\epsilon$, for which follows $\Delta t \sim \Delta/\epsilon \ll 1$.

3.5 Two subsequent measurements

A QND measurement implies that repeated measurements give the same result with certainty. In order to verify such a property of the measurement, we construct here the formalism that will allow us to study the correlations between subsequent measurements.

After the oscillator quadrature is measured in the first step at time t and the quadrature value x is detected, the total system composed of the qubit and the oscillator is left in the state $\boldsymbol{\rho}(x,t)\otimes|x\rangle\langle x|$. The fact that we can split the total state after the measurement into a product state is a consequence of the assumption that the measurement of the harmonic oscillator is a projection. Had a more general POVM of the harmonic oscillator be involved, then such a conclusion would not hold. After the first measurement is performed, the total system is left alone under the effects of dissipation affecting the oscillator. A harmonic oscillator which is initially prepared in a coherent state evolves, under weak coupling to a bath of harmonic oscillators in thermal equilibrium, to a mixture of coherent states with a Gaussian distribution centered around the vacuum state (zero amplitude coherent state) with variance $n_{\text{th}}=(\exp(\hbar\omega/k_B T)-1)^{-1}$, ω being the frequency of the harmonic oscillator, T the temperature, and k_B the Boltzmann constant, whereas in the case $T=0$ it evolves coherently to the vacuum $|\hat{0}\rangle$ [36].

We now assume that the state of the total system (qubit and oscillator) before the second measurement is

$$\boldsymbol{\rho}(x,t)\otimes|\hat{0}\rangle\langle\hat{0}|. \tag{3.26}$$

Following the previously described procedure for the qubit single- measurement, a second measurement of the quadrature $\hat{X}$ with outcome y performed at time t', having detected x at time t, would yield the conditional probability distribution

$$\text{Prob}(y,t'|x,t)=\text{Tr}\left[\mathbf{F}(y,t')\boldsymbol{\rho}(x,t)\right]. \tag{3.27}$$

Defining the continuous POVM qubit operators for two measurements as

$$\mathbf{F}(y,t';x,t)=\mathbf{N}^{\dagger}(x,t)\mathbf{F}(y,t'-t)\mathbf{N}(x,t), \tag{3.28}$$

the joint probability distributions for two subsequent measurements is

$$\begin{aligned}\text{Prob}(y,t';x,t) &= \text{Prob}(y,t'|x,t)\text{Prob}(x,t) && (3.29)\\ &= \text{Tr}\left[\mathbf{F}(y,t';x,t)\boldsymbol{\rho}_0\right]. && (3.30)\end{aligned}$$

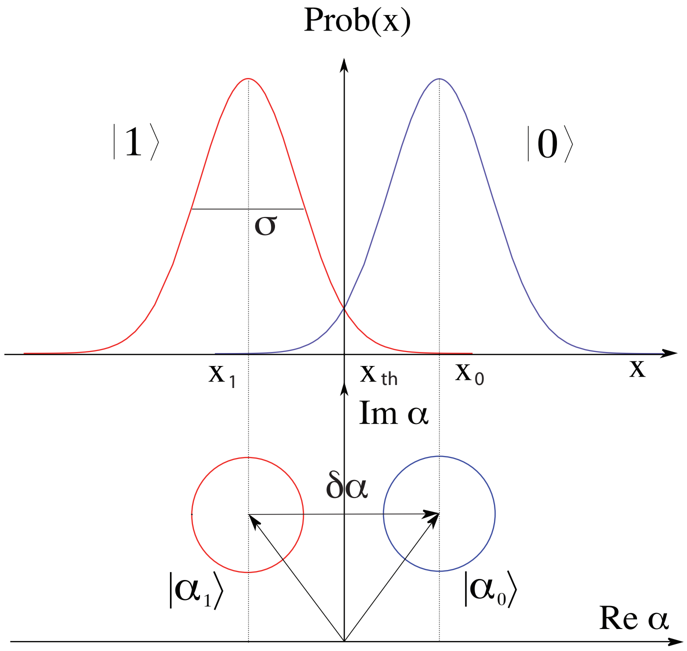

Figure 3.2: (Color online) Schematic description of the single measurement procedure. In the bottom panel the coherent states $|\alpha_0\rangle$ and $|\alpha_1\rangle$, associated with the qubit states $|0\rangle$ and $|1\rangle$, are represented for illustrative purposes by a contour line in the phase space at HWHM of their Wigner distributions, defined[36] as $W(\alpha,\alpha^*) = (2/\pi^2)\exp(2|\alpha|^2)\int d\beta\langle-\beta|\rho|\beta\rangle\exp(\beta\alpha^* - \beta^*\alpha)$. The corresponding Gaussian probability distributions of width σ centered about the qubit-dependent "position" x_s are shown in the top panel.

The operators $\mathbf{F}(y,t';x,t)$ satisfy the normalization condition $\int dx \int dy \mathbf{F}(y,t';x,t) = \mathbb{I}$, ensuring the normalization of the probability distribution $\int dx \int dy \text{Prob}(y,t';x,t) = 1$. By inspection of Eqs. (3.19) and (3.28), it follows that

$$\int dy\ \mathbf{F}(y,t';x,t) = \mathbf{F}(x,t), \tag{3.31}$$

and the marginal distribution for the first measurement is

$$\text{Prob}_M(x,t) \equiv \int dy\ \text{Prob}(y,t';x,t) = \text{Tr}[\mathbf{F}(x,t)\boldsymbol{\rho}_0], \tag{3.32}$$

stating that the probability to detect x in the first measurement is independent on whatever could be detected in the second measurement. On the other hand, the marginal probability distribution for the second measurement turns out to be

$$\text{Prob}_M(y,t') \equiv \int dx \text{Prob}(y,t';x,t) = \text{Tr}[\mathbf{F}(y,t'-t)\boldsymbol{\rho}(t)], \tag{3.33}$$

where $\boldsymbol{\rho}(t) = \mathrm{Tr}_S[\mathcal{U}_R(t)\boldsymbol{\rho}_0 \otimes |\hat{0}\rangle\langle\hat{0}|\mathcal{U}_R^\dagger(t)]$ is the qubit reduced density matrix at time t. We define the discrete POVM for the correlated outcome measurements as

$$\mathbf{F}(s',t';s,t) = \int_{\eta(s)} dx \int_{\eta(s')} dy\ \mathbf{F}(y,t';x,t). \tag{3.34}$$

Analogously to Eq. (3.31) it follows that $\mathbf{F}(s,t) = \sum_{s'} \mathbf{F}(s',t';s,t)$, and the probability distribution for the outcomes of the two subsequent measurement is simply given by

$$\mathrm{Prob}(s',t';s,t) = \mathrm{Tr}[\mathbf{F}(s',t';s,t)\boldsymbol{\rho}_0], \tag{3.35}$$

and it follows that $\sum_{s'} \mathrm{Prob}(s',t';s,t) = \mathrm{Prob}(s,t) = \mathrm{Tr}[\mathbf{F}(s,t)\boldsymbol{\rho}_0]$. The conditional probability to obtain a certain outcome s' at time t', having obtained s at time t, is given by

$$\mathrm{Prob}(s',t'|s,t) = \frac{\mathrm{Tr}[\mathbf{F}(s',t';s,t)\boldsymbol{\rho}_0]}{\mathrm{Tr}[\mathbf{F}(s,t)\boldsymbol{\rho}_0]}. \tag{3.36}$$

The discrete POVM for the double measurement can be in general written as

$$\mathbf{F}(s',t';s,t) \equiv \frac{1}{2}\left[\mathbf{F}(s',t')\mathbf{F}(s,t) + h.c.\right] + \mathbf{C}(s',t';s,t), \tag{3.37}$$

where we have symmetrized the product of the two single-measurement discrete POVM operators $\mathbf{F}(s',t')$ and $\mathbf{F}(s,t)$ in order to preserve the hermiticity of each of the two terms of Eq. (3.37).

Proceeding as for the case of a single qubit measurement, we expand $\mathbf{F}(y,t';x,t)$ in powers of Δ/ϵ. Equating all the equal powers of Δ/ϵ in the expansion it follows that

$$\mathbf{F}^{(n)}(s,t) = \sum_{s'} \mathbf{F}^{(n)}(s',t';s,t), \tag{3.38}$$

with $\sum_{ss'} \mathbf{F}^{(n)}(s't';s,t) = \delta_{n,0}\mathbb{I}$.

3.6 Ideal single measurement

The dynamics governed by $\mathcal{U}_R^{(0)}(t)$ produces a coherent state of the oscillator, whose amplitude depends on the qubit state, see Fig. 4.2. In this case the continuous POVM operators have the simple form $\mathbf{F}^{(0)}(x,t) = \langle\boldsymbol{\alpha}_Z(t)|x\rangle\langle x|\boldsymbol{\alpha}_Z(t)\rangle$, defined through Eq. (C.9) in the Appendix C. In the $\boldsymbol{\sigma}_Z$-diagonal basis $\{|i\rangle\}$, with $i = 0,1$, it is given by

$$\mathbf{F}^{(0)}(x,t)_{ij} = \delta_{ij}\mathcal{G}\left(x - x_i(t)\right), \tag{3.39}$$

where $x_i(t) = \sqrt{2}\sigma\mathrm{Re}[\alpha_i(t)]$ and $\mathcal{G}(x) = \exp(-x^2/\sigma^2)/\sigma\sqrt{\pi}$ is a Gaussian of width σ schematically depicted in Fig. 4.2. Introducing a rate κ that describes the Markovian damping of the harmonic oscillator by a zero-temperature bath of harmonic oscillators, the coherent state qubit-dependent amplitude $\alpha_i(t)$ is found to be [37]

$$\alpha_i(t) = A_i e^{i\phi_i}\left[1 - e^{-i\Delta\omega_i t - \kappa t/2}\right], \tag{3.40}$$

with $\Delta\omega_i = \omega_i - \omega_d$ and the qubit-dependent amplitudes and phases given by

$$A_i = \frac{f}{\sqrt{(\Delta\omega_i)^2 + \kappa^2/4}} \tag{3.41}$$

$$\phi_i = \arctan\left(\frac{\Delta\omega_i}{\kappa/2}\right) - \frac{\pi}{2}. \tag{3.42}$$

The probability distribution for the $\hat{X}$ quadrature outcomes is then given by the sum of the two qubit-dependent Gaussians, weighted by the initial state state occupancy, and the discrete POVM for the qubit measurement as given by Eq. (3.20) becomes

$$\mathbf{F}^{(0)}(s,t) = \frac{1}{2}\left[1 + s\ \mathrm{erf}\left(\frac{\delta x(t)}{\sigma}\right)\boldsymbol{\sigma}_Z\right], \tag{3.43}$$

where $s = \pm 1$ labels the two possible measurement outcomes, and $\delta x(t) = \sigma \mathrm{Re}\ \delta\alpha(t)/\sqrt{2}$, where $\delta\alpha(t) = \alpha_0(t) - \alpha_1(t)$. The indirect qubit measurement gives the outcome probability

$$\mathrm{Prob}(s,t) = \frac{1}{2}\left[1 + s\ \mathrm{erf}\left(\frac{\delta x(t)}{\sigma}\right)\langle\boldsymbol{\sigma}_Z\rangle_0\right], \tag{3.44}$$

with $\langle\boldsymbol{\sigma}_Z\rangle_0 = \mathrm{Tr}[\boldsymbol{\sigma}_Z\boldsymbol{\rho}_0]$. Supposing that the qubit is prepared in the $|0\rangle$ state, one expects to find $\mathrm{Prob}(0) = 1$ and $\mathrm{Prob}(1) = 0$. From Eq. (3.44), we see that even for $\Delta = 0$ this is not always the case.

3.6.1 Short time

We choose a time $t \approx 1/\epsilon$ and a driving frequency close to the bare harmonic oscillator frequency. We can then expand the qubit dependent signal and obtain the short time behavior of the signal difference,

$$\delta\alpha(t) \approx \sqrt{2}\ t\ A, \tag{3.45}$$

with $A = f(e^{2i\phi_0} - e^{2i\phi_1})/\sqrt{2}$. The first non-zero contribution is linear in t, because the signal is due to the time-dependent driving[6]. We measure a rotated quadrature $\hat{X}_\varphi = \sigma(ae^{-i\varphi} + a^\dagger e^{i\varphi})/\sqrt{2}$, and choose the phase of the local oscillator such that $\varphi = \arg A$. With this choice we have $\delta x(t) = \sigma|A|\ t$, and the probabilities for the two measurement outcomes

$$\mathrm{Prob}(s,t) = \frac{1}{2}\left[1 + s\langle\boldsymbol{\sigma}_Z\rangle_0 \mathrm{erf}\left(|A|\ t\right)\right]. \tag{3.46}$$

In Fig. 4.3 we plot the probability of measuring the 0 state $\mathrm{Prob}(0, t = 0.1\ \mathrm{ns})$ as a function of the detuning $\Delta\omega = \omega_{\mathrm{ho}} - \omega_d$ and the driving amplitude f, given that the initial state is 0, $\boldsymbol{\rho}_0 = |0\rangle\langle 0|$. It is possible to identify a region of values of f and $\Delta\omega$ where $\mathrm{erf}(|A|t) \approx 1$. It then follows that

$$\mathrm{Prob}(s) \approx \frac{1}{2}\left[1 + s\langle\boldsymbol{\sigma}_Z\rangle_0\right]. \tag{3.47}$$

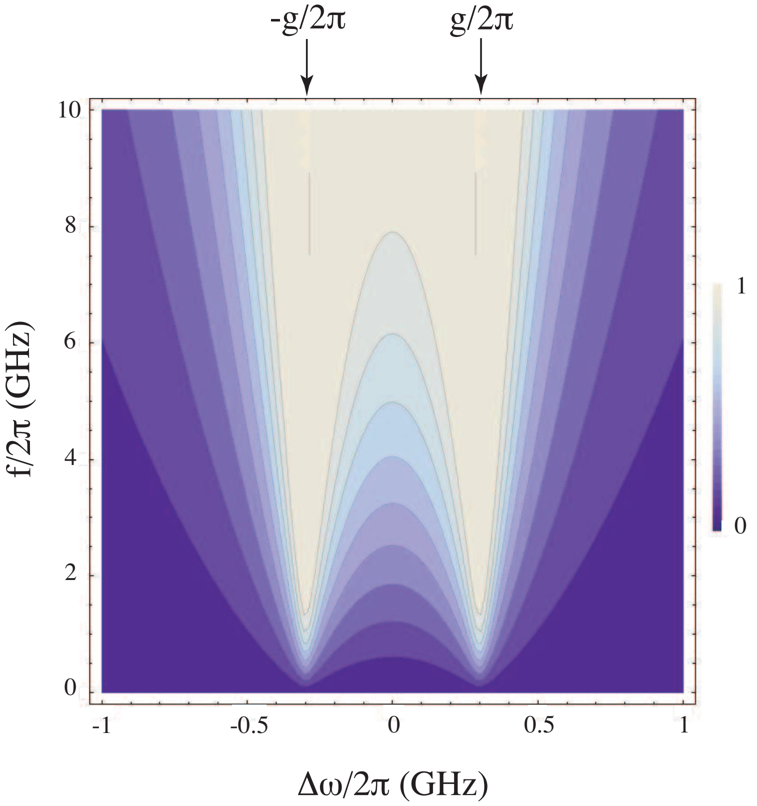

Figure 3.3: (Color online) Prob$(0, t = 0.1$ ns) for the initial state $|0\rangle\langle 0|$, as given by Eq. (3.46), plotted as a function of the detuning $\Delta\omega/2\pi$. The values of the parameters used are listed in Tab. 3.1.

This case corresponds to a strong projective measurement, for which the outcome probabilities are either 0 ore 1, thus realizing a good qubit single measurement.

For driving at resonance with the bare harmonic oscillator frequency ω_{ho}, the state of the qubit is encoded in the phase of the signal, with $\phi_1 = -\phi_0$, and the amplitude of the signal is actually reduced, as also shown in Fig. 4.3 for $\Delta\omega = 0$. When matching one of the two frequencies ω_i the qubit state is encoded in the amplitude of the signal, as also clearly shown in Fig. 4.3 for $\Delta\omega = \pm g$. Driving away from resonance can give rise to significant deviation from 0 and 1 to the outcome probability, therefore resulting in an imprecise mapping between qubit state and measurement outcomes and a weak qubit measurement.

3.7 Corrections due to tunneling

In order to compute the correction at first order in the tunneling term proportional to Δ we expand the evolution operator $\mathcal{U}_R(t)$ up to first order in Δt. By making use of the expression Eq. (C.12) for the perturbation in the interaction picture, the off-diagonal

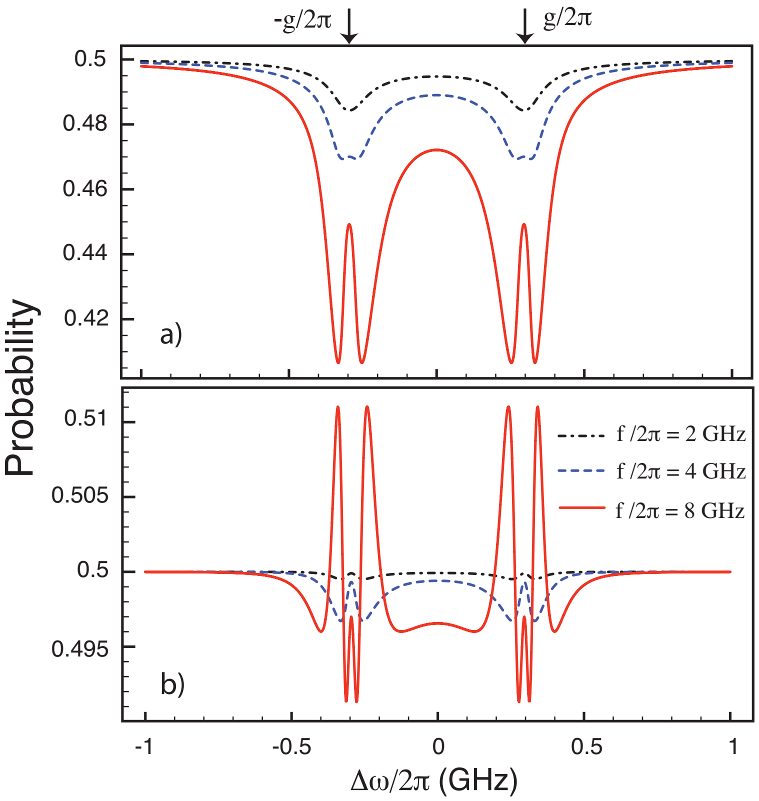

Figure 3.4: (Color online) Probability to detect the outcome $s = 1$, corrected by a) the real part of $F^{(1)}$, for the initial state $|+\rangle_X\langle+|$, and b) the imaginary part of $F^{(1)}$, for the initial state $|+\rangle_Y\langle+|$, plotted versus the detuning $\Delta\omega/2\pi$ for several values of the amplitude f. The values of the parameters used are listed in Tab. 3.1.

element of the first order correction to $\mathbf{F}(x,t)$ is given by

$$\begin{aligned} F^{(1)}(x,t)_{01} &= -i\frac{\Delta}{2}\int_0^t dt' \left[\mathcal{G}\left(x - x_0(t) + \delta z(t')\right)\right. \\ &- \left.\mathcal{G}\left(x - x_1(t) - \delta z(t')^*\right)\right] e^{i\epsilon t'}\Gamma(t'), \end{aligned} \tag{3.48}$$

with the complex displacement $\delta z(t) = \sigma\delta\alpha(t)/\sqrt{2}$ and the overlap $\Gamma(t) = \langle\alpha_0(t)|\alpha_1(t)\rangle$, where

$$\Gamma(t) = \exp\left(-\frac{1}{2}|\delta\alpha(t)|^2 - i\mathrm{Im}[\alpha_0^*(t)\alpha_1(t)]\right). \tag{3.49}$$

Here the state “0” is labeled by its $\boldsymbol{\sigma}_Z$-eigenvalue $s = 1$, whereas the state “1” by its $\boldsymbol{\sigma}_Z$-eigenvalue $s = -1$. Analogously to the unperturbed case, the first order contribution to the discrete POVM is obtained by integrating the continuous POVM in x over the subsets

$\eta(s)$. Defining the function

$$F^{(1)}(t) = i\frac{\Delta}{2}\int_0^t dt' e^{i\epsilon t'}\Gamma(t')\mathrm{erf}\left(\frac{\delta x(t)-\delta z(t')}{\sigma}\right), \tag{3.50}$$

we can write the first order contribution to the discrete POVM as

$$\mathbf{F}^{(1)}(s,t) = s\left(\mathrm{Re}\ F^{(1)}(t)\ \boldsymbol{\sigma}_X - \mathrm{Im}\ F^{(1)}(t)\ \boldsymbol{\sigma}_Y\right), \tag{3.51}$$

and the resulting first order correction to the probability follows directly from Eq. (3.17). This correction is valid only for short time, $t \ll 1/\Delta$. For times comparable with $1/\Delta$ a perturbative expansion of the time evolution operator is not valid. Choosing $t \approx 1/\epsilon$, we can effectively approximate the phase associated with two different coherent states as $\mathrm{Im}[\alpha_0(t)\alpha_1(t)^*] \approx \psi t^2$, with $\psi = f^2\sin(2\phi_0 - 2\phi_1)$, the expression for $F^{(1)}(t)$ further simplifies,

$$F^{(1)}(t) = i\frac{\Delta}{2}\int_0^t dt' e^{i\epsilon t' - \frac{1}{2}|A|^2 t'^2 - i\psi t'^2}\mathrm{erf}\left(|A|(t-t')\right). \tag{3.52}$$

We study the behavior of $F^{(1)}(t)$ as a correction to a qubit projective measurement, that is in the range of driving amplitudes and frequencies that ensure $\mathrm{erf}(|A|\ t) \approx 1$.

The real and imaginary part of $F^{(1)}(t)$ represent the first order correction to the outcome probability of the measurement for two particular initial states, respectively $|+\rangle_X\langle +|$ and $|+\rangle_Y\langle +|$, with $|\pm\rangle_X = (|0\rangle \pm |1\rangle)/\sqrt{2}$ and $|\pm\rangle_Y = (|0\rangle \pm i|1\rangle)/\sqrt{2}$. In the first case we have

$$\mathrm{Prob}(s,t) = \frac{1}{2} + s\ \mathrm{Re}F^{(1)}(t), \tag{3.53}$$

and analogously for the second case, with the imaginary part instead of the real one. We see that the probability to obtain "0" is increased by $\mathrm{Re}F^{(1)}(t)$ and the probability to obtain "1" is decreased by the same amount. Since the contribution to first order in Δt only affects the off-diagonal elements of $\boldsymbol{\rho}_0$, there is no effect at first order for the qubit basis states $|0\rangle$ and $|1\rangle$.

In Fig. 4.4 a) we plot the probability to detect the state 0, corresponding to the outcome $s = 1$, corrected up to first order in the perturbation for $\Delta t = \Delta/\epsilon = 0.1$, for the initial state $\boldsymbol{\rho}_0 = |+\rangle_X\langle +|$, that involves Re $F^{(1)}(t)$. We see that the effect of the tunneling is largest when driving at resonance with the two qubit-shifted frequencies, $\Delta\omega \approx \pm g$. For weak driving amplitude f, the phase ψ in Eq. (3.52) is small and the response is of order of $\sim 1\%$, close to the qubit-split frequency. By increasing the strength of the driving we see that the structure acquires two local minima in proximity of the resonance $\Delta\omega \approx \pm g$ and a maximum exactly at resonance $\Delta\omega = \pm g$. The strong oscillatory behavior of the probability is due to a rapid change of sign of the phase ψ in proximity of the qubit-split frequencies, that is enhanced when the driving strength f increases. In Fig. 4.4 b) we plot the probability to detect the outcome state "0", corresponding to the outcome $s = 1$ for the initial state $\boldsymbol{\rho}_0 = |+\rangle_Y\langle +|$, that involves Im $F^{(1)}(t)$. In comparison to Fig. 4.4 a) we find twice as many oscillations in the structure, typical for the imaginary part of a response function, when compared to the real part, and an overall scale factor of order 0.1. Besides, the sign of the response is not unique. The scale factor and the sign are understood from the Hamiltonian of the qubit, $\mathcal{H} = (\epsilon \boldsymbol{\sigma}_Z + \Delta \boldsymbol{\sigma}_X)/2$, with the condition $\Delta \ll \epsilon$. Under free evolution for a time $t \sim 1/\epsilon$, the initial state $|+\rangle_X \langle +|$ acquires a larger component in the Z-direction than the initial state $|+\rangle_Y \langle +|$. Deviation from this naive picture due to the coupling with the measurement apparatus translates in fluctuations that may determine a change of sign in the response for the case $\boldsymbol{\rho}_0 = |+\rangle_Y \langle +|$. Away from the resonances we see no significant contribution to the outcome probability.

First order effects in the tunneling cannot be responsible for qubit flip during the measurement. In order to estimate the deviation from a perfect QND measurement for the eigenstates of $\boldsymbol{\sigma}_Z$, we have to consider the effect of the perturbation at second order. We define $F^{(2)}(t)$ in Eq. (D.5) and the contribution at second order in Δt to the discrete POVM is then

$$\mathbf{F}^{(2)}(s,t) = -sF^{(2)}(t)\ \boldsymbol{\sigma}_Z. \tag{3.54}$$

The dependence on s factorizes, as expected from the symmetry between the states $|0\rangle$ and $|1\rangle$, in the picture we consider with no relaxation mechanism. The correction at second order in Δ/ϵ to the outcomes probability is given by

$$\text{Prob}^{(2)}(s,t) = -sF^{(2)}(t)\langle \boldsymbol{\sigma}_Z \rangle_0. \tag{3.55}$$

In Fig. 4.5 we plot the second order correction to the probability to obtain "1" having prepared the qubit in the initial state $\boldsymbol{\rho}_0 = |0\rangle\langle 0|$, corresponding to $F^{(2)}(t)$, for $\Delta t = \Delta/\epsilon = 0.1$. We choose to plot only the deviation from the unperturbed probability because we want to highlight the contribution to spin-flip purely due to tunneling in the qubit Hamiltonian. In fact most of the contribution to spin-flip arises from the unperturbed probability, as it is clear from Fig. 4.3. Around the two qubit-shifted frequencies, the probability has a two-peak structure whose characteristics come entirely from the behavior of the phase ψ around the resonances $\Delta\omega \approx \pm g$. We note that the tunneling term can be responsible for a probability correction up to $\sim 4\%$ around the qubit-shifted frequency.

From the analysis of the qubit single measurement in Fig. 4.3 we conclude that a weak POVM qubit measurement, that yields a large error in the determination of the qubit state, can arise when weakly driving the harmonic oscillator. Therefore, only a strong qubit projective measurement, obtained for strong driving of the oscillator, can produce a

Quantity	Symbol	Value for plots
Qubit detuning	ϵ	$2\pi \times 10$ GHz
Damping rate	κ	$2\pi \times 0.1$ GHz
Coupling strength	g	$2\pi \times 0.3$ GHz
Qubit tunneling	Δ/ϵ	0.1

Table 3.1: Values of the parameters used in the plots.

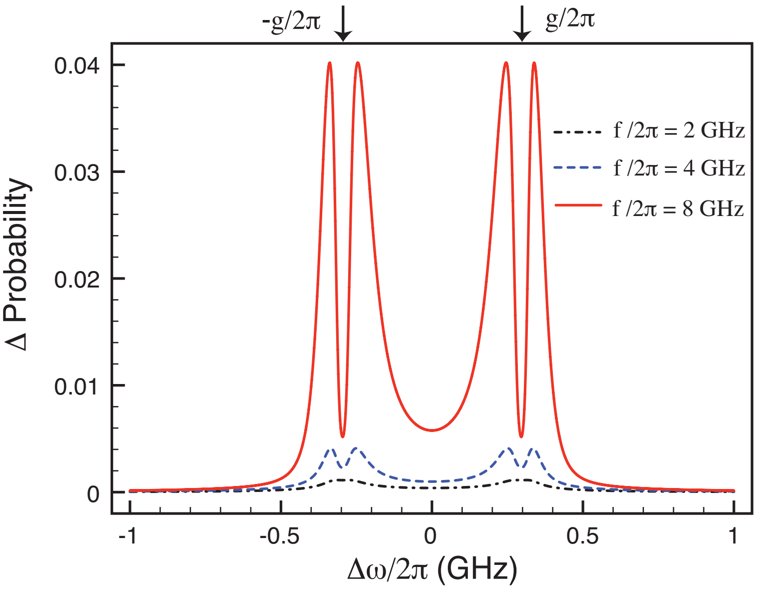

Figure 3.5: (Color online) Plot of the second order correction $\text{Prob}^{(2)}(s = 1)$ to detect "1" for the initial state $|0\rangle\langle 0|$, for $\Delta t = \Delta/\epsilon$, as a function of the detuning $\Delta\omega/2\pi$, for several values of the driving amplitude f. The values of the parameters for the evaluation used are listed in Tab. 3.1.

confident mapping of the qubit state at the level of a single measurement. In this case, a deviation on the order of a few percent in the state assignment can be ascribable to the tunneling term.

3.8 QND character of the qubit measurement

As explained in Sec. 3.5, repeated measurements should give the same result if the measurement is QND. Such a requirement means that if a measurement projects the system onto an eigenstate of the measured observable, then a subsequent measurement should give the same result with certainty. The presence of a term that does not satisfy the QND condition may affect the character of the measurement essentially in two ways: i) by introducing deviations from the projection character of the single measurement, and ii) by generating non-zero commutators in the two-measurement POVM. These may affect the two-outcome probabilities.

3.8.1 Ideal QND measurement

The case $\Delta = 0$ satisfies the requirement for a QND measurement of the qubit observable $\boldsymbol{\sigma}_Z$. The discrete POVM factorizes in this particular case, by virtue of the fact that

$$[\mathbf{N}^{(0)}(y,t'-t),\mathbf{N}^{(0)}(x,t)]=0,$$

$$\mathbf{F}^{(0)}(s',t';s,t)=\mathbf{F}^{(0)}(s',t'-t)\mathbf{F}^{(0)}(s,t). \tag{3.56}$$

Choosing, e.g., $t'=2t$ and using Eq. (3.35), the joint probability for the two measurements reads

$$\begin{aligned}\mathrm{Prob}(s';s) &= \frac{1}{4}\left[1+s's\ \mathrm{erf}\left(\frac{\delta x(t)}{\sigma}\right)^2\right.\\ &+ \left.(s'+s)\mathrm{erf}\left(\frac{\delta x(t)}{\sigma}\right)\langle\boldsymbol{\sigma}_Z\rangle_0\right]. \end{aligned}\tag{3.57}$$

In the region of driving frequency and amplitude that ensure $\mathrm{erf}(\delta x/\sigma)\approx 1$, we find

$$\mathrm{Prob}(s'|s)=\frac{1+s's+(s+s')\langle\boldsymbol{\sigma}_Z\rangle_0}{2(1+s\langle\boldsymbol{\sigma}_Z\rangle_0)}, \tag{3.58}$$

with $\mathrm{Prob}(s;s)=\mathrm{Prob}(s)$, and $\mathrm{Prob}(-s;s)=0$, and the conditional probability is $\mathrm{Prob}(s|s)=1$, and $\mathrm{Prob}(-s|s)=0$, regardless of $\langle\boldsymbol{\sigma}_Z\rangle_0$. However, it has to be noticed that in the case the condition $\mathrm{erf}(\delta x/\sigma)\approx 1$ does not perfectly hold, the conditional probability for the two measurements to give the same outcome becomes

$$\mathrm{Prob}(s|s)=\frac{1+\mathrm{erf}(\delta x/\sigma)^2+2s\ \mathrm{erf}(\delta x/\sigma)\langle\boldsymbol{\sigma}_Z\rangle_0}{2(1+s\ \mathrm{erf}(\delta x/\sigma)\langle\boldsymbol{\sigma}_Z\rangle_0)}, \tag{3.59}$$

and this does depend on the initial state $\langle\boldsymbol{\sigma}_Z\rangle_0$.

3.8.2 First order contribution

We now apply the perturbative approach in Δt to estimate the effect of the non-QND term for the joint and the conditional probabilities. Due to the transverse nature of the perturbation, it is possible to show that all the odd terms have off-diagonal entries, whereas even ones are diagonal. At first order in Δt the off-diagonal term of the discrete POVM is given by

$$F^{(1)}(s',t';s,t)=\frac{s}{2}F^{(1)}(t)+\frac{s'}{2}F^{(1)}(t'-t)+s'C^{(1)}(t';t), \tag{3.60}$$

with the quantity $C^{(1)}(t';t)$ given by Eq. (D.6) in Appendix D. For the particular choice $t'=2t$, for which the two measurement procedures are exactly the same, the joint probability for the initial state $\boldsymbol{\rho}_0=|+\rangle_X\langle+|$ is given at first order in Δt by

$$\begin{aligned}\mathrm{Prob}(s',s) &= \frac{1}{4}\left(1+s's\ \mathrm{erf}\left(\frac{\delta x(t)}{\sigma}\right)^2\right)\\ &+ \frac{1}{2}(s+s')\mathrm{Re}\ F^{(1)}(t)+s'\ \mathrm{Re}\ C^{(1)}(2t;t)\end{aligned} \tag{3.61}$$

We immediately observe that the probability is not symmetric with respect to s and s'. Although the driving times are the same, something is different between the first and the second measurement, and the probability to obtain different outcomes $s' = -s$ is different from zero. An analogous result holds for the initial state $\boldsymbol{\rho}_0 = |+\rangle_Y\langle+|$, with the imaginary part instead of the real one. Now, no matter the sign of $C^{(1)}$, the product $-s\,C^{(1)}$ is negative in one case ($s = \pm 1$). In order to ensure that probabilities are non-negative one has to choose Δt small enough such that the first order negative correction due to $C^{(1)}$ remains smaller than the unperturbed probability. If Δt is too large, one needs to take higher orders into account which should then ensure an overall non- negative probability. The behavior of $C^{(1)}$ as a function of the detuning $\Delta\omega$ and the driving amplitude f is very similar to that of $F^{(1)}$ and we choose not to display it. The only main difference arises in the magnitude, for which we have $|C^{(1)}| \ll |F^{(1)}|$. It is the clear that the main deviations in the two measurement probabilities are mainly due to the errors in the first or second measurement.

3.8.3 Second order contribution

The contribution to the discrete POVM at second order in Δt can be divided into a term that factorizes the contributions of the first and the second measurements, as well as a term that contains all the non-zero commutators produced in the rearrangement,

$$\begin{aligned}\mathbf{F}^{(2)}(s',t';s,t) &= \mathbf{F}^{(0)}(s,t)\mathbf{F}^{(2)}(s',t'-t)\\ &+ \mathbf{F}^{(2)}(s,t)\mathbf{F}^{(0)}(s',t'-t)\\ &+ \frac{1}{2}\left[\mathbf{F}^{(1)}(s,t)\mathbf{F}^{(1)}(s',t'-t)+h.c.\right]\\ &+ \mathbf{C}^{(2)}(s',t';s,t). \qquad (3.62)\end{aligned}$$

The full expression of the $\mathbf{C}^{(2)}$ at second order is rather involved. Choosing $t' = 2t$ we then obtain

$$C^{(2)}(p',2t;p,t)_{ss} = p'ps\;C^{(2)}(t) - p'p\left|F^{(1)}(t)\right|^2, \qquad (3.63)$$

with $C^{(2)}(t)$ given by Eq. (D.7) in Appendix D. The probability to obtain identical outcomes does depend on the outcome s itself, and this reflects the fact that the joint probability still depends on the initial states of the qubit. At the same time, the probability for obtaining different outcomes does not depend on s, as expected. However, direct evaluation of the function $C^{(2)}(p',2t;p,t)$ shows that its contribution to the probability is of order 0.1% and can be neglected.

3.9 Rabi oscillations between measurements

In order to gain a full insight in the QND character of the measurement, we analyze the behavior of the conditional probability to detect the outcomes s and s' in two subsequent measurements when we perform a rotation of the qubit between the two measurements.

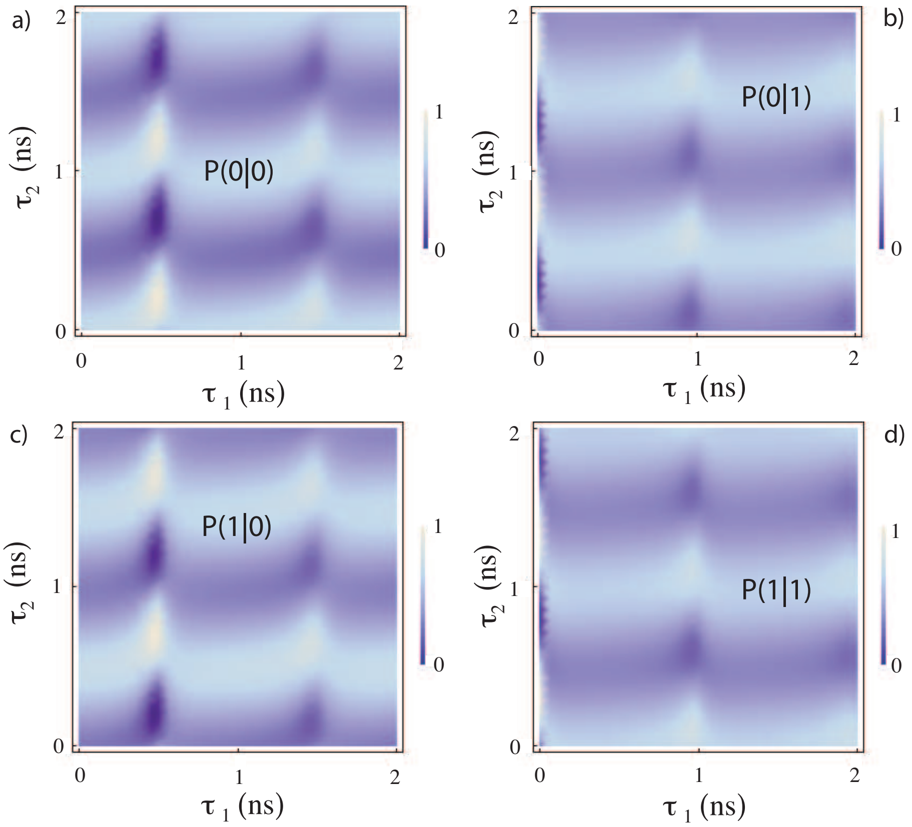

Figure 3.6: (Color online) Conditional probability to obtain a) $s' = s = 1$, b) $s' = -s = 1$, c) $s' = -s = -1$, and d) $s' = s = -1$ for the case $\Delta t = \Delta/\epsilon = 0.1$ and $T_1 = 10$ ns, when rotating the qubit around the y axis before the first measurement for a time τ_1 and between the first and the second measurement for a time τ_2, starting with the qubit in the state $|0\rangle\langle 0|$. Correction in Δt are up to second order. The harmonic oscillator is driven at resonance with the bare harmonic frequency and a strong driving together with a strong damping of the oscillator are assumed, with $f/2\pi = 20$ GHz and $\kappa/2\pi = 1.5$ GHz.

Such a procedure has been experimentally adopted in the work of Lupaşcu *et al.* [27]. When changing the qubit state between the two measurements, only partial QND behavior is expected. In addition to this, we apply an initial rotation to the qubit, such that a wide spectrum of initial states is tested. Ideally, the complete response of this procedure is supposed to be independent on the time τ_1, during which we rotate the qubit before the first measurement, and to depend only on the time τ_2, during which we rotate the qubit between the first and the second measurements, with probabilities ranging from zero to one as a function of τ_2. Such a prediction, once confirmed, would guarantee a full QND character of the measurement.

In Fig. 4.1 c) we plot the conditional probability $P(0|0)$ for the case $\Delta = 0$, when strongly driving the harmonic oscillator at resonance with the bare harmonic frequency, $\Delta\omega = 0$. The initial qubit state is chosen to be $|0\rangle\langle 0|$. No dependence on τ_1 appears and the outcomes s and s' play a symmetric role. This is indeed what we expect from a perfect QND measurement. In Fig. 4.6 we plot the four combinations of conditional probability $P(s'|s)$ up to second order corrections in $\Delta t = \Delta/\epsilon = 0.1$ and with a phenomenological qubit relaxation time $T_1 = 10$ ns. We choose $\Delta\omega = 0$, that is at resonance with the bare harmonic frequency. The initial qubit state is $|0\rangle\langle 0|$. Three features appear: i) a global reduction of the visibility of the oscillations, ii) a strong dependence on τ_1 when the qubit is completely flipped in the first rotation and iii) an asymmetry under change of the outcomes of the first measurement, with an enhanced reduction of the visibility when the first measurement produces a result that is opposite with respect to the initial qubit preparation $|0\rangle\langle 0|$. Furthermore, we find a weak dependence of the visibility on τ_1.

We now investigate whether it is possible to identify the contributions of different mechanisms that generate deviations from a perfect QND measurement. In Fig. 4.7 we study separately the effect of qubit relaxation and qubit tunneling on the conditional probability $P(0|0)$. In Fig. 4.7 a) we set $\Delta = 0$ and $T_1 = \infty$. The main feature appearing is a sudden change of the conditional probability $P \rightarrow 1 - P$ when the qubit is flipped in the first rotation. This is due to imperfection in the mapping between the qubit state and the state of the harmonic oscillator, already at the level of a single measurement. The inclusion of a phenomenological qubit relaxation time $T_1 = 2$ ns, intentionally chosen very short, yields a strong damping of the oscillation along τ_2 and washes out the response change when the qubit is flipped during the first rotation. This is shown in Fig. 4.7 b). The manifestation of the non-QND term comes as a global reduction of the visibility of the oscillations, as clearly shown in Fig. 4.7 c).

At this level it is clearly possible to associate the observed features to different originating mechanisms: i) qubit tunneling yields an overall reduction of the visibility of the oscillations and an asymmetry under exchange of the outcomes of the first measurement, ii) qubit relaxation results in damping along τ_2 and weak dependence of the oscillations on τ_1, and iii) deviations from projective measurement show up mostly when the qubit is flipped during the first rotation.

The combined effect of the quantum fluctuations of the oscillator, together with the tunneling between the qubit states, is therefore responsible for deviation from a perfect QND behavior, although a major role is played, as expected, by the non-QND tunneling term. Such a conclusion pertains to a model in which the qubit QND measurement is studied in the regime of strong projective qubit measurement and qubit relaxation is taken into account only phenomenologically. We compared the conditional probabilities plotted in Fig. 4.6 and Fig. 4.7 directly to Fig. 4 in Ref. [27], where the data are corrected by taking into account qubit relaxation, and find good qualitative agreement.

Our findings can also be compared to the experiment [28], in which the QND character of the measurement is addressed by studying a series of two subsequent measurements, but no qubit rotation is performed between the two measurements. The data in Ref. [28] are affected by strong qubit relaxation. However, from the analysis of the joint probabilities of the outcomes of the two measurements provided in Ref. [28], one can extract the conditional

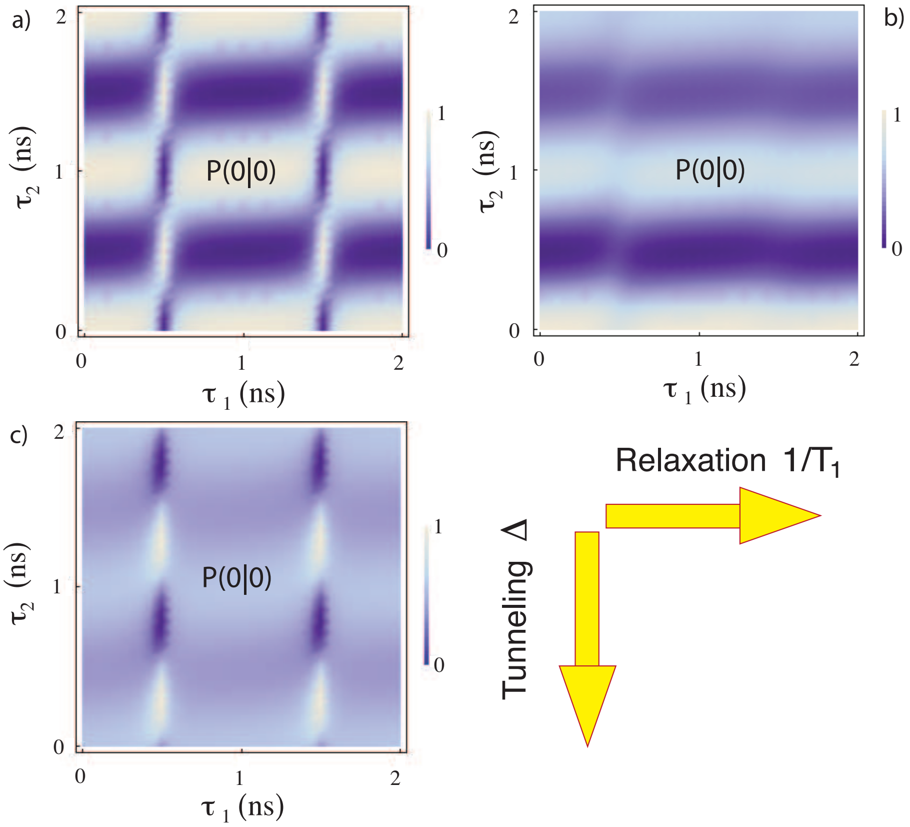

Figure 3.7: (Color online) Comparison of the deviations from QND behavior originating from different mechanisms. Conditional probability $P(0|0)$ versus qubit driving time τ_1 and τ_2 starting with the qubit in the state $|0\rangle\langle 0|$, for a) $\Delta = 0$ and $T_1 = \infty$, b) $\Delta = 0$ and $T_1 = 2$ ns, and c) $\Delta = 0.1\ \epsilon$ and $T_1 = \infty$. The oscillator driving amplitude is $f/2\pi = 20$ GHz and a damping rate $\kappa/2\pi = 1.5$ GHz is assumed.

probabilities $P(0|0) \sim 83\%$ (when starting with the qubit initially in the ground state and comparable to Fig. 4.6 a) at $\tau_1 = \tau_2 = 0$), and $P(0|0) \sim 77\%$ (after a π-pulse is applied to the qubit initially in the ground state, that is comparable to Fig. 4.6 a) at $\tau_1 = 0.5$ ns and $\tau_2 = 0$). In these cases one would expect a conditional probability of order 1 and a weak dependence on qubit relaxation. A deviation of order $\sim 20\%$ can be understood within the framework of our model as arising from the non-QND term and from a weak qubit measurement. Besides, from the data provided in Ref. [28], one can extract a probability of $\sim 17\%$ to obtain the excited state, when starting with the qubit in the ground state, already at the level of the single measurement. Such a behavior cannot be understood as a result of qubit relaxation and it can be ascribed to deviations from a projective qubit measurement.

3.10 Conclusion

In this paper we have analyzed the QND character of a qubit measurement based on coupling to a harmonic oscillator that works as a pointer to the qubit states. The Hamiltonian that describes the interaction between the qubit and the oscillator does not commute with the qubit Hamiltonian. This would in principle inhibit a QND measurement of the qubit. The term in the qubit Hamiltonian that gives rise to the non-zero commutator is small compared with the qubit energy gap, and in the short time qubit dynamics it can be viewed as a small perturbation. The perturbative analysis carried out for fast measurements leads us to the conclusion that the effect of the non-QND term can manifest itself as a non negligible correction. A perfect QND measurement guarantees perfect correlations in the outcomes of two subsequent measurements, therefore QND character of the measurement is understood in terms of deviations from the expected behavior. Corrections to the outcome probabilities have been calculated up to second order in the perturbing term.

The ground and excited states of the qubit are affected only at second order by the perturbation, but a general measurement protocol should prescind from the state being measured. Therefore, in the spirit of the experiment of Lupaşcu *et al.* [27], we have studied the conditional probability for the outcomes of two subsequent measurements when rotating the qubit before the first measurement and between the first and the second measurement. In the case where the QND condition is perfectly satisfied, that is when the perturbation is switched off, no dependence of the conditional probability on the duration of the first rotation appears and the Rabi oscillations between the two measurement range from zero to one. This behavior shows perfect QND character of the qubit measurement. On the other hand, the main effect of the non-QND term manifests itself as an overall reduction of the visibility of the oscillations and as an asymmetry between the outcomes of the measurements. An additional dependence on the duration of the first qubit rotation may appear if a projective measurement of the qubit is not achieved already in absence of the perturbing non-QND term. Experimentally the measurement is not projective and relaxation processes inhibit a perfect flip of the qubit before the first measurement.

We point out that our analysis is valid only when the non-QND term $\Delta\boldsymbol{\sigma}_X$ can be viewed as a perturbation, that is for short time $\Delta t \ll 1$ and when the qubit dynamics is dominated by the term $\epsilon\boldsymbol{\sigma}_Z$, for $\Delta/\epsilon \ll 1$. Our analysis is not valid for the case $\epsilon = 0$. In the present study we have neglected the non-linear character of the SQUID, which is not relevant to the fundamental issue described here, but plays an important role in some measurement procedures[25–28].

A way to improve the QND efficiency would be simply to switch the tunneling off. In the case of superconducting flux qubit, a possibility toward smaller Δ could be to gate the superconducting islands between the junctions of the qubit loop [39]. As an operational scheme one could think of working at finite Δ for logical operations and then at $\Delta = 0$ for the measurement.

References

[1] V. B. Braginsky and F. Ya. Khalili, *Quantum Measurement*, (Cambridge University Press, 1992).

[2] G. J. Milburn and D. F. Walls, Phys. Rev. A **28**, 2065 (1983)

[3] N. Imoto, H. A. Haus, Y. Yamamoto, Phys. Rev. A **32**, 2287 (1985)

[4] H.-A. Bachor, M. D. Levenson, D. F. Walls, S. H. Perlmutter, and R. M. Shelby, Phys. Rev. A **38**, 180 (1988)

[5] M. Fortunato, P. Tombesi, and W. P. Schleich, Phys. Rev. A **59**, 718 (1999)

[6] A. A. Clerk, S. M. Girvin, and A. D. Stone, Phys. Rev. B 67, 165324 (2003)

[7] D. H. Santamore, A. C. Doherty, and M. C. Cross, Phys. Rev. B **70**, 144301 (2004)

[8] I. Dotsenko, M. Mirrahimi, M. Brune, S. Haroche, J.-M. Raimond, and P. Rouchon, Phys Rev. A **80**, 013805 (2009)

[9] E. K. Irish and K. Schwab, Phys. Rev. B **68**, 155311 (2003)

[10] M. A. Nielsen and I. L. Chuang, *Quantum Computation and Quantum Information* (Cambridge University Press, Cambridge, U. K. , 2000).

[11] E. Il'ichev, N. Oukhanski, A. Izmalkov, Th. Wagner, M. Grajcar, H.-G. Meyer, A. Yu. Smirnov, A. MaassenvandenBrink, M. H. S. Amin, and A. M. Zagoskin, Phys. Rev. Lett. **91**, 097906 (2003)

[12] I. Chiorescu, P. Bertet, K. Semba, Y. Nakamura, C. J. P. M. Harmans, and J. E. Mooij, Nature **431**, 159-162 (2004)

[13] M. Grajcar, A. Izmalkov, E. Il'ichev, Th. Wagner, N. Oukhanski, U. Hübner, T. May, I. Zhilyaev, H. E. Hoenig, Ya. S. Greenberg, V. I. Shnyrkov, D. Born, W. Krech, H.-G. Meyer, A. Maassen van den Brink, and M. H. S. Amin, Phys. Rev. B **69**, 060501(R) (2004)

[14] P. Bertet, I. Chiorescu, G. Burkard, K. Semba, C. J. P. M. Harmans, D. P. DiVincenzo, and J. E. Mooij, Phys. Rev. Lett. **95**, 257002 (2005)

[15] M. A. Sillanpää, T. Lehtinen, A. Paila, Yu. Makhlin, L. Roschier, and P. J. Hakonen, Phys. Rev. Lett. **95**, 206806 (2005)

[16] T. Duty, G. Johansson, K. Bladh, D. Gunnarsson, C. Wilson, and P. Delsing, Phys. Rev. Lett. **95**, 206807 (2005)

[17] N. Katz, M. Ansmann, R. C. Bialczak, E. Lucero, R. McDermott, M. Neeley, M. Steffen, E. M. Weig, A. N. Cleland, J. M. Martinis, A. N. Korotkov, Science **312**, 1498 (2006)

[18] A. Wallraff, D. I. Schuster, A. Blais, L. Frunzio, R.- S. Huang, J. Majer, S. Kumar, S. M. Girvin, and R. J. Schoelkopf, Nature **431**, 162-167 (2004)

[19] A. Blais, R.-S. Huang, A. Wallraff, S. M. Girvin, and R. J. Schoelkopf, Phys. Rev. A **69**, 062320 (2004).

[20] D. I. Schuster, A. Wallraff, A. Blais, L. Frunzio, R.-S. Huang, J. Majer, S. M. Girvin, and R. J. Schoelkopf, Phys. Rev. Lett. **94**, 123602 (2005).

[21] A. Wallraff, D. I. Schuster, A. Blais, L. Frunzio, J. Majer, M. H. Devoret, S. M. Girvin, and R. J. Schoelkopf, Phys. Rev. Lett. **95**, 060501 (2005).

[22] J. Gambetta, A. Blais, D. I. Schuster, A. Wallraff, L. Frunzio, J. Majer, M. H. Devoret, S. M. Girvin, and R. J. Schoelkopf, Phys. Rev. A **74**, 042318 (2006).

[23] J. Gambetta, W. A. Braff, A. Wallraff, S. M. Girvin, and R. J. Schoelkopf, Phys. Rev. A **76**, 012325 (2007).

[24] M. Boissonneault, J. M. Gambetta, and A. Blais, Phys. Rev. A **79**, 013819 (2009)

[25] I. Siddiqi, R. Vijay, F. Pierre, C. M. Wilson, M. Metcalfe, C. Rigetti, L. Frunzio, and M. H. Devoret, Phys. Rev. Lett. **93**, 207002 (2004).

[26] I. Siddiqi, R. Vijay, M. Metcalfe, E. Boaknin, L. Frunzio, R. J. Schoelkopf, and M. H. Devoret Phys. Rev. B **73**, 054510 (2006).

[27] A. Lupaşcu, S. Saito, T. Picot, P. C. De Groot, C. J. P. M. Harmans and J. E. Mooij, Nature Phys. **3**, 119 (2007).

[28] N. Boulant, G. Ithier, P. Meeson, F. Nguyen, D. Vion, D. Esteve, I. Siddiqi, R. Vijay, C. Rigetti, F. Pierre, and M. Devoret, Phys. Rev. B **76**, 014525 (2007).

[29] F. Yoshihara, K. Harrabi, A. O. Niskanen, Y. Nakamura, and J. S. Tsai, Phys. Rev. Lett. **97**, 167001 (2006)

[30] I. Serban, E. Solano, and F. K. Wilhelm, Phys. Rev. B **76**, 104510 (2007).

[31] I. Serban, and F. K. Wilhelm, Phys. Rev. Lett. **99**, 137001 (2007).

[32] I. Serban, B. L. T. Plourde, and F. K. Wilhelm, Phys. Rev. B **78**, 054507 (2008).

[33] T. Picot, A. Lupascu, S. Saito, C. J. P. M. Harmans, J. E. Mooij, Phys. Rev. B **78**, 132508 (2008).

[34] Experimental data report a qubit-induced differential shift of the bare SQUID frequency about the 4%, yielding $g = 0.02$.

[35] C. W. Gardiner and P. Zoller, *Quantum Noise*, Springer Verlag, 2ed., Berlin, Germany (2000).

[36] M. O. Scully and M. S. Zubairy, *Quantum Optics*, Cambridge University Press, Cambridge, England (2001).

[37] The factor 1/2 multiplying the damping rate κ is typical of coherent states arising from driving of a quantum harmonic oscillator, subjected to Markovian damping due to weak coupling to a bath of harmonic oscillator. The damping rate κ can be related to the quality factor Q, $\kappa = \omega_{\mathrm{ho}}/2\pi Q$ [36].

[38] Strictly speaking, $\mathrm{erf}(x)$ approaches 1 only asymptotically, in the limit $x \to \infty$. However, for values of x such that $1 - \mathrm{erf}(x) < 10^{-4}$, we discard the small deviation from 1.

[39] L. Chirolli and G. Burkard, Phys. Rev. B **74**, 174510 (2006).

4. Electronic implementations of Interaction-Free Measurements

Based on novel and prototypical electronic interferometric setups we show that it is possible to realize interaction free measurements in solid state nanodevices. We discuss three different implementations. The first one is very close to the optical proposal and it is based on a series of concatenated Mach-Zehnder interferometers. We also discuss the case in which the interaction free measurement is realized by means of an asymmetric Aharonov-Bohm ring and the case in which coherent single-electron sources are used. For all the three cases we show how to detect the effect through a measurement of the current passing through the device. Beside the interest in realizing with electrons a fundamental interferometric effect already measured with photons, interaction free measurements in nanoelectronics may play a fundamental role as very accurate measuring devices. We show this by discussing how to reveal the presence of a dephasing source. In addition to the accuracy the new key ingredient here is that a flux of electrons may measure noise without any degradation of its coherence properties. [1]

4.1 Introduction

Interaction-free measurements (IFMs) were first introduced by Elitzur and Vaidman [1], who showed that he laws of quantum mechanics allow to reveal the presence of an object without disturbing it. The original proposal exploited the coherent splitting and the subsequent recombination of the wave-function of a photon entering a Mach-Zehnder (MZ) interferometer. The disturbance induced by the object once placed in one of the two arms of the interferometer (an absorber in the original proposal) appears in the properties of outgoing flux of photons. Upon proper setting of the parameters of the interferometer it has been shown that, even without the absorption taking place, the mere possibility of this to happen deeply modifies the state of the particle emerging from the interferometer. As a result an external observer will be able to gather information about the presence or absence of the absorber, without the photon being absorbed. The maximal success probability was bound to be 50% in the original proposal. A way to improve the efficiency of the scheme was put forward by P. Kwiat *et al.* [2], who suggested to use coherently repeated interrogations. In their scheme a photon was repeatedly sent into a MZ interferometer, with an absorber placed in one of the two arms. By properly tuning the MZ phase it is possible to enhance the efficiency of the setup arbitrarily close to 1. Such a scheme can be thought as an application of a discrete form of the quantum Zeno effect, since every step can be considered as a measurement accompanied by state reduction. IFMs were experimentally realized using single-photon sources [2–5] and in neutron interferometry [6]. The enhanced efficiency based on concatenated MZ interferometers was tested in [7] with an improvement up to 73%. Its application was extended to the case of semitransparent objects with classical light [8–11]. An important consequence of these works that IFM could be interpreted in terms of deterioration of a resonance condition [8] which, at least for optical realizations, does not necessarily need a quantum description ("classical" optical coherent is sufficient).

---

[1] This chapter is a manuscript under preparation by L. Chirolli, E. Strambini, V. Giovannetti, F. Taddei, V. Piazza, R. Fazio, F. Beltram, G. Burkard.

There are numerous reasons to look for an electronic version of interaction free measurements. In recent years advances in fabrication made possible the observation of interference phenomena in electronic transport experiments, opening the way to a variety of applications. Of particular interest for what follows are the achievements obtained in the context of two-dimensional electron gas in the integer quantum Hall effect regime [12]. Here, various experimental realizations of the MZ [13–17] and Hanbury-Brown-Twiss interferometers [18, 19] have been successfully implemented In addition quantized electron emitters have been recently realized [20–23]. The possibility to extend IFM to electronic systems seems therefore now at reach, paving the way to the development of novel non-invasive measurement schemes in mesoscopic systems, with possible important implications for quantum information processing. In any case, regardless of possible applications, the implementation of IFM in electronic devices deserves in our opinion a careful scrutiny as a test for quantum control and quantum mechanics in mesoscopic systems. It is worth nothing that, differently from the optical case, for electronic systems there is no classical corresponding model to realize an IFM.

A first application of IFM strategies to electronic systems was proposed in Ref. [24] to detect the presence of a current pulse in a circuit by monitoring the state of a superconducting qubit coupled to the circuit, without any energy exchange between the two. Subsequently, in the very same spirit of the original works [1, 2], it was shown how to employ IFM to detect with unitary efficiency a localized source of noise acting on one arm of an Aharonov-Bohm (AB) chiral ring without affecting the transmitted and reflected currents [25]. In view of its (unavoidable) presence in nanoelectronics, the proposal focused on the detection of external random fluctuating electric or magnetic fields, which represents the most common source of noise in nanoscale quantum devices [26–29]. Therefore, in Ref. [25] a classical fluctuating electrical field, that randomizes the phase of the electron traveling through it, plays the role of the absorber of the optical schemes [1–11]. The resulting apparatus operates as a sort of *quantum fuse* which, depending on the presence or on the absence of the dephasing source, opens or closes a contact. The results presented in Ref. [25] show that the mechanism underlying the IFM do not depend, to a large extent, on the type of disturbance which is induced in the interferometer.

In the present paper we extend our work on the electronic version of the IFM in several ways. First of all we introduce two alternative IFM implementations based on the integer quantum Hall effect. The first scheme closely resembles the optical setup of Ref. [7] and uses a recent proposal [30] for realizing concatenated MZ interferometers. The second scheme instead is based on the standard quantum Hall interferometric architecture [13–19] and assumes the presence of a quantized electron emitters [20–23]. As in Ref. [25], both the setups are shown to be capable of detecting the presence of a localized dephasing sources without affecting the coherence of the probing signals. Finally we also give a detailed derivation of the results of Ref. [25].

The paper is organized as follows. In Sec. 4.2 we present a noise-sensitive coherent electron channel, based on the concatenation of several MZ interferometers. We show that we can detect the presence of a dephasing source affecting the propagation in one of the interfering electronic path via measuring the output currents. We then study the coherence of the outgoing signal by computing the fraction of coherent signal and show that an IFM measurement of the dephasing source is achievable. In Sec. 4.3 we embed the device described in Sec. 4.2 in a larger Mach-Zehnder interferometer and study the visibility of the output currents, showing how the coherence of the outgoing signal can be experimentally addressed. In Sec. 4.4 we suggest to implement an IFM in a unique Mach-Zehnder interferometer that makes use of a quantized electron source and concatenation in the time domain. In Sec. 4.5 we present a double ring structure in which a small chiral AB ring is embedded in one arm of a larger AB ring. We study the current the flows through the whole device as a measure of the coherent character of the detection.

4.2 Coherent detection of noise with IFMs

A straightforward implementation of IFM along the lines developed originally in optics can be realized exploiting the edge-channel interferometric architecture suggested in [30] based on systems at filling factor $\nu = 2$. The feature of this architecture which is relevant for our pourposes is that it allows for successive concatenation of different interferometers as depicted in Fig. 4.1. In this scheme a beam splitter (BS) is realized by introducing a sharp potential barrier which mixes the two edges. Populating initially only one channel, after the BS we find the electrons in a superposition state. Additional phase shifters (PSs) can be easily realize by spatially separating the two channels (it is sufficient to apply a top gate that can locally change the filling factor to $\nu = 1$). This way, only one channel can traverse this region and the other is guided along the edges of the local region with $\nu = 1$. This is schematically shown in Fig. 4.1, where a phase difference ϕ is introduced between the channels by changing the path of the incoming channel.

Exploiting this approach we can now build a long sequence of concatenated interferometers, which, analogously to the original optical implementation proposed by Kwiat Ref. [7], implements our IFM scheme. The proposed setup is illustrated in Fig. 4.1. It consists in a sequence of N concatenated interferometers, in which the outputs edges emerging from the n-th interferometer are directly fed into the inputs of the $(n + 1)$-th one. By means of this setup it is possible to detect the presence of a fluctuating electromagnetic field in the vicinity of the Hall bar (depicted as a shaded area in Fig. 4.1). By applying external top gates that deviate the path of the i channel, we steer the electron propagation inside the

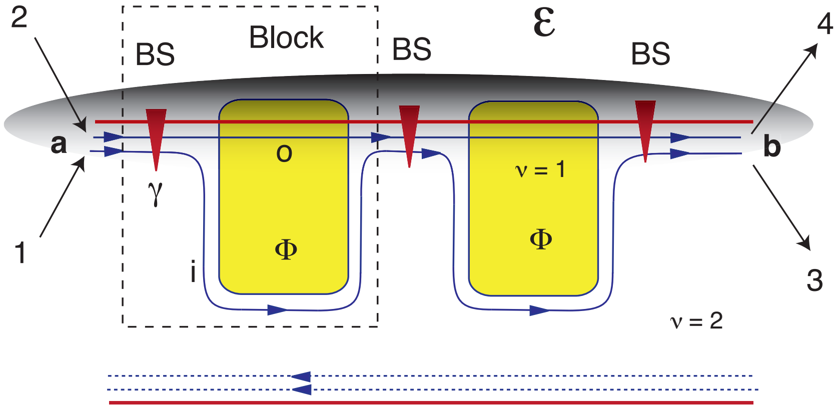

Figure 4.1: Schematic illustration of a noise-senitive coherent electron channel consisting of $N = 2$ representative blocks, implemented in a quantum Hall bar at integer filling $\nu = 2$. Incoming electrons in contact 1 and 2 are represented by their annihilation operators **a** and outgoing electrons in contact 3 and 4 by their annihilation operators **b**. Each block is constituted by a beam splitter (BS) and a phase shifter (PS). Each BS is characterized by a degree of admixture γ and mixes the incoming electron in the i and o edge states. The PS is constituted by an applied top gate (yellow area with filling factor $\nu = 1$) that spatially separates the edge channels and introduces a phase difference ϕ. An external fluctuating field of strength ϵ (shaded area) introduces dephasing by randomly shifting the phase of the electron traveling in the o edge state.

Hall bar, where the fluctuating field is supposed to be absent. Allowing only a small fraction of the electronic wavefunction to propagate through the region exposed to dephasing, it is possible to reveal the presence of the fluctuating field. If the dephasing field is absent, the electron coherently propagates towards the next step, that is nominally equal to the previous one. By properly tuning the degree of admixture of the channel populations, it is possible to gradually transfer the electron from the i (inner) channel to the o (outer) channel at the end of a chain of N interferometers. In case a dephasing field is present, that part of the wavefunction that propagates in the o channel, as a result of random phase shift, does not coherently add to the one propagating in the i channel, and the gradual transfer of electronic amplitude from the i channel to the o channel does not take place. At the same time the electron that propagates into the channel not exposed to the fluctuating field preserves its coherence. This way the presence or absence of noise is witnessed by the electron coming out in the lead 3 or 4 respectively and, as will be clear in the following, the setup manages to preserve the coherence of the emerging electronic signals.

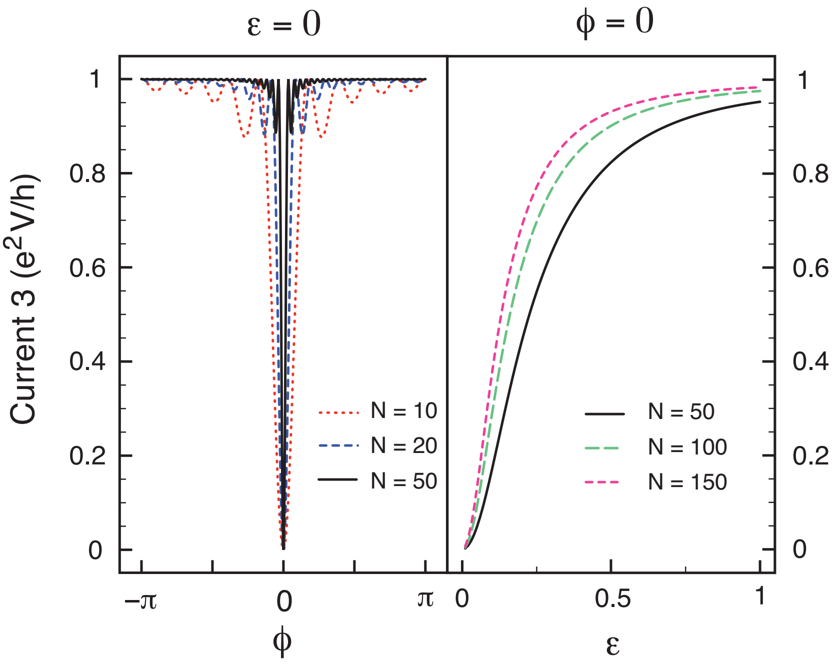

Figure 4.2: Current in contact 3 for different number N of blocks. (Left panel) I_3 versus the phase shift ϕ in the coherent case $\epsilon = 0$. By increasing N a narrow dip arises in the coherent case for $\phi = 0$, and all the current goes out in contact 4. (Right panel) I_3 versus the strength ϵ of the dephasing field, at the working point $\phi = 0$. As ϵ increases, the current tends to go out all from contact 3, thus witnessing the presence of the dephasing field.

4.2.1 Detection of a dephasing noise source

Electron propagation will be described in the formulation of Landauer and Büttiker of quantum transport [34, 35] and write the scattering matrix that describes the transport in each block as

$$S(\delta) = \begin{pmatrix} e^{i\phi}\cos(\gamma/2) & ie^{i\phi}\sin(\gamma/2) \\ ie^{i\delta}\sin(\gamma/2) & e^{i\delta}\cos(\gamma/2) \end{pmatrix}. \tag{4.1}$$

For the sake of simplicity it is possible to assume that the presence of a dephasing source is described by a random phase shift $\exp(i\delta)$. By using the above scattering matrix it is possible to relate electrons going out of a chain of N blocks to the incoming electrons at the beginning of the chain by

$$\mathbf{b} = \prod_{i=1}^{N} S(\delta_i)\, \mathbf{a}, \tag{4.2}$$

with $\mathbf{a} = (a_i, a_o)^T$ fermionic annihilation operator describing incoming electrons in the leads 1 and 2 connected respectively to channels i and o, and $\mathbf{b} = (b_i, b_o)^T$ fermionic annihilation operator describing outgoing electrons in the leads 3 and 4 connected. The contact 1 is biased at a chemical potential eV above the other reservoirs 2, 3, and 4 which are kept grounded. Setting the temperature to zero the current in contact 3 is

$$I_{3,N} = \frac{e^2 V}{h} \left| [S_N]_{11} \right|^2 , \tag{4.3}$$

with $S_N = \prod_{i=1}^{N} S(\delta_i)$. Here we do not take into consideration the electron spin degree of freedom.

The effect of the fluctuating field can be taken into account by averaging the phase over a generic distribution of width $2\pi\epsilon$ and zero mean. For simplicity we assume a uniform distribution. The outgoing currents depend now entirely on the degree γ of mixing of the edge states in the BS and on the phase shift ϕ. The average current in contact 3 is given by

$$\langle I_3 \rangle_\delta \equiv \frac{1}{(2\pi\epsilon)^N} \int_{-\pi\epsilon}^{\pi\epsilon} d\boldsymbol{\delta}\ I_{3,N}, \tag{4.4}$$

with $d\boldsymbol{\delta} = d\delta_1 \dots d\delta_N$. We define the two component vectors $\mathbf{e}_+ = (1,0)^T$, $\mathbf{e}_- = (0,1)^T$, that allow us to express

$$\begin{aligned} \left|[S_N]_{11}\right|^2 &= \mathbf{e}_+^T S_N^\dagger \mathbf{e}_+ \mathbf{e}_+^T S_N \mathbf{e}_+, & (4.5)\\ \left|[S_N]_{21}\right|^2 &= \mathbf{e}_+^T S_N^\dagger \mathbf{e}_- \mathbf{e}_-^T S_N \mathbf{e}_+. & (4.6) \end{aligned}$$

We introduce a representation of 2×2 matrices in terms of Pauli operators, concisely written in a Pauli vector defined as $\boldsymbol{\sigma} = (\sigma_0, \sigma_1, \sigma_2, \sigma_3)^T$, with $\sigma_0 = \mathbb{I}$. We can then write $\mathbf{e}_\pm \mathbf{e}_\pm^T = (\mathbb{I} \pm \sigma_Z)/2 \equiv \mathbf{p}_\pm \cdot \boldsymbol{\sigma}$, with $(\mathbf{p}_\pm)_i = \mathrm{Tr}(\mathbf{e}_\pm \mathbf{e}_\pm^T \sigma_i)/2$. This allows us to calculate the average over the phases δ_i as a matrix product. Defining the matrix

$$\mathcal{Q}_{ij} = \frac{1}{2} \int_{-\pi\epsilon}^{\pi\epsilon} \frac{d\delta}{2\pi\epsilon} \mathrm{Tr}\left[S^\dagger(\delta) \sigma_i S(\delta) \sigma_j \right], \tag{4.7}$$

we can write the zero temperature dephased current in the output 3 and 4 after N blocks as

$$\langle I_{3,4;N} \rangle_\delta = \frac{e^2 V}{h}\ \mathbf{p}_\pm \cdot \mathcal{Q}^N \cdot \left(\mathbf{e}_+^T\ \boldsymbol{\sigma}\ \mathbf{e}_+ \right). \tag{4.8}$$

We point out here that, due to the unitarity of $S(\delta)$, $\mathcal{Q}_{ij}$ defined in Eq. (4.24) preserves the trace. One can reduce the dimensionality of the problem and work with the Bloch representation of 2×2 density matrices.

The behavior of the output currents in the limit of large N is obtained by studying the eigenvalues of the 4×4 matrix $\mathcal{Q}$. Choosing the working point $\phi = 0$, the matrix $\mathcal{Q}$ assumes a diagonal block form, that allows for a direct solution, $\mathcal{Q} = U^{-1}\mathrm{diag}(1, \sin(\pi\epsilon)/\pi\epsilon, \lambda_-, \lambda_+)U$, with U and $\lambda_\pm$ given by Eqs. (E.2,E.3) in Appendix E. The currents in the terminal 3 and 4 can be then written as

$$\langle I_{3,4;N} \rangle_\delta = \frac{e^2 V}{h} \frac{1}{2} \left(1 \pm \frac{\lambda_+^N u_+ - \lambda_-^N u_-}{u_+ - u_-} \right), \tag{4.9}$$

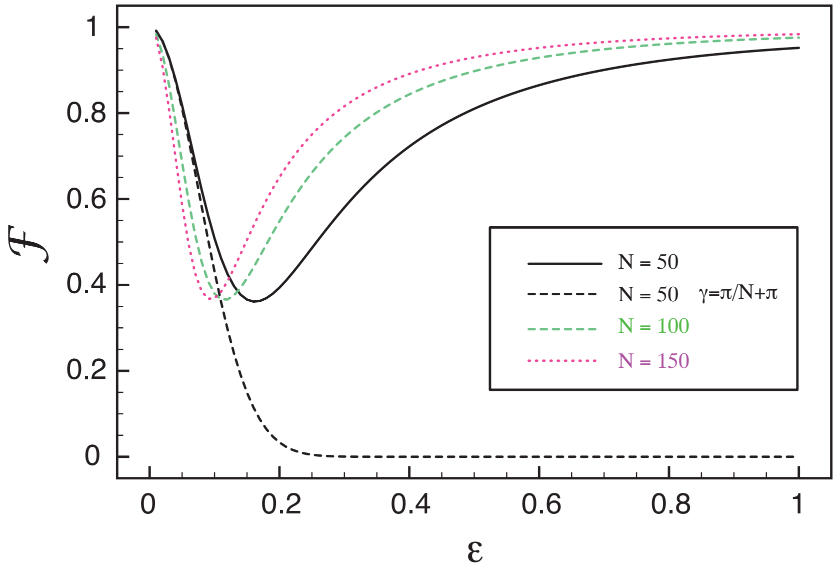

Figure 4.3: Fraction of coherent signal $\mathcal{F}$ versus the strength ϵ of the fluctuating field. Choosing the degree of admixture of the BSs to be $\gamma = \pi/N$, with most of the electron amplitude injected in the coherent i channel, the outgoing signal initially partially dephases for small ϵ, reaches a minimum, and then recovers its coherence as ϵ approaches one. To the contrary, injecting most of the electron amplitude in the channel affected by random phase shift by setting $\gamma = \pi/N + \pi$, the coherence of the outgoing signal is totally lost.

with $u_\pm$ given in Eq. (E.1) in Appendix E.

For the case of no dephasing $\epsilon = 0$, the outgoing currents at the working point $\phi = 0$ are given by $I_3 = 0$ and $I_4 = e^2V/h$. In Fig. 4.2 left panel we plot the current in terminal 3 versus the phase shift ϕ. We see that the current is approximately e^2V/h for almost all the range of values of the phase ϕ, and that only at the working point $\phi = 0$ it drops very rapidly to zero. Such a behavior corresponds to a very narrow resonance condition for which interference gives rise to a gradual transfer of the electron wavefunction to the o channel and all the current goes out from contact 4. Such a resonance is very sensitive to small deviations of the phase ϕ from the working point that imply a large variation of the current response. Increasing N further shrinks the dip at $\phi = 0$, as it is shown in Fig. 4.2 left panel for different N.

In the opposite case of strong dephasing case $\epsilon = 1$ the current behaves as $I_{3,4;N} = \frac{1}{2}(1 \pm \cos^N(\gamma))e^2V/h$. If the asymmetry of the BS is properly tuned at the value $\gamma = \pi/N$, the outgoing current are

$$\langle I_{3,4;N} \rangle_\delta = \frac{e^2V}{h}\frac{1}{2}\left(1 \pm \cos^N\left(\frac{\pi}{N}\right)\right). \tag{4.10}$$

In the limit of large N it follows that $I_3 = e^2V/h$ and $I_4 = 0$. The behavior of the current

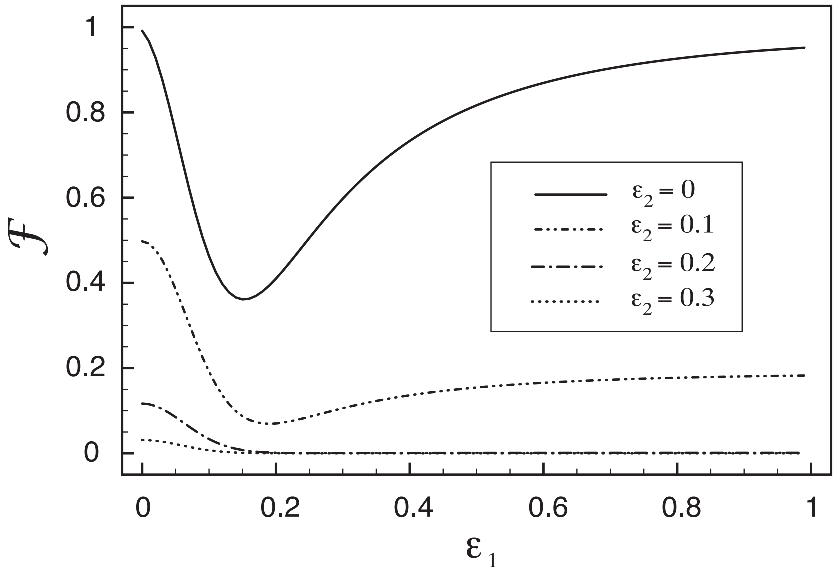

Figure 4.4: Fraction of coherent signal when the dephasing field affects both channels, respectively o with strength ϵ_1 and i with strength ϵ_2. The degree of admixture is set to $\gamma = \pi/N$, with $N = 50$, and most of the electron amplitude is injected in channel i. By increasing ϵ_2 the coherence is rapidly lost.

in contact 3 versus the dephasing strength ϵ is shown in Fig. 4.2, right panel. It is evident that the presence of a strong dephasing source changes the interference response, such that the electrons asymptotically exit the device all from the terminal 3, whereas in the coherent case they would exit all from the terminal 4. By inspecting Eq. (4.10), we notice that the current remains unchanged even in the highly asymmetric case when the electronic amplitude is diverted in the noisy channel o, $\gamma \to \gamma + \pi$ for N even. The system composed by the interferometer and the dephasing source behaves like a "which-path" interferometer.

4.2.2 Coherence of the outgoing signal

A key feature of the IFM detection of noise is that the the coherence of the outgoing signal is preserved, which in turn can open the way to novel application in quantum coherent electronics. Depending on whether the electron is mostly injected into the secure i channel by setting $\gamma = \pi/N$ or into the o channel subject to dephasing, by setting $\gamma = \pi/N + \pi$, the coherence of the outgoing signal can be asymptotically preserved or totally lost.

A convenient way to quantify the coherence of the outgoing signal by the fraction of coherent signal is

$$\mathcal{F} \equiv |\langle [S_N]_{11} \rangle_\delta|^2 + |\langle [S_N]_{21} \rangle_\delta|^2. \tag{4.11}$$

In the case $\epsilon = 0$, one has $|[S_N]_{11}|^2 + |[S_N]_{21}|^2 \equiv 1$, and the function $\mathcal{F}$ is identically one. In Fig. 4.3 we plot $\mathcal{F}$ for different choices of N and γ. For the particular choice $\gamma = \pi/50+\pi$, the $\mathcal{F}$ drops rapidly to zero, as a result of the strong dephasing experienced by the electron. On the other hand, one can see that by choosing $\gamma = \pi/N$, the fraction of coherent signal initially decreases, as a result of a small disturbance induced by the fluctuating field, but then saturates to one, witnessing the coherence of the outgoing signal. This behavior is sharpened for higher N.

Until now we have considered an ideal situation in which dephasing takes place only in one channel. In Fig. 4.4 we plot the behavior of the $\mathcal{F}$ versus the strength ϵ_1 of the dephasing field acting on channel o, when a fluctuating field of strength ϵ_2 affects the propagation in the i channel. We see that a strong response corresponds to a slight increase of ϵ_2, with the coherence of the outgoing signal significantly degraded.

In order to convey a small fraction of the electron wavefunction towards the dephasing region and realize the particular conditions for an IFM to be possible, it is necessary to set the degree of admixture in the BS to the precise value $\gamma = \pi/N$. This might represent a technical obstacle to an experimental realization, in that the BSs are very difficult to tune all at the same precise degree of admixture, and a high efficiency IFM is obtained in the limit of large N. We then study the behavior of the fraction of coherent signal when the condition $\gamma = \pi/N$ is not perfectly matched. This is done by averaging Eq. (4.24) over γ, obtained by convolution with a distribution of mean $\gamma = \pi/N$ and width 2η. The result is shown in Fig. 4.5 for the case $\gamma = \pi/100$. We notice that, as an overall behavior, the magnitude of $\mathcal{F}$ is decreased by an increase of η. Interestingly, the behavior of $\mathcal{F}$ versus ϵ is not qualitatively changed. As a result of the average over γ, the fraction of coherent signal is no longer equal to one in absence of dephasing. As ϵ is increased, $\mathcal{F}$ initially decreases and then asymptotically reaches the value it has in the case of no dephasing. Data not shown confirm that for a π-shift of the mean, $\gamma = \pi/N + \pi$, the fraction of coherent signal rapidly goes to zero. We therefore conclude that the phenomenon of IFM is quite robust against small deviation from the condition $\gamma = \pi/N$ and can in principle be addressed experimentally.

4.3 Detection of the coherent signal

The fraction of coherent signal quantified by the function $\mathcal{F}$ defined in Eq. (4.11), although containing all the information concerning the coherence of the signals coming out from the device, does not represent an experimentally measurable quantity. In order to test the coherent behavior of the device one has to compare the outgoing signal with a known phase. This could be done, for instance, by embedding the N concatenated blocks in a Mach-Zehnder interferometer, as schematically illustrated in Fig. 4.6. We apply a voltage V to contact 1 and ground all the other contacts. A beam splitter BST separates the signal coming from contact 1 into two amplitudes in such a way that one enters the N-block system from channel i, and the other follows a path whose length (and phase φ) can be arbitrarily adjusted. The amplitude coming out from the N-block system in the channel i is then mixed with the signal of known phase in BSB, and the two outgoing signals collected in contacts 3 and 3'. The amplitude coming out from the N-block system

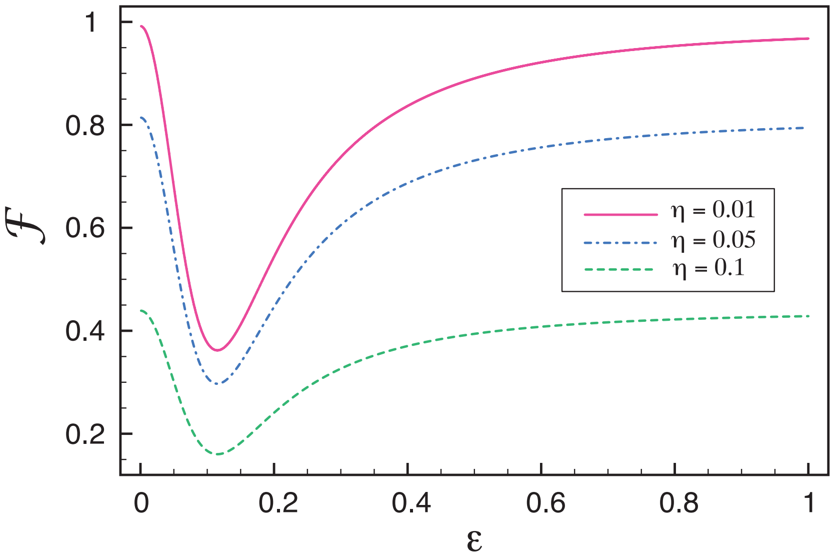

Figure 4.5: Fraction of coherent signal $\mathcal{F}$ versus the strength ϵ of the dephasing field, studied when the condition on the degree of admixture $\gamma = \pi/N$ is not matched exactly. The function $\mathcal{F}$ is convoluted with a distribution of the width 2η and mean $\gamma = \pi/100$, with most of the electron amplitude injected in channel i. By increasing η the magnitude of $\mathcal{F}$ rapidly decreases but the behavior with respect to ϵ persists, signature of a partial preservation of coherence.

in channel o is drained separately in contact 4.

By denoting with $t = [S_N]_{11}$ the amplitude coming out from the N concatenated interferometers in channel i, and $r = [S_N]_{21}$ the amplitude coming out from the device in channel o the transmission probability in contact 3 is given by

$$\begin{aligned} \mathcal{T}_3(\varphi) &= \frac{1}{2}\left\langle \left|t + e^{i\varphi}\right|^2 \right\rangle_\delta \qquad (4.12) \\ &= \frac{1}{2}(\langle T\rangle_\delta + 1) + |\,\langle t\rangle_\delta\,| \cos\left(\arg(\langle t\rangle_\delta) - \varphi\right), \qquad (4.13) \end{aligned}$$

with $T = |t|^2$. The visibility of $\mathcal{T}_3(\varphi)$ can be quantified by the maximal normalized amplitude of the φ-oscillation,

$$\mathcal{V}_3 = \frac{2|\,\langle t\rangle_\delta\,|}{\langle T\rangle_\delta + 1}. \qquad (4.14)$$

In Fig. 4.7 we plot the function $\mathcal{V}_3$ versus ϵ for different number N of interferometers, keeping the degree of admixture $\gamma = \pi/N$. For $\epsilon = 0$ the destructive interference for $\phi = \pi$ produces a zero amplitude signal t, from which follows a zero visibility. Switching on the dephasing field we see that the visibility rapidly increases to saturate to one, therefore revealing the coherence of the amplitude t with respect to the phase φ.

In order to measure the function $\mathcal{F}$ defined in the previous section we need an more complex setup. Indeed, two signals come out of the N-block system and we have to measure current and visibility of both signals. This mean that one has to modify the setup of Fig. 4.6 such that the amplitude that goes out from the N-block system in the channel o interferes with a signal of known phase φ' before going out from the whole device from contact 4. By measuring the transmission amplitudes $\mathcal{T}_3(\varphi)$ and

$$\mathcal{T}_4(\varphi') = \frac{1}{2}(\langle R\rangle_\delta + 1) + |\,\langle r\rangle_\delta\,| \cos\left(\arg(\langle r\rangle_\delta) - \varphi'\right), \tag{4.15}$$

with $R = |r|^2$, and their visibilities $\mathcal{V}_3$ and $\mathcal{V}_4$ in contact 3 and 4 we can reconstruct the function $\mathcal{F}$. Denoting $\bar{\mathcal{T}}_3$ and $\bar{\mathcal{T}}_4$ the mean values of the transmission probabilities in 3 and 4, we can write

$$\mathcal{F} = \mathcal{V}_3^2\bar{\mathcal{T}}_3^2 + \mathcal{V}_4^2\bar{\mathcal{T}}_4^2. \tag{4.16}$$

This relation allows us to understand the behavior of the $\mathcal{F}$ as a function of ϵ. The visibility $\mathcal{V}_3$ necessarily starts from zero, as $T = 0$ for $\epsilon = 0$, as shown in Fig. 4.7. To the contrary, the visibility $\mathcal{V}_4$ necessarily starts from one, as $T = 0$ for $\epsilon = 0$ and $R = 1-T$. At small but non-zero ϵ one has a reduction of the $\mathcal{F}$ due to the non linear dependence on the currents and visibilities in Eq. (4.16). Hence the minimum in the visibility, as shown in Figs. 4.3 and 4.4. As $\epsilon \to 1$, in the case of IFM one of the two addenda in Eq. (4.16) survives, and $\mathcal{F} \to 1$ asymptotically, otherwise it monotonically decreases to zero.

4.4 Multiple interference in the time domain

It is possible to realize an IFM scheme based on the Mach-Zehnder (MZ) interferometer in the integer quantum Hall architecture at filling factor $\nu = 1$, experimentally realized in Ref. [13–19]. To this end one needs to employ a quantized electron emitter [20–23], as illustrated in Fig. 4.8.

The periodic time-dependent potential $V(t)$ applied to a small circular cavity produces, on a linear extended channel connected to contact 1, an ac current composed by a very well time-resolved electron and hole pair [20–23]. A quantum point contact (QPC1), driven by a time-dependent external potential $U_1(t)$, connects the linear edge to the MZ and lets only electrons to be transmitted in the interferometer, while reflecting holes in the lead 1. Suppose that after an electron has been injected into the MZ, the QPC1 closes and completely detaches the MZ from lead 1. The transmitted electron travels with a precise velocity v_F along the edge e_{bl} in the MZ until it encounters the first beam splitter BSL. There it is split into two packets that follow two different edges e_{tr} and e_{br} of equal length L and will collide at BSR after a time L/v_F. The two packets then mix together at BSR and then follow the edges e_{bl} and e_{tl} of length L. The sequence repeats itself many times, with the electronic wavepacket being split and reunited many times at the beam splitters BSL and BSR. Due to the fact that the drift velocity on the edge is constant and by engineering the arms of the MZ to have all equal lengths, we can map the time propagation in the MZ into a spatial concatenation of BSs and phase shifters PSs. Via properly tuning the degree

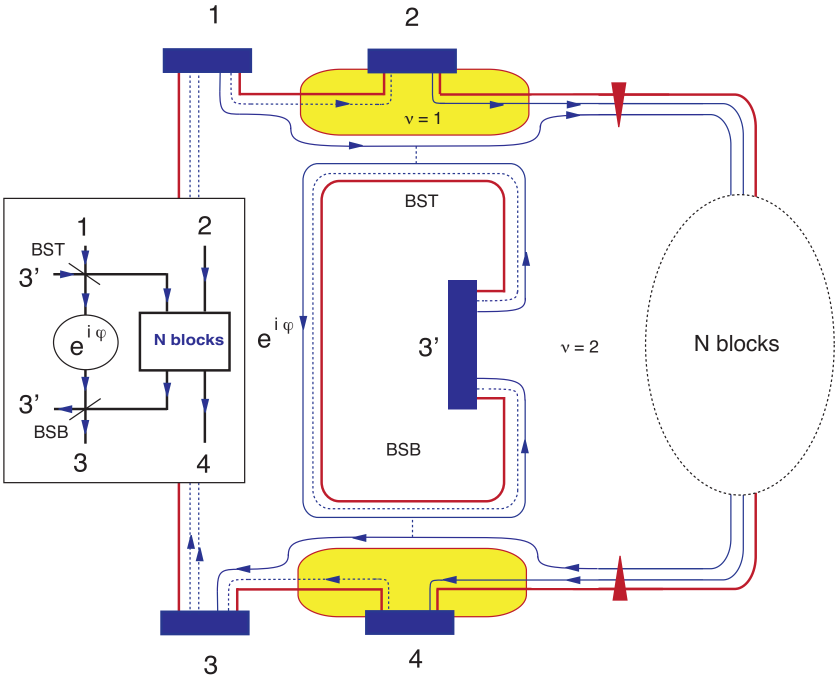

Figure 4.6: Schematic representation of the proposal for an experimental realization of an N-block noise-sensitive electron channel embedded in a Mach-Zehnder interferometer. Electrons entering the a Hall bar from contact 1 split at the beam splitter BST. The electrons transmitted will traverse the N-block system and eventually go out from contact 4 or impinge onto BSB. The latter mix with those initially reflected at BST and interfere. The result of the interference can be collected in contact 3 or 3’. In the yellow areas the filling factor is $\nu = 1$ and in the rest of the Hall bar the filling factor is $\nu = 2$. The coherence of the outgoing signal can be directly addressed by measurement of the visibility of current in contact 3 versus the tunable phase φ acquired during the propagation by the electron reflected at BST. Inset: Schematics of the main picture.

of channel admixture at the BSs, we make the electron appear after N rounds entirely in front of QPC2, that can be opened in a time-resolved way, such that the electron can be collected into lead 2.

A dephasing source affecting the propagation of the electron in the edge e_{tr} can be simply described by randomly shifting the phase of the corresponding wavepacket. The electron will have very high probability to be in front of QPC1. By opening the latter one can collect a coherent electron in contact 1, thus performing an IFM of the dephasing source. This protocol should operate in a cyclic way. The periodic potential $V(t)$ produces an electron at time t_+ and a hole at time t_- in front of the QPC1 every cycle, with $0 \leq t_+ \leq \mathcal{T}/2$ and $\mathcal{T}/2 \leq t_- \leq \mathcal{T}$, and with $\mathcal{T}$ the period of the cycle. The QPC1 will be open during

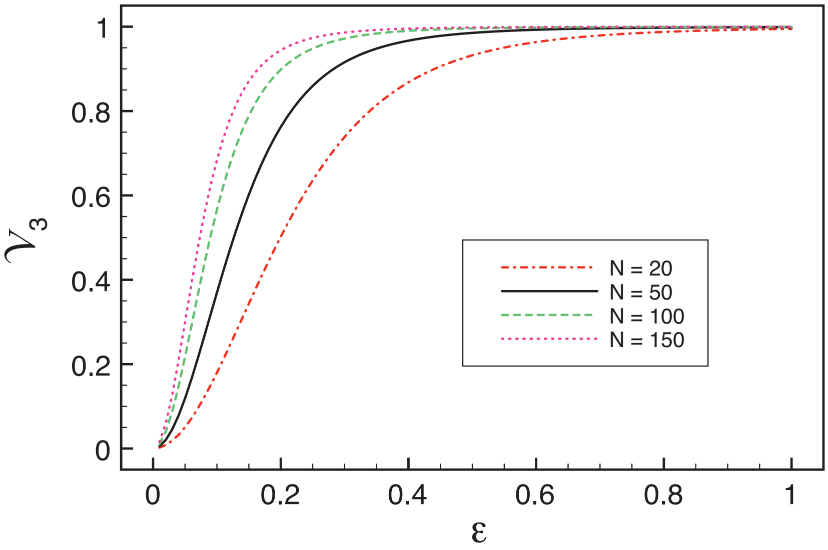

Figure 4.7: Visibility $V_{\mathcal{T}}$ of the current in contact 3 versus the strength of the dephasing field, for several number of blocks N. In the coherent case $\epsilon = 0$ the current in contact 3 is zero, for which also $V_{\mathcal{T}}$. Increasing ϵ the visibility approaches one. We set $\gamma = \pi/N$.

first half cycle, to let the electron in, and closed for the second half cycle. The two QPCs open and close simultaneously. An electron emitted in front of the QPC1 at time t_+ will appear in front of one of the two QPCs after a time $t_+ + N\Delta t$, with $\Delta t \equiv 2L/v_F$, having performed N rounds. With the choice $t_+ = (1/2 - 1/M)\mathcal{T}$ and $\Delta t = (m + 1/M)\mathcal{T}$, with $m, M = 1, 2, 3 \ldots$, an electron makes $N_{max} = M/2$ rounds inside the MZ before finding the QPCs open. Depending on the interference conditions the electron will be found either in front of QPC1, in case of no dephasing, or in front of QPC2, in presence of a dephasing source.

In the case for which no dephasing field is present, $\epsilon = 0$, it is possible to tune the MZ such that after N_{max} rounds the electron is exactly in front QPC2 and can be collected in contact 2. The current in contact 1 will be given by a train of holes, whereas the current in contact 2 by a train of electrons. In the case of maximal dephasing, $\epsilon = 1$, no current is expected in contact 2, and a train of coherent electron-hole pairs per cycle is expected in contact 1.

The energy level spacing inside the MZ can be estimated as $\Delta E \sim h/\Delta t = \frac{h}{(m+1/M)\mathcal{T}}$. For large M it is determined by the size of m, that can be chosen to be large enough for a continuum approximation of the level spacing to be valid. This picture allows us to describe the physics in the Landauer-Büttiker formulation of quantum transport[34, 35], with no needs of the Floquet treatment of the time-dependent problem. We introduce the electron annihilation operators $\{\hat{e}_{tr}, \hat{e}_{br}, \hat{e}_{bl}, \hat{e}_{tl}\}$ that annihilate an electron on the edge

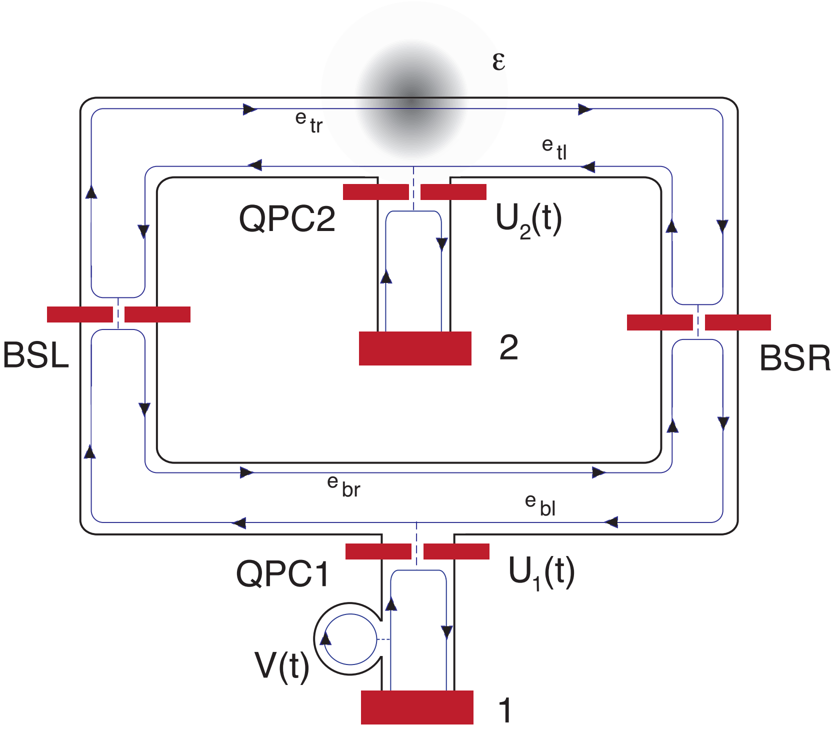

Figure 4.8: Mapping of concatenation in space to the time domain in a Mach-Zehnder interferometer. A time-dependent voltage generates a current of well separated electron and holes. The QPC1 let the electrons enter the Mach-Zehnder, perform N rounds in the interferometer and then collect them back into contact 1 in the case a dephasing field of strength ϵ affects the dynamics of the channel e_{tr}. In the coherent case $\epsilon = 0$ the electrons are collected in contact 2.

states $\{e_{tr}, e_{br}, e_{bl}, e_{tl}\}$. In order to obtain the transport regime described in the previous section we have to tune the beam splitters BSL and BSR such that

$$S_{BSL} = S_{BSR} = \begin{pmatrix} \cos(\gamma/2) & i\sin(\gamma/2) \\ i\sin(\gamma/2) & \cos(\gamma/2) \end{pmatrix}, \tag{4.17}$$

with $(\hat{e}_{tr}, \hat{e}_{br})^T = S_{BSL}(\hat{e}_{bl}, \hat{e}_{tl})^T$ and $(\hat{e}_{bl}, \hat{e}_{tl})^T = S_{BSR}(\hat{e}_{tr}, \hat{e}_{br})^T$, with the particular choice $\gamma = \pi/N_{max}$. Concerning with the dynamical phase acquired by propagating along the edge channels, arms of equal length L give rise to no phase shift between the arms, and the condition for the working point $\phi = 0$ depends only upon proper tuning of the magnetic field.

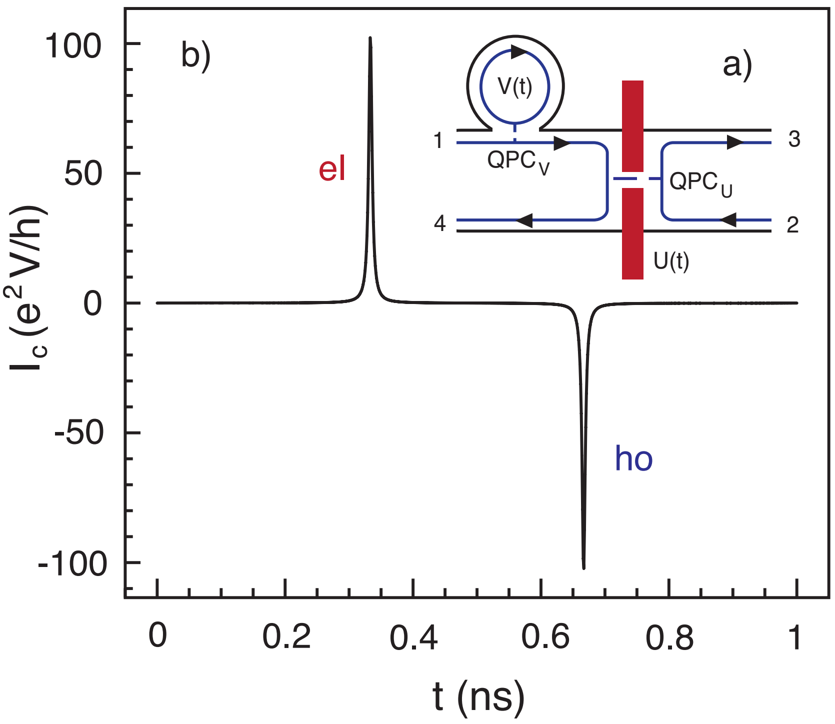

Figure 4.9: a) Schematic representation of a time-dependent electron-hole switch. The cavity driven by the potential $V(t)$ is connected via QPC_V to a linear edge and produces a well separated pair of electron and hole per cycle. The potential $U(t)$ drives the QPC_U that connects contacts 1 and 2 to contacts 3 and 4 and periodically transmits the electron to contact 3 and reflects the hole to contact 4. b) Time-resolved electron-hole current produced by the driven cavity in front of QPC_V, as given by Eq. (G.5).

4.5 IFM with an Aharonov-Bohm ring

In this section we review the idea of implementing an IFM with an asymmetric Aharonov-Bohm ring, as suggested in [25], and we corroborate the discussion presenting an operative scheme that allows to directly measure the visibility of the outgoing signal. As shown in [25], the difference in performing an IFM and a "which-path" detection consists in the possibility to preserve the coherence of the outgoing signal with respect to a signal of known phase. We suggest to embed the asymmetric AB ring in a further larger symmetric AB ring, with the smaller ring to be placed in the upper arm of the larger one, as shown in Fig. 4.10. This way, the phase that an electron accumulates while traveling in the lower arm of the large ring represents a reference for studying the coherence of the electron that traverses the asymmetric ring exposed to dephasing. By tuning the magnetic field that pierces the large ring, we can control the current flowing in the device and study the visibility of the current as a figure of merit in the study of coherence.

As the small asymmetric AB ring, we consider a one channel measoscopic ring and characterize its dynamics in the Landauer-Büttiker formalism of quantum transport[34, 35]. We assume an asymmetric electron injection, with higher probability to send the electron in the lower (upper) arm of the ring. Following [25], we parametrize the unitary scattering matrix connecting the incoming to the outgoing modes in the node A as

$$S_A = \begin{pmatrix} r_A & \bar{\mathbf{t}}_A \\ \mathbf{t}_A & \bar{\mathbf{r}}_A \end{pmatrix} = \begin{pmatrix} a & b\cos(\frac{\pi}{2}\gamma) & b\sin(\frac{\pi}{2}\gamma) \\ b\sin(\frac{\pi}{2}\gamma) & a & b\cos(\frac{\pi}{2}\gamma) \\ b\cos(\frac{\pi}{2}\gamma) & b\sin(\frac{\pi}{2}\gamma) & a \end{pmatrix}$$

with $r_A = a$, $\mathbf{t}_A$ the 2×1 bottom left block, $\bar{\mathbf{t}}_A$ the 1×2 top right block and $\bar{\mathbf{r}}_A$ the remaining 2×2 bottom right block, with $a = -\sin(\pi\gamma)/(2 + \sin(\pi\gamma))$ and $b = \sqrt{1 - a^2}$. For the node B we analogously define

$$S_B = \begin{pmatrix} \bar{r}_B & \mathbf{t}_B \\ \bar{\mathbf{t}}_B & \mathbf{r}_B \end{pmatrix}. \tag{4.18}$$

We further assume invariance of the injection under exchange of the nodes. Such a configuration has been theoretically studied and experimentally realized at low magnetic fields [31–33], and can be understood as the effect of the Lorentz force. We denote the annihilation operators for the incoming (L) and the outgoing (u, d) modes in the node A as $\mathbf{a}_L \equiv (a_L, a_u, a_d)^T$ and $\mathbf{b}_L \equiv (b_L, b_u, b_d)^T$ respectively. We then assume that $\mathbf{b}_L = S_A \mathbf{a}_L$. Analogously we denote the incoming and the outgoing modes in the node B as $\mathbf{a}_R \equiv (a_R, a'_u, a'_d)^T$ and $\mathbf{b}_R \equiv (b_R, b'_u, b'_d)^T$ respectively, with $\mathbf{b}_B = S_B \mathbf{a}_R$. Symmetry under cyclic exchange of the nodes A and B implies that

$$\begin{pmatrix} b_R \\ b'_d \\ b'_u \end{pmatrix} = S_A \begin{pmatrix} a_R \\ a'_d \\ a'_u \end{pmatrix}. \tag{4.19}$$

By rearranging the order of the vector components we obtain $S_B = S_A^T$. The parameter γ controls the asymmetry of the nodes A and B, such that for $\gamma = 0$ or 1 a complete asymmetry is achieved, with the electron entering from the left lead being injected totally in the lower or upper arm respectively, whereas for $\gamma = 1/2$ the injection is symmetric. An external magnetic field is applied perpendicularly to the plane and it is responsible for the magnetic Aharonov-Bohm (AB) phase acquired in the ring. At the same time it determines the amplitude of the electron going in the upper branch and in the lower branch via the Lorenz force. Electron propagation in the two arms is described by the matrices $S_p(\delta) = e^{ik_F\ell}\,\mathrm{diag}(e^{i\phi/2+i\delta}, e^{-i\phi/2})$, for the transmission from left to right, and $\bar{S}_p(\delta) = e^{ik_F\ell}\,\mathrm{diag}(e^{-i\phi/2+i\delta}, e^{i\phi/2})$, for the transmission from right to left. Here ϕ is the ratio of the magnetic field flux through the asymmetric ring to the flux quantum, k_F is the Fermi wavenumber, ℓ is the length of the arms and δ is an additional random phase. In the following we shall set $k_F\ell = \pi/2$ and anticipate that a different choice does not change qualitatively our findings.

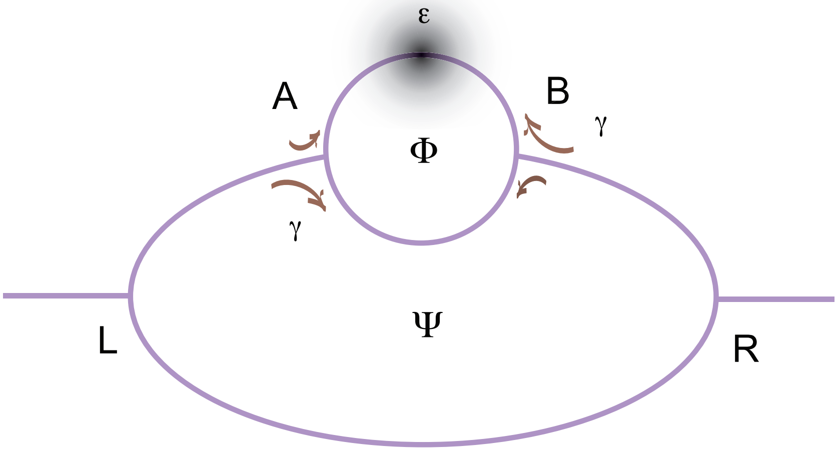

Figure 4.10: Schematic representation of a double ring setup that allow to quantify via a current measurement the degree of coherence of the signal going out from the small ring. The large ring is pierced by a magnetic flux Ψ and the small ring by a flux Φ. The nodes L and R of large ring split the electron amplitude impinging on them in the two arms of the large ring in a symmetric way, whereas The nodes A and B of small ring split the electron amplitude impinging on them in the two arms of the small ring in a non symmetric way according to the parameter γ. A dephasing field of strength ϵ affects the dynamics of electrons traveling in the upper arm of the small ring by randomly shifting their phase.

We embed the asymmetric AB ring in a larger symmetric AB ring. We describe the scattering at the node L and R of the large ring by a scattering matrix

$$S_L = \begin{pmatrix} r_L & \bar{\mathbf{t}}_L \\ \mathbf{t}_L & \bar{\mathbf{r}}_L \end{pmatrix} = \begin{pmatrix} c & \sqrt{g} & \sqrt{g} \\ \sqrt{g} & d & e \\ \sqrt{g} & e & d \end{pmatrix}, \tag{4.20}$$

with $r_L = c$, $\mathbf{t}_L$ the 2×1 bottom left block, $\bar{\mathbf{t}}_L$ the 1×2 top right block and $\bar{\mathbf{r}}_L$ the remaining 2×2 bottom right block. The scattering matrix depends only on one parameter, g that controls the strength of the coupling of the leads to the ring, $0 < g < 1/2$, via $c = \sqrt{1-2g}$, $d = -(1+c)/2$, $e = (1-c)/2$. On the right node we have $S_R = S_L^\dagger$. The free propagation in the large ring can be taken into account by a 2×2 diagonal matrix, with the dynamical and geometric phases acquired in the propagation in the upper and lower arm of the large ring. We assume the arms of the ring to be of equal length L, and split the arms into two nominally equal branches, before and after the smaller asymmetric ring. We further assume the propagation in the different branches to be described by $P = e^{ik_F L/2}\mathrm{diag}(e^{i\varphi/4}, e^{-i\varphi/4})$, for the motion from the left toward the right, and $\bar{P} = e^{ik_F L/2}\mathrm{diag}(e^{-i\varphi/4}, e^{i\varphi/4})$, with φ is the ratio of the magnetic field flux through the large symmetric ring to the flux quantum.

The amplitude for transmission from the left lead to the right lead can be thought as a interference process between possible paths that the electron can take to go from the left to the right. A useful way to calculate the transmission amplitude from the left lead to the right lead is to separately consider the propagation in the large ring from the node L to the node A, and from the node B to the node R. This way we can concisely include the effect of the large ring into multichannel effective transmission and reflection amplitudes in node A and B, $\boldsymbol{\tau}_A$, $\boldsymbol{\rho}_A$, $\bar{\boldsymbol{\tau}}_A$, and $\bar{\boldsymbol{\rho}}_A$, and similarly in node B. This procedure is particularly useful in that we want to consider the presence of a dephasing field acting on one of the two arms of the small asymmetric AB ring that joins the nodes A and B. In the coherent case, the total transmission amplitude is then given by the coherent sum of all paths in which an electron winds one time, two times, etc. in the small ring, and it is given by

$$t = \boldsymbol{\tau}_B (\mathbb{I} - \Gamma)^{-1} S'_p \boldsymbol{\tau}_A, \tag{4.21}$$

with $\Gamma = S'_p \bar{\boldsymbol{\rho}}_A \bar{S}'_p \boldsymbol{\rho}_B$. The matrix S'_p and the effective transmission and reflection amplitudes in node A and B are given in Appendix F.

4.5.1 Transmission in the presence of a dephasing field

We now assume a fluctuating external field (dephasing source) to be placed in the upper arm of the small asymmetric ring. To account for it we define the partial transmission amplitude of order N as

$$t_N = \boldsymbol{\tau}_B \sum_{n=0}^{N} \prod_{j=0}^{n} \Gamma_{(n-j)} S'_{p,0} \boldsymbol{\tau}_A \tag{4.22}$$

where $\Gamma_{(j)} \equiv \Gamma(\delta_j, \delta'_j) = S'_p(\delta_j) \bar{\boldsymbol{\rho}}_A \bar{S}'_p(\delta'_j) \boldsymbol{\rho}_B$ depends on two random phases δ_j and δ'_j, and $S'_{p,0} \equiv S'_p(\delta_0)$. We then choose the random phases from a distribution $g_\varepsilon(\delta)$ of zero mean and width $2\pi\varepsilon$ and compute the averaged partial transmission probability as $\langle t^*_N t_N \rangle_\delta$, where $\langle \ldots \rangle_\delta = \int d\boldsymbol{\delta} g_\varepsilon(\boldsymbol{\delta}) \ldots$, and $g_\varepsilon(\boldsymbol{\delta}) = g_\varepsilon(\delta_0) \ldots g_\varepsilon(\delta_{2N})$. In what follows we choose a uniform distribution of width $2\pi\epsilon$, centered around $\delta = 0$. It can be shown that the following recursive relation holds:

$$\langle t^*_N t_N \rangle_\delta = \langle t^*_{N-1} t_{N-1} \rangle_\delta + \Xi_N. \tag{4.23}$$

By iterating the procedure, the averaged transmission probability $\langle T \rangle_\delta = \lim_{N\to\infty} \langle t^*_N t_N \rangle_\delta$ can be written as $\langle T \rangle_\delta = \sum_{N=0}^{\infty} \Xi_N$. To compute such limit we introduce the Gell-Mann matrix vector $\boldsymbol{\Sigma} = (\Sigma_0, \Sigma_1, \ldots, \Sigma_8)^T$, with $\Sigma_0 = \sqrt{2/3} \times \mathbb{I}$, write $\boldsymbol{\tau}^\dagger_B \boldsymbol{\tau}_B = \mathbf{p}_B \cdot \boldsymbol{\Sigma}$, with $(\mathbf{p}_B)_i = \frac{1}{2} \mathrm{Tr}(\boldsymbol{\tau}^\dagger_B \boldsymbol{\tau}_B \Sigma_i)$, and define the following decoherence matrix

$$\mathcal{Q}_{ij} = \frac{1}{2} \int d\boldsymbol{\delta}\; g_\varepsilon(\boldsymbol{\delta}) \mathrm{Tr}\left[\Gamma^\dagger(\boldsymbol{\delta}) \Sigma_i \Gamma(\boldsymbol{\delta}) \Sigma_j\right], \tag{4.24}$$

which allows us to perform the average over the random phase as a matrix product. Similarly we define $\Gamma_{\mathrm{av}} = \int d\boldsymbol{\delta}\; g_\varepsilon(\boldsymbol{\delta}) \Gamma(\boldsymbol{\delta})$, and the decoherence map $\mathcal{P}$ with entries

$$\mathcal{P}_{ij} = \frac{1}{2} \int d\delta g_\varepsilon(\delta) \mathrm{Tr}\left[S^\dagger_p(\delta) \Sigma_i S_p(\delta) \Sigma_j\right], \tag{4.25}$$

that describes the average over the random phase in $S'_{p,0}$. This way Ξ_N can be concisely written as

$$\Xi_N = \left(\mathbf{p}_B \cdot \mathcal{Q}^N + \sum_{k=1}^{N} \mathbf{p}_k \cdot \mathcal{Q}^{N-k} \right) \cdot \mathcal{P} \cdot \; \boldsymbol{\tau}_A^\dagger \, \boldsymbol{\Sigma} \, \boldsymbol{\tau}_A, \tag{4.26}$$

with the vector $(\mathbf{p}_k)_i = \frac{1}{2} \left[\mathrm{Tr}(\boldsymbol{\tau}_B^\dagger \boldsymbol{\tau}_B \Gamma_{\mathrm{av}}^k \Sigma_i) + c.c \right]$. By writing $\mathbf{p}_k = \mathrm{Re}[\lambda_1^k \Lambda_1 + \lambda_2^k \Lambda_2 + \lambda_3^k \Lambda_3] \cdot \mathbf{p}_B$, with λ_i the eigenvalues of Γ_{av}, U the matrix of the eigenvectors of Γ_{av}, and $(\Lambda_i)_{jk} = (U \Sigma_j \Sigma_k U^{-1})_{ii}$, that satisfy $(\Lambda_1 + \Lambda_2 + \Lambda_3)/2 = \mathbb{I}$, we can perform the sum on N obtaining

$$\langle T \rangle_\delta \;\; = \;\; \mathbf{p}_B \cdot (\mathcal{T} - \mathbb{I}) \cdot (\mathbb{I} - \mathcal{Q})^{-1} \cdot \mathcal{P} \cdot \; \boldsymbol{\tau}_A^\dagger \, \boldsymbol{\Sigma} \, \boldsymbol{\tau}_A, \tag{4.27}$$

with $\mathcal{T}$ being a 9×9 matrix defined by $\mathcal{T} = \sum_{i=1}^{3} \mathrm{Re}[(1 - \lambda_i)^{-1} \Lambda_i^T]$. The averaged transmission probability $\langle T \rangle_\delta$ is now function of the AB phase φ.

4.5.2 Current as a measure of coherence

We are interested in measuring the coherence of the signal going out from the small asymmetric AB ring. An electron entering the large symmetric ring from the node L will partially go towards the small ring and partially toward the node R via the lower arm of the large ring. If we set to zero the phase difference φ accumulated between the upper and the lower arm of the large ring, $\varphi = 0$, it follows that for $g \lesssim 1/2$ the amplitude for entering and for going out from the large ring are close to one. An electron will then test only few times the coherent behavior of the small asymmetric ring (asymptotically only once for $g = 1/2$). On the other hand for $g \ll 1/2$ the electron has small amplitude to enter the large ring and, once entered, small amplitude to go out from the large ring, and the electron will be reflected many times between the nodes L and R and will test many times the small asymmetric AB ring. This picture is reversed if $\varphi = \pi$. The coherent behavior of the device is better studied in the case $g \lesssim 1/2$, for which the transmission probability of the large ring is the result of the constructive interference of only two paths and recalls the behavior of the Mach-Zehnder interferometer analyzed in Sec. 4.2.1. We then choose $g = 0.49$. As an optimal working point for the study of the coherence of the outgoing signal, and for an entire manifestation of the IFM effect, we also adjust the external magnetic field and the length of the arms such that $\phi = \pi$, $\varphi = 0$, $k_F \ell = \pi$ and $k_F L = \pi$.

The zero-temperature current through the whole device is

$$I = \frac{e^2 V}{h} \langle T \rangle_\delta \tag{4.28}$$

and it is shown in Fig. 4.11 for an applied bias voltage $\mu_L - \mu_R = eV$, with μ_L and μ_R the chemical potential of the leads attached respectively to the node L and R of the large ring. In the coherent case $\epsilon = 0$, the current is zero, independently on the degree of asymmetry γ of the small ring. This is because the small ring totally reflects electrons incoming from

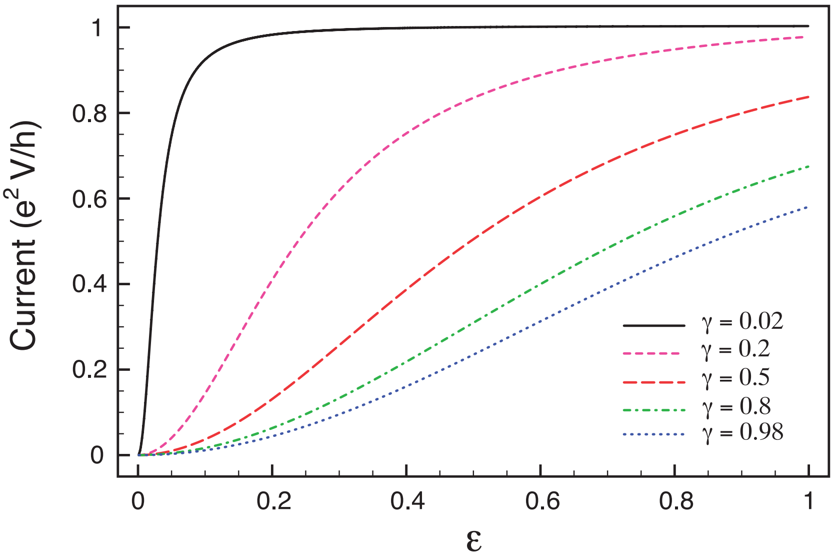

Figure 4.11: Plot of the current in units of e^2V/h, flowing from the left lead to the right lead of the double ring structure represented in Fig. 4.10, versus the strength ϵ of the dephasing field, at several degree of asymmetry γ. For $\gamma \to 1$ we divert the electrons mostly toward the dephasing source and consequently we have a reduction of the current flowing in the device. For $\gamma \to 0$ we divert the electron mostly toward the dephasing-free region and the coherent propagation gives rise to a maximal current flowing in the device.

the node L that, consequently, gain a phase difference of π with respect to those that flow in the lower arm of the large ring and totally destructive interference occurs. As the strength ϵ of the dephasing is increased, the current increases with a behavior that strongly depends on the degree of asymmetry of the small ring. When $\gamma \sim 0, 1$ the small ring transmits completely and the total current that comes out from the large ring depends on the interference between the upper and lower branch of the large ring. For $\gamma = 0.98$ most of the electron amplitude that impinges from the left into the small ring will go into the upper arm of the small ring, where a random fluctuating field is present, and undergoes a strong dephasing. It then follows that the interference between the upper and lower arms of the large ring is totally washed out by dephasing and the current is given by the incoherent sum of the contributions of the upper and lower arms of the large ring and it asymptotically saturates to $1/2$ (in units of e^2V/h). For $\gamma = 0.02$ the electron amplitude that comes out from the small ring is still coherent and constructive interference with the amplitude that travels in the lower arm of the large ring can take place. The current saturates to the maximum value e^2V/h already for small ϵ, reflecting the strong sensibility of the small ring to the presence of a dephasing field. We interpret this behavior as an IFM of the dephasing field. The current that comes out of the large ring has clear signatures of the coherence of the signal going out from the small asymmetric ring.

4.6 Conclusion

In this work we have considered the possibilities to implement interaction free measurements in electronic systems. By further developing the idea first suggested in Ref. [25] and directly inspired to the original proposal of A. Eliztur and L. Vaidman [1], we focus on studying and detecting the presence of a classical external random fluctuating electric or magnetic fields, which represent a common source of dephasing for quantum devices. The noise source, that randomizes the phase of electron traveling through, plays the role of absorption in the optical schemes, while the lost of coherence of the outgoing electrons mimics the photon absorption. The fraction of coherent signal going out from the device, or alternatively the visibility of the outgoing signal, represent the figures of merit that qualify the character of IFM. The study of this quantities allow to point out the difference between a "which-path" detection and an IFM, the former allowing only to detect the presence of a dephasing source, at the expense of a degradation of the visibility of the outgoing signal, whereas the latter allows a coherent detection of a dephasing source.

We have discussed three possible implementations of an IFM scheme. The first system is a concatenation of interferometers based on the integer quantum Hall interferometric architecture proposed in Ref. [30]. The dynamics of electrons traveling on the edge channels is exposed to the action of an external fluctuating field. We suggest to steer the propagation of one channel in the inner part of the Hall bar, where dephasing is minor or absent, and by separating and recombining many times the two channels we reproduce an electronic analogue of the high efficiency scheme proposed in optics by P. Kwiat *et al.* in Ref. [2]. Our device can represent a noise-sensitive coherent electron channel, that is able to detect the presence of an external fluctuating field and at the same time preserve the coherence of electrons traveling through the system. We have shown that, for a strong dephasing source, we manage to lose only an asymptotically negligible amount of coherent signal, by proper tuning the degree of admixture of the channels at the beam splitters. Moreover, the effect is very robust against small fluctuation about the exact value of adimixture required. Indeed, although the fraction of coherent signal is reduced in magnitude by the average process, its qualitative behavior is not affected.

The second system we have considered is based on a standard quantum Hall electronic Mach-Zehnder interferometer and assumes the presence of a quantized electron emitter. A very well time-resolved electronic wave packet is sent into a Mach-Zehnder interferometer in which an arm is affected by external classical noise. The packet travels at a precise speed and tests the region affected by noise many times, being split and recombined until it is allowed to escape the interferometer and recollected. The entire sequence can be mapped in the concatenation in the space domain that characterizes the noise-sensitive coherent electron channel previously described, and the same results and conclusions apply to this system. It has the advantage that it is experimentally much easier to realize, since it is based on a system already available.

The last system we have considered is a double ring structure based on the proposal suggested in Ref. [25]. There, the authors consider an Aharonov-Bohm chiral ring in which a localized source of noise affect one arm of the ring and studied the fraction of coherent signal that goes out from the device. However, such a quantity is not measurable in that setup. We suggest to embed the chiral AB ring in one arm of a larger AB ring and measure the total current flowing through the device as a figure of merit of the coherence of the signal that goes out from the small chiral AB ring. Such a setup has the advantage to overcome the difficulties arising from concatenating many interrogation steps, necessary in order to achieve a high efficiency IFM in the noise-sensitive coherent electron channel, or from dealing with very precise time-resolved electronics, on which our second proposal is based.

We point out here that the IFM can be designed also in case an absorption mechanism takes place and the same results obtained with a dephasing source apply. All the different implementations described can find useful applications in quantum coherent electronics and quantum computations, where the coherence of the signals is always threatened by the presence of fluctuating external fields.

References

[1] A. Elitzur and L. Vaidman, Found. Phys. **23**, 987 (1993)

[2] P. Kwiat, H. Weinfurter, T. Herzog, A. Zeilinger, M. A. Kasevich, Phys. Rev. Lett. **74**, 4763 (1995)

[3] T. Tsegaye, E. Goobar, A. Karlsson, G. Björk, M. Y. Loh, and K. H. Lim, Phys. Rev. A **57**, 3987 (1998)

[4] G. White, J. R. Mitchell, O. Nairz, and P. Kwiat, Phys. Rev. A **58**, 605 (1998)

[5] E. H. du Marchie van Voorthuysen, Am. J. Phys. **64**, 1504 (1996)

[6] M. Hafner and J. Summhammer, Phys. Lett. A **235**, 563 (1997)

[7] P. Kwiat, A. G. White, J. R. Mitchell, O. Nairz, G. Weihs, H. Weinfurter, and A. Zeilinger, Phys. Rev. Lett. **83**, 4725 (1999)

[8] H. Paul and M. Pavicic, Int. J. of Th. Phys., **35** 2085 (1996); J. Opt. Soc. Am. B **14**, 1275 (1997); Found. of Phys. , **28** 6 (1998).

[9] J.-S. Jang, Phys. Rev. A **59**, 2322 (1999).

[10] S. Inoue and G. Björk, J. Opt. B: Quantum Semiclass. Opt. **2** 338 (2000).

[11] V. Giovannetti, S. Lloyd, and L. Maccone, Opt. Exp. **14**, 8622 (2006)

[12] M. O. Goerbig, Eprint arXiv:0909.1998.

[13] Y. Ji, Y. Chung, D. Sprinzak, M. Heiblum, D. Mahalau, and H. Shtrikman, Nature (London) **422**, 415 (2003)

[14] I. Neder, M. Heiblum, Y. Levinson, D. Mahalu, and V. Umansky, Phys. Rev. Lett. **96**, 016804 (2006)

[15] L. V. Litvin, H. -P. Tranitz, W. Wegscheider, and C. Strunk, Phys. Rev. B **75**, 033315 (2007).

[16] P. Roulleau, F. Portier, D. C. Glattli, P. Roche, A. Cavanna, G. Faini, U. Gennser, and D. Mailly, Phys. Rev. B **76**, 161309(R) (2007).

[17] I. Neder, F. Marquardt, M. Heiblum, D. Mahalu, and V. Umansky, Nat. Phys. **3**, 534 (2007).

[18] P. Samuelsson, E. V. Sukhorukov, ans M. Büttiker, Phys. Rev. Lett. **92**, 026805 (2004).

[19] I. Neder, N. Ofek, Y. Chung, M. Heiblum, D. Mahalu, and V. Umansky, Nature (London) **448**, 333 (2007).

[20] J. Gabelli, , G. Fève, J.-M. Berroir, B. Pla?ais, A. Cavanna, B. Etienne, Y. Jin, and D. C. Glattli, Science **313**, 499 (2006)

[21] G. Fève, A. Mahé, J.-M. Berroir, T. Kontos, B. Pla?ais, D. C. Glattli, A. Cavanna, B. Etienne, and Y. Jin, Science **316**, 1169 (2007)

[22] M. Moskalets, P. Samuelsson, and M. Büttiker, Phys. Rev. Lett. **100**, 086601 (2008)

[23] J. Splettstoesser, S. Ol'khovskaya, M. Moskalets, and M. Büttiker Phys. Rev. B **78**, 205110 (2008)

[24] G. S. Paraoanu, Phys. Rev. Lett. **97**, 180406(2006).

[25] E. Strambini, L. Chirolli, V. Giovannetti, F. Taddei, R. Fazio, V. Piazza, and F. Beltram, Eprint arXiv:.....

[26] C. H. Wu and D. Ramamurthy, Phys. Rev. B **65**, 075313 (2002).

[27] F. Marquardt, and C. Bruder, Phys. Rev. B **65**, 125315 (2002);

[28] F. Marquardt, and C. Bruder, Phys. Rev. B **68**, 195305 (2003);

[29] F. Marquardt, and C. Bruder, Phys. Rev. Lett. **92**, 56805 (2004).

[30] V. Giovanetti, F. Taddei, D. Frustaglia, and R. Fazio, Phys. Rev. B **77**, 155320 (2008)

[31] B. Szafran and F. M. Peeters, Phys. Rev. B **72**, 165301 (2005)

[32] B. Szafran and F. M. Peeters, Europhys. Lett. **70**, 810 (2005)

[33] E. Strambini, V. Piazza, G. Biasiol, L. Sorba, and F. Beltram, Phys. Rev. B **79**, 195443 (2009)

[34] M. Büttiker, Y. Imry, R. Landauer, and S. Pinhas, Phys. Rev. B **31**, 6207 (1985)

[35] M. Büttiker, Phys. Rev. B **38**, 9375 (1988)

5. Scanning probe imaging of chiral charge flow in graphene

We theoretically propose to directly observe the chiral nature of charge carriers in graphene mono- and bilayers within a controlled scattering experiment. The charge located on a capacitively coupled scanning probe microscope (SPM) tip acts as a scattering center with controllable position on the graphene sheet. Unambiguous features from the chirality of the particles in single and bilayer graphene arise in the ballistic transport in the presence of such a scattering center. To theoretically model the scattering from the smooth potential created by the SPM tip, we derive the space-dependent electron Green function in graphene and solve the scattering problem within first-order Born approximation. We calculate the current through a device with an SPM tip between two constrictions (quantum point contacts) as a function of the tip position. [1]

5.1 Introduction

The isolation of few and single layer graphene [1–3], the two-dimensional carbon allotrope, triggered tremendous research activities (for a review, see [4]). Graphene is technologically of high interest [5–7], as it exhibits large mean-free paths and is chemically stable. The material is also very appealing for fundamental scientific research; since the conduction electrons in graphene behave like chiral massles Dirac particles [2, 3, 8], many concepts of solid-state physics are now being reconsidered for pseudo-relativistic carriers while at the same time, effects known from relativistic quantum mechanics can be found in solid state physics. Examples for this are the unusual energies of the Landau levels and the Klein paradox [8]. Moreover, long spin relaxation lengths [9] make graphene an interesting system for spintronics [10] and spin-based quantum information processing [11].

The high carrier mobility of graphene has lead to an active discussion of impurity scattering. Currently, it is assumed that scattering from Coulomb potentials [12–21] limits the conduction electron mobility, while short-ranged defects are less relevant [22].

In the following, we discuss the possibility for a controlled experiment to test whether the charge carriers in graphene behave like chiral particles in a scattering event. We propose to use the method of mapping electron flow by scanning probe microscopy (SPM) as developed and applied to two-dimensional electron gases (2DEGs) in semiconductors by the Westervelt group [23]. Topinka *et al.* [24, 25] demonstrated that coherent electron

---

[1] This chapter has been published in Physical Review B **77**, 115433 (2008).

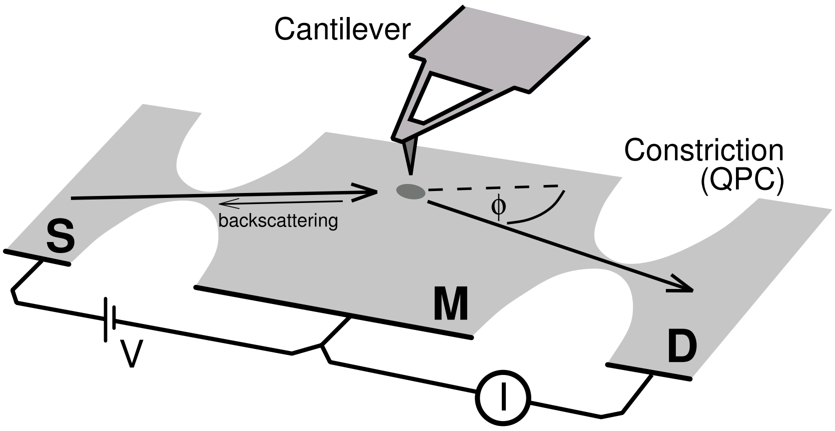

Figure 5.1: The proposed setup. An applied bias voltage V between the source S and the middle region M injects a current into the graphene sheet. The injected electrons scatter from an artificial scatterer created by a SPM tip above the surface. The flux of electrons that are coherently scattered into the drain D can be detected in the drain current I.

flow in a 2DEG formed in a GaAs/GaAlAs heterostructure can be imaged directly by placing a charged SPM tip on top of the sample. The tip, being capacitively coupled to the sample, repels the conduction electrons beneath, forming a circular scatterer with a precisely controllable position. By scanning the tip over the conductor, the conductance of the sample is modified depending on the current density beneath. By putting the SPM tip directly behind a constriction (quantum point contact, QPC) [24, 25], the dominant mechanism of the conductance change is direct backscattering through the QPC next to the source, see Fig. 5.1. In single layer graphene, this backscattering is forbidden [8], and therefor one can not expect any resistance change between the respective contacts S and M in such a setting. To actually use forward scattering from the tip, one might consider putting the tip *in front* of the constriction. Such a setup, however, suffers from the uncontrolled direction of propagation of the incoming particles. To control the direction of propagation of in- and outgoing particles, i.e., the scattering angle, we propose to use two constrictions (QPCs), as in Ref. [26]. By applying a voltage V between the regions S and M a current is injected into the middle region (M). The coherent scattering from one QPC to the other gives rise to a measurable current I in the drain D (or, alternatively, a voltage between M and D [27]). The middle region M is supposed to be large, acting as a reservoir, absorbing all electrons that are not scattered into the drain D. Such an experiment could directly probe the differential scattering cross section for pseudo-relativistic chiral particles, and thus demonstrates the chiral nature of the particles.

5.2 Green's function in graphene

For the microscopic description of scattering, and in the closely related Coulomb impurity problem [28], the method of partial-wave expansion was adapted [21, 22, 29, 30]. This method is primarily suitable for strong short-ranged potentials such as impurities. To describe the scattering from the weak potential created by a SPM tip, we apply the method of first-order Born approximation by deriving the Green functions for single and bilayer graphene, in real space representation [29].

For single layer graphene, the free Dirac Hamiltonian for the envelope wave function at the K-point is given by $H = -i\hbar v_F(\sigma_x\partial_x + \sigma_y\partial_y)$ and in cylindrical coordinates $\mathbf{r} = (r, \phi)$ by

$$H = -i\hbar v_F \begin{bmatrix} 0 & e^{-i\phi}(\partial_r - \frac{i}{r}\partial_\phi) \\ e^{+i\phi}(\partial_r + \frac{i}{r}\partial_\phi) & 0 \end{bmatrix} . \tag{5.1}$$

The scattering solution of the Dirac equation $[H + U(\mathbf{r})]\psi = \mathbf{E_k}\psi$, with $E_k = \hbar v_F k$, can be constructed using the Green function

$$G(\rho) = -\frac{\mathbf{i}}{\mathbf{4}}\frac{\mathbf{k^2}}{\mathbf{E_k}} \begin{bmatrix} H_0(k\rho) & -iH_{-1}(k\rho)e^{-i\theta} \\ iH_1(k\rho)e^{i\theta} & H_0(k\rho) \end{bmatrix} , \tag{5.2}$$

where $\rho = \mathbf{r} - \mathbf{r}' = (\rho, \theta)$. The Green function is a solution of $(H - E)G = -\delta(\rho)$, satisfying the outgoing radiation condition; thus the use of the n-th order Hankel function $H_n(z) \equiv H_n^{(1)}$. The functional form of the Green function is consistent with Ref. [31]. Since the Dirac Hamiltonian is formally closely related to the Rashba spin-orbit interaction, the derivation of the Green function in Eq. (5.2) is analogous to Ref. [32, 33].

The idealized scattering experiment is depicted in Fig. 5.2. A chiral plane wave $\psi_0(\mathbf{r}) = \mathbf{e^{ikx}[1, 1]^T}$ propagating along the (so chosen) x-axis hits the scattering potential. After the interaction with the potential, a detector measures the flux of the scattered wave as function of the deflection angle ϕ. Within first-order Born approximation, the total wave function $\psi(\mathbf{r})$ of an electron which scatters at a potential $U(\mathbf{r})$ is given by $\psi(\mathbf{r}) = \psi_\mathbf{0}(\mathbf{r}) + \int \mathbf{d^2r'G(r - r')U(r')}\psi_\mathbf{0}(\mathbf{r'})$. Far away from the scattering center the wave function has the asymptotic form $\psi(\mathbf{r}) = \psi_\mathbf{0}(\mathbf{r}) + \mathbf{f}(\phi)\, \mathbf{e^{ikr}}\, [\mathbf{1}, \mathbf{e^{i\phi}}]^\mathbf{T}/\sqrt{\mathbf{r}}$. The scattered wave describes a chiral circular outgoing wave. The scattering amplitude is given by

$$f(\phi) = -e^{-i\frac{\phi}{2}} \sqrt{\frac{ik^3}{2\pi}} \cos\frac{\phi}{2}\, \frac{U(\mathbf{q})}{E_k}, \tag{5.3}$$

with the Fourier transform $U(\mathbf{q}) = \int d^2r'\, U(\mathbf{r'})\, \mathbf{e^{iqr'}}$. The orientation of the vector $\mathbf{q} = \mathbf{k}(\mathbf{e_k} - \mathbf{e_r})$ of the momentum transfer during the scattering process is determined by the unit vectors $\mathbf{e_r}$ and $\mathbf{e_k}$ in r and k direction, while its magnitude is given by $q = 2k\sin(\phi/2)$. The functional form of the scattering amplitude is in close analogy to non-relativistic 2-dimensional scattering [35]. Two main differences appear: First, the prefactor $e^{-i\phi/2}\cos\frac{\phi}{2}$ [29] leads to the absence of any backscattering at potentials, irrespective of the potential

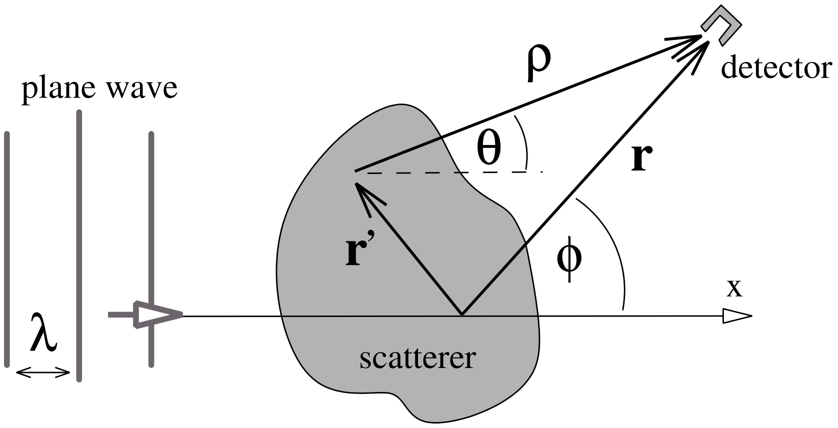

Figure 5.2: Formulation of the scattering problem: An incoming plane wave propagating along the x-direction hits the scattering potential. A detector measures the outgoing flux of the scattered wave as function of the deflection angle ϕ.

shape. Second, the forward scattering is enhanced by a factor of two compared to classical electrons. In gapped 2DEGs, scattering at potentials smaller than the Fermi wave length is dominated by s-wave scattering. For chiral particles in graphene, the free angular momentum eigenstates bear half-integer angular momentum related to the appearance of a Berry phase of π [12]. Therefore, the scattering amplitude is dominated by states with orbital angular momentum $+1/2$ and $-1/2$. In backward direction, the interference of the two states is destructive, leading to a suppression of scattering. In forward direction the interference is constructive, enhancing the scattering amplitude by a factor of 2. For scatterers larger than the Fermi wave length (beyond the range of validity of the Born approximation) one can expect that the enhancement of forward scattering becomes non-universal, depending on the details of the potential.

5.3 Stepwise cylindrical potential

By comparison with the exactly solvable problem of a stepwise constant potential, the range of validity for the Born approximation can be estimated as $(kR)^2 \lesssim E_k/U_0$, where R and U_0 denote the characteristic potential size and strength. As an interesting side note, for the physically relevant Coulomb potential, the first-oder Born approximation generates accidentally good results, in three as well as in two dimensions [35].

When we restrict the calculation to circularly symmetric potentials, the scattering amplitude Eq. (5.3) can be further simplified using

$$U(\mathbf{q}) = 2\pi \int dr'\, r'\, J_0(qr')\, U(r')\,. \tag{5.4}$$

The integral in Eq. (5.4) can be solved analytically for a variety of different scattering

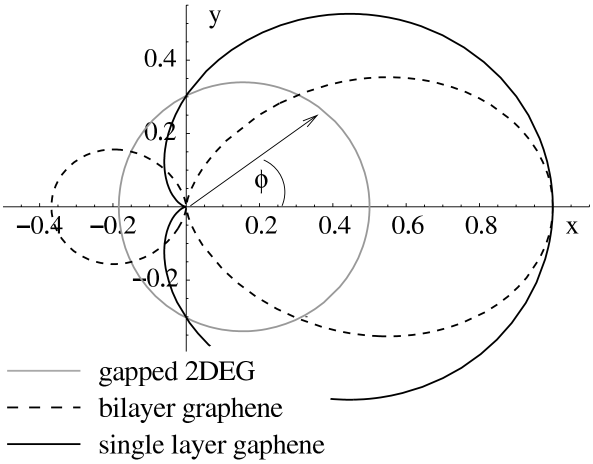

Figure 5.3: Differential cross section normalized by $2\pi(kR)^4(U_0/E)^2$ in units of $1/k$ for a circular scatterer of Gaussian shape. For single layer graphene, the Berry phase of π prohibits backscattering while for bilayer graphene, it the Berry phase of 2π prohibits rectangular deflection. The radius of the scatterer is chosen $kR = 0.5$ for this plot.

potentials, including an unscreened and the exponentially screened Coulomb potential, the stepwise constant potential, potentials of Lorentzian and Gaussian forms, and the potential of a point charge above the graphene sheet.

In graphene bilayers the charge carriers behave like massive gapless Dirac fermions. To compute the Green function, one can directly make an ansatz motivated by the observation that the operators $a = -ie^{-i\phi}(\partial_r - \frac{i}{r}\partial_\phi)$ and $a^\dagger = -ie^{i\phi}(\partial_r + \frac{i}{r}\partial_\phi)$ in Eq. (5.1) act as a type of ladder operators on the Hankel functions, i.e., $a^\dagger H_n(k\rho)e^{in\theta} = +ikH_{n+1}(k\rho)e^{i(n+1)\theta}$ and $aH_n(k\rho)e^{in\theta} = -ikH_{n-1}(k\rho)e^{i(n-1)\theta}$ [36]. Note the relative minus sign for $a^\dagger$ and a. With this representation, the Hamiltonian for the bilayer as derived in Ref. [37] is

$$H = -\frac{\hbar^2}{2m}\begin{bmatrix} 0 & aa \\ a^\dagger a^\dagger & 0 \end{bmatrix}, \tag{5.5}$$

and the basic functional structure of the Greens function for particle energy $E_k = \hbar^2k^2/2m$ directly follows as

$$G(\rho) = -\frac{\mathbf{i}\,\mathbf{k^2}}{\mathbf{4}\,\mathbf{E_k}}\begin{bmatrix} H_0(k\rho) & H_{-2}(k\rho)e^{-2i\theta} \\ H_2(k\rho)e^{2i\theta} & H_0(k\rho) \end{bmatrix}. \tag{5.6}$$

The overall prefactor can be deduced using [38] that $i/4(k^2 + \nabla^2)H_0(k\rho) = -\delta(\rho)$ and the fact that $aa^\dagger = a^\dagger a = -\nabla^2$. Using the Green function Eq. (5.6), we now construct the scattering wave function. Within first order Born approximation, the wave function takes the asymptotic form $\psi(\mathbf{r}) = \psi_0(\mathbf{r}) + f(\phi)e^{ikr}\left[1, -e^{2i\phi}\right]^T/\sqrt{r}$. The scattering amplitude $f(\phi)$ is then given by Eq. (5.3) with the substitution $\phi \to 2\phi$.

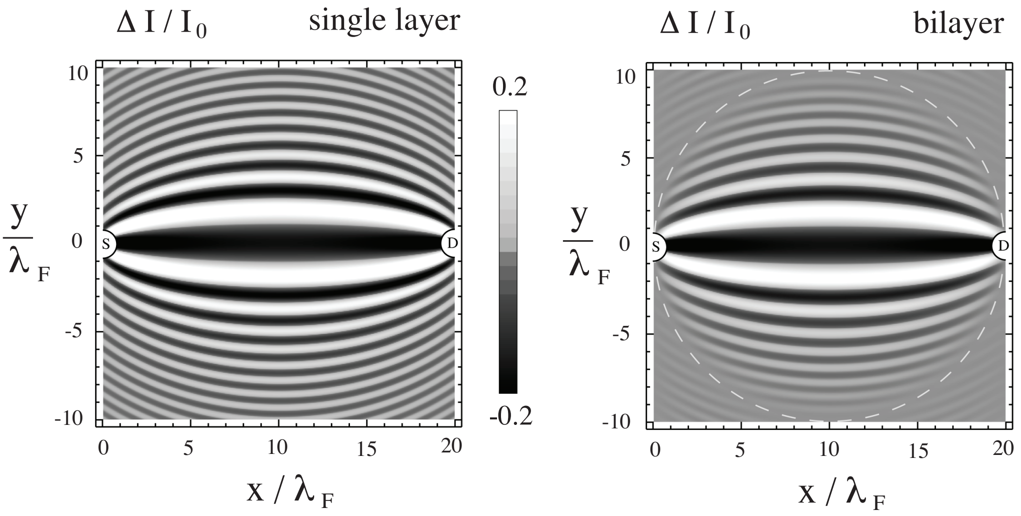

Figure 5.4: Relative change $\Delta I/I_0$ of the drain (D) current as a function of the tip position (x, y) in units of λ_F. The existence of two possible trajectories, one directly from source (S) to drain, the other via the scatterer at (x, y), generates an interference pattern. Since scattering under an angle of $\pi/2$ is forbidden for a bilayer, a circle without signal (dashed white line) appears. The scattering potential radius and strength was chosen to be $Rk = 1$, and $U_0/E = 0.3$ respectively.

For a circularly symmetric potential, the scattering amplitude can again be simplified further by using Eq. (5.4). The cases of non-relativistic particles in a 2DEG ($j = 0$), and of single layer ($j = 1$) and bilayer ($j = 2$) graphene are distinguished by their respective factors $e^{-ij\phi/2}\cos(j\phi/2)$ which are due to the Berry phase $j\pi$ acquired during the adiabatic propagation along a closed orbit. For a Gaussian potential $U(\mathbf{r}) = \mathbf{U_0 e^{-r^2/2R^2}}$, the resulting cross section $d\sigma/d\phi = |f(\phi)|^2$ becomes

$$\frac{d\sigma}{d\phi} \propto e^{-[2Rk\sin(\phi/2)]^2}\cos^2\frac{j\phi}{2}. \tag{5.7}$$

We plot this result in Fig. 5.3. While the Berry phase prohibits backscattering in single layer graphene, backscattering is allowed in bilayer graphene, while scattering by an angle of $\pm\pi/2$ is forbidden in bilayers.

These results are equivalent to the calculation of the scattering cross section via the k-dependent Greens function as done in the group of Fal'ko [29, 34].

5.4 Imaging chiral charge flow

To describe the SPM experiment as shown in Fig. 5.1, we model the potential of the charged tip as a Gaussian. Moreover, we consider the QPC at the source S as point source

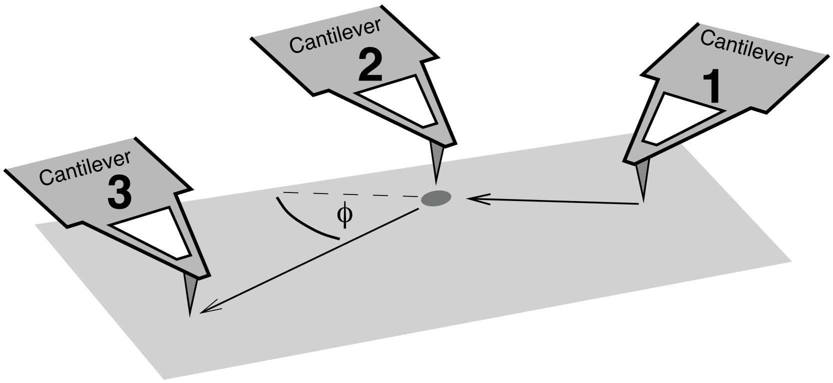

Figure 5.5: Alternative setup: Instead of QPCs, one can also inject and extract the current by 2 additional SPM-tips.

of chiral electrons (as determined by the Green function) at position $(x, y) = (0, 0)$. In the proximity of the scatterer, we approximate the incoming spherical wave ψ (centered around the QPC) as plane wave, and derive the scattered outgoing spherical wave (centered around the SPM-tip). The drain current I is calculated as the current at the location of the drain QPC at $(x, y) = (d, 0)$, where d is the distance between the source and drain QPCs. The normal component of the current is given by $J_x = v_F \psi^\dagger \sigma_x \psi$ for single layer, and by $J_x = -\frac{\hbar}{m} \mathrm{Im}[\psi^\dagger(\sigma_x \partial_x + \sigma_y \partial_y)\psi]$ for bilayer graphene. Here ψ labels the sum of the incoming and outgoing spherical wave. In Fig. 5.4, we plot the relative change of the drain current $\Delta I/I_0$ due to the presence of the tip as a function of the tip position (x, y). Here, $\Delta I = I - I_0$ where I_0 is the current in the absence of the SPM tip.

In the presence of the scatterer, two ballistic trajectories lead from source to drain: either the electrons travel directly form the source (S) to the drain (D), or they scatter at the SPM tip potential and from there into the drain (D). The spatial pattern due to the interference between these two trajectories reveals the Fermi electron wave length $\lambda_F = 2\pi/k = h v_F/E_F$, the degree of coherence, as well as the scattering phase [39].

The required scattering angle to pass from source to drain is a function of the tip position relative to source and drain. Therefore this experiment realizes to some extent an angle-resolved measurement of $d\sigma/d\phi$. We assume the middle region (M) of the graphene sample to be large (but not larger than the coherence length l_ϕ), i.e., $R \ll d \ll l_\phi$, so that scattering events with other angles will not significantly contribute to the drain current. For single layer graphene one can expect a rapid loss of signal if $\phi > \pi/2$, as scattering by larger angles is strongly suppressed. For bilayer graphene, one can expect forward as well as backscattering. However, a scattering angle of $\phi = \pi/2$ is forbidden. Therefore, a circular line appears (according to Thales' theorem), indicating a total absence of scattering. In contrast, for a conventional semiconductor-based 2DEG, the intensity distribution is much more homogeneous.

As shown in recent experiments [40], the minimal tip-induced potential with is about 300 nm at a potential height of 1 meV. At a Fermi energy of 10 meV in the graphene sheet, the range ov validity of the first order Born approximation $(kR)^2 \lesssim E_k/U_0$ is violated by about one order of mangitude. This violation leads to deviations mainly for forward scattering. Since in the proposed experiment the large angle scattering is of primary interest, first order Born approximation is still expected to deliver qualitatively correct results.

Furthermore, sample roughness and disorder will also significantly modify this idealized experimental result, as already observed in 2DEGs [23–25]. Even so, if one assumes that small-angle disorder scattering is dominant, then disorder will be of most importance, when the tip is directly in between the source and the drain. With increasing scattering angle, the experimental result will be more and more robust against weak disorder. The assumption of small-angle disorder scattering is consistent with the observations in semiconductor 2DEGs and is expected from the measurements of large mean free paths (it is also predicted in the large scatterer limit of our calculation).

Our calculation was done for one of the two degenerate valleys (the Dirac point at momentum K). For the other valley (K'), only the sign of ϕ must be reversed in Eq. (5.1). Therefore, the results for the scattering cross section Eq. (5.7) and the current (Fig. 5.4) remain unchanged for K', as they are even functions of ϕ. Therefore, we expect these results to persist for arbitrary incoherent mixtures of K and K' without any loss of interference visibility.

5.5 Conclusion

To test the ballistc curent through a graphene sheet, it would be aslo possible to use a multi-tip setup, as were developed recently [41], see Fig. 5.5. Thereby one contacted SPM-tip injects the current in the graphene, and another contacted tip extract the current. The third tip, ehich is coupled only capacitively creates the scattering center. The small crossections of the contacts on the graphene ensure the angular resolution of the scattering experiment.

In conclusion, we propose to test the chirality of electrons in graphene mono- and bilayers in potential scattering, probed by an SPM tip in a transport setting with two QPCs. We describe the scattering within first-order Born approximation, which requires the derivation of the electron Green function in real space.

References

[1] K. S. Novoselov, A. K. Geim, S. V. Morozov, D. Jiang, Y. Zhang, S. V. Dubonos, I. V. Grigorieva, and A. A. Firsov, Science **306**, 666 (2004).

[2] K. S. Novoselov, A. K. Geim, S. V. Morozov, D. Jiang, M. I. Katsnelson, I. V. Grigorieva, S. V. Dubonos, and A. A. Firsov, Nature **438** 197 (2005).

[3] Y. Zhang, Y.-W. Tan, H. L. Stormer, and P. Kim, Nature **438**, 201 (2005).

[4] A. K. Geim and K. S. Novoselov, Nature Mater. **6**, 183 (2007).

[5] Z. Chen, Y.-M. Lin, M. J. Rooks, P. Avouris, arXiv:cond/mat/0701599.

[6] M. Y. Han, B. Ozyilmaz, Y. Zhang, P. Kim, Phys. Rev. Lett. **98**, 206805 (2007).

[7] M. C. Lemme, T. J. Echtermeyer, M. Baus, H. Kurz, IEEE Electron Device Lett. **28**, 282 (2007).

[8] M. I. Katsnelson, K. S. Novoselov, and A. K. Geim, Nature Phys. **2**, 620 (2006).

[9] N. Tombros, C. Jozsa, M. Popinciuc, H. T. Jonkman, B. J. van Wees, arXiv:0706.1948.

[10] E. W. Hill, A. K. Geim, K. Novoselov, F. Schedin, and P. Blake, arXiv:0704.3165.

[11] B. Trauzettel, D. V. Bulaev, D. Loss, and G. Burkard, Nature Physics **3**, 192 (2007), cond-mat/0611252.

[12] D. P. DiVincenzo and E. J. Mele, Phys. Rev. B **29**, 1685 (1984).

[13] T. Ando, J. Phys. Soc. Japan **75**, 074716 (2006).

[14] M. I. Katsnelson, Phys. Rev. B **74**, 201401(R) (2006).

[15] R. R. Biswas, S. Sachdev, and D. T. Son, arXiv:0706.3907.

[16] B. I. Shklovskii, arXiv:0706.4425.

[17] S. Adam, E. H. Hwang, V. M. Galitski, S. Das Sarma, arXiv:0705.1540; E. H Hwang, S. Adam, and S. Das Sarma, Phys. Rev. Lett. **98**, 186806 (2007).

[18] K. Nomura and A. H. MacDonald Phys. Rev. Lett. **98**, 076602 (2007).

[19] P. M. Ostrovsky, I. V. Gornyi, and A. D. Mirlin, Phys. Rev. B **74**, 235443 (2006).

[20] N. M. R. Peres, F. Guinea, and A. H. Castro Neto, Phys. Rev. B **73**, 125411 (2006).

[21] M. I. Katsnelson, and A. K. Geim, arXiv:0706.2490.

[22] M. I. Katsnelson, arXiv:0706.1351.

[23] M. A. Topinka, R. M. Westervelt, and E. J. Heller, Phys. Today **56**, 12 (2003).

[24] M. A. Topinka, B. J. LeRoy, S. E. J. Shaw, E. J. Heller, R. M. Westervelt, K. D. Maranowski, and A. C. Gossard, Science **289**, 2323 (2000).

[25] M. A. Topinka, B. J. LeRoy, R. M. Westervelt, S. E. J. Shaw, R. Fleischmann, E. J. Heller, K. D. Maranowski, and A.C. Gossard, Nature **410**, 183 (2001).

[26] K. E. Aidala, R. E. Parrott, E. J. Heller, and R. M. Westervelt, Physica E **34**, 409 (2006) [arXiv:cond-mat/0603035]; K. E. Aidala, R. E. Parrott, T. Kramer, E. J. Heller, R. M. Westervelt, M. P. Hanson, and A. C. Gossard, arXiv:0704.1491.

[27] H. van Houten, C. W. J. Beenakker, J. G. Williamson, M. E. I. Broekaart, P. H. M. van Loosdrecht, B. J. van Wees, J. E. Mooij, C. T. Foxon and J. J. Harris, Phys. Rev. B **39**, 8556 (1989).

[28] V. M. Pereira, J. Nilsson, and A. H. Castro Neto, arXiv:0706.2872.

[29] D. S. Novikov, arXiv:0706.1391.

[30] J. Cserti, A. Palyi, and C. Peterfalvi, arXiv:0706.4034.

[31] C. Bena, arXiv:0706.4111.

[32] J. D. Walls, J. Huang, R. M. Westervelt, and E. J. Heller, Phys. Rev. B **73**, 035325 (2006).

[33] J. Cserti, A. Csordas, and U. Zülicke, Phys. Rev. B **70**, 233307 (2004); A. Csordás, J. Cserti, A. Pályi and U. Zülicke, Eur. Phys. J. **B** 54, 189 (2006)

[34] V. V. Cheianov, and V. I. Fal'ko, Phys. Rev. Lett. **97**, 226801 (2006).

[35] I. R. Lapidus, Am. J. Phys. **50**, 45 (1982); G. Barton, Am. J. Phys. **51**, 420 (1983);

S. K. Adhikari, Am. J. Phys. **54**, 362 (1986).

[36] Note that $e^{-i\phi}(\partial_r - \frac{i}{r}\partial_\phi)H_n(k\rho)e^{in\phi} = e^{-i\theta}(\partial_\rho - \frac{i}{\rho}\partial_\theta)H_n(k\rho)e^{in\phi}$ due to translational invariance.

[37] E. McCann and V. I. Fal'ko, Phys. Rev. Lett. **96** 086805 (2006).

[38] P. M. Morse and H. Feshbach, *Methods of Theoretical Physics*, McGraw-Hill, New York, 1953.

[39] B. J. LeRoy, A. C. Bleszynski, K. E. Aidala, R. M. Westervelt, A. Kalben, E. J. Heller, S. E. J. Shaw, K. D. Maranowski, and A. C. Gossard, Phys. Rev. Lett. **94**, 126801 (2005).

[40] A. E. Gildemeister, T. Ihn, M. Sigrist, K. Ensslin, D. C. Driscoll and A. C. Gossard, Phys. Rev. B **75**, 195338 (2007).

[41] P. Jaschinsky, P. Coenen, G. Pirug, and B. Voigtländer, Rev. Sci. Instrum. 77, 093701 (2006).

6. Photon beam splitting with superconducting resonators

We consider a system of two superconducting transmission line resonators coupled by an externally driven SQUID. In the low temperature regime, each of the two resonators can be described by its lowest frequency bosonic degree of freedom and it can formally quantized as a harmonic oscillator. The SQUID dynamics can be effectively described by an externally controllable inductance that mediates a quadratic interaction between the two transmission line resonator. Such a system is suitable for the implementation of a qubit in which one photon is shared between the two superconducting transmission line resonators. In the direction of linear optics quantum computation we consider a beam splitting operation in this system. An equal weight superposition of the states $|1\rangle_1|0\rangle_2$ and $|0\rangle_1|1\rangle_2$ is obtained by applying a driving to the initial state $|1\rangle_1|0\rangle_2$. We study the quality of the rotating wave approximation by comparing it with the exact solution of the time dependent problem. [1]

6.1 Introduction

One of the earliest schemes for quantum computing is based on the implementation of a quantum bit with two optical modes that share one photon [1]. The two orthogonal polarization states of light, horizontal and vertical polarization, represent two independent optical modes that can constitute two quantum logical states of one photon. Optical systems are particularly suited for long-distance quantum communication and photon interference can be easily observed. Among the appealing quantum computing schemes that have been proposed, linear optics quantum computation [2] plays a fundamental role. Efficient quantum information processing can be obtained by means of solely single photon sources, beam splitters, phase shifters and photodetectors, with no need of direct non-linear coupling between the two optical modes. The computational schemes exploit feedback from photodetectors and are particularly robust against errors detector inefficiency and photon loss.

The achievement of strong coupling between a single photon and a superconducting qubit [3] and the realization of arbitrary photon states in superconducting transmission line resonators (STL resonators)[4] open the possibility to investigate quantum information processing in circuit quantum electrodynamics, a field in which quantum optics and solid state physics merge together and provide a playground to study quantum phenomena. In particular, STL resonators can constitute independent bosonic modes that can be used to implement linear optics quantum computing schemes. One can consider a system of two STL resonators, 1 and 2, and assign the logical qubit state $|\hat{0}\rangle$ to the state $|1\rangle_1|0\rangle_2$, with one photon in the first resonator, and the logical qubit state $|\hat{1}\rangle$ to the state $|0\rangle_1 1\rangle_2$, with one photon in the second resonator. A generic qubit state is then given by a linear combination of these two fundamental states,

---

[1] This chapter is part of a manuscript in preparation by L. C., S. Kumar, G. Burkard and D. P. DiVincenzo.

$$|\psi\rangle = \alpha|1\rangle_1|0\rangle_2 + \beta|0\rangle_1 1\rangle_2. \tag{6.1}$$

One of the fundamental operations necessary for quantum processing with linear optics is the beam splitting operation. In the language of optics, it consists of a linear map between incoming modes and outgoing modes of the field. By identification of the incoming modes with the field operators of the two resonators at time $t = 0$, $a_1^\dagger$ and $a_2^\dagger$, and the outgoing modes with the field operators at time $t = \tau$, $a_1^\dagger(\tau)$ and $a_2^\dagger(\tau)$, with $a_i^\dagger(\tau) = U^\dagger(\tau)a_i^\dagger U(\tau)$, the beam splitting operation can be written as

$$\begin{pmatrix} a_1^\dagger(\tau) \\ a_2^\dagger(\tau) \end{pmatrix} = \begin{pmatrix} \cos\theta(\tau) & ie^{-i\varphi(\tau)}\sin\theta(\tau) \\ -ie^{i\varphi(\tau)}\sin\theta(\tau) & \cos\theta(\tau) \end{pmatrix} \begin{pmatrix} a_1^\dagger \\ a_2^\dagger \end{pmatrix}, \tag{6.2}$$

for a given $\theta(\tau)$ and $\varphi(\tau)$. In a Bloch representation of the qubit, the state $|0\rangle$ is given by the north pole of a sphere and the state $|1\rangle$ by the south pole. A beam splitting operation consists in generating a state on the equatorial line $\theta = \pi/4$ of the sphere for a given azimuth φ, when starting, i.e., from the north pole.

In this work we consider a system of two STL resonators coupled by two superconducting quantum interference devices (SQUIDs) introduced in Ref. [5] and study a regime in which the SQUIDs behave as tunable linear inductances that provide a quadratic coupling between the two resonators. Such a scheme is suitable for the implementation of a beam splitting gate between the two qubit states. We study the regime in which the resonators constitute bosonic single modes and can be represented by two quantum harmonic oscillators quadratically coupled by an effective inductance that can be made time-dependent by an external driving.

6.2 Effective model

We start from the effective circuit depicted in Fig. 6.1, containing two LC series and a harmonically driven inductance $K(l)$, all shunted in parallel. Representing the circuit as a graph [6], we apply circuit theory to derive the classical Hamiltonian of the circuit. We define a tree constituted by the two capacitors C_1 and C_2 and the driven inductance $K(t)$, and consider the inductances L_1 and L_2 as chords (branches not belonging to the tree). We choose as independent conjugate dynamical variables the fluxes $\mathbf{\Phi} = (\Phi_1, \Phi_2)^T$ and the charges $\mathbf{Q} = (Q_1, Q_2)^T$ associated with the tree capacitances. The capacitance matrix $\mathbf{C} = \mathrm{diag}(C_1, C_2)$ and the time independent inductance matrix $\mathbf{L} = \mathrm{diag}(L_1, L_2)$

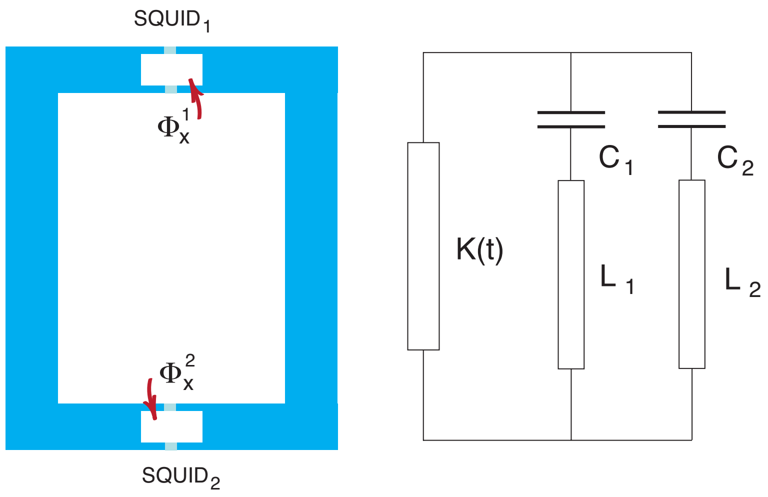

Figure 6.1: Schematics of the effective circuit representing two superconducting microwave resonators coupled by a time-dependent inductance. Each resonator is effectively described by a series of an inductance and a capacitance, with L_1 and L_2 the effective inductances and C_1 and C_2 the effective capacitances of the two resonators respectively. The coupling is mediated by a time-dependent effective inductance $K(t)$ that shunts the parallel of the two resonators.

are diagonal, whereas the term associated with the harmonically driven inductance $K(t)$ provides a time dependent coupling of the two fluxes. Assuming that $K(t) \ll L_1, L_2$, we define $\mathbf{M} \equiv \mathbf{M}_0 + \mathbf{M}(t)$, with $\mathbf{M}_0 = \mathbf{L}^{-1}\mathrm{diag}(1/L_1, 1/L_2)$ and

$$\mathbf{M}(t) = -\frac{K(t)}{L_1 L_2}\begin{pmatrix} \frac{L_2}{L_1} & 1 \\ 1 & \frac{L_1}{L_2} \end{pmatrix}. \tag{6.3}$$

See Appendix H for a derivation of the matrix $\mathbf{M}$. The classical time-dependent Hamiltonian can then be written as [6]

$$\begin{aligned} \mathcal{H} &= \frac{1}{2}\mathbf{Q}^T\mathbf{C}^{-1}\mathbf{Q} + \frac{1}{2}\mathbf{\Phi}^T\mathbf{M}_0\mathbf{\Phi} + \frac{1}{2}\mathbf{\Phi}^T\mathbf{M}(t)\mathbf{\Phi}, && (6.4) \\ &= \sum_{i=1,2}\left(\frac{Q_i^2}{2C_i} + \frac{\Phi_i^2}{2L_i}\right) - \frac{K(t)}{2}\left(\frac{\Phi_1}{L_1} + \frac{\Phi_2}{L_2}\right)^2. && (6.5) \end{aligned}$$

We assume that the harmonically driven inductance $K(t)$ is composed by a constant plus an oscillating term, $K(t) = K_0 + \delta K \cos(\omega_d t)$, and that both K_0 and δK can be separately addressed by means of external control and that each can be switched off independently. This provides complete freedom to dynamically couple and decouple the two resonators and perform the desired quantum gate operations.

6.2.1 Quantum Hamiltonian

Under the assumption that the time dependent driving is the smallest energy scale in the problem, we quantize the time independent problem in the usual way, by imposing commutation rules between canonically conjugate variables, $[\Phi_i, Q_j] = i\hbar\delta_{ij}$. We go a step further and directly second quantize the problem, by introducing annihilation and creation operators for the two modes of the field ($i = 1, 2$),

$$\Phi_i = \sigma_i \sqrt{\frac{\hbar}{2}}(a_i + a_i^\dagger), \tag{6.6}$$

$$Q_i = \frac{-i}{\sigma_i}\sqrt{\frac{\hbar}{2}}(a_i - a_i^\dagger), \tag{6.7}$$

with $\sigma_i = (L_i/C_i)^{1/4}$. We then define the two resonant harmonic frequencies $\omega_i = 1/\sqrt{L_i C_i}$ and split the Hamiltonian in a time-independent term $\mathcal{H}_0$, that describes the two harmonic modes separately,

$$\mathcal{H}_0 = \sum_{i=1,2} \hbar\omega_i \left(a_i^\dagger a_i + \frac{1}{2} \right), \tag{6.8}$$

and a time-dependent term $V(t)$, quadratic with respect to the components of the fields, a_i and $a_i^\dagger$, with $i = 1, 2$, that describes the interaction between the modes mediated by the externally driven inductance $K(t)$,

$$V(t) = \hbar f(t) \left(\lambda(a_1 + a_1^\dagger) + \frac{1}{\lambda}(a_2 + a_2^\dagger) \right)^2, \tag{6.9}$$

with $f(t) = -\sigma^2 K(t)/4L^2$ and $\lambda = (L_2\omega_1/L_1\omega_2)^{1/4}$ where $C = \sqrt{C_1 C_2}$ is a reference capacitance and $L = \sqrt{L_1 L_2}$ a reference inductance. The total Hamiltonian can then be written as

$$\mathcal{H}(t) = \mathcal{H}_0 + V(t). \tag{6.10}$$

By properly choosing the capacitances C_1 and C_2 and the inductances L_1 and L_2 we can set $\lambda = 1$, from which follows that

$$\frac{L_1}{L_2} = \frac{\omega_1}{\omega_2}. \tag{6.11}$$

6.3 Rotating wave approximation

The beam splitting problem is exactly solvable in the rotating wave approximation (RWA). Roughly speaking, it consists in neglecting the effect of terms that do not conserve the number of photons, like a_i^2 and $(a_i^\dagger)^2$. In order to perform a good approximation, we move to an interaction picture with respect to H_0 and study the effective dynamics induced by the interaction term $V_I(t) = e^{iH_0t/\hbar}V(t)e^{-iH_0t/\hbar}$, that is given by

$$\begin{aligned} V_I(t) &= f(t)\lambda^2\left(a_1^2e^{-2i\omega_it} + (a_1^\dagger)^2e^{2i\omega_it} + 2a_1^\dagger a_1\right) \\ &+ \frac{f(t)}{\lambda^2}\left(a_2^2e^{-2i\omega_it} + (a_2^\dagger)^2e^{2i\omega_it} + 2a_2^\dagger a_2\right) \\ &+ 2f(t)\left(a_1a_2e^{-i\bar{\omega}t} + a_1^\dagger a_2^\dagger e^{i\bar{\omega}t} + a_1a_2^\dagger e^{-i\Delta\omega t} + a_1^\dagger a_2e^{i\Delta\omega t}\right). \end{aligned} \tag{6.12}$$

We can get a deeper insight in the physics of the problem by studying the Fourier transform $V_I(\omega)$ of the potential $V_I(t)$, defined as

$$V_I(t) = \int_{-\infty}^{\infty}\frac{d\omega}{2\pi}e^{-i\omega t}V_I(\omega), \tag{6.13}$$

$$V_I(\omega) = \int_{-\infty}^{\infty}dte^{i\omega t}V_I(t). \tag{6.14}$$

We assume $f(t) = \bar{f} + \delta f\cos(\omega_dt)$, with $\omega_d = \Delta\omega = \omega_1 - \omega_2$, and study the limit $\Delta\omega \ll \omega_i$. By retaining only terms that produce an exchange of energy quanta of order $\Delta\omega$ and $2\Delta\omega$ we obtain a potential $\tilde{V}_I(\omega)$ that depends only on terms like $a_2^\dagger a_1$ and $a_1^\dagger a_2$. Back to the time domain we can cast the effective potential $\tilde{V}_I(t)$ in the form

$$\tilde{V}_I(t) = \hbar g_0(t)\left(\lambda^2a_1^\dagger a_1 + \frac{1}{\lambda^2}a_2^\dagger a_2\right) + \hbar g_1(t)a_1a_2^\dagger + \hbar g_1^*(t)a_1^\dagger a_2, \tag{6.15}$$

with the time-dependent interaction parameters $g_0(t)$ and $g_1(t)$ given by

$$g_0(t) = 2(\bar{f} + \delta f\cos(\Delta\omega t)), \tag{6.16}$$

$$g_1(t) = 2\bar{f}e^{-i\Delta\omega t} + \delta f(1 + e^{-2i\Delta\omega t}). \tag{6.17}$$

We then move to the interaction picture with respect to $\left(\lambda^2a_1^\dagger a_1 + 1/\lambda^2a_2^\dagger a_2\right)$ and obtain

$$\tilde{V}_{II}(t) = g(t)a_1a_2^\dagger + g^*(t)a_1^\dagger a_2, \tag{6.18}$$

with $g(t) = g_1(t)e^{-i\mathcal{G}_0(t)(\lambda^2-1/\lambda^2)}$ and $\mathcal{G}_0(t) \equiv \int_0^t dt'g_0(t')$.

Now many different approximation can be made. One can set $\bar{f} = 0$ and $\lambda = 1$, from which follows

$$\tilde{V}_{II}(t) = \delta f\left[a_1a_2^\dagger(1 + e^{-2i\Delta\omega t}) + a_1^\dagger a_2(1 + e^{2i\Delta\omega t})\right], \tag{6.19}$$

The terms oscillating at frequency $2\Delta\omega$ produce Bloch-Siegert oscillations [7, 8]. If we neglect the terms oscillating at frequency $2\Delta\omega$, the potential W becomes time-independent and the evolution operator is easily obtained and the beam-splitting operation is given by

$$U_I^{RWA}(t) = \exp\left(i\frac{2\delta f}{\Delta\omega}\sin(\Delta\omega t)(a_1^\dagger a_1 + a_2^\dagger a_2)\right)\exp\left(-i\delta ft(a_1a_2^\dagger + a_1^\dagger a_2)\right). \tag{6.20}$$

This result is valid only in the case $\delta f/\Delta\omega \ll 1$, since for a higher value of the ratio $\delta f/\Delta\omega$ the effect of the terms that oscillate at frequency $2\Delta\omega$ cannot be neglected. We can make a crude rotating wave approximation, which correspond to considering only the term proportional to $\delta(\omega)$ in the potential $V_I(\omega)$ Eq. (6.14).

$$U^{RWA}(t) \approx \exp\left(-i\delta f t(a_1 a_2^\dagger + a_1^\dagger a_2)\right). \tag{6.21}$$

This expression does not depend on $\Delta\omega$ and holds as long as $\Delta\omega \ll \omega_1, \omega_2$. It provides an approximation for the envelope of the oscillations induced by the driving.

6.3.1 Beam splitting fidelity in the RWA

We suppose to switch on the quadratic coupling between the two resonators at time $t = 0$ and that initially one of the two modes contains exactly one photon, resulting in the initial state

$$|\psi_i\rangle = a_1^\dagger|0\rangle_{12}, \tag{6.22}$$

with $|0\rangle_{12} = |0\rangle_1|0\rangle_2$. We then apply a pulse of duration τ to the initial state that propagates the state to $U(\tau)|\psi_i\rangle$. The final state we aim is, in the rotating frame,

$$|\psi_f\rangle = \frac{1}{\sqrt{2}}(a_1^\dagger + e^{-i\varphi}a_2^\dagger)|0\rangle_{12}, \tag{6.23}$$

for a generic phase φ. We then define the fidelity to be $\mathcal{F}(\tau) = |\langle\psi_f|U(\tau)|\psi_i\rangle|^2$. Both the evolution operators Eq. (6.20) and Eq. (6.21) produce the same result for the fidelity, because the number of photon is the same in the initial and final states. For the particular case $\varphi = \pi/2$ by direct evaluation the fidelity is found to be

$$\mathcal{F}(\tau) = \frac{1}{2}\left(1 + \sin(2\delta f\tau)\right). \tag{6.24}$$

For $2\delta f\tau = \pi/2$, we obtain $\mathcal{F}(\tau) = 1$, that is applying a driving for a time $\tau = \pi/4\delta f$ we obtain the state $\frac{1}{\sqrt{2}}(|1\rangle_1|0\rangle_2 - i|0\rangle_1|1\rangle_2)$, therefore obtaining the beam splitting operation. The Rabi frequency $\Omega_R = 2\delta f$ can be expressed as

$$\Omega_R = \frac{\delta K}{2L}\omega. \tag{6.25}$$

6.4 Equations of motion

In order to determine the quality of the rotating wave approximation, we calculate the fidelity of the beam splitting operation by numerically integrating the equation of motion. We start from the full time dependent Hamiltonian Eq. (6.10) and then move to the Heisenberg picture. We introduce a representation in terms of canonically conjugate quadratures $\boldsymbol{\xi} = (\hat{q}_1, \hat{q}_2, \hat{p}_1, \hat{p}_2)^T$, that are related the original fluxes and charges by

$(\hat{\Phi}_1, \hat{\Phi}_2, \hat{Q}_1, \hat{Q}_2)^T = \sqrt{\hbar} D_\sigma \boldsymbol{\xi}$, with the diagonal matrix $D_\sigma = \mathrm{diag}(\sigma_1, \sigma_2, 1/\sigma_1, 1/\sigma_2)$. We then introduce the vector of field operators $\mathbf{a} = (a_1, a_2, a_1^\dagger, a_2^\dagger)^T$ and relate the quadratures $\boldsymbol{\xi}$ to the creation and annihilation operators $\mathbf{a}$ by $\boldsymbol{\xi} = \Sigma \mathbf{a}$, with

$$\Sigma = \frac{1}{\sqrt{2}} \begin{pmatrix} 1 & 0 & 1 & 0 \\ 0 & 1 & 0 & 1 \\ -i & 0 & i & 0 \\ 0 & -i & 0 & i \end{pmatrix}, \tag{6.26}$$

and write the equations of motion for the field operators a_i and $a_i^\dagger$ in a compact form

$$\frac{d}{dt}\mathbf{a}(t) = \frac{i}{\hbar}[\mathcal{H}(t), \mathbf{a}(t)], \tag{6.27}$$

with the time-dependent field operator given by $\mathbf{a}(t) = U^\dagger(t)\mathbf{a}U(t)$ and the time evolution operator given by $U(t) = \mathcal{T} \exp\left(-\frac{i}{\hbar}\int^t dt' \mathcal{H}(t')\right)$. The equations of motion are explicitly given by,

$$\frac{d}{dt}\mathbf{a}(t) = iA(t)\mathbf{a}(t), \tag{6.28}$$

with the 4×4 real matrix $A(t)$ given by

$$A(t) = \begin{pmatrix} -\Omega & 0 \\ 0 & \Omega \end{pmatrix} + 2f(t) \begin{pmatrix} -\Lambda & -\Lambda \\ \Lambda & \Lambda \end{pmatrix} \tag{6.29}$$

and the matrices $\Omega = \mathrm{diag}(\omega_1, \omega_2)$ and

$$\Lambda = \begin{pmatrix} \lambda^2 & 1 \\ 1 & 1/\lambda^2 \end{pmatrix}. \tag{6.30}$$

The equations of motion (6.28) can be formally integrated,

$$\mathbf{a}(t) = S_{(c)}(t)\mathbf{a}(0), \tag{6.31}$$

with the complex 4×4 matrix $S_{(c)}(t) = \mathcal{T} \exp\left(i \int^t d\tau A(\tau)\right)$ that provides a linear mapping between the Schrödinger and the Heisenberg field operators. The complex matrix $S_{(c)}(t)$ can be related to a real symplectic matrix $S(t)$ that describes the time evolution of the real quadratures $\boldsymbol{\xi}$, $S_{(c)}(t) = \Sigma^\dagger S(t) \Sigma$, with $S^T(t) J S(t) = J$ and J the antisymmetric matrix

$$J = \begin{pmatrix} 0 & 1 \\ -1 & 0 \end{pmatrix}. \tag{6.32}$$

The matrix $S(t)$ is the solution of the Heisenberg equations of motion $\dot{\boldsymbol{\xi}} = \Xi(t)\boldsymbol{\xi}$ for the quadratures $\boldsymbol{\xi}$, with $\Xi(t) = i\Sigma A(t) \Sigma^\dagger$ and the matrix $\Xi(t)$ that has a simple block form,

$$\Xi(t) = \begin{pmatrix} 0 & \Omega \\ -\Omega - 4f(t)\Lambda & 0 \end{pmatrix}, \tag{6.33}$$

that admits the general solution $S(t) = \mathcal{T} \exp\left(\int^t d\tau \Xi(\tau)\right)$.

In the case our initial state is a Gaussian state, the problem simplifies greatly. We introduce the Wigner distribution $W(\bar{\xi})$, with $\bar{\xi}$ the coordinates in the phase space, that relates a given density matrix ρ to a quasi-probability distribution in the phase space,

$$W(\bar{\xi}) = \int \frac{d\bar{\zeta}}{4\pi^2} \mathrm{Tr}\left[\rho \exp(i\bar{\zeta}^T \cdot J \cdot \boldsymbol{\xi})\right] \exp(i\bar{\zeta}^T \cdot J \cdot \bar{\xi}). \tag{6.34}$$

The Wigner distribution of a Gaussian state has the form

$$W(\bar{\xi}) = \frac{1}{\pi^2} \exp\left(-(\bar{\xi} - \bar{\xi}_0)^T V^{-1} (\bar{\xi} - \bar{\xi}_0)\right), \tag{6.35}$$

with V the real symmetric variance matrix defined by

$$V_{ij} = V_{ji} = \frac{1}{2}\langle\{\hat{\xi}_i, \hat{\xi}_j\}\rangle = \int d\bar{\xi}\; \bar{\xi}_i \bar{\xi}_j W(\bar{\xi}), \tag{6.36}$$

and $\{A, B\} = AB + BA$ the anticommutator. Under the unitary transformation $\mathcal{U}(S)$ associated with the symplectic transformation S, the density matrix changes as $\rho' = \mathcal{U}(S)\rho\mathcal{U}^{-1}(S)$, and the variance matrix V of the Wigner distribution changes as $V' = SVS^T$ [9–11]. The symplectic matrix S admits a unique polar decomposition that satisfies [11]

$$S = S(X, Y)P \tag{6.37}$$

with $P, S(X, Y) \in Sp(4, \mathbb{R})$ both real symplectic matrices, $P \in \Pi$ and $U = X - iY \in U(2)$, with $\Pi = \{S \in Sp(4, \mathbb{R}) \mid S^T = S, S \text{ positive definite}\}$ and

$$S(X, Y) = \begin{pmatrix} X & Y \\ -Y & X \end{pmatrix}. \tag{6.38}$$

From the unitarity of U follows that $S(X, Y)^T S(X, Y) = \mathbb{I}$ and consequently that $S^T S = P^2$. From the polar decomposition it follows that $\mathcal{U}(S) = \mathcal{U}(P)\mathcal{U}(S(X, Y))$ [11]. The transformation $\mathcal{U}(S(X, Y))$ conserves the photon number and for this reason it is called "passive", whereas the transformation $\mathcal{U}(P)$ does not conserve the number of photons and it is called active. When starting from a non-squeezed state only the $\mathcal{U}(P)$ transformation can produce squeezing. For this reason we can study all the departures from a perfect beam splitting transformation as arising uniquely from the presence of an active term P.

6.5 Beam splitting fidelity

We consider the initial state $\rho_i = |\psi_i\rangle\langle\psi_i|$ and as a final state $\rho_f = |\psi_f\rangle\langle\psi_f|$, with $|\psi_i\rangle$ and $|\psi_f\rangle$ given by Eqs. (6.22,6.23). The fidelity of the gate can be written as $\mathcal{F}(t) = |\langle\psi_f|U(t)|\psi_i\rangle|^2 = \mathrm{Tr}[\rho_f \rho(t)]$, with $\rho(t) = U(t)\rho_i U^\dagger(t)$. The state $\rho(t)$ can be written as

$$\begin{aligned} \rho(t) &= U(t)a_1^\dagger|0\rangle\langle 0|a_1 U^\dagger(t) && (6.39) \\ &= \left(U(t)a_1^\dagger U^\dagger(t)\right)\left(U(t)|0\rangle\langle 0|U^\dagger(t)\right)\left(U(t)a_1 U^\dagger(t)\right) && (6.40) \\ &= a_1^\dagger(-t)\left(U(t)|0\rangle\langle 0|U^\dagger(t)\right) a_1(-t). && (6.41) \end{aligned}$$

By cycling the operators inside the trace sign, the fidelity then becomes

$$\mathcal{F}(t) = \mathrm{Tr}[\tilde{\rho}_f(-t)\rho_0(t)], \tag{6.42}$$

with the backward-in-time evolved non-normalized state $\tilde{\rho}_f(-t) = a_1(-t)\rho_f a_1^\dagger(-t)$ and the forward-in-time evolved vacuum $\rho_0(t) = U(t)|0\rangle\langle 0|U^\dagger(t)$. By writing

$$\begin{aligned} a_1(-t) &= \sum_{i=1,2} (S_{(c)}(t)^{-1})_{1,i} a_i + (S_{(c)}(t)^{-1})_{1,i+2} a_i^\dagger, & (6.43)\\ a_1^\dagger(-t) &= \sum_{i=1,2} (S_{(c)}(t)^{-1})_{3,i} a_i + (S_{(c)}(t)^{-1})_{3,i+2} a_i^\dagger, & (6.44) \end{aligned}$$

the state $\tilde{\rho}_f(-t)$ can be written as $\tilde{\rho}_f(-t) = |\tilde{\psi}(-t)\rangle\langle\tilde{\psi}(-t)|$, with

$$|\tilde{\psi}(-t)\rangle = c_{00}(t)|0\rangle + c_{11}(t)|1,1\rangle + c_{20}(t)|2,0\rangle + c_{02}(t)|0,2\rangle, \tag{6.45}$$

with the coefficient $c_i(t)$ linear combinations of the entries of the matrix $S_{(c)}^{-1}(t)$,

$$\begin{aligned} c_{00}(t) &= ([S_{(c)}^{-1}(t)]_{11} + e^{-i\varphi}[S_{(c)}^{-1}(t)]_{12})/\sqrt{2}, & (6.46)\\ c_{11}(t) &= ([S_{(c)}^{-1}(t)]_{14} + e^{-i\varphi}[S_{(c)}^{-1}(t)]_{13})/\sqrt{2}, & (6.47)\\ c_{02}(t) &= e^{-i\varphi}[S_{(c)}^{-1}(t)]_{14}, & (6.48)\\ c_{20}(t) &= [S_{(c)}^{-1}(t)]_{13}. & (6.49) \end{aligned}$$

In the Fock basis $\tilde{\rho}_f(-t)$ is a 4×4 matrix. We can choose to normalize the state $\tilde{\rho}_f(-t)$ and write

$$\mathcal{F}(t) = \mathrm{Tr}[\tilde{\rho}_f(-t)]\mathrm{Tr}[\rho_f(-t)\rho_0(t)], \tag{6.50}$$

with

$$\rho_f(-t) = \frac{\tilde{\rho}_f(-t)}{\mathrm{Tr}[\tilde{\rho}_f(-t)]}. \tag{6.51}$$

The time-evolved vacuum $\rho_0(t)$ is initially a pure Gaussian state and its time evolution is easily calculated its Wigner distribution. By expressing the Wigner distribution of $\rho_0(t)$ in the Fock basis, we have an operative way to calculate the fidelity of the beam splitter,

$$\mathcal{F}(t) = \mathrm{Tr}[\tilde{\rho}_f(-t)] \sum_{\{n\},\{m\}} \rho_f(-t)_{\{n\},\{m\}} \rho_0(t)_{\{m\},\{n\}}, \tag{6.52}$$

with $\{n\} = n_1, n_2$ and $\rho_{\{n\},\{m\}} = \langle n_1 n_2|\hat{\rho}|m_1 m_2\rangle$.

We now express the Wigner function defined in Eq. (6.34) as a function of the complex amplitudes of the fields, $\bar{\alpha} = (\alpha_1, \alpha_2, \alpha_1^*, \alpha_2^*)^T$. The Wigner function of the squeezed vacuum $\rho_0(t)$ is given by

$$W_{0,t}(\bar{\alpha}) = \frac{4}{\pi^2} e^{-\bar{\alpha}^\dagger V_{(c)}^{-1}(t)\bar{\alpha}} \tag{6.53}$$

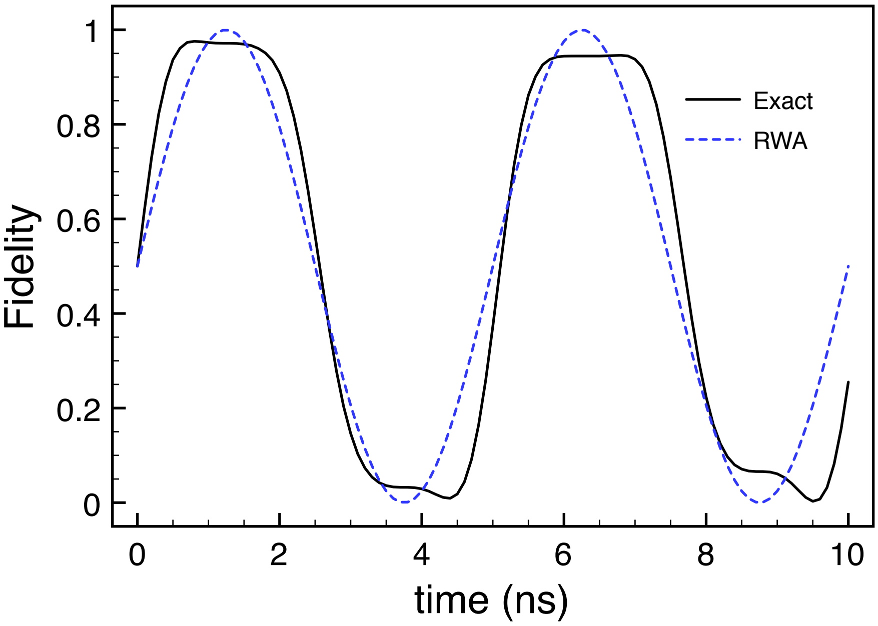

Figure 6.2: Fidelity of the beam splitting gate. Parameters: $\omega_1/2\pi = 7$ GHz, $\omega_2/2\pi = 7.2$ GHz, $\lambda = 1$, $\delta f/2\pi = 0.1$ GHz, and $\varphi = \pi/2$. The black solid curve represents the result of the exact calculation provided by Eq. (6.42), whereas the blue dashed curve shows the result of the rotating wave approximation as given by Eq. (6.24).

with the matrix $V_{(c)}(t) = S_{(c)}(t)V_{(c)}(0)S_{(c)}(t)^\dagger$, the matrix $V_{(c)}^{-1}(0) = \mathbb{I}_{4\times 4}$, with $V_{(c)} = \Sigma^\dagger V \Sigma$. The matrix elements of a density operator in the Fock space can be obtained from the Wigner function by

$$\rho_{\{n\},\{m\}} = \int \frac{d\bar{\alpha}}{\pi^2} \chi_W(\bar{\alpha}) D_{n_1,m_1}(\alpha_1) D_{n_2,m_2}(\alpha_2) \tag{6.54}$$

where $\chi_W(\vec{\alpha}, \vec{\alpha}^*)$ is the characteristic function, that is defined by $\chi_W(\bar{\alpha}) \equiv \mathrm{Tr}[\rho D(\bar{\alpha})]$, with $D(\bar{\alpha}) = \exp(-\alpha^\dagger \cdot \Sigma_Z \cdot \mathbf{a})$ the two-mode displacement operator and the matrix $\Sigma_Z = \mathrm{diag}(\mathbb{I}, -\mathbb{I})$. The characteristic function is related to the Wigner function by a Fourier transfom,

$$\chi^W(\bar{\alpha}) = \int d\bar{\beta}\ \exp\left(\bar{\beta}^\dagger \cdot \Sigma_Z \cdot \bar{\alpha}\right) W(\bar{\beta}) \tag{6.55}$$

The coefficients $D_{n,m}(\alpha)$ that appear in Eq. (6.54) are defined by

$$D_{n,m}(\alpha) \equiv \langle n|D(\alpha)|m\rangle = \sqrt{\frac{m!}{n!}} \alpha^{n-m} e^{-|\alpha|^2/2} L_m^{(n-m)}(|\alpha|^2), \tag{6.56}$$

with $L_m^{(n-m)}(r)$ the Laguerre polynomials and $D(\alpha) = \exp(\alpha a^\dagger - \alpha^* a)$ the single-mode displacement operator. The characteristic function of the squeezed vacuum Eq. (6.53) is

$$\chi^{W}_{0,t}(\bar{\alpha}) = \exp\left(-\frac{1}{4}\bar{\alpha}^{\dagger}\cdot\Sigma_Z V_{(c)}(t)\Sigma_Z\cdot\bar{\alpha}\right). \tag{6.57}$$

In Fig. 6.2 we plot the fidelity of the beam splitting gate obtained by exact integration of the equation of motion and compare it to the result of the rotating wave approximation, Eq. (6.24). We chose the two resonant frequencies to be $\omega_1/2\pi = 7$ GHz $\omega_2/2\pi = 7.2$ GHz, respectively. The interaction potential has been chosen to couple the two modes in a symmetrical way, that is $\lambda = 1$. The amplitude of the driving is $\delta f/2\pi = 0.1$ GHz. The dashed blue curve represents the result of the RWA and clear Rabi oscillations at a frequency $\Omega_R = 2\delta f$ appear. The exact solution is given by the black solid curve. The beam splitting is obtained when the fidelity reaches one. We see that there is only partial agreement between the exact solution and the rotating wave approximation. In particular the crude RWA provides a good approximation for the Rabi period, and the error in fidelity of the beam splitting gate is on order of 5%. A better result can be obtained by taking into consideration one- and two-photon processes, that result in Bloch-Siegert oscillations superimposed to the crude RWA envelope.

6.6 Conclusion

In this work we have provided an exact derivation of the fidelity of a beam splitting gate in a system of two superconducting line resonators, coupled by an externally driven SQUID. We have used an effective equivalent circuit for the two coupled resonators and studied its quantum dynamics. In the linear response of the SQUID dynamics, the two resonators turn out to be quadratically coupled and in the rotating wave approximation we find analytically that the fidelity of the beam splitting reaches unity. We have then studied the accuracy of the rotating wave approximation by providing an exact derivation of the fidelity of the beam splitting gate and by making comparison with rotating wave result. We find that the exact solution beam splitting fidelity can reach more than 95% in a time $\tau = \pi/4\delta f$.

References

[1] Q. A. Turchette, C. J. Hood, W. Lange, H. Mabuchi, and H. J. Kimble, Measurement of conditional phase shifts for quantum logic, Phys. Rev. Lett. **75**, 4710 (1995).

[2] E. Knill, R. Laflame and G. J. Milburn, A scheme for efficient quantum computation with linear optics, Nature **409**, 46 (2001).

[3] A. Wallraff, D. I. Schuster, A. Blais, L. Frunzio, R.- S. Huang, J. Majer, S. Kumar, S. M. Girvin, R. J. Schoelkopf, Strong coupling of a single photon to a superconducting qubit using circuit quantum electrodynamics, Nature **431**, 162-167 (2004).

[4] M. Hofheinz, H. Wang, M. Ansmann, Radoslaw C. Bialczak, E. Lucero, M. Neeley, A. D. O'Connell, D. Sank, J. Wenner, J. M. Martinis and A. N. Cleland, Synthesizing arbitrary quantum states in a superconducting resonator, Nature **459**, 546-549 (2009).

[5] S. Kumar and D. P. DiVincenzo, Exploiting Kerr cross non-linearity in circuit quantum electrodynamics for non-demolition measurements, arXiv: 0906.2979 (2009).

[6] G. Burkard, R. H. Koch, D. P. DiVincenzo, Multilevel quantum description of decoherence in superconducting qubits, Phys. Rev. B **69**, 064503 (2004).

[7] F. Bloch and A. Siegert, Magnetic resonance for nonrotating fields, Pfys. Rev. **57**, 522 (1940).

[8] M. S. Shahriar, P. Pradhan, J. Morzinski, Driver-phase-correlated fluctuations in the rotation of a strongly driven qubit, Phys. Rev. A **69**, 032308 (2004).

[9] R. Simon, N. Mukunda, B. Dutta, Quantum-noise matrix for multimode systems: $U(n)$ invariance, squeezing, and normal forms, Phys. Rev. A **49**, 1567 (1994).

[10] Arvind, B. Dutta, N. Mukunda, R. Simon, Two-mode quantum systems: Invariant classification of squeezing transformations and squeezed states, Phys. Rev. A **52**, 1609 (1995).

[11] Arvind, B. Dutta, N. Mukunda, R. Simon, The real symplectic groups in quantum mechanics and optics, quant-ph/9509002 (1995).

A. Matrices $\mathcal{C}$, $\mathbf{C}_V$, $\mathbf{M}_0$, and $\mathbf{N}$

The definitions of the derived matrices $\mathcal{C}$, $\mathbf{C}_V$, $\mathbf{M}_0$ and $\mathbf{N}$ that enters the Hamiltonian are given in [6, 27] for the general case. Here we apply the theory and derive the matrices for the particular case of the circuit of Fig. 2.2. The derived capacitance matrices are

$$\begin{aligned} \mathcal{C} &\equiv \mathbf{C}_J + \begin{pmatrix} \mathbf{C} & 0 \\ 0 & 0 \end{pmatrix}, && \text{(A.1)} \\ \mathbf{C}_V &\equiv (\mathbf{C}, \mathbf{0})^T. && \text{(A.2)} \end{aligned}$$

The inductance matrices that enter the potential are

$$\begin{aligned} \mathbf{M}_0 &= \frac{1}{K}\mathbf{F}_{JK}\mathbf{F}_{JK}^T, && \text{(A.3)} \\ \mathbf{N} &= -\frac{1}{K}\mathbf{F}_{JK}, && \text{(A.4)} \end{aligned}$$

and $\mathbf{M}_0^T = \mathbf{M}_0$. For the circuit studied here, we obtain

$$\mathbf{M}_0 = \frac{1}{K}\begin{pmatrix} 1 & -1 & -1 \\ -1 & 1 & 1 \\ -1 & 1 & 1 \end{pmatrix}, \ \mathbf{N} = \frac{1}{K}\begin{pmatrix} 1 \\ -1 \\ -1 \end{pmatrix}. \tag{A.5}$$

Projected matrices

The three-dimensional problem is mapped into a two-dimensional one in Sec. 2.3 with the matrix

$$\mathcal{P} = \begin{pmatrix} 1 & 0 \\ 0 & 1 \\ 1 & -1 \end{pmatrix}, \tag{A.6}$$

via the relation $(\varphi_1, \varphi_2, \varphi_3)^T = \mathcal{P}(\varphi_1, \varphi_2)^T$. In the case of symmetric double well potential, the inductance linearized matrix $\mathbf{L}^{-1}_{\text{lin;L,R}}$ is given by

$$\mathbf{L}^{-1}_{\text{lin;L,R}} = \mathbf{M}_0 + \mathbf{L}_J^{-1}\mathbf{cos}\boldsymbol{\phi}_{\text{L,R;i}}. \tag{A.7}$$

Because of the symmetry of the potential, we drop the subscripts R and L. Applying the matrix $\mathcal{P}$ we obtain $\mathbf{L}^{-1}_{\text{lin},P} = \mathcal{P}^T\mathbf{L}^{-1}_{\text{lin}}\mathcal{P}$,

$$\mathbf{L}^{-1}_{\text{lin},P} = \frac{1}{L_J}\begin{pmatrix} \alpha & \frac{1}{2\alpha} - \alpha \\ \frac{1}{2\alpha} - \alpha & \alpha \end{pmatrix}. \tag{A.8}$$

In order to simplify the calculation we assume the two capacitance C_1 and C_2 to be equal, $C_1 = C_2 \equiv C$ and define $\gamma = C/C_J$. The projected capacitance matrix $\mathcal{C}_P = \mathcal{P}^T \mathcal{C} \mathcal{P}$ is then found to be

$$\mathcal{C}_P = C_J \begin{pmatrix} 1+\gamma+\alpha & -\alpha \\ -\alpha & 1+\gamma+\alpha \end{pmatrix}. \tag{A.9}$$

In this case, the orthogonal matrices that diagonalize the capacitance matrix $\mathcal{C}_P$ the linearized inductance matrix $\mathbf{L}^{-1}_{\text{lin},P}$ are identical, $\mathcal{C}_P = \mathbf{O}^T \mathcal{C}_d \mathbf{O}$ and $\mathbf{L}^{-1}_{\text{lin},P} = \mathbf{O}^T \mathbf{\Lambda} \mathbf{O}$. The frequency matrix $\mathbf{\Omega} = \text{diag}(\omega_\perp, \omega_\parallel)$ is given by

$$\mathbf{\Omega}^2 = \omega_{LC}^2 \begin{pmatrix} \frac{1}{4\alpha^2(1+\gamma)^2} & 0 \\ 0 & \frac{1-4\alpha^2}{4\alpha^2(1+2\alpha+\gamma)^2} \end{pmatrix}, \tag{A.10}$$

where $\omega_{LC}^2 = 1/L_J C_J$. The matrix $\mathcal{M}$ is then diagonalized by the same orthogonal matrix $\mathbf{O}$ and, in the basis where it is diagonal, can be written as

$$\mathcal{M} = \sqrt{\frac{E_J}{8E_C}} \begin{pmatrix} \sqrt{\frac{1+\gamma}{2\alpha}} & 0 \\ 0 & \sqrt{\frac{(4\alpha^2-1)(1+2\alpha+\gamma)}{2\alpha}} \end{pmatrix}. \tag{A.11}$$

B. The functions $\mathcal{F}_1$ and $\mathcal{F}_\phi$

We give here an explicit formula for the intra-cell and inter-cell overlaps s_1 and s_2 as functions of α, E_J/E_C and C/C_J,

$$\begin{aligned}
s_1 &= \exp\left\{-\frac{E_J}{4\sqrt{2\alpha}E_C}\arccos^2\left(\frac{1}{2\alpha}\right)\sqrt{(4\alpha^2-1)(1+2\alpha+C/C_J)}\right\}, && \text{(B.1)}\\
s_2 &= \exp\left\{-\frac{E_J}{16E_C}\left[\left(\pi-2\arccos\left(\frac{1}{2\alpha}\right)\right)^2\sqrt{\frac{(4\alpha^2-1)(1+2\alpha+C/C_J)}{2\alpha}}\right.\right.\\
&+ \left.\left.\pi^2\sqrt{\frac{1+C/C_J}{2\alpha}}\right]\right\}. && \text{(B.2)}
\end{aligned}$$

Through these quantities we can express $\mathcal{F}_1$ and $\mathcal{F}_\phi$ as functions of k_1 and k_2, with $k_i = C_iV_i/2e$,

$$\begin{aligned}
\mathcal{F}_1(k_1,k_2) &= \frac{|\Delta(k_1,k_2)|}{E_J}\coth\left(\frac{|\Delta(k_1,k_2)|}{2k_BT}\right)\tilde{\mathcal{F}}_\phi(k_1,k_2), && \text{(B.3)}\\
\mathcal{F}_\phi(k_1,k_2) &= \frac{4}{\det^2(\mathcal{C})}\sum_{i=1,2}\left[\pi(\mathcal{C}_{1i}\mathcal{M}_{22}\sin(2\pi k_2-\theta)-\mathcal{C}_{2i}\mathcal{M}_{11}\sin(2\pi k_1+\theta))\right.\\
&+ (\mathcal{C}_{2i}\mathcal{M}_{11}+\mathcal{C}_{1i}\mathcal{M}_{22})\arccos\left(\frac{1}{2\alpha}\right)\\
&\times \left.\left(\frac{s_1}{s_2}\sin(\theta)+\sin(2\pi k_1+\theta)-\sin(2k_2-\theta)\right)\right]^2, && \text{(B.4)}
\end{aligned}$$

where $\tilde{\mathcal{F}}_\phi$ is given by $\mathcal{F}_\phi$, once the sin are replaced by cos. $\mathcal{C}_{ij}$ and $\mathcal{M}_{ij}$ are the entries of the matrices $\mathcal{C}$ and $\mathcal{M}$ defined in Appendix A. The gap $|\Delta|$ and the relative phase between the states $|0\rangle$ and $|1\rangle$ are given by

$$\begin{aligned}
\frac{1}{4}|\Delta(k_1,k_2)|^2 &= (t_1+2t_2\cos[\pi(k_1-k_2)]\cos[\pi(k_1+k_2)])^2\\
&+ 4t_2^2\cos[\pi(k_1+k_2)]\sin[\pi(k_1-k_2)], && \text{(B.5)}\\
\tan\theta &= \frac{2t_2\cos[\pi(k_1+k_2)]\sin[\pi(k_1-k_2)]}{t_1+2t_2\cos[\pi(k_1-k_2)]\cos[\pi(k_1+k_2)]}. && \text{(B.6)}
\end{aligned}$$

C. Perturbation theory in Δ

In order to determine the evolution governed by the Hamiltonian Eq. (3.11) we single out the term $\mathcal{H}_0$ diagonal in the $\{|s,n\rangle\}$ basis, with $|s\rangle$ the eigenstates of $\boldsymbol{\sigma}_Z$ and $|n\rangle$ the oscillator Fock states,

$$\mathcal{H} = \mathcal{H}_0 + f(a + a^\dagger) + \frac{\Delta}{2}\boldsymbol{\sigma}_X, \tag{C.1}$$

with $\mathcal{H}_0 = \epsilon\boldsymbol{\sigma}_Z/2 + \Delta\boldsymbol{\omega}_Z a^\dagger a$. We then work in the interaction picture with respect to $\mathcal{H}_0$. The Heisenberg equation for the density operator reads $\dot{\boldsymbol{\rho}}_I = -i\,[\mathcal{H}_I, \boldsymbol{\rho}_I]$, with

$$\begin{aligned} \mathcal{H}_I &= \mathcal{H}_I^{(0)} + V_I, && \text{(C.2)}\\ \mathcal{H}_I^{(0)} &= f(ae^{-i\Delta\boldsymbol{\omega}_Z t} + a^\dagger e^{i\Delta\boldsymbol{\omega}_Z t}), && \text{(C.3)}\\ V_I &= \frac{\Delta}{2}\left(e^{i\hat{\Omega}_n t}\boldsymbol{\sigma}_+ + e^{-i\hat{\Omega}_n t}\boldsymbol{\sigma}_-\right), && \text{(C.4)} \end{aligned}$$

where we define $\hat{\Omega}_n = \epsilon + 2ga^\dagger a$, and $\boldsymbol{\sigma}_\pm = (\boldsymbol{\sigma}_X \pm i\boldsymbol{\sigma}_Y)/2$. We will call $\mathcal{U}_I(t)$ the evolution operator generated by $\mathcal{H}_I$.

The evolution operator is given by $\mathcal{U}(t) = \exp(-i\omega_d t a^\dagger a - i\mathcal{H}_0 t)\mathcal{U}_I(t)$. For the measurement procedure so far defined we are interested in the evolution operator in the frame rotation at the bare harmonic oscillator frequency. Therefore

$$\mathcal{U}_R(t) = \exp(-i\epsilon t\boldsymbol{\sigma}_Z/2 - i\mathcal{H}_{\text{int}}t)\mathcal{U}_I(t). \tag{C.5}$$

For the case $\Delta = 0$ the model is exactly solvable and $\mathcal{U}_I^{(0)}(t)$ can be computed via a generalization of the Baker-Hausdorff formula [35],

$$\mathcal{U}_I^{(0)}(t) = D(\boldsymbol{\gamma}_Z(t)), \tag{C.6}$$

with the qubit-dependet amplitude $\boldsymbol{\gamma}_Z(t) = -if\int_0^t ds e^{i\Delta\boldsymbol{\omega}_Z s}$. The operator $D(\alpha) = \exp(a^\dagger\alpha - a\alpha^*)$ is a displacement operator [36], and it generates a coherent state when applied to the vacuum $|\alpha\rangle \equiv D(\alpha)|0\rangle = e^{-|\alpha|^2/2}\sum_n(\alpha^n/\sqrt{n!})|n\rangle$. In the frame rotating at the bare harmonic oscillator frequency, the state of the oscillator is a coherent state whose amplitude depends on the qubit state. A general initial state

$$\boldsymbol{\rho}_{\text{tot}}(0) = \sum_{ij=0,1}\rho_{ij}|i\rangle\langle j| \otimes |\hat{0}\rangle\langle\hat{0}|, \tag{C.7}$$

where $|\hat{0}\rangle$ is the harmonic oscillator vacuum state, evolves to

$$\boldsymbol{\rho}_R(t) = \sum_{ij=0,1}\rho_{ij}|i\rangle\langle j| \otimes |\alpha_i(t)\rangle\langle\alpha_j(t)|, \tag{C.8}$$

where we define the qubit operators $\boldsymbol{\alpha}_Z(t) \equiv \boldsymbol{\gamma}_Z(t) e^{-igt\boldsymbol{\sigma}_Z}$, and the object

$$|\boldsymbol{\alpha}_Z(t)\rangle \equiv D(\boldsymbol{\alpha}_Z)|\hat{0}\rangle, \tag{C.9}$$

that gives a qubit-dependent coherent state of the harmonic oscillator, once the expectation value on a qubit state is taken, $|\alpha_i(t)\rangle = \langle i|\boldsymbol{\alpha}_Z(t)|i\rangle$, for $i = 0, 1$.

For non-zero Δ, a formally exact solution can be written as

$$\mathcal{U}_I(t) = \mathcal{U}_I^{(0)}(t) \mathcal{T} \exp\left(-i\ \Delta \int_0^t dt' \mathcal{V}_I(t')\right), \tag{C.10}$$

with $\mathcal{V}_I(t) = \mathcal{U}_I^{(0)\dagger}(t) V_I(t) \mathcal{U}_I^{(0)}(t)$ and $\mathcal{T}$ the time order operator. For a time scale $t \ll 1/\Delta$ we expand the evolution operator in powers of $\Delta t \ll 1$,

$$\mathcal{U}_I(t) \approx \mathcal{U}_I^{(0)}(t) \left(\mathbb{I} - i\Delta t \int_0^1 ds \mathcal{V}_I(s\ t) - (\Delta t)^2 \int_0^1 ds \int_0^s ds' \mathcal{V}_I(s\ t) \mathcal{V}_I(s'\ t)\right). \tag{C.11}$$

The interaction picture potential can be written as

$$\mathcal{V}_I(t) = \frac{1}{2}\left[\mathcal{D}(t)\boldsymbol{\sigma}^+ + \mathcal{D}^\dagger(t)\boldsymbol{\sigma}^-\right], \tag{C.12}$$

with the oscillator operators $\mathcal{D}(t)$ defined as

$$\begin{aligned} \mathcal{D}(t) &= D^\dagger(\gamma_0(t)) e^{i\Omega_n t} D(\gamma_1(t)) && \text{(C.13)} \\ &= \exp\left(i\epsilon t - i\mathrm{Im}[\alpha_0(t)\alpha_1(t)^*]\right) D(-\delta\alpha(t) e^{igt}) e^{2igta^\dagger a}. && \text{(C.14)} \end{aligned}$$

Here $\delta\alpha(t) = \alpha_0(t) - \alpha_1(t)$ is the difference between the amplitudes of the coherent states associated with the two possible qubit states.

D. First and Second order contribution to the two-measurement POVM

In this Appendix we provide the full expression for the quantities $C^{(1)}$, $F^{(2)}$ and $C^{(2)}$ that enter in the expression of the two-measurement POVM. For time $t \approx 1/\epsilon$, we expand the evolution operator in Δt and collect the contributions that arise at second power in (Δ/ϵ). By making use of the expression Eq. (C.12) for the perturbation in the interaction picture we can compute the qubit components of the second order contribution to the continuous POVM. We define

$$\begin{aligned} \mathcal{O}_s(t',t'') &= \exp\left(is\epsilon(t'-t'') - is\psi(t'^2 - t''^2)\right) \\ &\times \langle \delta\alpha(t')e^{isgt'} | \delta\alpha(t'')e^{isgt''}\rangle, \end{aligned} \tag{D.1}$$

and $\langle\alpha|\beta\rangle$ is the overlap between coherent states, and

$$\xi_s^{(2)}(t',t'') = \delta x_s^{(1)}(t')^* + \delta x_s^{(1)}(t''), \tag{D.2}$$

$$\zeta_s^{(2)}(t',t'') = -\delta x_s^{(1)}(t') + \delta x_s^{(1)}(t''). \tag{D.3}$$

The first term $\xi_s^{(2)}(t',t'')$ represents the complex displacement of the oscillator position due to the perturbation acting one time at $t'' < t$ (forward in time), and one time at $-t' > -t$ (backward in time). The second term $\zeta_s^{(2)}(t',t'')$ represents the displacement of the oscillator due to the perturbation acting two times at $t'' < t' < t$. Between the two perturbations the system evolves freely for the time $t'' - t'$ and accumulates a phase that depends on the difference of the effective qubit-dependent frequencies. In the short time approximation $t \approx 1/\epsilon$ such a phase can be neglected. Integrating the position degree of freedom over the subsets $\eta(s')$, we obtain

$$\begin{aligned} F^{(2)}(s',t)_{ss} &= -s's\frac{\epsilon^2}{4}\int_0^t dt' \int_0^{t'} dt'' \mathrm{Re}\left\{\mathcal{O}_s(t',t'')\right. \\ &\times \left.\left[\mathrm{erf}\left(\frac{\delta x(t) + \xi_{\bar{s}}^{(2)}(t',t'')}{\sigma}\right) + \mathrm{erf}\left(\frac{\delta x(t) + \zeta_s^{(2)}(t',t'')}{\sigma}\right)\right]\right\}, \end{aligned} \tag{D.4}$$

where $\bar{s} = -s$. This expression has meaning only in the short time approximation. By setting $t \approx 1/\epsilon$, the correction $F^{(2)}(t)$ at second order to the discrete POVM is evaluated to be

$$\begin{aligned} F^{(2)}(t) &= \frac{\epsilon^2}{4}\int_0^t d\tau_1 \int_0^{t'} dt'' \cos\left(\epsilon(t'-t'') - \psi\left(t'^2 - t''^2\right)\right) e^{-\frac{1}{2}|A|^2(t'-t'')^2} \\ &\times \left(\operatorname{erf}(|A|(t+t'+t'')) + \operatorname{erf}(|A|(t-t'+t''))\right). \end{aligned} \tag{D.5}$$

In an analogue way we calculate the elements of the first and second order contributions to the double measurement operator $\mathbf{C}$. The off-diagonal matrix element of the first order contribution $C^{(1)}$ is

$$C^{(1)}(t';t) = \frac{1}{2}\left(\Gamma(t) - 1\right) F^{(1)}(t'-t) + \frac{i\Delta}{4}\operatorname{erf}\left(\frac{\delta x(t'-t)}{\sigma}\right)\int_0^t dt'' e^{i\epsilon t''}\Gamma(t''), \tag{D.6}$$

and the full expression of the diagonal matrix element of the second order contribution $C^{(2)}$ is

$$\begin{aligned} C^{(2)}(t) &= \frac{\epsilon^2}{8}\int_0^t dt' \int_0^t dt'' e^{i(\epsilon(t'-t'')-\psi(t'^2-t''^2))} e^{-\frac{|A|^2}{2}(t'-t'')^2}\operatorname{erf}(|A|(t+t'+t'')) \\ &- \operatorname{Im}\left[F^{(1)}(t)\epsilon\int_0^t dt' e^{-i\epsilon t'}\Gamma(t)\Gamma(t')^* e^{-\frac{1}{2}|At'|^2+|A|^2t't}\operatorname{erf}\left(\delta x_-^{(1)}(t')/\sigma\right)\right]. \end{aligned} \tag{D.7}$$

E. Eigenvalue problem

Defining

$$u_{\pm} = \frac{1}{2\tan(\gamma)}\left(1 - \mathrm{sinc}(\epsilon) \pm \sqrt{(1+\mathrm{sinc}(\epsilon))^2 - 4\frac{\mathrm{sinc}(\epsilon)}{\cos^2(\gamma)}}\right) \tag{E.1}$$

The matrix U assumes the simple form

$$U = \begin{pmatrix} 1 & 0 & 0 & 0 \\ 0 & 1 & 0 & 0 \\ 0 & 0 & u_+ & u_- \\ 0 & 0 & 1 & 1 \end{pmatrix}, \tag{E.2}$$

with $\mathrm{sinc}(\epsilon) = \sin(\pi\epsilon)/\pi\epsilon$, that allows for a simple solution of the eigenvalue problem in terms of a Jordan decomposition, $\mathcal{Q} = U^{-1}\mathrm{diag}(1, \sin(\pi\epsilon)/\pi\epsilon, \lambda_-, \lambda_+)U$, with

$$\begin{aligned} \lambda_{\pm} &= \frac{1}{2}\cos(\phi)(1+\mathrm{sinc}(\epsilon)) \\ &\pm \frac{1}{2}\sqrt{\cos^2(\phi)(1+\mathrm{sinc}(\epsilon))^2 - \mathrm{sinc}^2(\epsilon)}. \end{aligned} \tag{E.3}$$

F. Double ring transmission and reflection amplitudes

The transmission amplitude for electrons coming from the left lead L and going to the right lead R can be calculated as

$$t = \boldsymbol{\tau}_B (\mathbb{I} - \mathbf{\Gamma})^{-1} S'_p \boldsymbol{\tau}_A, \tag{F.1}$$

with $\mathbf{\Gamma} = S'_p \bar{\boldsymbol{\rho}}_A \bar{S}'_p \boldsymbol{\rho}_B$, and $S'_p = \begin{pmatrix} S_p & 0 \\ 0 & 1 \end{pmatrix}$. We define the following transmission matrices in node A and B that take into account the lower arm of the large ring,

$$\begin{aligned} \mathbf{t}'_A &= \begin{pmatrix} \mathbf{t}_A & 0 \\ 0 & 1 \end{pmatrix}, \qquad \mathbf{t}'_B = \begin{pmatrix} \mathbf{t}_B & 0 \\ 0 & 1 \end{pmatrix}, && \text{(F.2)} \\ \bar{\mathbf{t}}'_A &= \begin{pmatrix} \bar{\mathbf{t}}_A & 0 \\ 0 & 1 \end{pmatrix}, \qquad \bar{\mathbf{t}}'_B = \begin{pmatrix} \bar{\mathbf{t}}_B & 0 \\ 0 & 1 \end{pmatrix}, && \text{(F.3)} \end{aligned}$$

with $\mathbf{t}'_A$ and $\bar{\mathbf{t}}'_B$ of dimension 3 × 2, and $\bar{\mathbf{t}}'_A$ and $\mathbf{t}'_B$ of dimension 2 × 3. Analogously we define the reflection matrices

$$\begin{aligned} \mathbf{r}'_A &= \begin{pmatrix} r_A & 0 \\ 0 & 0 \end{pmatrix}, \qquad \bar{\mathbf{r}}'_B = \begin{pmatrix} \bar{r}_B & 0 \\ 0 & 0 \end{pmatrix}, && \text{(F.4)} \\ \bar{\mathbf{r}}'_A &= \begin{pmatrix} \bar{\mathbf{r}}_A & 0 \\ 0 & 0 \end{pmatrix}, \qquad \mathbf{r}'_B = \begin{pmatrix} \mathbf{r}_B & 0 \\ 0 & 0 \end{pmatrix}, && \text{(F.5)} \end{aligned}$$

with $\mathbf{r}'_A$ and $\bar{\mathbf{r}}'_B$ of dimension 2 × 2, and $\bar{\mathbf{r}}'_A$ and $\mathbf{r}'_B$ of dimension 3 × 3. The effective transmission amplitudes $\boldsymbol{\tau}_A$ and $\boldsymbol{\tau}_B$ are given by the matrices

$$\begin{aligned} \boldsymbol{\tau}_A &= \mathbf{t}'_A \left(\mathbb{I} - P\bar{\mathbf{r}}_L \bar{P} \mathbf{r}'_A\right)^{-1} P \mathbf{t}_L, && \text{(F.6)} \\ \boldsymbol{\tau}_B &= \mathbf{t}_L \left(\mathbb{I} - P\bar{\mathbf{r}}'_B \bar{P} \mathbf{r}_R\right)^{-1} P \mathbf{t}'_B, && \text{(F.7)} \end{aligned}$$

with dimension respectively 3 × 1 and 1 × 3. The effective reflection amplitudes $\bar{\boldsymbol{\rho}}_A$ and $\boldsymbol{\rho}_B$ are given by the matrices

$$\begin{aligned} \bar{\boldsymbol{\rho}}_A &= \bar{\mathbf{r}}'_A + \mathbf{t}'_A P \left(\mathbb{I} - \bar{\mathbf{r}}_L \bar{P} \mathbf{r}'_A P\right)^{-1} \bar{\mathbf{r}}_L \bar{P} \bar{\mathbf{t}}'_A, && \text{(F.8)} \\ \boldsymbol{\rho}_B &= \mathbf{r}'_B + \bar{\mathbf{t}}'_B \bar{P} \left(\mathbb{I} - \mathbf{r}_R P \bar{\mathbf{r}}'_B \bar{P}\right)^{-1} \mathbf{r}_R P \mathbf{t}'_B. && \text{(F.9)} \end{aligned}$$

G. Electron-hole switch

Let us consider in details the mechanism suggested to inject and collect electron from the MZ. The system, depicted in Fig. 4.9 a), is composed by a cavity, formed by a circular edge state, that is coupled to a linear edge channel by a QPC$_V$ of transmission $\tilde{t}$ and reflection $\tilde{r}$. It has been experimentally demonstrated [20, 21] that such a device, if periodically driven by a time dependent potential $V(t)$, produces a periodic current composed by an electron in one half-period and a hole in the other half-period, shown in Fig. 4.9 b). We wish to separate the electron and the hole by transmitting the electron through a barrier towards contact 3, and reflecting the hole into the contact 4. A time-dependent QPC$_U$ driven by an external potential $U(t)$ behaves like a beam splitter that mixes the incoming channels, from the contact 1 and 2, into the outgoing channels 3 and 4. If properly driven, it works as a switch that separates the electrons and holes generated by the cavity into different edge channels. Following [22, 23] we describe the effect of the time-dependent potential QPC$_U$ by a scattering matrix

$$S_U(t) = \begin{pmatrix} S_{31}(t) & S_{32}(t) \\ S_{41}(t) & S_{42}(t) \end{pmatrix}. \tag{G.1}$$

In the symmetric case one has $S_{31}(t) = S_{42}(t)$ and $S_{32}(t) = S_{41}(t)$. From the unitarity of $S_U(t)$ follows that

$$\begin{aligned} 1 &= \sum_j |S_{jk}(t)|^2, & \text{(G.2)} \\ 0 &= S^*_{32}(t)S_{31}(t) + S^*_{42}(t)S_{41}(t). & \text{(G.3)} \end{aligned}$$

The dynamics of the cavity can be described by a time-dependent scattering amplitude $S_c(t, E)$, that describes the amplitude to be reflected at QPC$_V$ towards QPC$_U$, and satisfies $|S_c(t, E)|^2 = 1$. In the adiabatic regime, keeping all the reservoirs at the same chemical potential μ, the zero-temperature current in the contacts 3 and 4 can be written as

$$I_j(t) = |S_{j1}(t)|^2 I_c(t) + \frac{e}{2\pi i} \sum_{k=1,2} S_{jk}(t) \frac{\partial}{\partial t} S^*_{jk}(t), \tag{G.4}$$

with $j = 3, 4$. Here $I_c(t)$ is the current produced by the cavity, that can be written as[22, 23]

$$I_c(t) = \frac{e}{2\pi i} S_c(t, \mu) \frac{\partial}{\partial t} S^*_c(t, \mu), \tag{G.5}$$

with μ the chemical potential of all the leads. The current $I_c(t)$ is plotted in Fig. 4.9 b) for a harmonic driving $V(t) = V_0 \cos(\Omega t)$, for the choice $\Omega/2\pi = 1$ GHz and $|\tilde{t}|^2 = 0.1$. We choose the QPC_U such that we can write $S_{31}(t) = \sqrt{T(t)}$ and $S_{41}(t) = i\sqrt{1 - T(t)}$. It then follows that $I_3(t) = T(t)I_c(t)$ and $I_4(t) = (1 - T(t))I_c(t)$, with $T(t)$ related to the applied external potential $U(t)$. By choosing a proper modulation of QPC, it is then possible to separate the electrons from the holes.

H. Inductance Matrices

We can write $\mathbf{M} = \mathbf{F}_{CL}\tilde{\mathbf{L}}_L^{-1}\bar{\mathbf{L}}\mathbf{L}_{LL}^{-1}\mathbf{F}_{CL}$, and given that $\mathbf{L}_{LK} = 0$, $\mathbf{L}_K = K$, with

$$\mathbf{F}_{CL} = \begin{pmatrix} 1 & 0 \\ 0 & 1 \end{pmatrix}, \tag{H.1}$$

and $\mathbf{F}_{KL} = (1, 1)$, we obtain

$$\mathbf{L}_{LL} = \mathbf{L} + \tilde{\mathbf{K}} \tag{H.2}$$

with the definition

$$\tilde{\mathbf{K}} = \mathbf{F}_{LK}^T \mathbf{L}_K \mathbf{F}_{LK} = K \begin{pmatrix} 1 & 1 \\ 1 & 1 \end{pmatrix}. \tag{H.3}$$

We then have $\mathbf{M} = (\mathbf{L} + \tilde{\mathbf{K}})^{-1}$. $\mathbf{M} \approx \mathbf{L}^{-1} - \mathbf{L}^{-1}\tilde{\mathbf{K}}\mathbf{L}^{-1}$.

Curriculum Vitae

January 2010	Dissertation in Theoretical Physics about *Quantum Control and Quantum Measurement in Solid State Qubits*, under the supervision of Prof. Dr. Guido Burkard.
2005 - 2009	Graduate student under the supervision of Prof. Guido Burkard. 05.2008 - 12.2009 University of Konstanz, Germany. 05.2008 - 05.2009 Scientific visit in Scuola Normale Superiore, Pisa, Italy. 05.2007 - 05.2008 RWTH Aachen, Germany. 09.2005 - 05.2007 University of Basel, Switzerland.
March 2005	Laurea in Theoretical Physics. Title of the thesis: *Entanglement and phase transitions in spin-1/2 chains*, under the supervision of Prof. Giuseppe Morandi.
1999 - 2005	Study Physics at the University of Bologna, Italy.
1999	Diploma di Maturita', Liceo Scientifico Niccolo' Copernico, Bologna, Italy.
25.09.1980	Born in Parma, Italy.

Publications

- E. Strambini, L. Chirolli, V. Giovannetti, F. Taddei, R. Fazio, V. Piazza, F. Beltram,
  Coherent detection of electron dephasing
  arXiv:0909.2197 (2009).

- Luca Chirolli, Guido Burkard,
  Quantum non-demolition measurements of a qubit coupled to a harmonic oscillator
  Phys. Rev. B **80**, 184509 (2009).

- Luca Chirolli, Guido Burkard,
  Decoherence in Solid State Qubits
  Advances in Physics **57**, 225 (2008).

- Matthias Braun, Luca Chirolli, Guido Burkard,
  Signature of chirality in scanning-probe imaging of charge flow in graphene
  Phys. Rev. B **77**, 115433 (2008).

- Luca Chirolli, Guido Burkard,
  Full control of qubit rotations in a voltage-biased superconducting flux qubit
  Phys. Rev. B **74**, 174510 (2006).